

**Proceedings of the 1999 Antenna Applications Symposium
Volume II**

Daniel H. Schaubert, et al.

**University of Massachusetts
Department of Electrical and Computer Engineering
Amherst, MA 01003**

September 1999

Approved for Public Release; Distribution Unlimited.

20010215 114



**AIR FORCE RESEARCH LABORATORY
Sensors Directorate
80 Scott Dr
AIR FORCE MATERIEL COMMAND
Hanscom AFB, MA 01731-2909**

Title of Report: PROCEEDINGS OF THE 1999 ANTENNA APPLICATIONS SYMPOSIUM

PUBLICATION REVIEW

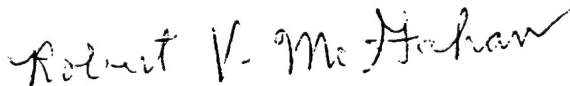
This report has been reviewed and is approved for publication.

APPROVED:



ZACHARY O. WHITE
Contract Monitor
Antenna Technology Branch
Electromagnetics Technology Division

APPROVED:



ROBERT V. McGAHAN
Division Technical Advisor
Electromagnetics Technology Division

REPORT DOCUMENTATION PAGE			Form Approved OMB No. 0704-0183	
Public reporting burden for this collection of information is estimated to average 1 hour per response, including the time for reviewing instructions, searching existing data sources, gathering and maintaining the data needed, and completing and reviewing the collection of information. Send comments regarding this burden estimate or any other aspect of this collection of information, including suggestions for reducing this burden, to Washington Headquarters Services, Directorate for Information Operations and Reports, 1215 Jefferson Davis Highway, Suite 1204, Arlington, VA 22202-4302, and to the Office of Management and Budget, Paperwork Reduction Project (0704-0188), Washington, DC 20503				
1. AGENCY USE ONLY (Leave blank)		2. REPORT DATE September 1999		3. REPORT TYPE AND DATES COVERED Final Report
4. TITLE AND SUBTITLE PROCEEDINGS OF THE 1999 ANTENNA APPLICATIONS SYMPOSIUM			5. FUNDING NUMBERS C: F19628-99-C-0053 PE: 62702F PR: 4600 TA: 01 WU: 01	
6. AUTHOR(S) Daniel H. Schaubert, et al				
7. PERFORMING ORGANIZATION NAME(S) AND ADDRESS(ES) University of Massachusetts Department of Electrical & Computer Engineering Amherst, MA 01003			8. PERFORMING ORGANIZATION REPORT NUMBER	
9. SPONSORING/MONITORING AGENCY NAME(S) AND ADDRESS(ES) Air Force Research Laboratory/SNHA 80 Scott Drive Hanscom AFB, MA 01731-2909			10. SPONSORING/MONITORING AGENCY REPORT NUMBER AFRL-SN-HS-TR-2000-008 (II)	
11. SUPPLEMENTARY NOTES SNHA Project Engineer: Zachary O. White, AFRL/SNHA, (781) 377-3191 Volume I contains pages 1 through 270 Volume II contains pages 280 through 538				
12a. DISTRIBUTION AVAILABILITY STATEMENT Approved for Public Release; Distribution Unlimited			12b. DISTRIBUTION CODE	
13. ABSTRACT (Maximum 200 words) The Proceedings of the 1999 Antenna Applications Symposium is a collection of state-of-the-art papers relating to phased array antennas, multibeam antennas, satellite antennas, microstrip antennas, reflector antennas, HF, VHF, UHF and various other antennas.				
14. SUBJECT TERMS Antennas Microstrip Multibeam Antenna Satellite Antennas Reflector Array Antennas Broadband Antennas HF, VHF, UHF			15. NUMBER OF PAGES 270	
			16. PRICE CODE	
17. SECURITY CLASSIFICATION OF REPORT Unclassified	18. SECURITY CLASSIFICATION OF THIS PAGE Unclassified	19. SECURITY CLASSIFICATION OF ABSTRACT Unclassified	20. LIMITATION OF ABSTRACT UL	

1999 ANTENNA APPLICATIONS SYMPOSIUM

Initial Bistatic Measurements of Electromagnetic Propagation in an Enclosed Ship Environment E.L. Mokole, M. Parent, J. Valenzi, E. Tomas, B.T. Gold, T.T. Street and S.N. Samaddar	1
Examining the Performance Benefits of Antenna Diversity Systems in Portable Wireless Environments P. Irazoqui-Pastor and J.T. Bernhard	30
The Circularly Polarized Cylindrical Patch Z. Sipus, N. Herscovici and D. Bonefacic	41
Study of Broadband Dielectric Resonator Antennas A.A. Kishk, A.W. Glisson, and G.P. Junker	45
Electrical Tuning of Integrated Mobile Phone Antennas J.P.Louhos and I. Pankinaho	69
Array Antenna Design for Base Station Application B. Johannisson and A. Derneryd	98
A Circular Coaxial Orthogonal Mode Junction Diplexer and Potential Benefit of Incorporated with Ridges and T-Septa in its Inner Conductor H.Z. Zhang	107
Low VHF Antenna Location and Design for the EZ-6B J. Lebaric and C.C. Miller	*
VHF or UHF Grounded Vertical Dipole V. Trainotti and J. Skora	124
Noise Contribution Analysis for the Arecibo Gregorian Radio Telescope G. Cortes-Medellin, P.F. Goldsmith, L. Baker, M.M. Davis and D.B. Campbell	145

*Not Included In This Volume

Methods of Moment Analysis of Electrically Large Square and Rectangular Loop Antenna with Non-Uniform Current C.P. Lim, L.W. Li and M.S. Leong	166
Dielectric Cover Effect on Mutual Coupling between Cylindrical-Rectangular Microstrip Antennas using FDTD J. Byun, F.J. Harackiewicz and J. Lindsey	183
Patch Antennas on Photonic Crystal Structures R. Gonzalo, B. Martinez, P. de Maagt and M. Sorolla	195
MEMS and Advanced Radar J. Smith	*
An Overview of Micro-Electro-Mechanical System (MEMS) J.R. Reid	*
Electromagnetic and Mechanical Modeling of Microwave/MW-Wave MEMS Switches J.B. Muldavin, N.S. Barker and G.M. Rebeiz	*
MEMS-Switched Reconfigurable Multi-Band Antenna: Design and Modeling W.H. Weedon and W.J. Payne and G.M. Rebeiz	203
Finite Dipole Arrays Over a Wideband R.C. Hansen	232
Spinning-Array 2-D Beam-Steering MMW Antenna V.A. Manasson, L.S. Sadovnik, V.A. Yepishin L. Timashpolsky and R. Mino	243
Low Sidelobe Partially-Overlapped Feed Network for Time Delayed Subarrays R.J. Mailloux	251
Experimental Radiation and Mutual Coupling Characteristics Of Dual-Polarized Tapered Slot Antenna (TSA) Arrays T.H. Chio, D.H. Schaubert and H. Holter	280
Ultra-Broadband Phased-Array Antenna W.R. Pickles and M. Kragalott	310

*Not Included In This Volume

An Affordable Scanning Array Using a Radant Lens	331
J.B.L. Rao, J.B. Evins, S.M. Brockett, M. Parent, J. Valenzi, D. Wilson, A. Moffat, S. Krystofik, J. Maciel, V. Philbrook and F. Ziolkowski	
Millimeter-Waves Radial-Line Slot Array Antenna	349
A.A. Boryssenko	
An Implementation of a 0.5 to 2.0 GHz Circular 360 Degree Direction Finding Antenna	374
T.R. Holzheimer	
Source Separation Operating on a Set of Collocated Antennas: Theory and Application in the H.F. Band (3-30 MHz)	405
C. LeMeins, Y. Erhel, L. Bertel and F. Marie	
Study of Aerial Target Radar Recognition by Method Of Backscattering Computer Simulation	431
J.D. Shirman, S.A. Gorshkov, S.P. Leshenko and V.M. Orlenko	
Radar Tracing of Stealth Targets in the Background Of Intensive Multiple Jamming	448
Y.N. Sedyshev	
Design of Ultra Wide Band Antennas for the Detection of Buried Objects	470
N. Verneuil and A. Bourdillon	
Ultra-Wide Band Impulse Antennas for Subsurface Radar Applications	478
A.A. Boryssenko	
Integrated Omni-Directional Microstrip Antenna System on A Ballistic Helmet	505
Dr. Probir K. Bondyopadhyay	
Circular Polarized Microstrip Lens Array Antenna System For Satellite Signal Reception	510
Dr. Probir K. Bondyopadhyay	
Performance Testing of a Wideband Phased Array for Shipboard Application	515
P. Beyak, D. Bobowicz, and D. Collier	

Identifiers for Proceedings of Symposia
The USAF Antenna Research and Development Program

Year	Symp. No.	Identifier
1951	First	
1952	Second	C054 520
1953	Third	AD63794
1954	Fourth	AD63139
1955	Fifth	AD90397
1956	Sixth	AD114702
1957	Seventh	AD138500
1958	Eighth	AD301151
1959	Ninth	AD314721
1960	Tenth	AD244388 (Vol. 1)
		AD319613 (Vol. 2)
1961	Eleventh	AD669109 (Vol. 1)
		AD326549 (Vol. 2)
1962	Twelfth	AD287185 (Vol. 1)
		AD334484 (Vol. 2)
1963	Thirteenth	AD421483
1964	Fourteenth	AD609104
1965	Fifteenth	AD474238L
1966	Sixteenth	AD800524L
1967	Seventeenth	AD822894L
1968	Eighteenth	AD846427L
1969	Nineteenth	AD860812L
1970	Twentieth	AD875973L
1971	Twenty-First	AD888641L
1972	Twenty-Second	AD904360L
1973	Twenty-Third	AD914238L

Antenna Applications Symposium

		TR#	ADA#
1977	First	None	955413
1978	Second	None	955416
1979	Third		077167
1980	Fourth		205907
1981	Fifth		205816
1982	Sixth		129356
1983	Seventh		142003; 142754
1984	Eighth	85-14	153257; 153258
1985	Ninth	85-242	166754; 165535
1986	Tenth	87-10	181537; 181536
1987	Eleventh	88-160	206705; 206704
1988	Twelfth	89-121	213815; 211396
1989	Thirteenth	90-42	226022; 226021
1990	Fourteenth	91-156	237056; 237057
1991	Fifteenth	92-42	253681; 253682
1992	Sixteenth	93-119	268167; 266916
1993	Seventeenth	94-20	277202; 277203
1994	Eighteenth	95-47	293258; 293259
1995	Nineteenth	96-100	309715; 309723
1996	Twentieth	97-189	341737
1997	Twenty First		
1998	Twenty Second	1999-86	
1999	Twenty Third		

Experimental Radiation and Mutual Coupling Characteristics of Dual-Polarized Tapered Slot Antenna (TSA) Arrays

T-H. Chio¹, D.H. Schaubert² and H. Holter³

¹DSO National
Laboratory,
Republic of Singapore

²Antenna Laboratory, U. of
Massachusetts, Amherst, MA
01003, USA.

³Royal Institute of
Technology, Stockholm,
Sweden

Abstract: Two 8×9 dual-polarized TSA arrays are designed and built based on infinite array calculations. In an infinite array environment, scanning up to $\theta = 50^\circ$, they are expected to have about 4.2:1 and 5.8:1 bandwidth respectively. Plated-through vias are used to simplify the construction process. Simulations showed that the vias also eliminated most of the H-plane scan anomalies that are typically associated with these arrays. This paper presents experimental radiation characteristics and mutual coupling results from these arrays. The results showed that finite array effects are very severe at the low end of the operating band. Also, cumulative mutual coupling contribution from co-polarized elements is more significant than that from cross-polarized elements. The results suggest that a TSA array should be more than $4\lambda_0$ in dimension so that the center element sees a large array environment.

I. Introduction

Since its introduction by Lewis *et. al.* [1] in 1974, the TSA antenna has been touted as a potential candidate for wideband, widescan phased array applications. There has been some progress recently when [2], [3] presented design data for large single-polarized TSA array. In a more recent development, Wunsch [4] presented a full-wave MoM analysis program that is capable of analyzing dual-polarized infinite TSA arrays. In an independent development Holter [5] presented a Finite Difference Time Domain (FDTD) code that allows the dual-polarized TSA infinite array to be analyzed efficiently. A unit cell and a small array are shown in Fig. 1.

In a parameter study [6], it is shown that a large wideband, widescan, dual-polarized TSA array is indeed possible. The design example in [6] has a bandwidth of about 4.5:1, up to $\theta = 50^\circ$ in all scan planes. Generally, the high end of the operating band is limited by H-plane scan anomalies that typically characterize such array. Using [5], it was found that most of the H-plane scan anomalies are eliminated by strategic placement of plated-through vias in the ground plane of the slotline [7]. It extends the bandwidth of the array to about 5.8:1 while scanning up to $\theta = 50^\circ$ in all planes. However, at the low end of the operating frequency band, each antenna element is small, typically less than one-tenth of a wavelength. The TSA array was designed with data from the parameter

study of the infinite array and the extent of the impact of its small size on array performance was not known. Therefore, the focus of this work is a relatively low cost experimental investigation of a small dual-polarized Tapered Slot Antenna (TSA) array. The objective of this paper is to present measured radiation and mutual coupling data that may be useful to array designers and that may point towards the required size of the TSA array so that infinite array design data may be valid.

Section II describes the design considerations and fabrication procedures. The data from the parameter study [6] are used to design two dual-polarized TSA arrays. Practical issues like material selection and fabrication process are addressed. Section III presents the results. The mutual coupling coefficients between elements are measured. They are analyzed at various frequencies to observe the effects of the finite size of the array. The "active" reflection coefficients are also computed and presented. The "active" antenna patterns are measured in an anechoic chamber. The gain obtained is compared with the theoretical gain of a single element. Co- and cross-polarization radiation patterns are also given for the cardinal planes and $\phi = 45^\circ$. The results are analyzed and discussed at various points in this section.

II. Design Procedure

This section outlines the design procedure and considerations. The design parameters are obtained from the parameter study [6]. The parameters are frequency scaled to make use of commercially available materials. Considerations are also given to the fabrication and assembly process. The details are given below.

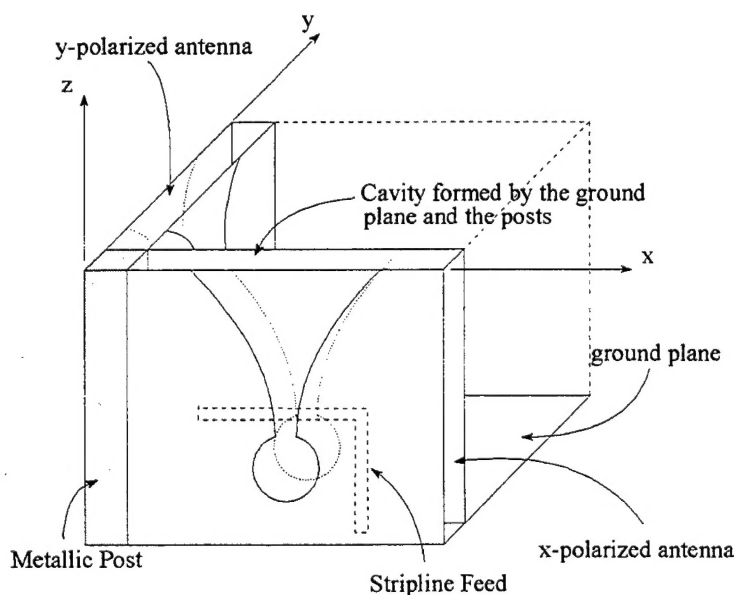


Fig. 1a. Dual-polarized TSA element: unit cell.

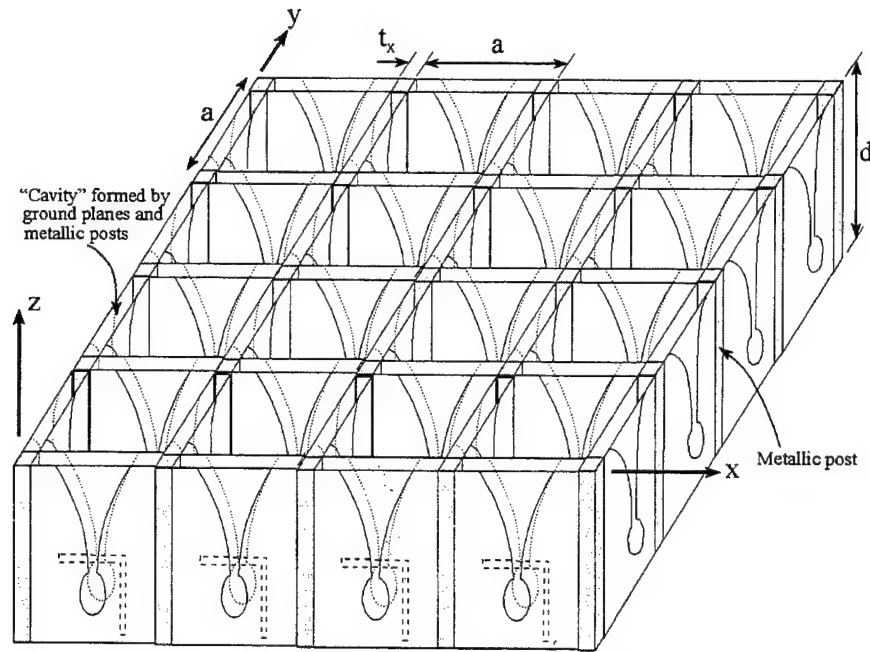


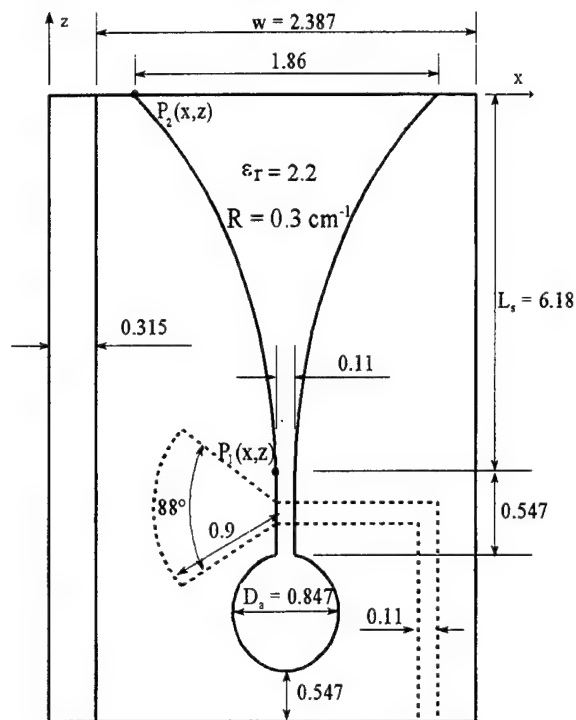
Fig. 1b: A small dual-polarized TSA array.

A. Design considerations

A number of parameters (the stripline-slotline transition, stripline stub and thickness and dielectric constant of the substrate) affect the performance of the array. This was studied in detail in [2] and [3] for single-polarized TSA arrays. When the data are used in dual-polarized TSA array designs, the results are comparable with that of the single-polarized version. The parameter study in [6] presents the effects of various parameters on the performance of TSA element in an infinite dual-polarized array environment. The parameters that strongly impact the performance are the circular slotline cavity D_a , the length of the tapered slotline L_s , the exponential opening rate of the tapered slotline R and the element width w (see Fig. 2). The design example in [6] illustrated that one can choose a particular parameter with good performance in a sub-band to mitigate another that degrades the performance in that sub-band. Typically, as the array is scanned off-broadside, its performance improves when scanning in the E-plane but deteriorates when scanning in the H-plane. For a given scan angle θ in intercardinal scan planes, the performance is somewhat like a weighted average of the E- and H-plane scans at that angle. This means that the array's overall performance is bounded by its performance in the E- and H-plane scans. The collective results of [2], [3] and [6] provided a guide to design a large dual-polarized TSA array.

Using the results of the parameter study as a guide, the design (see Fig. 2) for substrate thickness of 0.315cm and $\epsilon_r = 2.2$ (Taconic® 2×62 mils TLY-5) is chosen. Using the FDTD code in [5], the predicted VSWR for this antenna for H-plane scan, $\theta = 50^\circ$, is shown in Fig. 3. VSWR vs. frequency plots for H-plane

scans are shown here because they represent the worst performance of the array. In an infinite array environment, this design is expected to have about 4.2:1 bandwidth, scanning up to $\theta = 50^\circ$ in all planes.



All dimensions in cm

Fig. 2: Final design parameters.

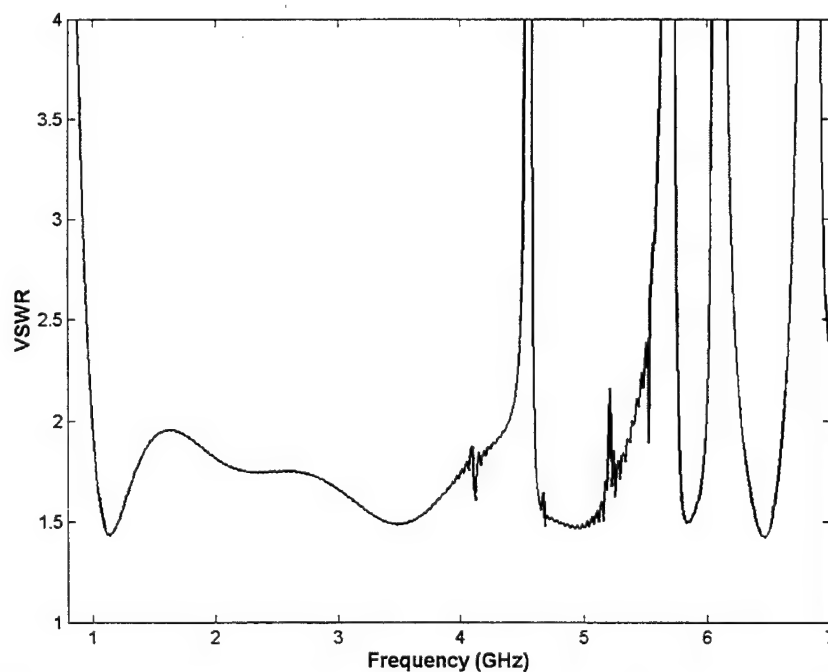


Fig. 3: VSWR vs. frequency plot of the design in Fig. 2; H-plane scan, $\theta = 50^\circ$.

B. Fabrication process

The stripline structure is constructed using standard photolithography techniques and bonded together by Rogers® 3001 bonding film. To construct the dual-polarized TSA array, the PC boards are slotted so that they can be interleaved as shown in Fig. 4. The three small slots shown below the circular cavities are provisions for a low-loss transition from a standard SMA connector to the stripline. However, a troublesome characteristic of the dual-polarized TSA is that there must be good electrical contact between all corners of the deep and narrow boxes of the unit cell in Fig. 1a. It is shown in [8] that several severe resonances will occur in single-polarized TSA arrays if the electrical contracts are not present. This effect is also observed in the dual-polarized arrays. To overcome this problem, plated-through vias, connecting the ground planes of the stripline feed, are introduced to simulate the narrow metallic walls between the ground planes as shown in Fig. 5. The array is assembled by soldering the intersecting corners of orthogonal PC boards along the entire length of the antenna element. Two 8×9 arrays were built; 8 elements in E-plane and 9 elements in the H-plane. The final configurations of the elements for the two arrays, shown in Figs. 5a and b, have exactly the same dimensions except that the vias are placed differently. The array with the vias that are placed along the edge of the element is named "SV" (for *straight vias*), while the array with vias that are placed along the contour the exponential taper is named "CV" (for *contoured vias*).

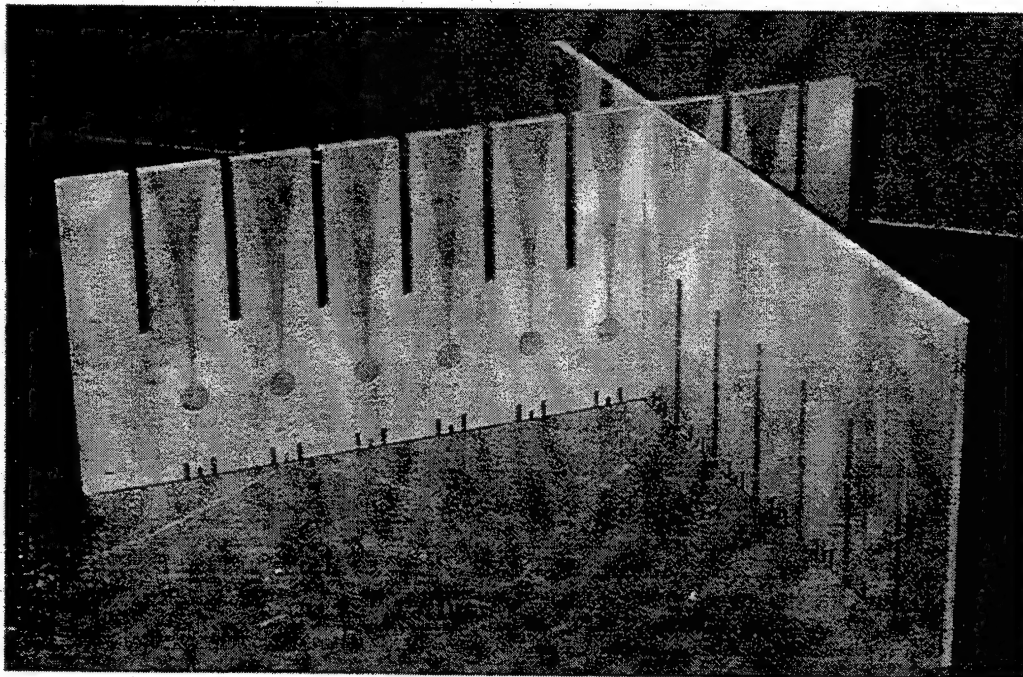


Fig. 4: Interleaved PC boards to form dual-polarization.

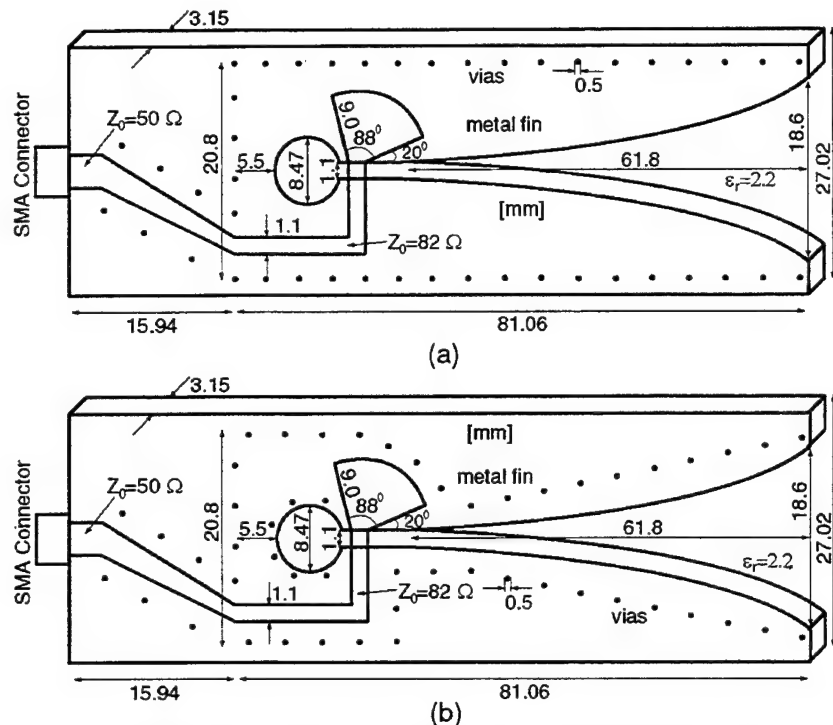


Fig. 5: Schematic diagram showing the plated-through vias of (a) "SV" and (b) "CV".

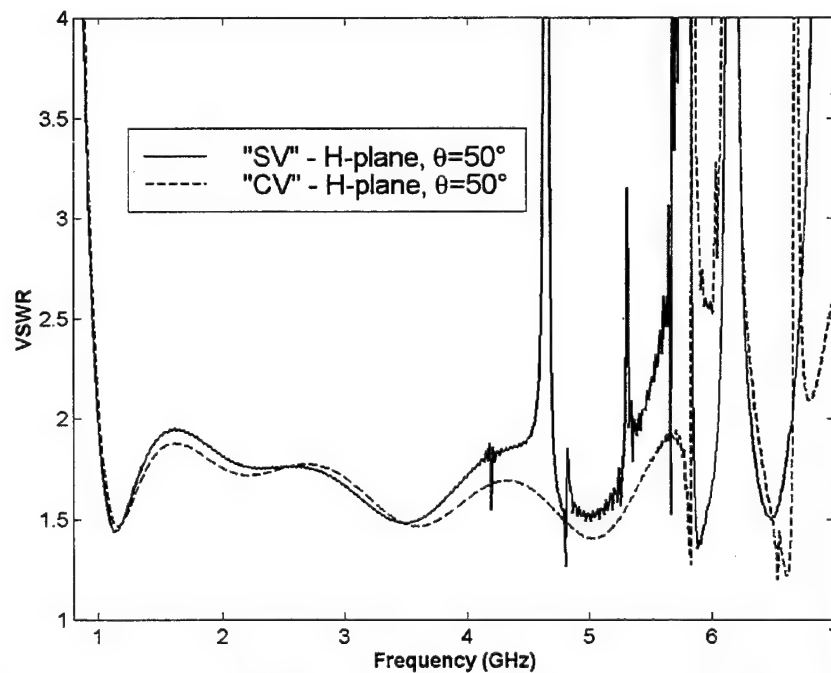


Fig. 6: Comparing VSWR vs. frequency performance of "SV" and "CV".

Fig. 6 shows the simulated results of "SV" and "CV" in the infinite array environment. Compared to Fig. 3, other than a very slight frequency shift, the results of "SV" showed that the vias perform essentially the same as solid metal

posts. More interestingly, when the vias are placed as in "CV", almost all of the H-plane scan anomalies are eliminated. In [7], it was found that some of these anomalies are related to resonance due to the cavity formed by the metallic posts and the ground planes of the stripline. By placing the plated-through vias strategically, most H-plane scan anomalies are eliminated. The effects on the D-plane scan angles are similar to the H-plane scans while there are no effects at broadside and E-plane scan angles. At about 6.3 GHz, the onset of the grating lobe can be seen.

Figs. 7 and 8 show the assembled array with the connectors. In Fig. 7, the dots that run along the exponential taper are the plated-through vias that connect the ground planes of the stripline feed. In this design, the ground plane at the bottom of the larger square cavity (see Fig. 1a) has been omitted, which simplifies the assembly process further. This is shown in Fig. 8. Using the FDTD code of [5], it was determined that excluding the ground plane does not affect the performance of an infinite TSA array in any significant way. This is because the large cavity is like a square, air-filled waveguide that is operated below cut-off. However, an effective ground plane is maintained within the dielectric-filled region by a row of plated-through vias placed below the circular slotline cavity.

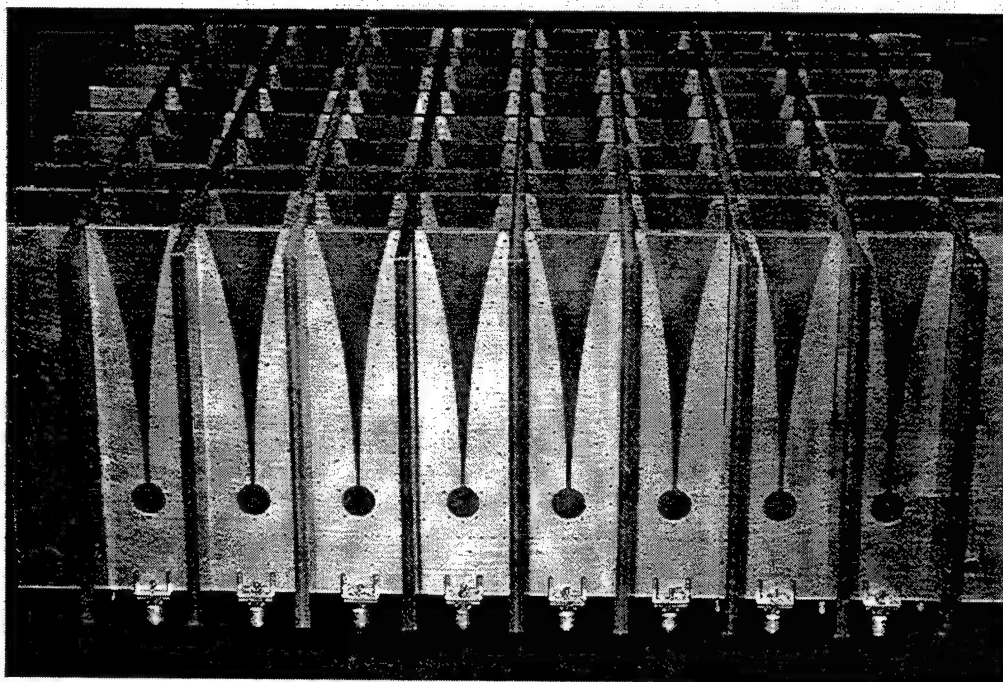


Fig. 7: Front view of the dual-polarized TSA array

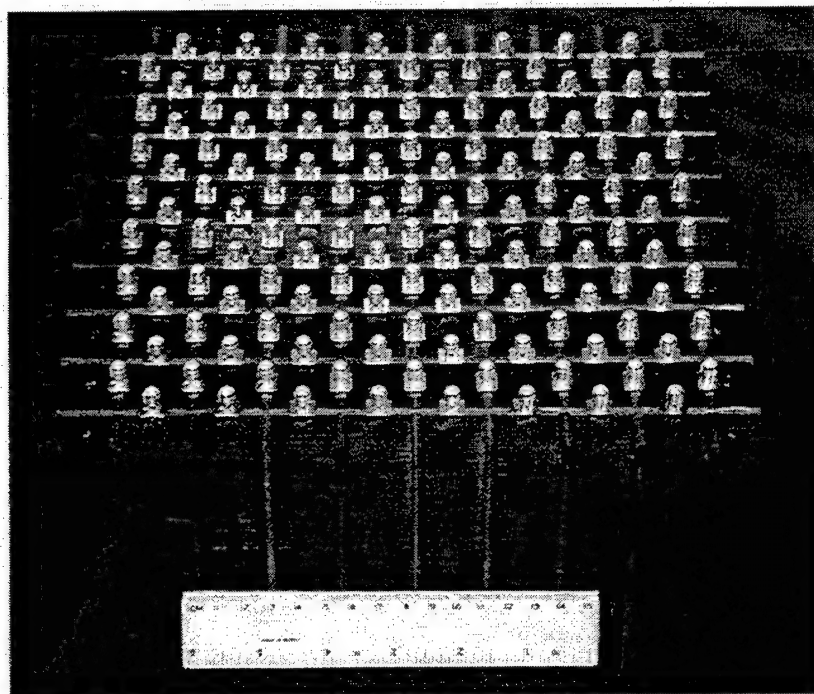


Fig. 8: Bottom view of dual-polarized TSA array

C. *Experimental Setup*

For identification purposes, the elements are referred to using their assigned numbers, as shown in Fig. 9. The first and second digits refer to the square cells in the x- and y-directions respectively. A "1" in the third digit refers to the x-polarized element while a "2" refers to the y-polarized element, located at the bottom and left side of that cell, respectively. The x-polarized elements nearest to the center of the array are "451", "551" while the y-polarized center elements are "542" and "552". Most of the experiments are performed on these center elements.

For the "SV" and "CV" arrays, two sets of experiments were performed. The *first* was to measure the radiation characteristics, i.e. "active" element patterns and gain of the center elements. The co- and cross-polarized element patterns are taken for a selected center element, e.g. "542", with the other elements terminated in match loads. The *second* was to measure the coupling coefficients (scattering parameters) between a selected center element and the rest of the elements in the array using a vector network analyzer. For these measurements, the antenna is placed in the UMass Antenna Laboratory's ground-plane/anechoic chamber. From the coupling coefficients, a number of parameters like the "active" reflection coefficient, the "active" element patterns are computed. Rigorously, the "active" element pattern and "active" reflection coefficient techniques are only valid for infinite periodic arrays. However, these methods are used here as an approximation so that the effects of the mutual

coupling and the finite size of the array can be studied.

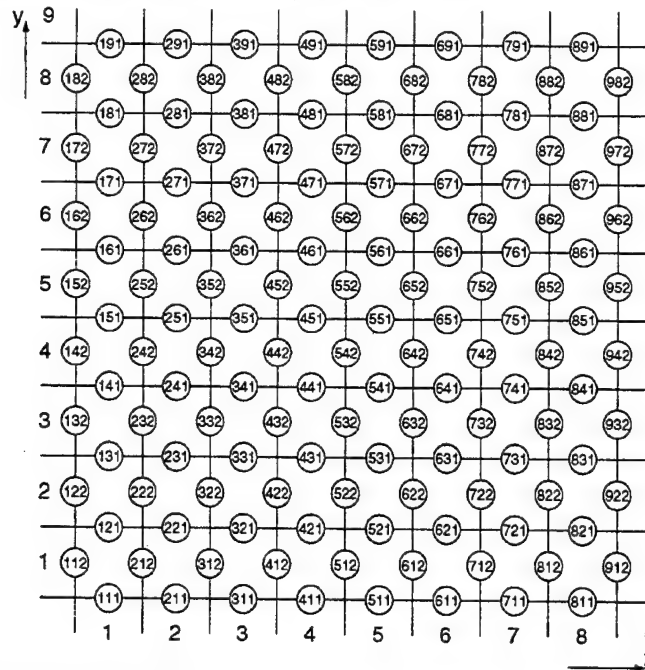


Fig. 9: Bottom view of array; element connector numbering system

III. Results and Discussions

A. Radiation characteristics

Due to the limitations of the anechoic chamber, the pattern and gain measurements are taken for frequencies between 2.6 GHz and 5.8 GHz. Element patterns for the frequencies below 2.6 GHz may be estimated from the “active” reflection coefficient computed from mutual coupling measurements. This is based on the assumption, although not rigorous for a finite array, that there is direct one-to-one relationship between the magnitude of the “active” reflection coefficient and the “active” element pattern [9], [10].

Figs. 10 – 11 show the H- and E-plane co-polarized patterns of “SV” at 2.8 and 4.8 GHz, and their associated cross polarization. The maximum gain of each pattern is also shown in the figures. The H-plane patterns are taken with element “542” while the E-plane patterns are taken with element “451”. Notwithstanding the ripples in the patterns, the “active” element has wide beamwidth in both the H- and E-planes. Typically, the ripples vary slower at lower frequencies than at higher frequencies indicating that they may be finite array effects although a simple relationship between the size of the array and the ripples at all frequencies is not found.

The cross-polarization levels in both planes and at all the frequencies are no worse than -14.7 dB. This could be better if the orthogonal PC boards are

assembled with tighter tolerance. Results from "CV" are very similar and therefore not shown here. Furthermore, the effects of plated-through vias, placed along the contour of the exponentially tapered slotline of "CV", are not obvious in the element patterns of these small arrays.

Element patterns are also taken in the D-plane. In this case, the transmitter horn is fixed at $\phi = 45^\circ$ while "SV" is scanning in the $\phi = 45^\circ$ plane. This is the co-polarized direction of element "542". Next, the transmitter horn is rotated by 90° to $\phi = 135^\circ$, which is the cross-polarized direction of the element. Typical co- and cross-polarization patterns are shown in Fig. 12. Figs. 12a and b show the co- and cross-polarized D-plane patterns at 3.6 GHz and 5.4 GHz, respectively. The ripples of the D-plane patterns are more severe than those of the cardinal plane scans at comparable frequencies. However, as frequency increase, the ripples tend to smooth out. The cross-polarization levels in the D-plane scan, in general, are also higher than those of the cardinal plane scans. The cross-polarization level remains relatively good up to beam angles of about $\theta = 30^\circ$ and increases beyond that. Cross-polarization levels for these measurements reach a maximum at around $\theta = 60^\circ$. It was shown in [4] that TSA arrays are linearly polarized in their principal planes, but they become elliptically polarized in the intercardinal planes. This contributes to the higher cross-polarization levels in the D-plane.

The "active" element gain at a specified scan angle, versus frequency (2.6 GHz – 5.8 GHz) was also measured in the anechoic chamber for "SV" and "CV". 801 frequency points were taken in each standard waveguide horn band. The results are compared with those computed from measured coupling coefficients (see next section) and from the infinite array theory using

$$G^e(\phi, \theta) = \frac{4\pi A}{\lambda_0^2} (1 - |\Gamma_a(\phi, \theta)|^2) \cos \theta. \quad (1)$$

where A is the area of a unit cell and Γ_a is the "active" reflection coefficient. Figs. 13 and 14 show the plots for "SV" at broadside and $\theta = 50^\circ$ in E-plane. The results for "CV" are very similar and are not shown. The gap between 3.8 GHz and 4.0 GHz is because the standard gain horn information is not available at those frequencies.

Generally, the agreement with all three methods for broadside and E-plane scan is reasonable. However, in H-plane scan, $\theta = 50^\circ$ (see Fig. 15), the agreement is not as good. Where H-plane scan anomalies are predicted between 4.0 and 5.3 GHz for "SV", the measured gain has large swings. Comparatively, the results for E-plane (see Fig. 14) do not vary as much in the same frequency band.

Finally, the measured element gain of "SV" and "CV" for H-plane scan, $\theta = 50^\circ$, are compared in Fig. 16 to observe the effects of vias that are placed along the contour of the tapered slotline. The gain-frequency plots of the two arrays

show the same trend. However, at frequencies between 4.0 and 5.0 GHz, where anomalies in “SV” are expected, the vias of “CV” seem to smooth out the large fluctuations. This indicates that the vias placed along the contour of the array element improve the performance of the array at those frequencies where abnormal results are expected.

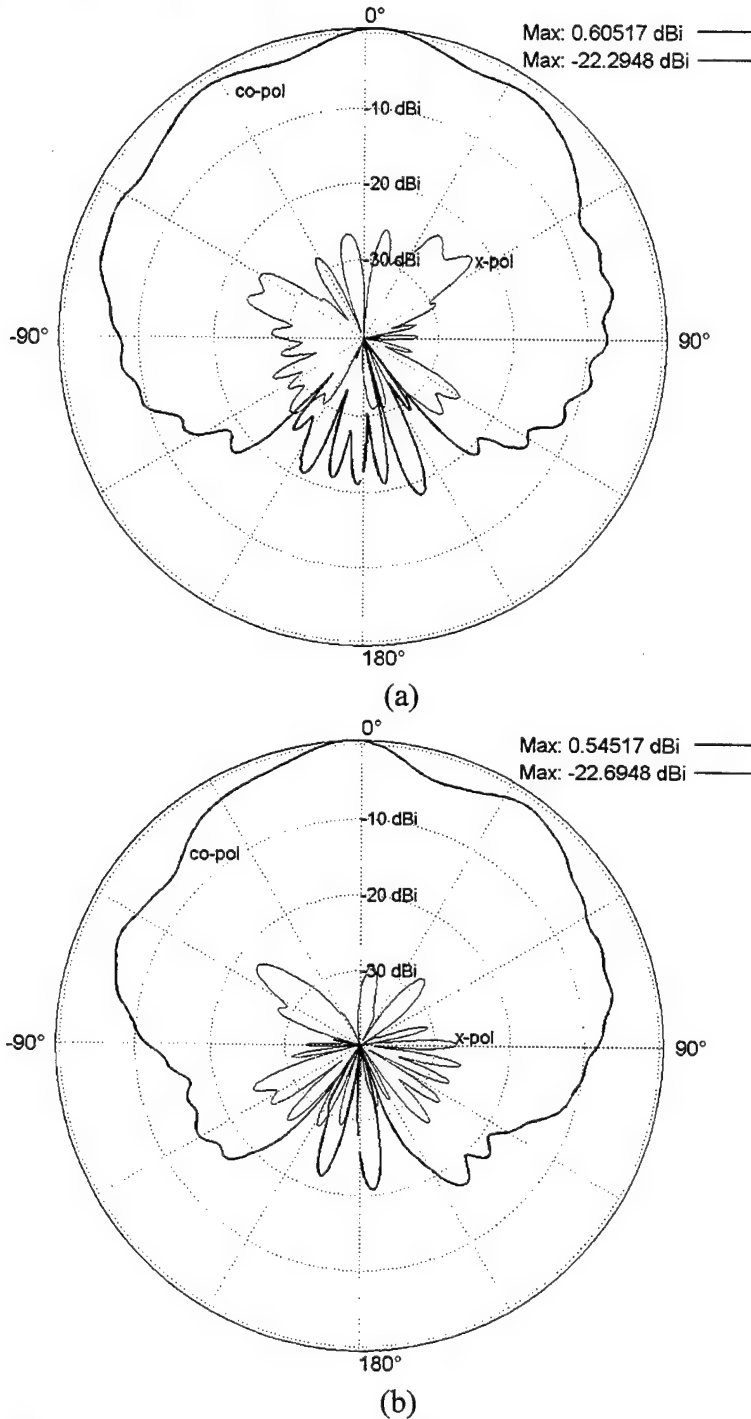
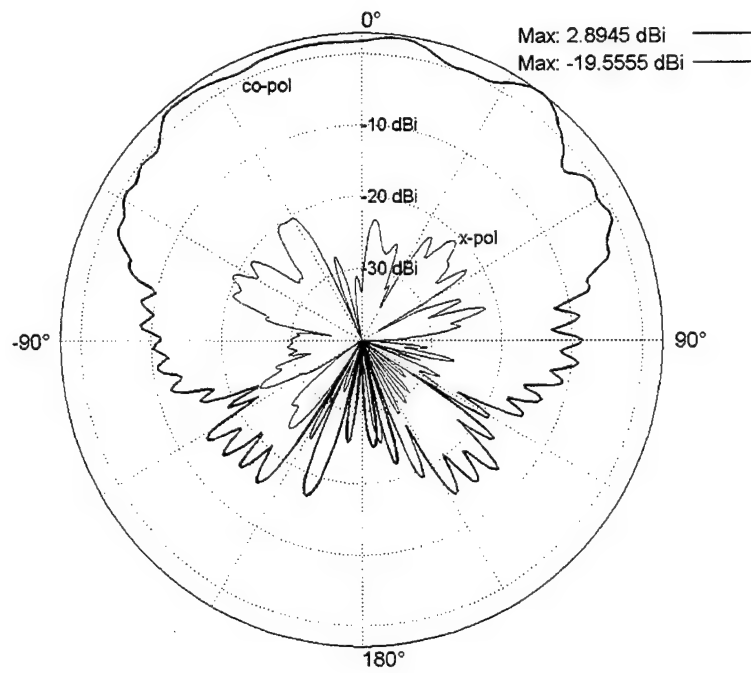
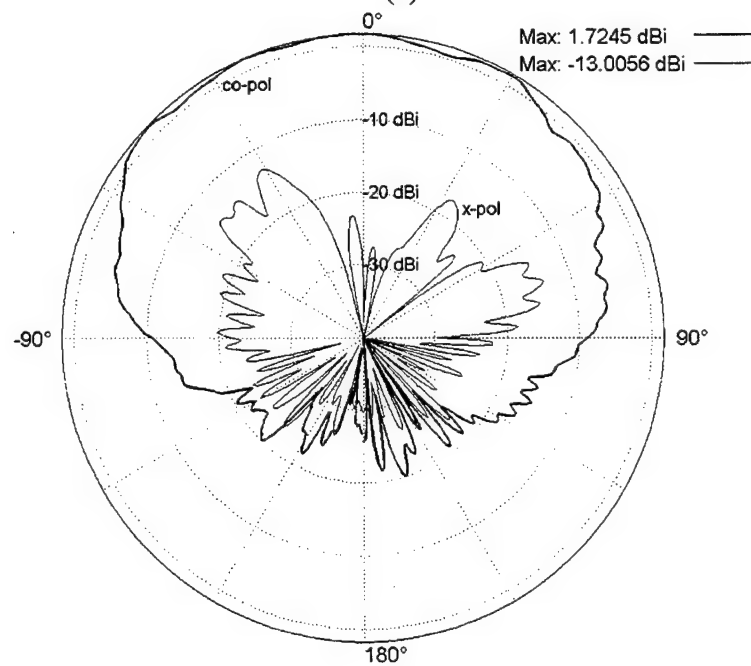


Fig. 10: Measured pattern and gain (in dBi) of center elements, freq = 2.8 GHz:
(a) H-plane scan of element “542”, (b) E-plane scan of element “451”.

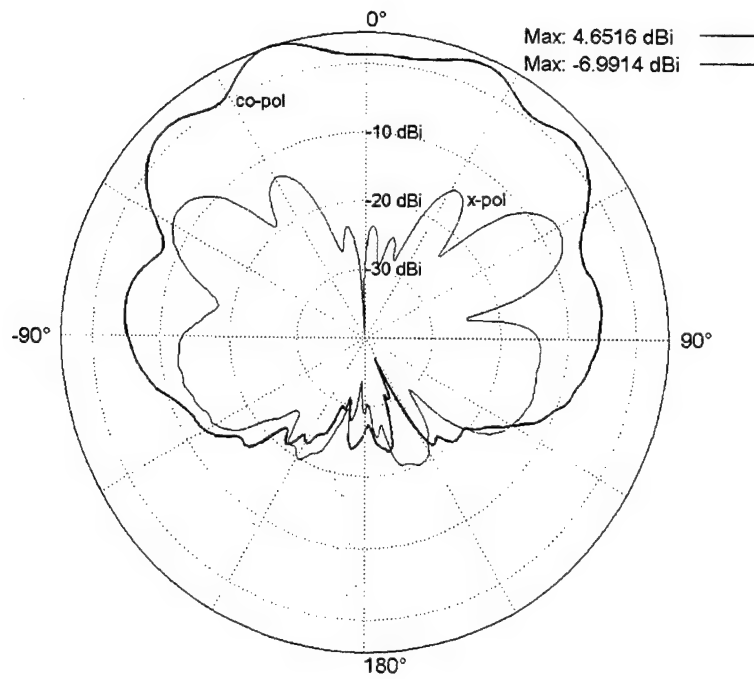


(a)

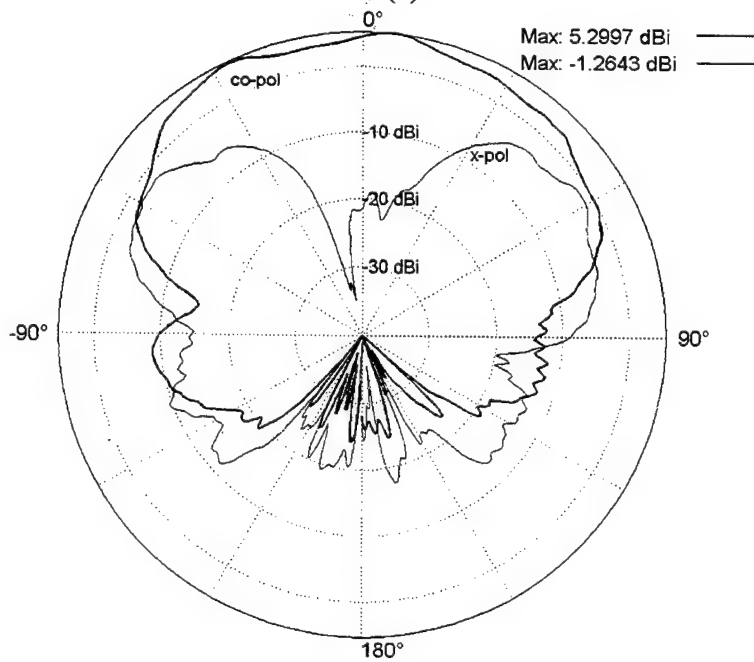


(b)

Fig. 11: Measured pattern and gain (in dBi) of center elements, freq = 4.8 GHz:
(a) H-plane scan of element "542", (b) E-plane scan of element "451".



(a)



(b)

Fig. 12: Measured pattern and gain (in dBi) of center element "542", D-plane scan, (a) freq = 3.6 GHz, (b) freq = 5.4 GHz.

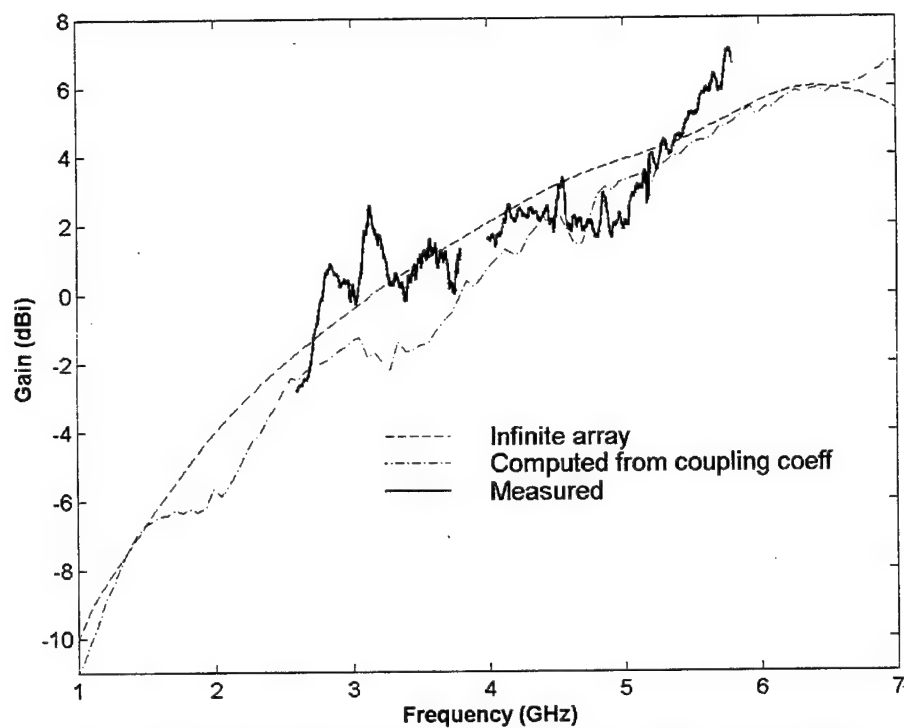


Fig. 13: "Active" element gain of "SV", broadside scan angle.

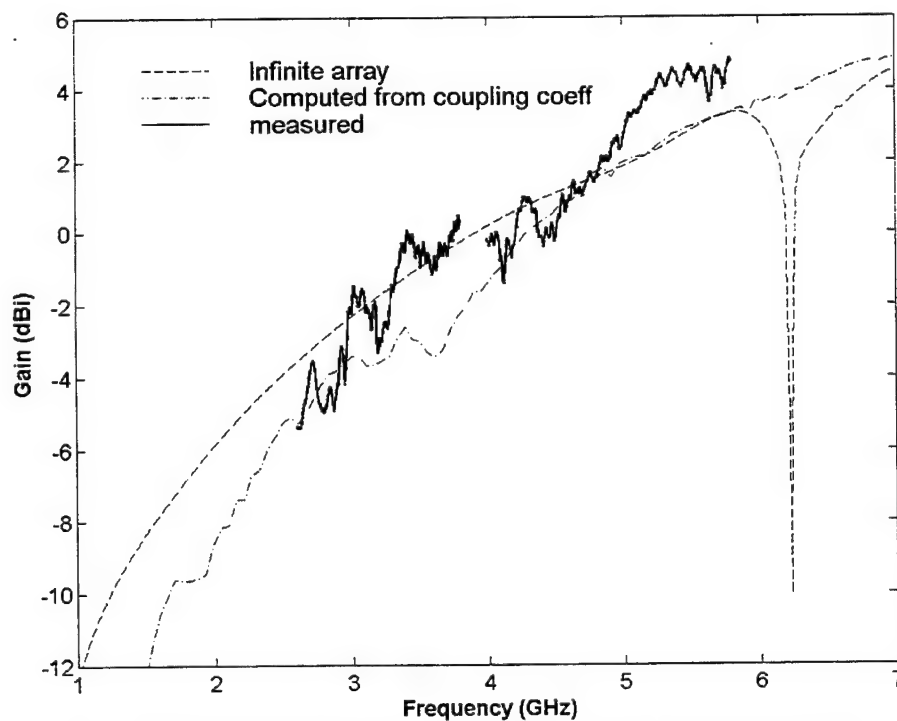


Fig. 14: "Active" element gain of "SV", E-plane scan, $\theta = 50^\circ$.

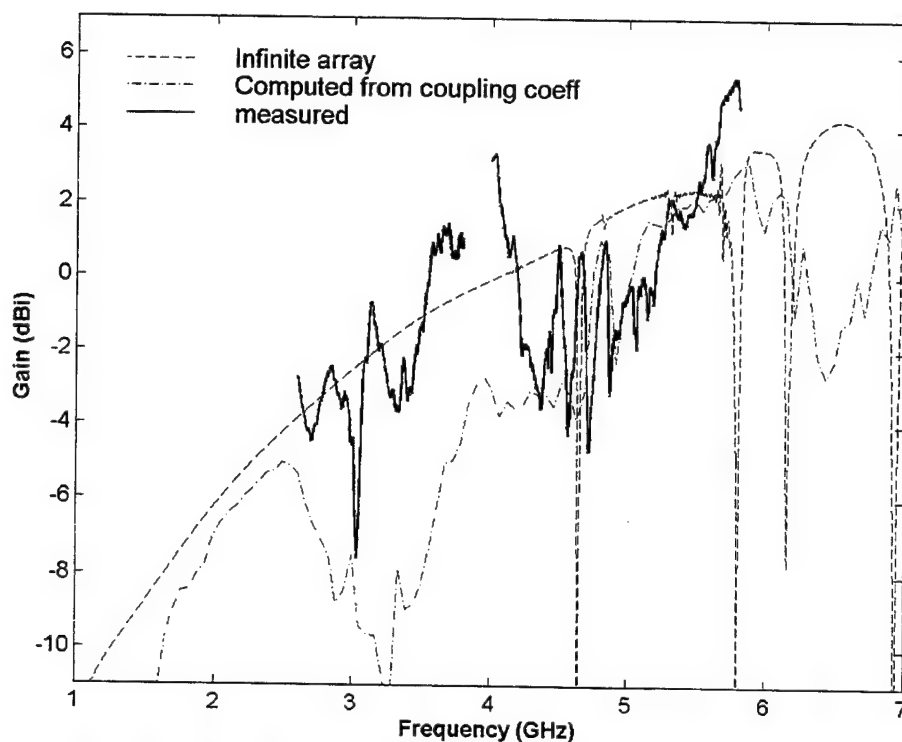


Fig. 15: "Active" element gain of "SV", H-plane scan, $\theta = 50^\circ$.

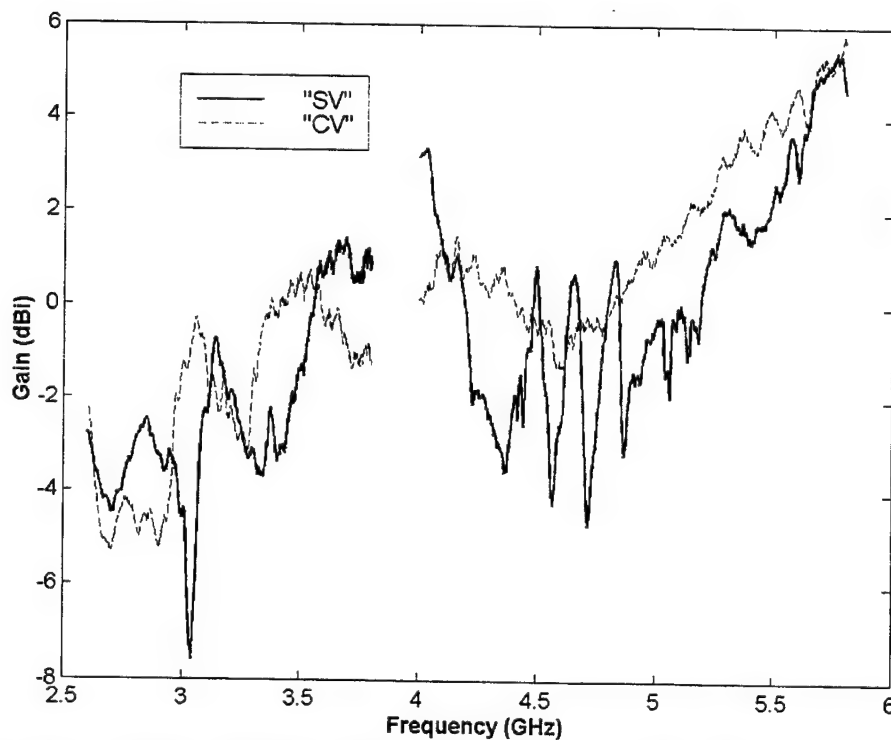


Fig. 16: "Active" element gain of "SV" and "CV", H-plane scan, $\theta = 50^\circ$.

B Mutual Coupling measurements and analysis

The coupling coefficients C_m between a selected center element, element "542" in this case, and all of the other elements in the array were measured with a vector network analyzer. Denoting the center element "542" by the index $m = 0$ and numbering all other elements consecutively, an approximation to the "active" reflection coefficient can be computed by evaluating

$$\Gamma_a(\phi, \theta) = \sum_{m=0}^M C_m e^{jkx_m \cos \phi \sin \theta} e^{jky_m \sin \phi \sin \theta} \quad (2)$$

where M is the total number of elements in the array, C_m is the complex coupling coefficient between element "542" and m^{th} element in the array, and x_m and y_m are the coordinates of the m^{th} element relative to element "542". C_0 is the reflection coefficient of the 0^{th} element when all other elements are terminated in 50Ω loads. The rest of the variables are defined in the usual manner.

VSWR is computed from the "active" reflection coefficient, Γ_a . Fig. 17 shows the VSWR of "SV" and "CV" at broadside beam angle. In Fig. 17, the expected VSWR of an "active" element in an infinite array environment is also shown. The agreement between the infinite array results and the measured results is poor. This may be due to the finite array effect. On closer examination, one side of the array measures about 21.6 cm. At the lowest frequency of 1 GHz, each side of the array is only $0.72\lambda_0$. Therefore, the center element of the array is not expected to perform as if it is in an infinite array environment. Another indication of the finite array effect is the two peaks (at about 2.0 and 3.4 GHz) seen in the VSWR plots in Fig. 17. The two peaks are approximately about 1.4 GHz apart, which translates to a wavelength of about 21.4 cm which is in close agreement with the length of one side of the array.

Another experiment was carried out to investigate the effects of the finite array. When computing the "active" reflection coefficient Γ_a (Eqn. 2) at broadside scan angle for "SV", the coupling coefficients due to elements in the outer-most rings were excluded. In the first case, one ring of elements was removed, and in the second, two rings were removed. The corresponding VSWR are shown in Fig. 18. The results obtained from the full 8×9 array are also shown for comparison. At frequencies from 1.0 – 5.0 GHz, the VSWR plots differ significantly. However, at frequencies above 5.3 GHz, all the three cases agree quite well. This indicates that the center element starts to perform as if it is in an infinite array environment only at frequencies where the size of the array is about $4\lambda_0$. This is consistent with measured results from a 10×10 single-polarized TSA array [11].

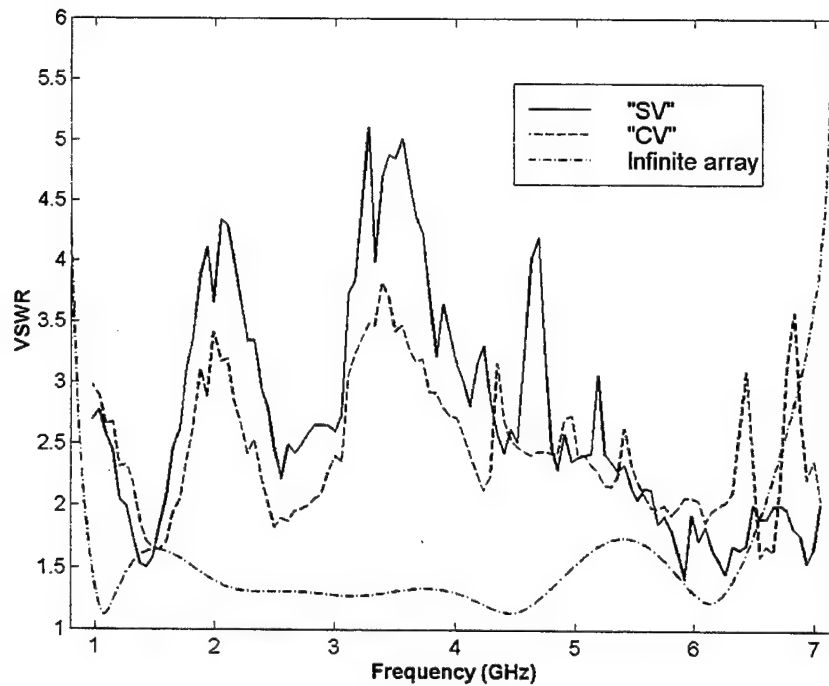


Fig. 17: VSWR of “active” element computed using measured coupling coefficients C_m and VSWR expected in an infinite array environment: broadside scan.

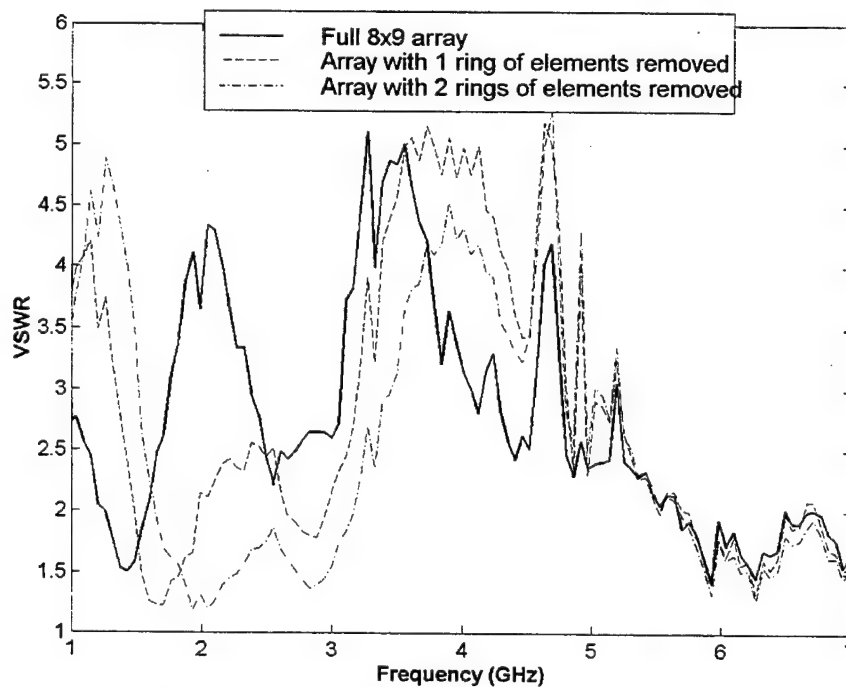


Fig. 18: Effects on VSWR when rings of elements are removed.

Next, the mutual coupling characteristics between the center element and every other element of the “SV” array are investigated. Figs. 19 and 20 show the magnitude of coupling coefficients between “542” and the y-directed elements

(i.e. co-polarized elements with respect to "542") of the central column and row of the array respectively. Figs. 21 and 22 show the magnitude of coupling coefficients between "542" and the x-directed elements (i.e. cross-polarized elements with respect to "542") of the central column and row of the array respectively. $|S_{11}|$ is used for self-coupling terms, i.e. the "542" - "542" term. Note that the contour plots in Fig. 19 are quite similar to Fig. 20. Comparing Figs 21 and 22 yields similar results. This indicates that the coupling mechanism is dependent on the how the element is oriented with respect to another, and also a function of distance.

For mutual coupling between co-polarized elements in the same column (see Fig. 19), coupling coefficients remain somewhat constant for elements near to element "542" at all frequencies while mutual coupling drops off more rapidly at higher frequencies for outer elements. Coupling between co-polarized elements that are in the same row remains relatively strong for elements adjacent to "542" but decay more rapidly for other elements when compared to similarly located co-polarized elements in the same column as "542" (see Fig. 20). For mutual coupling between cross-polarized elements, except for the deep null in Figs. 21 and 22 at about 1.5 GHz, there is a tendency for the coupling coefficients to diminish faster with respect to distance as frequency increases. This is expected since the array is electrically larger at higher frequencies and distances are greater with respect to the wavelength.

Next, the coupling coefficients between "542" and all the other elements are plotted for 1.2 GHz, 3.0 GHz and 4.8 GHz in Figs. 23, 24 and 25, respectively. Since element "542" is not exactly in the center of the array, some contour plots are slightly asymmetric. Part (a) of each figure shows magnitude of coupling coefficients with the y-directed elements while part (b) shows the same with the x-directed elements. These figures show the rate at which the magnitude of the coupling coefficients decays with respect to distance at the said frequencies.

Fig. 23a shows the mutual coupling from co-polarized elements at 1.2 GHz. Below 2.0 GHz, coupling from co-polarized elements looks similar to that of Fig. 23a where the coupling decays slower in the principal planes. Figs. 24a and 25a show the plots for 3.0 and 4.8 GHz. These plots are typical mutual coupling plots between co-polarized elements above 2.0 GHz. Note that the rate of decay in all direction is lower at 3.0 GHz than at 4.8 GHz. This indicates that mutual coupling from outer elements at the edge of the array is more important at lower frequencies than at higher frequencies. Also, in the D-plane, the rate of decay is lower when compared to the same at frequencies below 2.0 GHz.

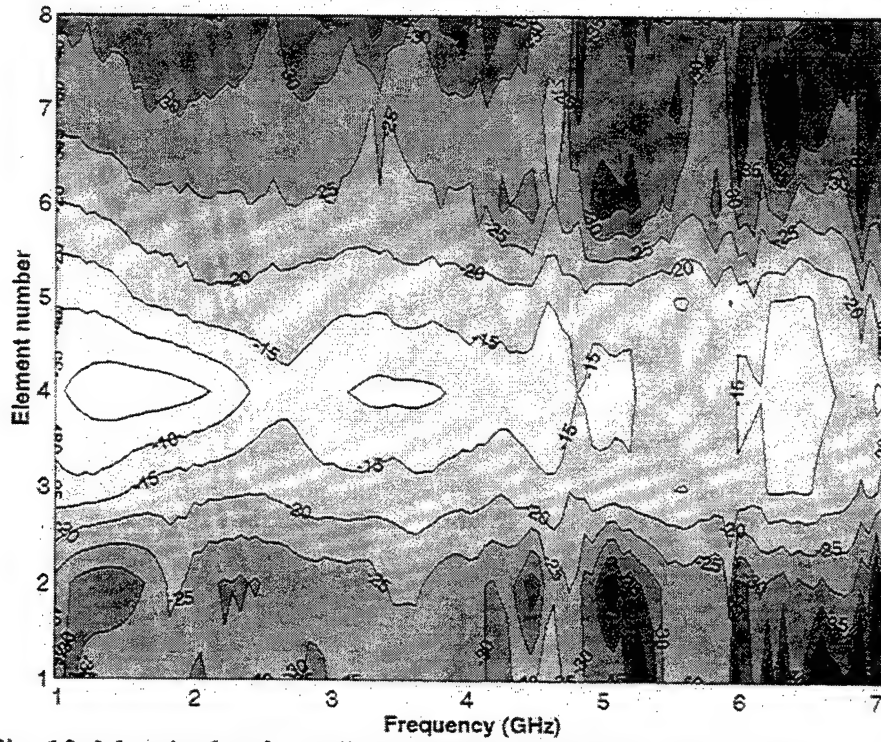


Fig. 19: Magnitude of coupling coefficient between "542" and y-directed elements "512", "522", "532", "542" ($|S_{11}|$ is used), "552", "562", "572" and "582" of "SV". Contour intervals are 5 dB.

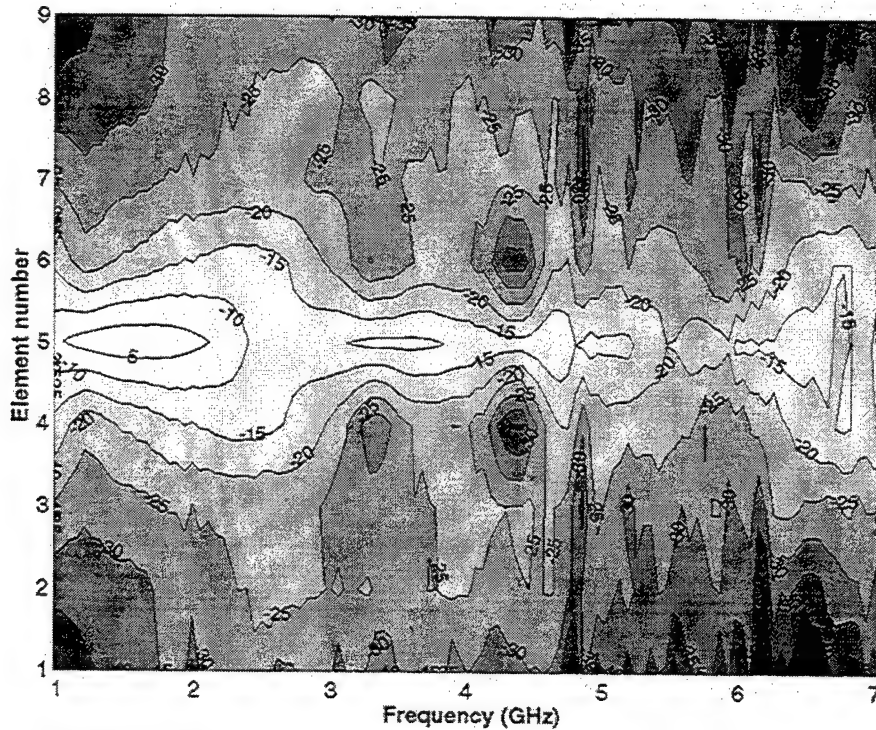


Fig. 20: Magnitude of coupling coefficient between "542" and y-directed elements "142", "242", "342", "442", "542" ($|S_{11}|$ is used), "642", "742", "842" and "942" of "SV". Contour intervals are 5 dB.

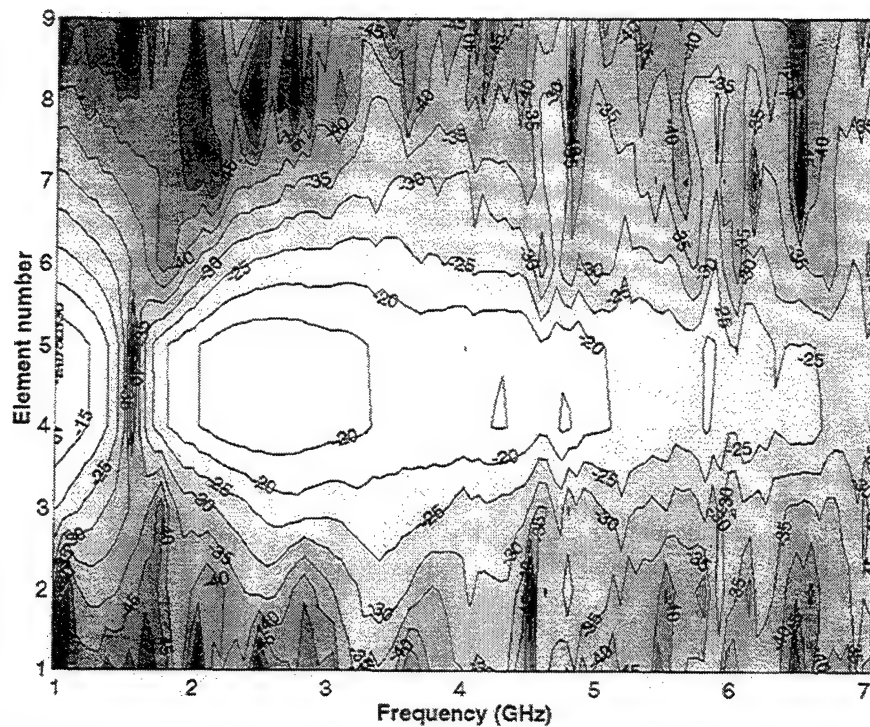


Fig. 21: Magnitude of coupling coefficient between "542" and x-directed elements "511", "521", "531", "541", "551", "561", "571", "581" and "591" of "SV". Contour intervals are 5 dB.

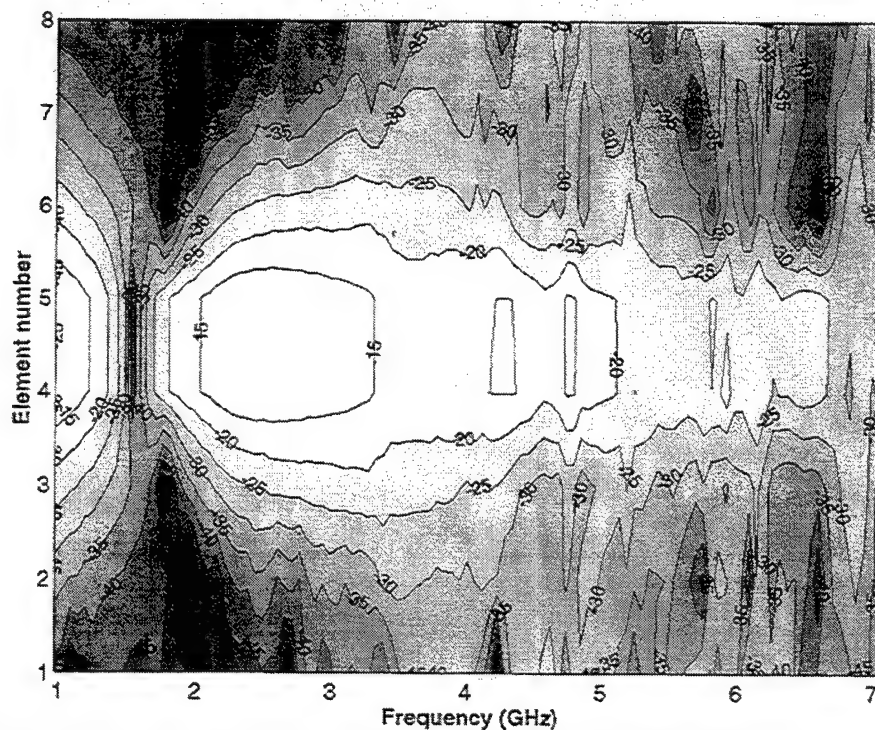


Fig. 22: Magnitude of coupling coefficient between "542" and x-directed elements "141", "241", "341", "441", "541", "641", "741" and "841" of "SV". Contour intervals are 5 dB.

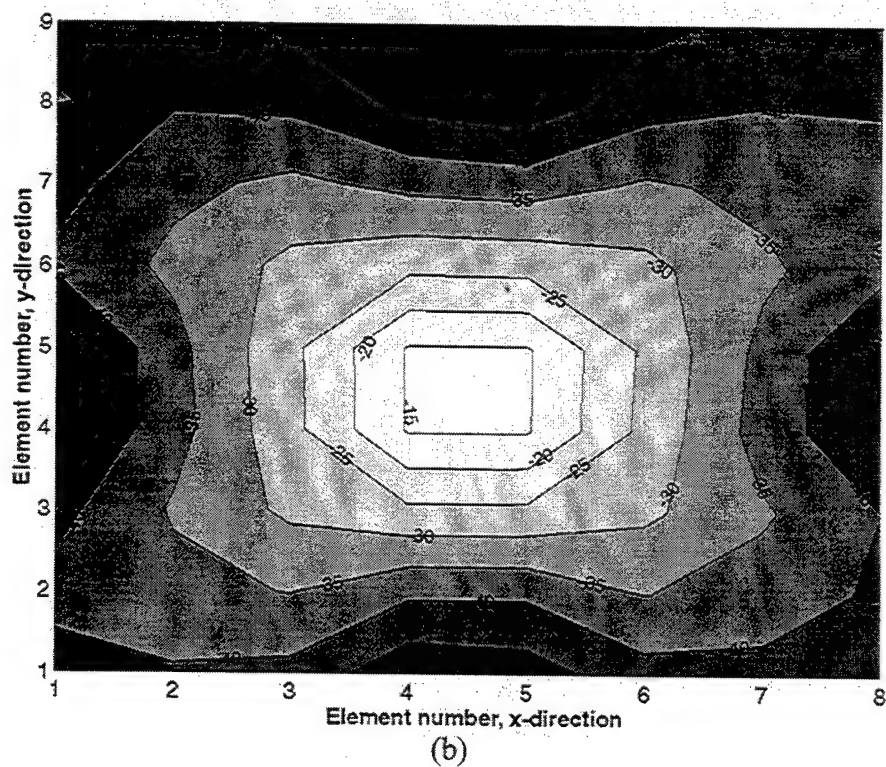
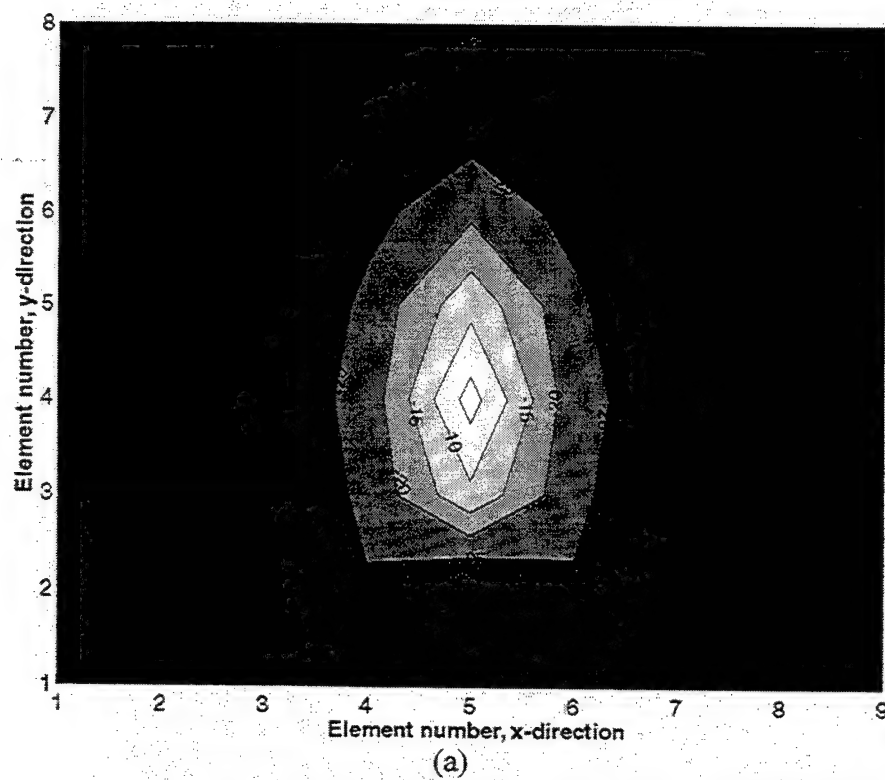


Fig. 23: Magnitude of coupling coefficient between element "542" and
 (a) all y-directed elements, (b) all x-directed elements at 1.2 GHz.

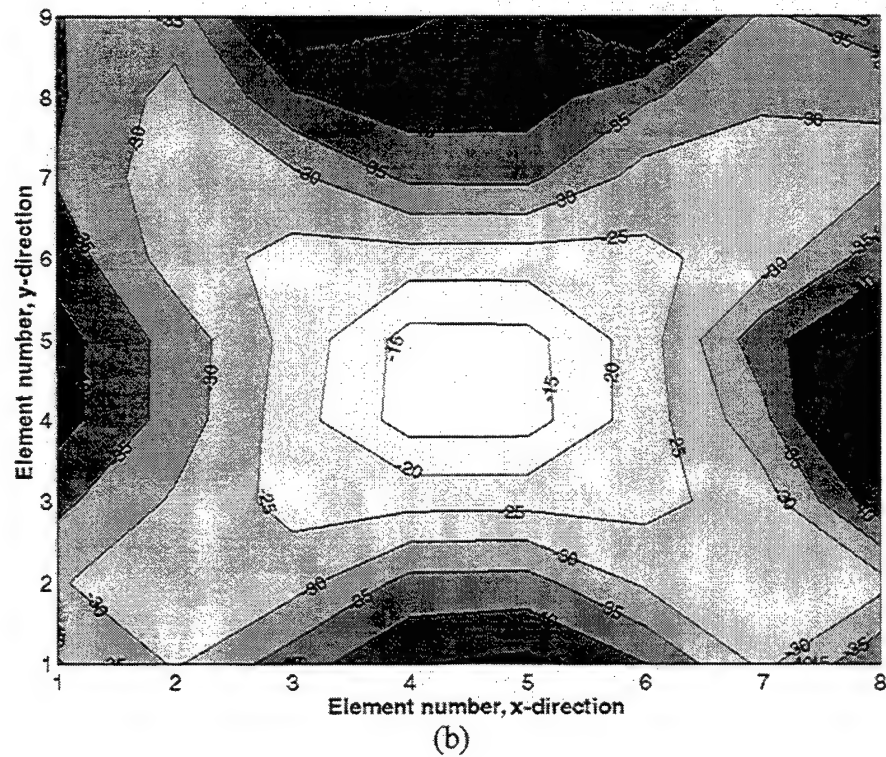
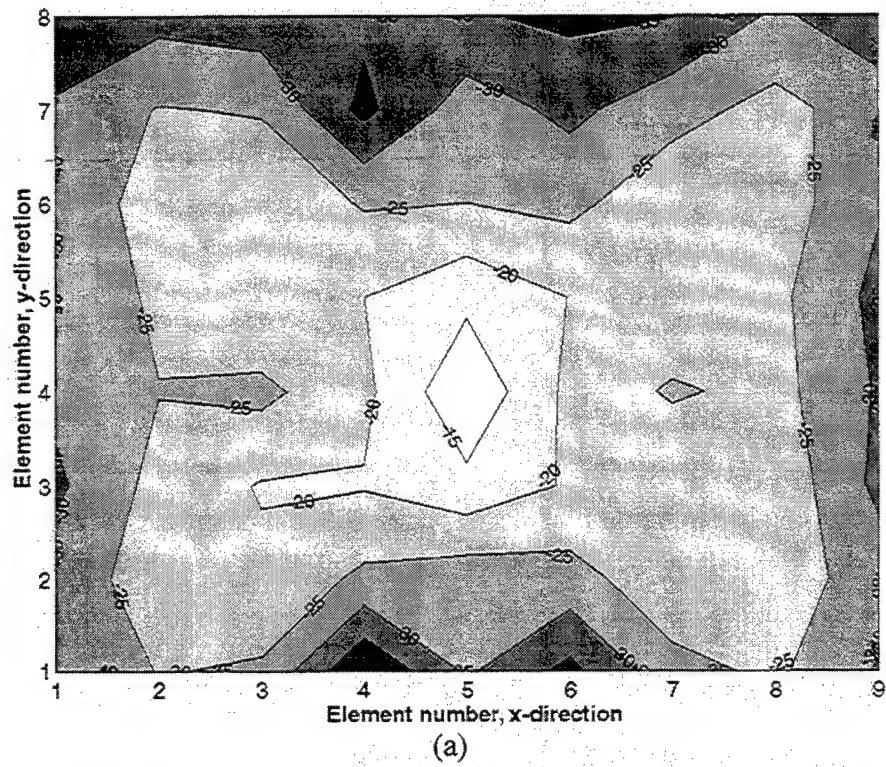


Fig. 24: Magnitude of coupling coefficient between element "542" and
 (a) all y-directed elements, (b) all x-directed elements at 3.0 GHz.

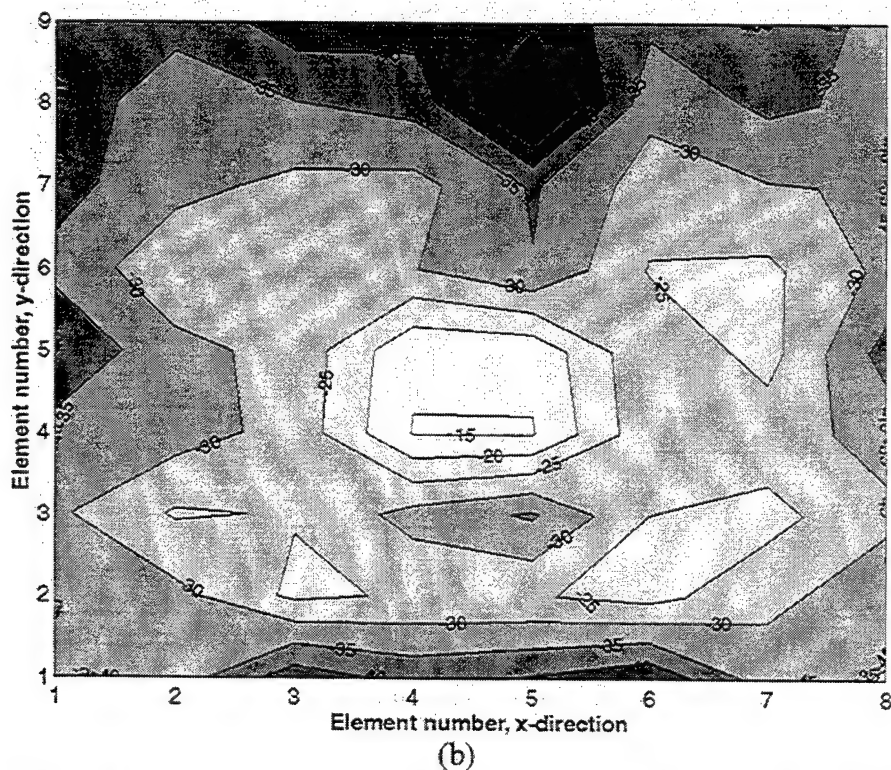
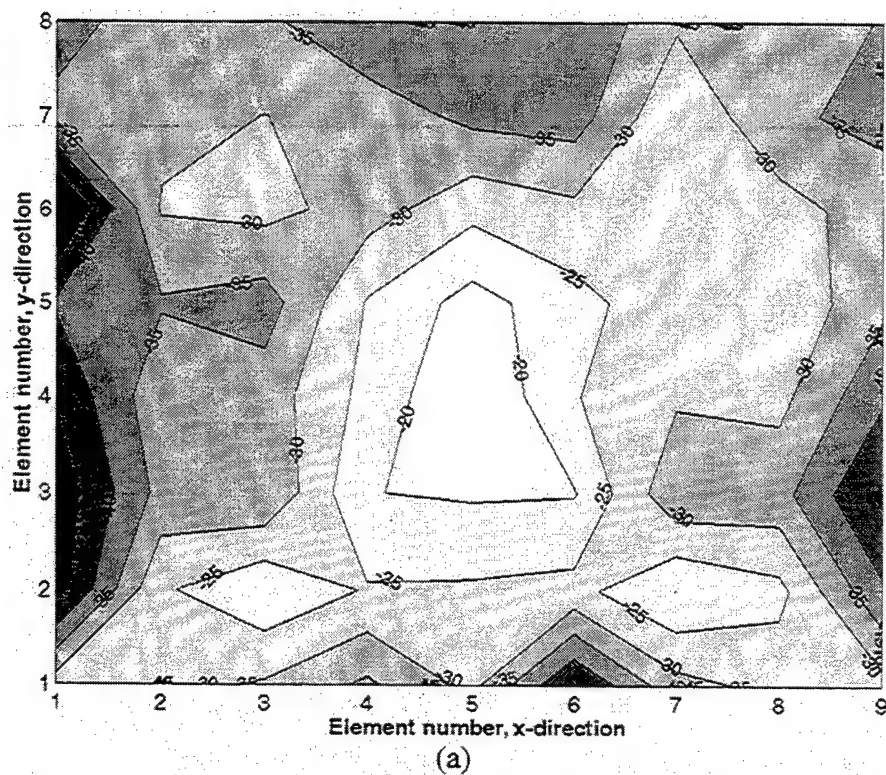


Fig. 25: Magnitude of coupling coefficient between element "542" and
 (a) all y-directed elements, (b) all x-directed elements at 4.8 GHz.

To investigate the effects of mutual coupling from co- and cross-polarized elements on element "542", the self-coupling term is excluded from Eqn (2), and the coupling coefficients from co- and cross-polarized elements are summed up separately. In this manner, mutual coupling effects of co- and cross-polarized elements can be observed separately. This is shown in Fig. 26 for broadside beam angle for "CV". Note that the cumulative contribution from cross-polarized elements is small compared to that from co-polarized elements. This is due to pair-wise cancellation of the cross-polarized element coupling, as illustrated in Fig. 27. For example, it indicates that the phases of the coupling from "542" to "541" and "551", respectively, are opposite. Similarly, other pairs like "441"- "451" and "461"- "561" also have opposite phase. When summed in Eqn (2) with $\theta = 0^\circ$ (broadside), these terms cancel pair-wise.

For scanning in the H-plane, the two exponential terms of Eqn (2) are identical for elements "541" and "551", so the net contribution from this pair is zero. Similarly, pairs of elements taken symmetric about row 4 in Fig. 9 will cancel for H-plane scanning. Note that the exclusion of the S_{11} term causes the coupling coefficient to sum to more than unity near 1.5 GHz in Fig. 28. For scanning in the E-plane, pair-wise cancellation occurs for elements symmetric about the column of elements that has element "542". Comparing Figs. 28 and 29, cross-polarization level is slightly higher for H-plane scan. This is because there are no elements to cancel the contributions from the row of cross-polarized elements containing "491" (see Fig. 9). Eliminating contributions from elements "191" through "891" in the summation in Eqn (2) yields the lower value in Fig. 28 at most frequencies.

In other scan planes, the coupling between cross-polarized elements do not cancel and therefore mutual coupling is higher. For example, compared to the cardinal scan plane, the contribution from cross-polarized elements is higher for $\theta = 30^\circ$ in the D-plane (see Fig. 30), although contributions from co-polarized elements are still higher at most frequencies. Also, contributions from co-polarized elements are higher at a larger scan angle in the D-plane. This may contribute to higher cross-polarization at large angles off broadside for D-plane scans as shown in Fig. 12. The above observations suggest that mutual coupling from co-polarized elements has a greater effect on the performance of the TSA array than mutual coupling from cross-polarized elements.

The above results support Hemmi's [12] observation that mutual coupling from cross-polarized elements is insignificant in the H-plane. Therefore, it is possible to use waveguide simulators as a first-cut tool to validate dual-polarized TSA array designs.

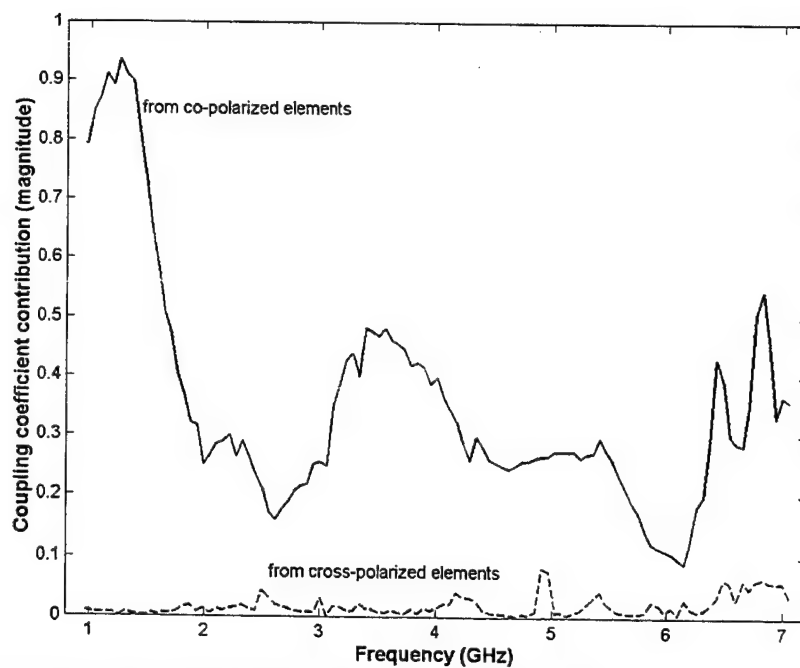


Fig. 26: Comparing mutual coupling contribution from co- and cross-polarized elements to element "542" at broadside beam angle.

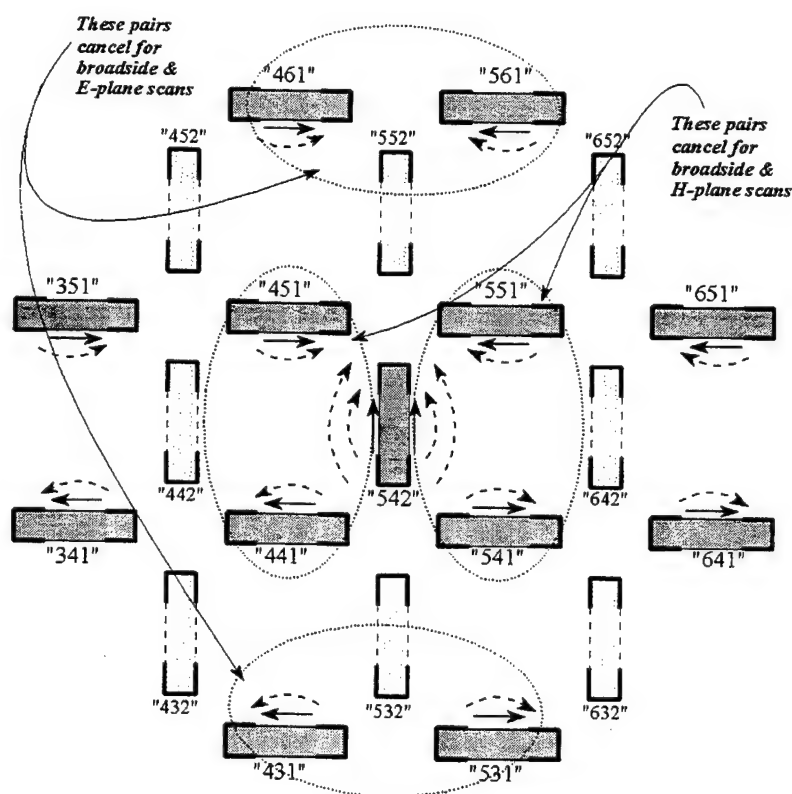


Fig 27: Symmetry of coupling between "542" and cross-polarized elements.

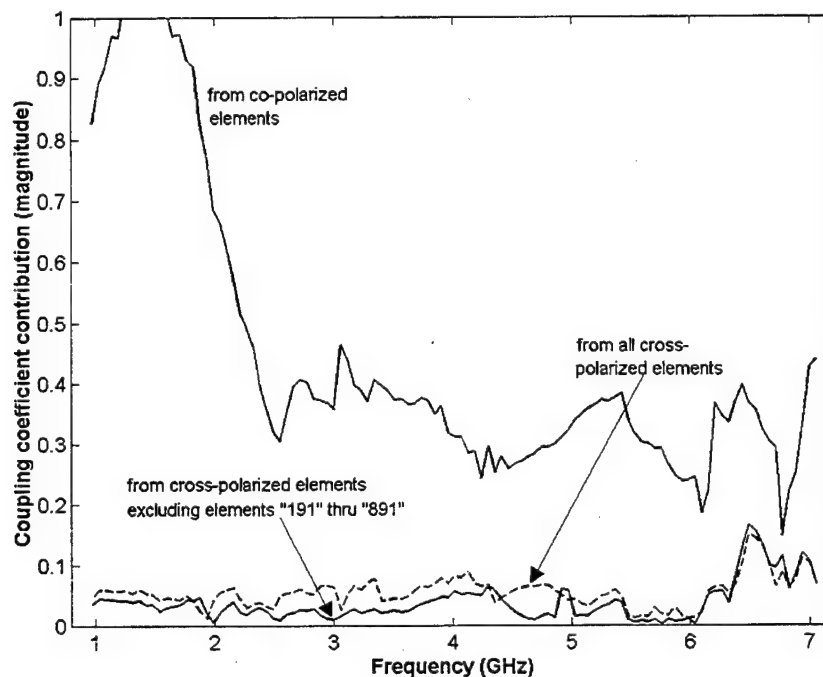


Fig. 28: Comparing mutual coupling contribution from co- and cross-polarized elements to element "542", H-plane scan, $\theta = 30^\circ$.

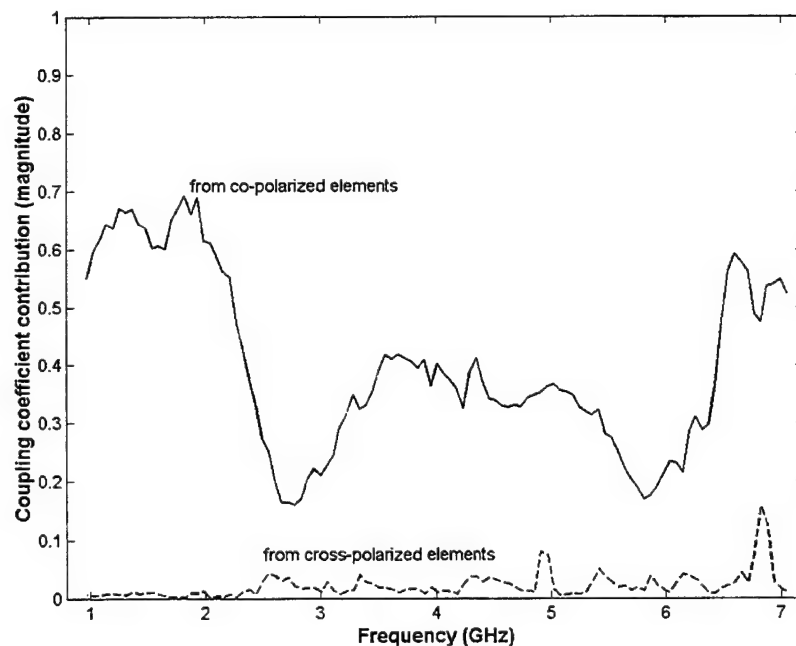


Fig. 29: Comparing mutual coupling contribution from co- and cross-polarized elements to element "542", E-plane scan, $\theta = 30^\circ$.

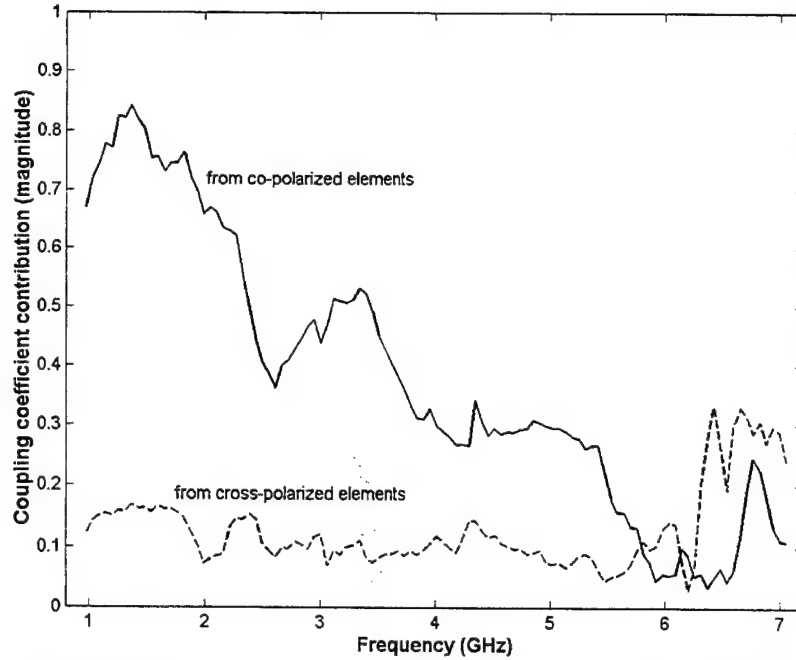


Fig. 30: Comparing mutual coupling contribution from co- and cross-polarized elements to element "542", (d) D-plane, $\theta = 30^\circ$.

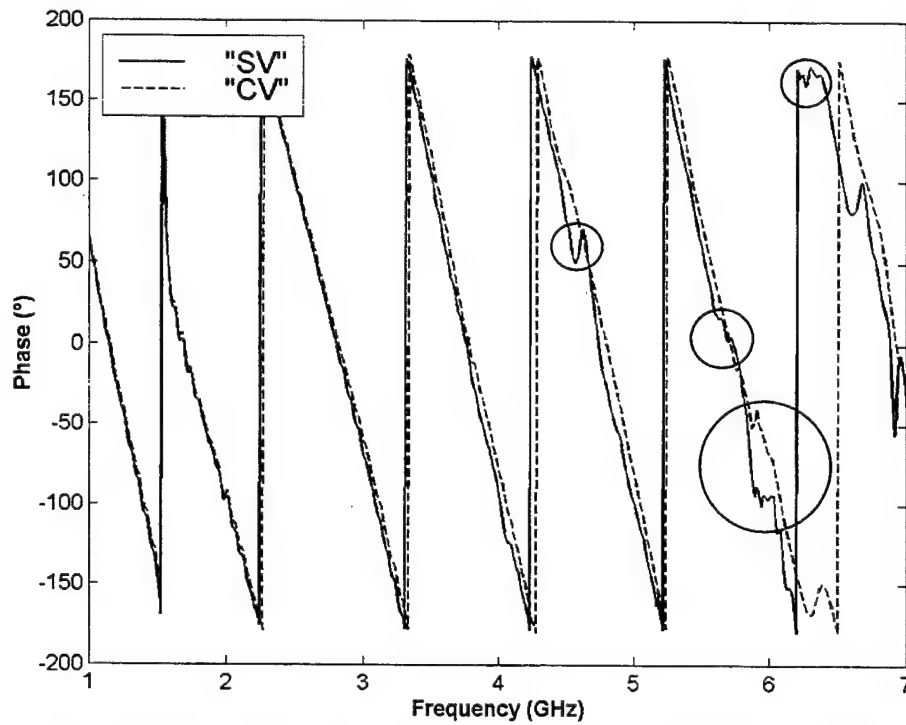


Fig. 31: Phase of coupling coefficient of element "451" and "542", Comparison between "SV" and "CV".

The phase of the mutual coupling may be also an important factor in determining the performance of the array. Specifically, the phase may be more

sensitive to phenomena like scan anomalies and element resonances. The phase of the coupling coefficients between "451"- "542", "542"- "552" and "442"- "642" of "SV" and "CV" are shown in Figs. 31, 32 and 33 respectively. Since the pairs of elements are selected to be the same for both arrays, the agreement between phase of the two arrays is quite good, as expected.

However, looking at Figs 31 – 33 collectively, there are small differences between "SV" and "CV" and some are highlighted. The phase of "CV" is mostly well behaved while that of "SV" has anomalies at the frequencies between 4.3 GHz and 5.8 GHz. In most cases, the occurrence of this anomalous phase behavior can be associated with the occurrence of the H-plane scan anomalies in infinite array version of "SV" (see Fig. 6). Therefore, the phase information may be a key factor in identifying the anomalies. Furthermore, since the only difference between the "SV" and "CV" is the placement of the plated-through vias, the vias placed along the contour of the exponentially tapered slotline seem to reduce the anomalous effects and effectively control the H-plane scan anomalies. This was also observed when the gain versus frequency was analyzed in above section.

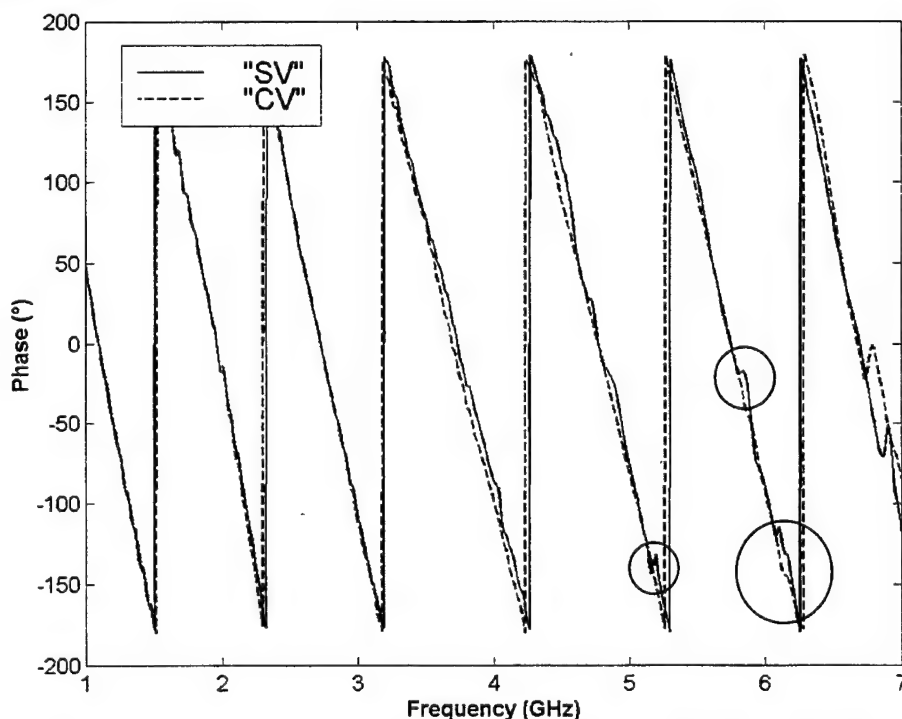


Fig. 32: Phase of coupling coefficient of element "542" and "552", Comparison between "SV" and "CV".

Another interesting observation is that at about 5.8 GHz, where there is an H-plane scan anomaly in "CV", the phase of the coupling coefficient deviates from the expected locus. For both "SV" and "CV", where there are grating lobes and anomalies at frequencies greater than 6.3 GHz, some abnormal phase

behavior is observed. This indicates that scan anomalies and/or grating lobes affect the phase of the coupling coefficients and, therefore, may be identified by observing the phase of the coupling coefficients between selected elements.

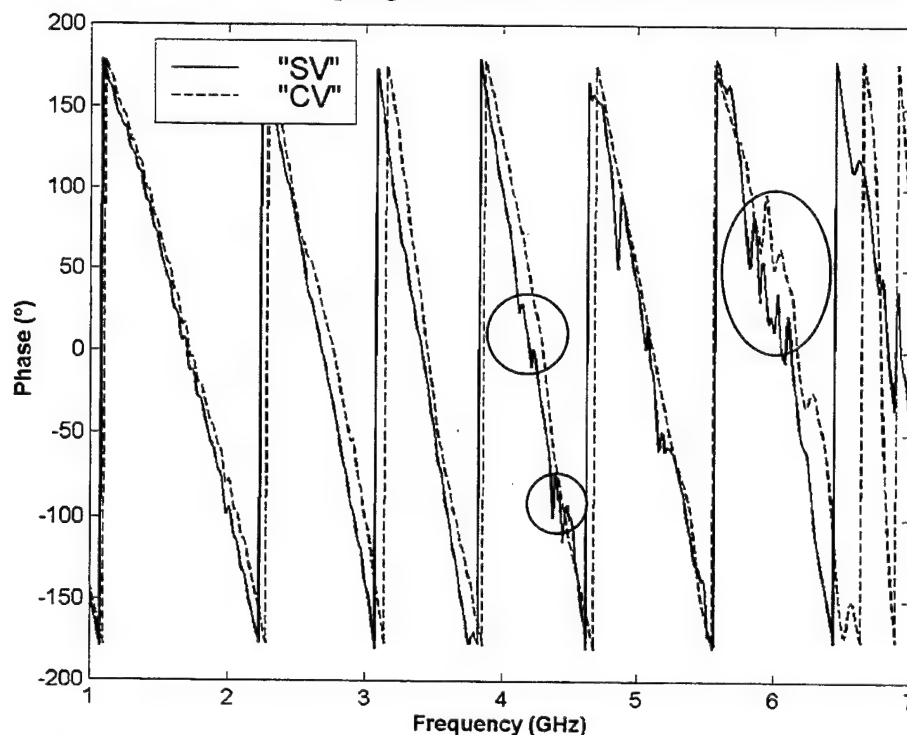


Fig. 33: Phase of coupling coefficient of element "442" and "642", Comparison between "SV" and "CV".

IV. Summary

Two small 8×9 dual-polarized arrays were designed, fabricated and tested. An important feature is the use of plated-through vias to connect the ground planes of the stripline near the edge of the array element. In this way, when the array is assembled, the soldering process is easier and good electrical contact between the ground planes of orthogonal elements in the array is achieved. It was also discovered that by placing the plated-through vias along the contour of the tapered slotline and along the circumference of the circular slot cavity, most of the H-plane impedance anomalies are eliminated. A design with 5.8:1 bandwidth, scanning up to $\theta = 50^\circ$ in all scan planes, is achieved with such an arrangement. However, measurements on the two arrays showed that the finite array effects are severe for the 8×9 array. As expected, the effects are more severe at lower frequencies. Measured results suggest that an array must be at least $4\lambda_0$ in dimension for the center element of the array to see a large array environment. The TSA "active" element patterns of center elements have a wide beamwidth and exhibit cross-polarization characteristics predicted by previous workers. The gain-versus-frequency measurements follow the trend of the theoretical results. The coupling coefficients between selected elements were measured and it was

found that the cumulative mutual coupling contribution from co-polarized elements is more significant than that from cross-polarized elements. Several H-plane scan anomalies and element resonances have also been identified by looking at the phase of coupling coefficients.

References

- [1] Lewis, L.R., Fasset, M. and Hunt, J., "A broadband stripline array element", IEEE Antennas Propagat. Soc. Int'l. Symp. Dig., pp. 335-337, 1974.
- [2] Shin, J. and Schaubert, D.H., "Toward a better understanding of wideband Vivaldi notch antenna arrays", Proc. Of 1995 Antenna Applications Symp., Allerton Park, Monticello, IL, September 1995.
- [3] Shin, J. and Schaubert, D.H., "Parameter study of stripline-fed Vivaldi notch antenna arrays", To appear in IEEE Transactions on Antennas and Propagation.
- [4] Wunsch, G.J., Radiation characteristics of dual-polarized notch antenna arrays, Ph.D. dissertation, University of Massachusetts, Amherst, MA, February 1997.
- [5] Holter, H., "Unit cell FDTD analysis applied to dual-polarized phased arrays with tapered slot elements, Accepted for publication in the IEEE Transactions on Antennas and Propagation.
- [6] Chio, T-H., Schaubert, D.H., "Parameter study and design of wideband, widescan dual-polarized tapered slot antenna arrays", Submitted to IEEE Transactions on Antennas and Propagation.
- [7] Holter, H., Chio, T-H., Schaubert, D.H., "Elimination of impedance anomalies in single- and dual-polarized endfire tapered slot phased arrays", Submitted to IEEE Transactions on Antennas and Propagation.
- [8] Schaubert, D.H., "A gap-induced element resonance in single polarized arrays of notch antennas", IEEE Antennas Propagat. Soc. Int'l. Symp. Dig., pp. 1264-1267, 1994.
- [9] Hannan, P.W., "The element-gain paradox for a phased array antenna", IRE Trans. Antennas and Propagat., Vol. AP-12, pp. 423-433, July 1964.
- [10] Pozar, D.M. "Active element pattern", IEEE Trans. Antennas and Propagat., Vol. AP-42, pp. 1176-1178, August 1994.
- [11] Chang, W.-C., and Schaubert, D.H., private communications.
- [12] Hemmi, C., Dover, R. T., German, F., Vespa, A., "Multifunction wide-band array design", IEEE Trans. Antennas Propagat., vol. 47, pp. 425-431, March 1999.

ULTRA-BROADBAND PHASED-ARRAY ANTENNA

W.R. Pickles and M. Kragalott
U.S. Naval Research Laboratory
Washington, D.C. 20375

Abstract: An ultra-broad band array suitable for Phased-Array applications is described. The array design presented here maintains a VSWR less than 2:1 from boresight out to scan angles of 50 degrees in both the E and H planes over a five to one bandwidth. The important features of this design responsible for the wide bandwidth are the stripline to notch transition, the notch taper, and the beneficial effects of mutual coupling between elements. Radiation patterns and impedance data for broadside and scanned configurations are shown for one polarization. Additionally, preliminary results of extending the design to two polarizations are given. Details of the design are presented.

1.0 Introduction

It is the goal of a continuing effort at the Naval Research Laboratory to design a planar phased array with a VSWR of less than 2:1 over a five to one bandwidth which is capable of scanning to 50 degrees in both the E and H planes.

A singly polarized array meeting these specifications has been realized and is the subject of this paper. The flared notch design shown in Fig. 1. was chosen because of previous experience by this author[1] and others[2] indicating that it had excellent wide band behavior. Previous experience and Finite Difference Time Domain (FDTD) analysis showed that ultra wide band flared notch elements must be studied in an array environment because their behavior is markedly different than when studied individually. Printed stripline circuit techniques were used to simplify the construction of many identical elements and their feed networks. Teflon-fiberglass with a relative dielectric constant of 2.22 and a loss tangent of 0.00012 was used. The element spacing in the E and H planes was made the same with a view to making a dual polarized array with identical characteristics for each polarization. The array was designed using FDTD analysis, and the highlights of that analysis will be given here. The FDTD analysis predicted that impedance matching of the flared

notch element is helped by mutual coupling and gave some insight into the mechanism. Experimental data corroborating the FDTD calculated impedance match will be given along with radiation patterns.

2.0 Double Y Transition

Initially we tried a Marchand-like stripline to slotline transition as shown in Fig. 2, but we were unable to obtain a low VSWR within the space limitations imposed by the array. As an alternate we tried a double Y transition. It was initially proposed as a microstrip to slotline transition[3] but we adapted it to stripline.

The double Y transition consists of collinear stripline and slotline feeds as shown in Fig. 3. Each feed line is terminated by an open circuit stub and a short circuit stub. All four stubs are designed to have the same electrical length βl where β is the propagation constant and l is the physical length. The equivalent circuit[4] of an idealized double Y transition is shown in Fig. 4(a). Stripline propagates a TEM mode so the idealized model is satisfactory for it. However, the slotline is more complicated. Even when analyzed with uniform conductors, slotline radiates and is dispersive. The proximity of matching structures and adjacent elements aggravates these effects. Therefore, deviation from the model of Fig. 4(a) is to be expected. The effects of a mismatch between the stripline characteristic impedance, Z_S and the slotline characteristic impedance, Z_N and the electrical length βl on VSWR at the stripline port is shown in Fig. 4(b). It can be seen that there is a resonance at $\beta l = 45^\circ$ and that the resonance gets wider for larger mismatches¹. Very short stub lengths would put the stub ends in the region where the fields are disturbed by the Y junctions. In addition there is a gentle dip in the VSWR between zero length and $\beta l = 45^\circ$. We chose a length of $\beta l = 22^\circ$ at 5 GHz to maximize space for the cavity.

The cavity approximated an open circuit which, strictly, cannot be constructed in slotline. Fig. 5 shows the results of FDTD analysis for different size cavities. Hexagonal cavities were used as an approximation of round cavities. The VSWR of the double Y transition must be very low so that the overall VSWR does not exceed 2:1. The hexagonal cavity which gives such a low VSWR is too big for the available space. However, FDTD analysis showed that an elongated cavity would fit in the available space. The response of this cavity is close to that of the largest hexagonal cavity, as shown in Fig. 5.

¹A resonance should occur for $Z_S = Z_N$ because any two consecutive impedance in the bridge cancel, but it did not show up in simulations.

3.0 Element Size

An inter-element spacing of one half wavelength at 5 GHz ($\lambda_H/2$) was chosen to avoid grating lobes in the scanned patterns. The initial FDTD analysis was performed on a linear array of seven elements in the E-plane with an element aperture size of $\lambda_H/2$. Starting with a flare length of one half wavelength at 5 GHz ($\lambda_H/2$) the element flare length was increased until an acceptable VSWR was obtained. This occurred for an element length of $2 \frac{1}{4} \lambda_H$. Further increases in element length had minimal impact. Three representative curves of this study are shown in Fig. 6. An array with a flare length of $1 \frac{1}{8} \lambda_H$, eight elements wide in the E-plane, and four elements wide in the H-plane was built and tested. The array is shown in Fig. 7(a) and its VSWR is shown in Fig. 7(b). The measured VSWR is better than the $1.0 \lambda_H$ flare length results in Fig. 6, but considerably worse than both the FDTD analysis and measured data for $2 \frac{1}{4} \lambda_H$ long elements, as expected.

4.0 Mutual Coupling

Mutual coupling between elements can be studied using FDTD by analyzing the currents which flow in each element. The seven element hypothetical array was excited with a pulse having significant energy from 0.75 GHz to 5.25 GHz. Fig. 8(a) shows the time domain currents induced at element 4 due to self coupling and mutual coupling from elements 3 and 2 (The small contribution from element 1 was omitted so as not to clutter the graph.) The self coupling current in the first nanosecond comes from the excitation. The self-coupled current in the 2 to 3 nanosecond period is large, indicating that the element is poorly matched. However the mutually coupled current from element 3 is opposite in phase and nearly half the amplitude of this current. The mutually coupled current from element 5 is the same as from element 3 so when all three are combined, the remaining current on element 4 is significantly reduced. When the coupled currents from elements 2 and 6 and 1 and 7 are added, the delayed current on element 4 is reduced even more. Increasing the size of the array to 9, 11, or 13 causes a small low frequency improvement. However, elements more than 6 positions away from a given element have a negligible effect on impedance match.

Fig. 8(b) shows the currents on element 1 caused by self coupling and mutual coupling from element 2. Edge elements such as element 1 do not get as much cancellation as central elements, so they have a higher active VSWR.

5.0 Comparison of Theoretical and Measured VSWR

Calculations of the planar array VSWR at broadside, 50° H-plane, and 50° E-plane scans were performed with waveguide simulators. The broadside scan configuration, shown in Fig. 9(a) used a single element in a square waveguide with electric walls oriented in the H-plane and magnetic walls oriented in the E-plane. This configuration simulates an array which is infinite in both directions. The H-plane scan VSWR was calculated by modeling a five element linear H-plane array, scanned in the H-plane, and positioned in parallel plate electric wall waveguide as shown in Fig. 9(b). Finally the E-plane scan VSWR was calculated using a 7 element E-plane array, scanned in the E-plane, and placed in a parallel plate magnetic wall waveguide as shown in Fig 9(c). In all three cases the distance between the walls is the same as the element spacing and the element(s) are centered in between.

The array shown in Fig 10 was experimentally constructed to verify the results of the FDTD analysis. It is ten elements wide in the E-plane and eight elements wide in the H-plane. The top and bottom elements in each E-plane column are terminated in 50 ohm loads so the active part of the array is eight elements by eight elements. In view of the above discussion on mutual coupling it would have been better to drive the outside elements and ignore their contributions to VSWR, but that would have been complicated. However, one can expect that in a larger array the impedance match would be slightly better than the results given below for an eight element by eight element array.

Before the results of the VSWR comparison are given, a brief discussion is included here on the construction of the array. The back edge of each E-plane column array mates directly with the power divider or with a 50 degree scan time delay network/power divider network combination as shown in Fig. 11. The back edge of the antenna, both edges of the time delay network and the power divider have keyed serrations so that the delay network cannot be installed backwards. The serration pattern on the front edge of the delay network matches that on the power divider and the serration pattern on the back edge matches that on the array so that the delay network can be inserted or removed. The serration pattern on the top circuit boards is staggered from the bottom pattern so that metal traces on the top circuit cards can make electrical contact between traces that abut one another on the bottom circuit boards. Finally, to complete electrical contact between outside ground planes, aluminum strips are clamped across the adjoining power divider, delay network and antenna edges. One such strip is shown in Fig. 10 with the clamping standoffs protruding from it. The clamping standoffs provide the added benefit of precisely positioning adjacent E-plane columns of the array.

Fig. 12 shows comparison plots of the calculated VSWR for broadside, and 50° scans in the E and H planes. The agreement between calculated and measured VSWR for this array is very satisfactory. The largest discrepancy between calculated and measured data is for the E-plane scan configuration. Both calculated and measured data also show the worst performance for E-plane scan data. This is probably because E-plane scanning disrupts the beneficial effects of mutual coupling discussed earlier.

6.0 Radiation Patterns

Radiation patterns and gain measurements of the antenna shown in Fig 10 were made for a number of configurations: broadside, 50 degree E-plane scan, and 50 degree H-plane scan. Broadside E-plane and H-plane patterns are shown in Figs. 13(a) and 13(b) for representative frequencies and their features are summarized in Table 1. The beamwidth in both planes decreases with frequency as expected - roughly halving as the frequency doubles. The gain is more problematic. When the frequency doubles the gain should increase by 6 dB. This only occurs in the middle of the band for both E and H plane patterns. Furthermore the gain falls off badly for both polarizations at 5 GHz. Measurements of the power distribution network show about 1 dB loss at 1 GHz and 2 dB loss at 5 GHz and the patterns do not show any serious anomalies. We are continuing to investigate these discrepancies.

Table 1. Summary of Broadside Patterns				
	E-Plane		H-Plane	
freq	BW(deg)	Gain(dB)	BW(deg)	Gain(dB)
1.0	66.5	9.1	56.0	8.3
1.5	40.0	11.7	36.8	12.2
2.0	29.2	12.3	27.8	12.6
2.5	23.8	15.2	22.8	14.9
3.0	20.1	12.4	16.9	13.0
3.5	18.6	18.9	16.5	18.9
4.0	15.8	19.7	14.2	19.4
4.5	14.0	20.0	12.7	16.5
5.0	12.3	15.8	10.8	14.6

The patterns for the 50 degree E- and H- plane scans are shown in Figs. 14(a) and 14(b) for representative frequencies and their characteristics are summarized in Table 2. These patterns show more variation than the unscanned patterns and there

are several reasons why this is to be expected: First the aperture width is nearly decreased by half when scanned to 50 degrees and the array was small to begin with. Second, straight corporate power dividers, not Wilkinson power dividers, were used in order to get an unobscured measurement of reflections. For broadside patterns this would have little effect, but for scanned patterns, the reflected signals inside the power divider could disrupt the radiation pattern.

Table 2. Summary of 50° E- and H- Plane scanned radiation patterns.				
	E-Plane		H-Plane	
freq	BW(deg)	Squint	BW(deg)	Squint
1.0	57.5	40.2	92.8	56.1
1.5	55.0	48.5	35.4	46.0
2.0	35.2	49.4	53.2	57.4
2.5	30.5	50.8	25.3	46.3
3.0	28.5	51.4	21.9	47.8
3.5	25.8	52.9	22.4	45.5
4.0	25.1	52.4	22.4	47.8
4.5	20.7	54.6	23.2	51.0
5.0	20.2	52.3	19.5	48.2

7.0 Dual Polarized Antenna

FDTD analysis predicted that it is important to maintain electrical continuity between elements around the tips of the flares. This was confirmed by making slits between the elements and increasing their length until a change was observed in the VSWR. An increase in the VSWR began to occur for a slit length of about one fifth wavelength at the upper frequency limit ($\lambda_H/5$). As a result of these findings, a simple egg crate construction of the dual polarized antenna was ruled out because it would sacrifice the continuity around the element tips in one polarization for the sake of the orthogonal polarization. The dual polarized antenna was constructed by cutting slots near the tips of the elements in the singly polarized array and running conducting fingers through the slots to contact adjacent elements in the orthogonal polarization. The orthogonal elements must be assembled individually instead of in sheets, complicating the construction.

Preliminary results show that the dual polarized array has a bit higher VSWR but somewhat better radiation patterns than the singly polarized array.

8.0 Conclusion

NRL has produced a singly polarized ultra-wideband array that covers a five to one bandwidth and scans to 50 degrees in the E and H planes. The VSWR remains less than 2:1 except for isolated frequencies in the scanned E-plane pattern. Additional improvements are being pursued on the singly polarized array and more work is planned on the dual polarized design.

The array was designed using FDTD numerical techniques. FDTD can provide valuable insights into the behavior of antennas that cannot be easily obtained in the laboratory. However, it is important to have a simultaneous experimental model effort. The FDTD analysis and the experimental models benefitted from each other. The FDTD analysis made it much easier to build a working model. On the other hand, the data from the experimental model was used to refine the FDTD analysis.

9.0 References

- [1]W. R. Pickles and J. B. L. Rao, "Broadband Array of Dual Flared Notch Elements", *1992 Antenna Applications Symposium*, Allerton Park, University of Illinois.
- [2]Mark J. Povinelli, "Experimental Design and Performance of Endfire and Conformal Flared Slot(Notch) Antennas and Application to Phased Arrays: An Overview of Development", *1988 Antenna Applications Symposium*, Allerton Park, University of Illinois.
- [3]B. Schiek and J. Kohler, "An Improved Microstrip-to-Microslot Transition", *IEEE Trans. Microwave Theory Tech.*, pp 231-233, April 1976.
- [4]V. Trifunovic and Branka Jokanovic, "Review of Printed Marchand and Double Y Baluns: Characteristics and Application", *IEEE Trans. Microwave Theory Tech.*, vol. MTT-42, pp.1545-1462, Aug. 1994

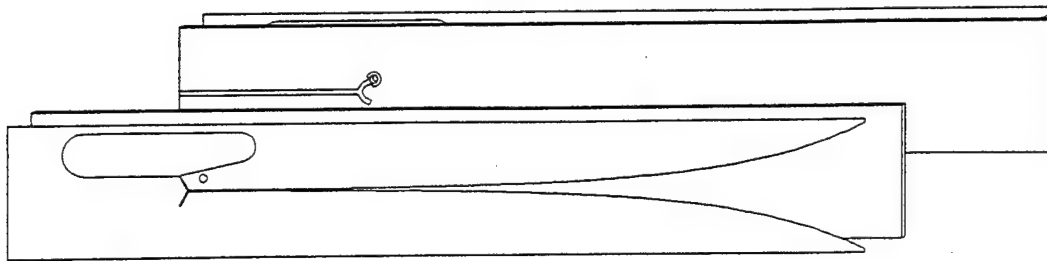


Figure 1. Basic flared notch radiating element.

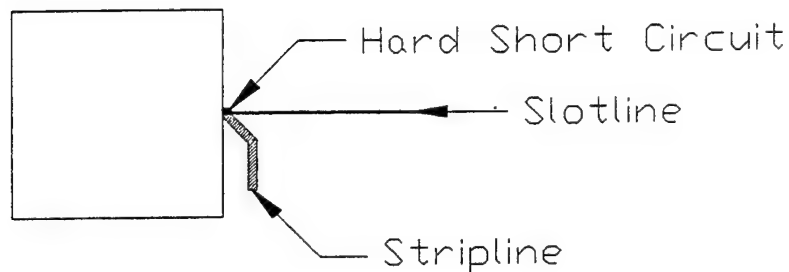


Figure 2. Marchand-like stripline to slotline transition.

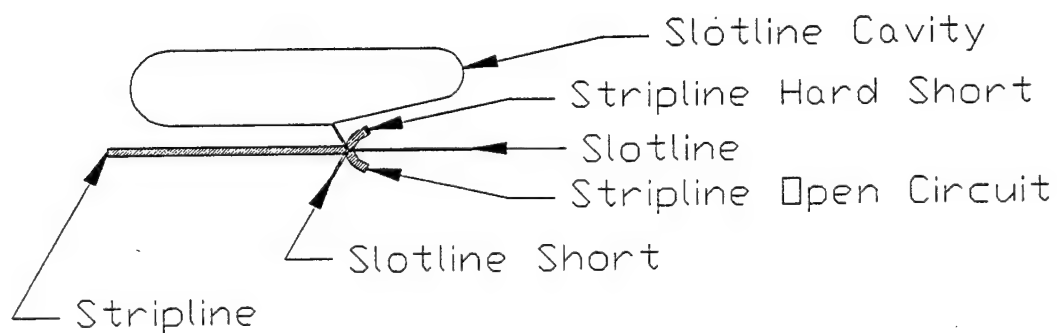


Figure 3. Double Y stripline to slotline transition.

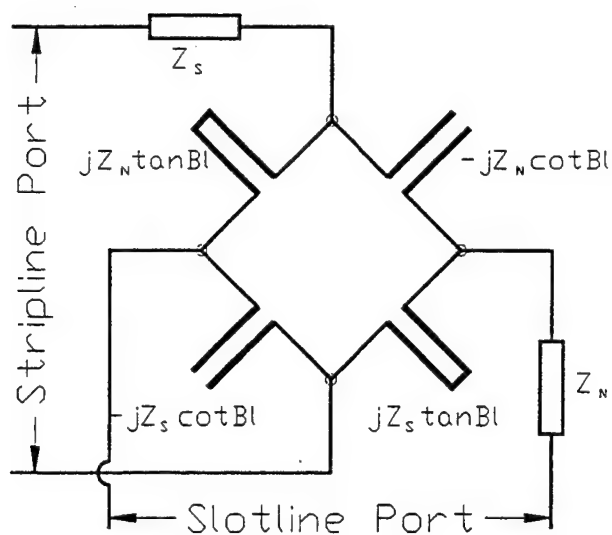


Figure 4(a) - Equivalent circuit of double Y stripline to slotline transition.

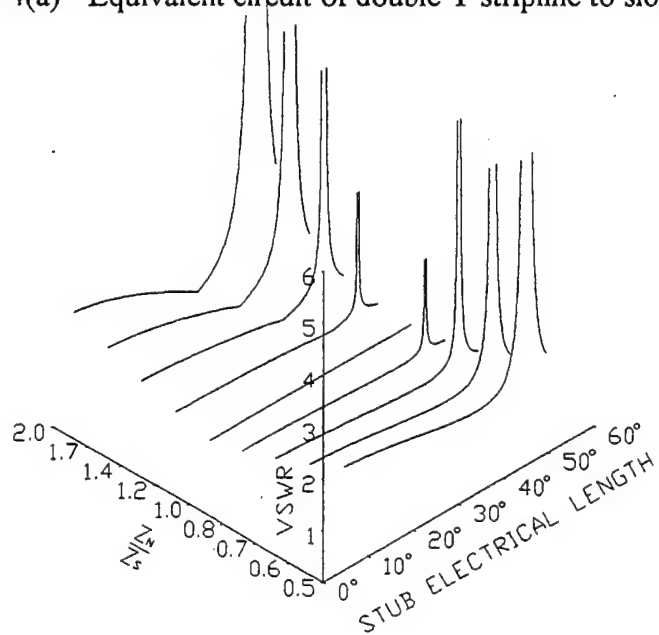


Figure 4(b) - VSWR of above circuit plotted vs. ratio of Z_N/Z_s and stub electrical length.

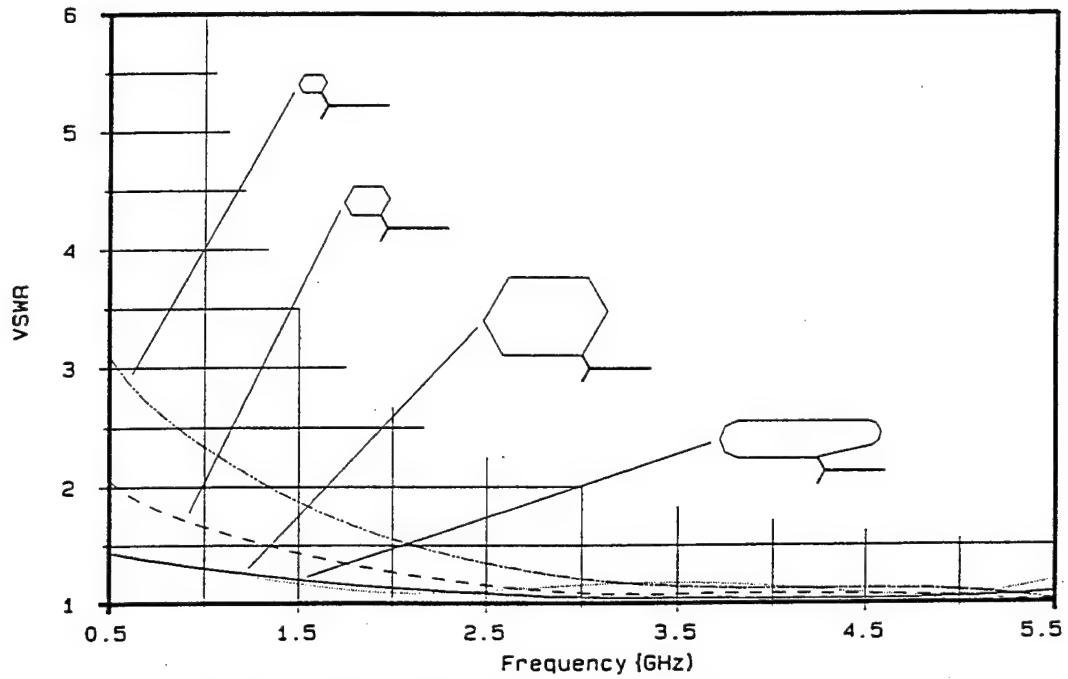


Figure 5 - Double Y VSWR as a function of cavity size

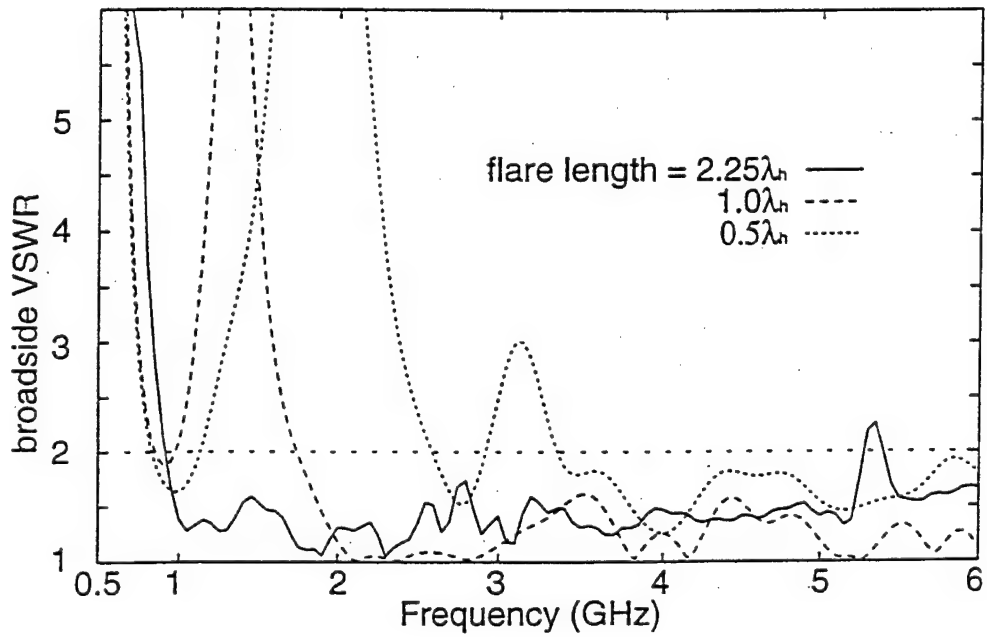


Figure 6 - Array VSWR as a function of element flare length.

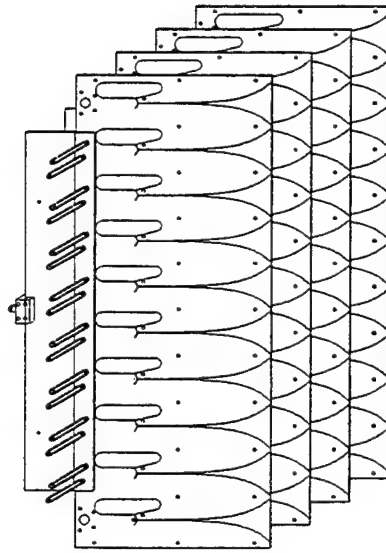


Figure 7(a) - Array used for $1 \frac{1}{8} \lambda_H$ element length impedance measurements.

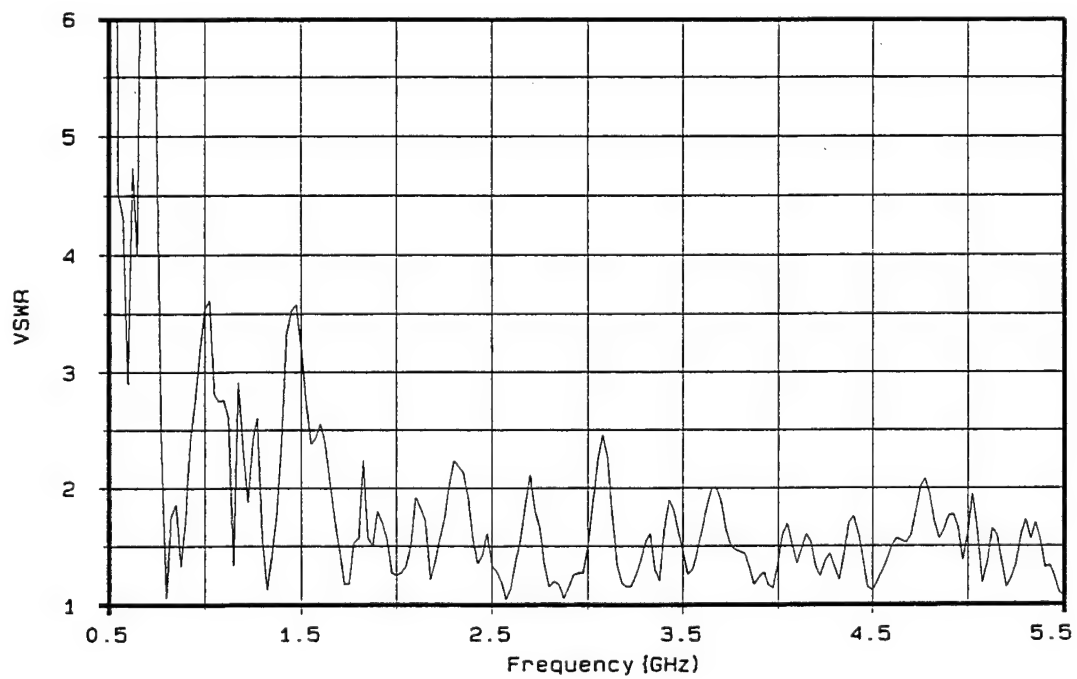


Figure 7(b) - VSWR of array with $1 \frac{1}{8} \lambda_H$ long elements

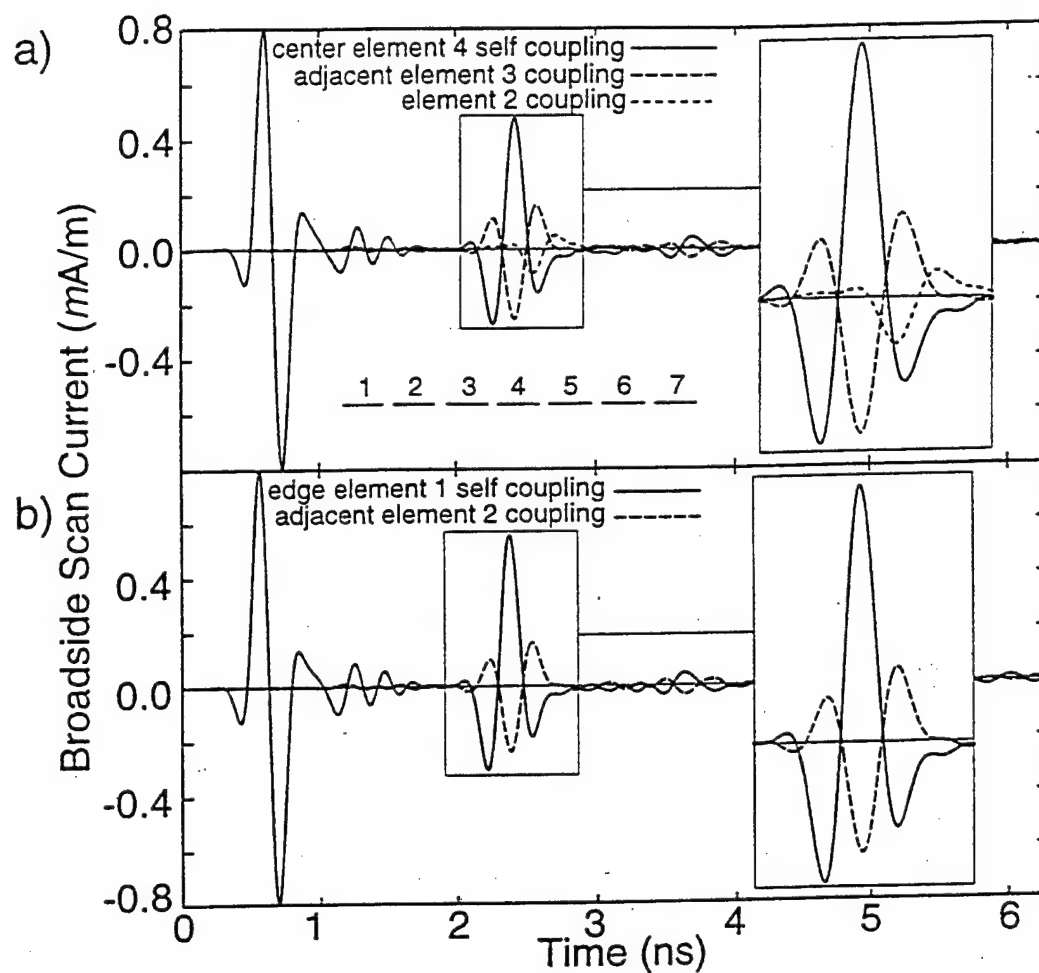
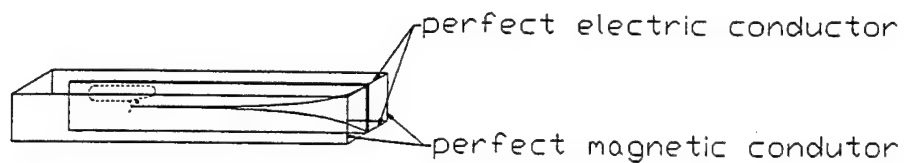
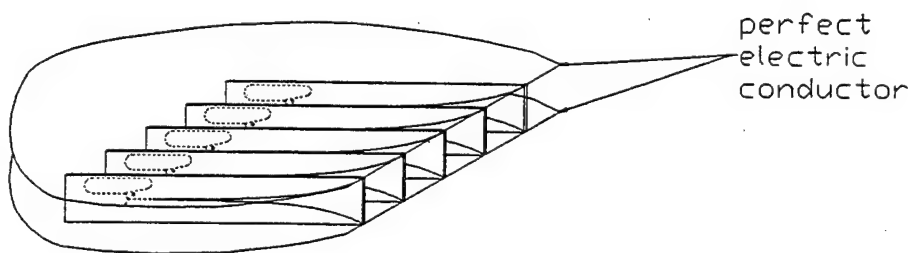


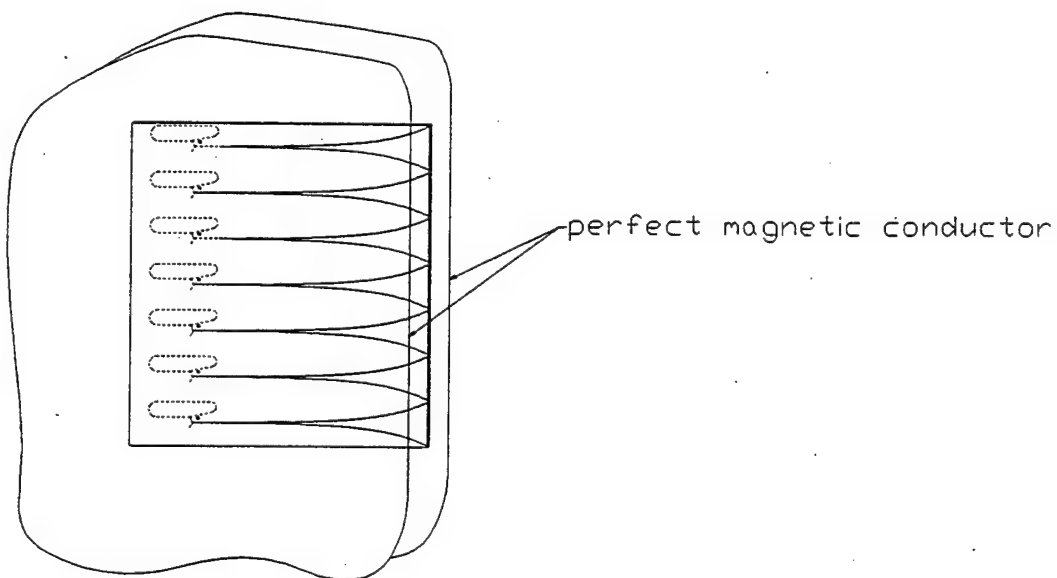
Figure 8 - (a) Time domain current coupling at the center element of a 7 element linear array and (b) coupling at the edge element of the array.



(a) Broadside scan simulator



(b) H-plane scan simulator



(c) E-plane scan simulator

Figure 9 - Waveguide simulator configurations for FDTD analysis of broadside (a), H-plane (b), and E-plane(c) scanning.

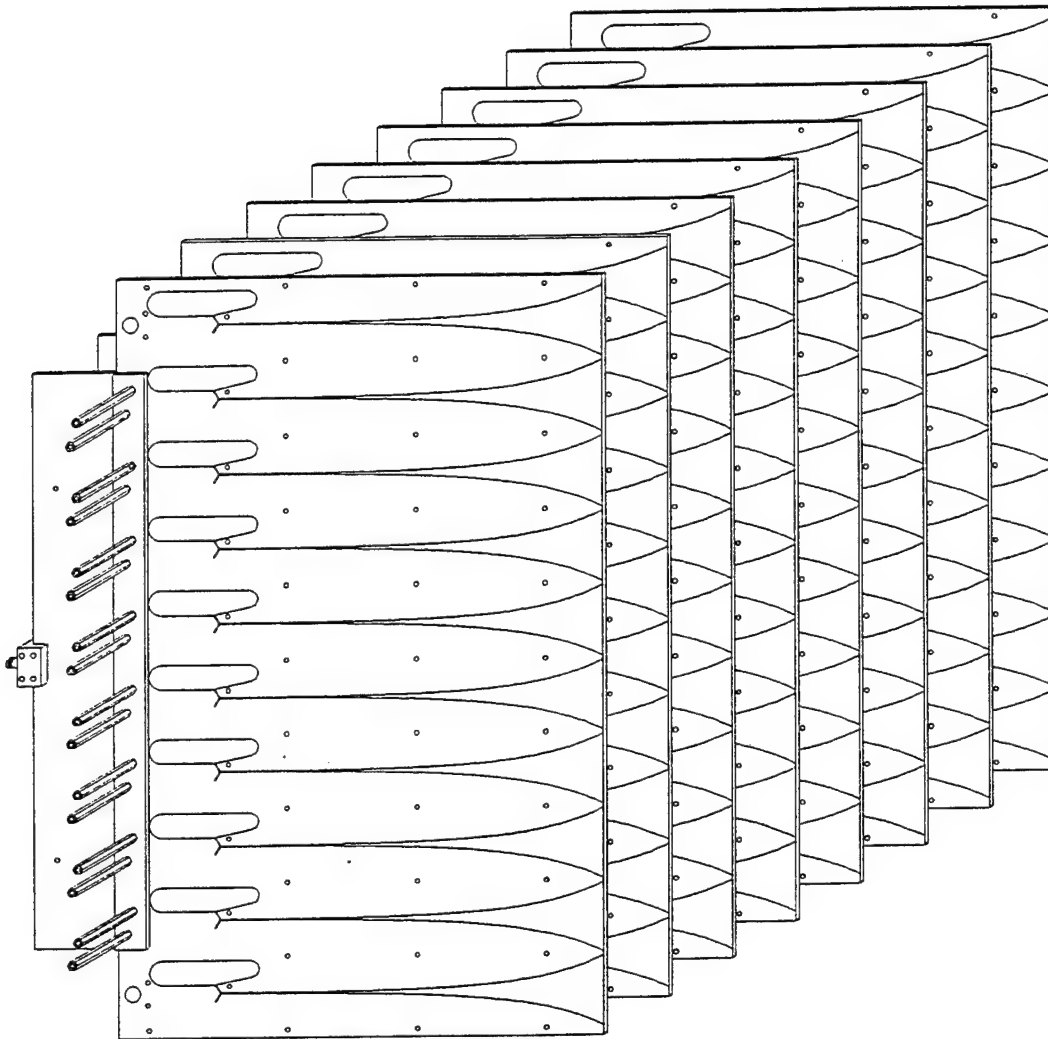


Figure 10 - 8 x 8 element array used to verify FDTD impedance calculations and measure radiation patterns.

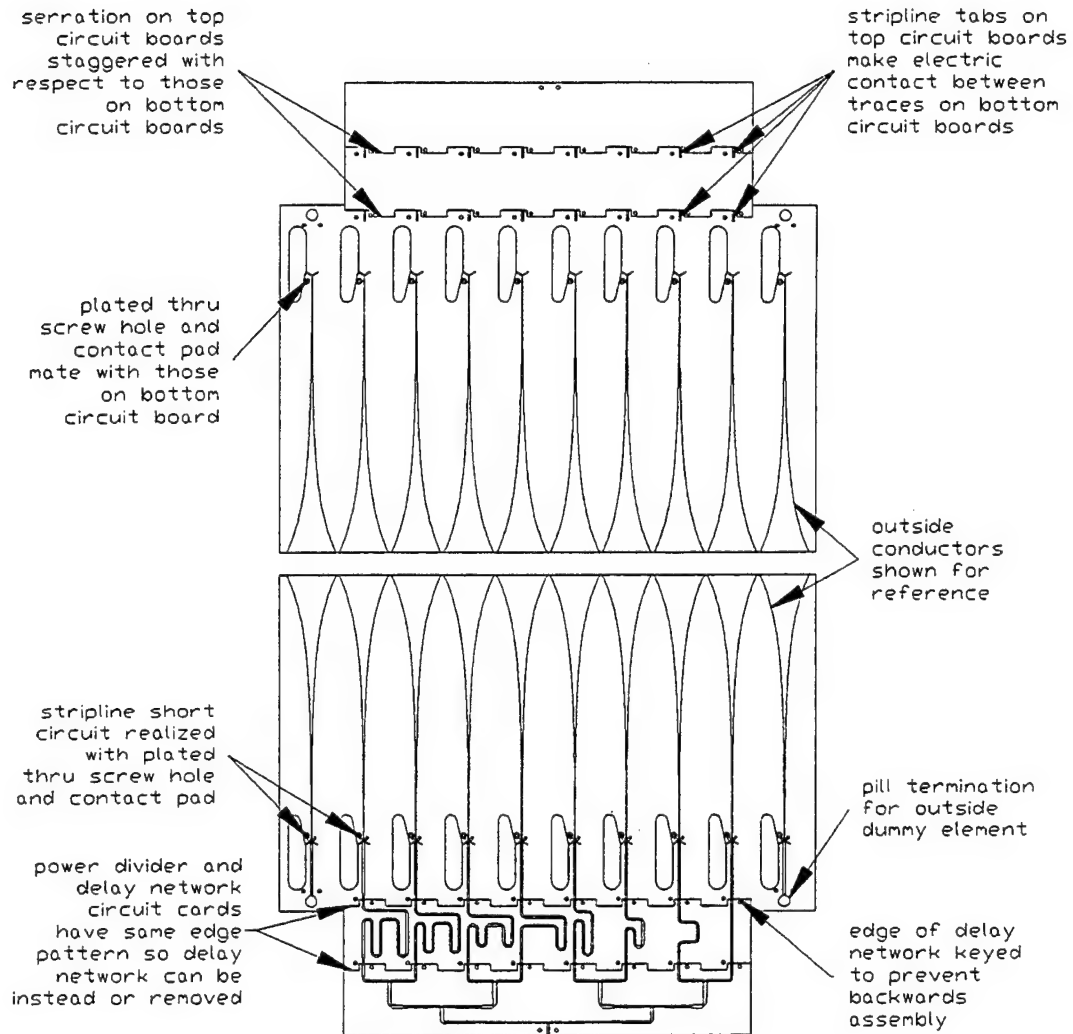


Figure 11 - Internal view of E - plane column sub-array showing details of how power divider and delay network are joined to the sub-array.

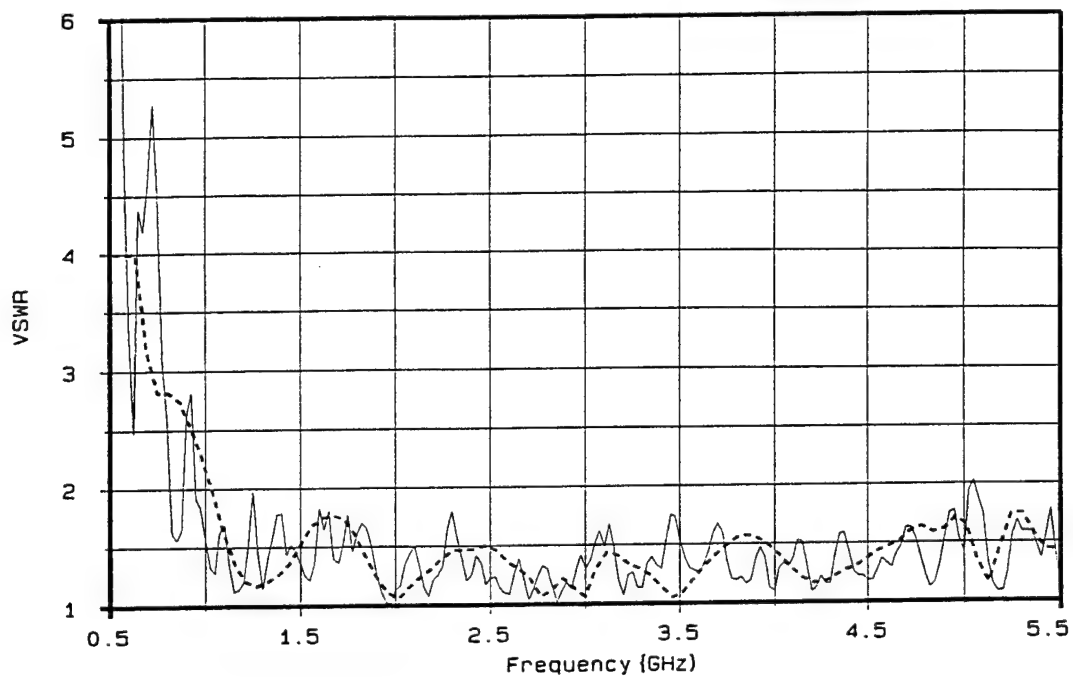


Figure 12(a) - Calculated (dashed) and measured array VSWR: boresight.

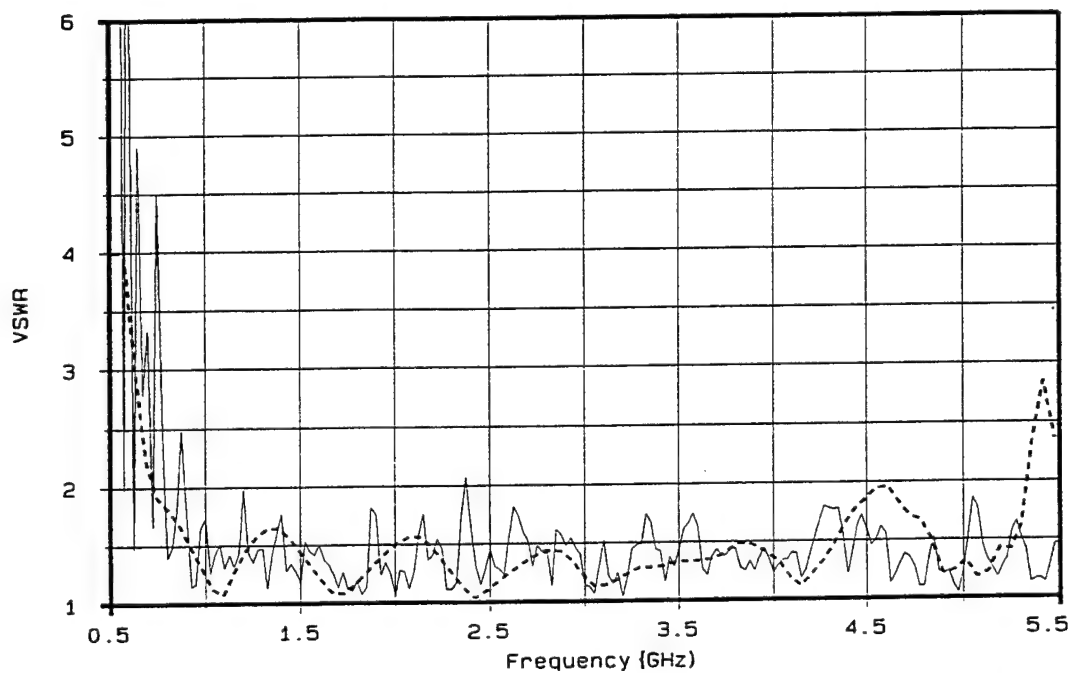


Figure 12(b) - Calculated (dashed) and measured array VSWR: 50° H-plane scan.

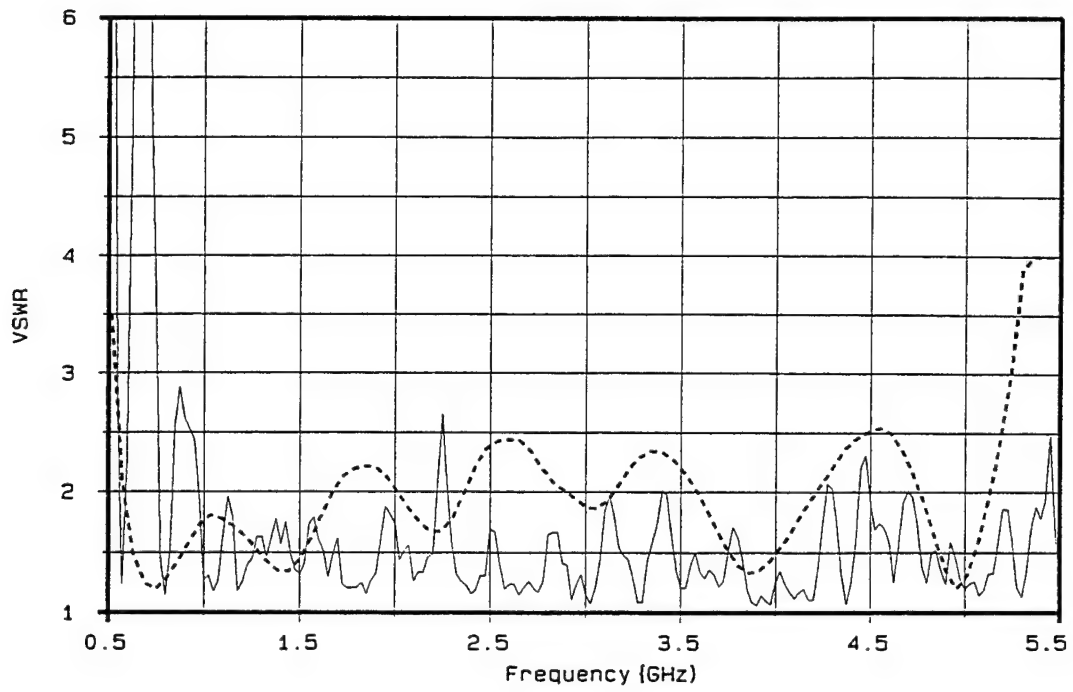


Figure 12(c) - Calculated (dashed) and measured array VSWR: 50° E-plane scan.

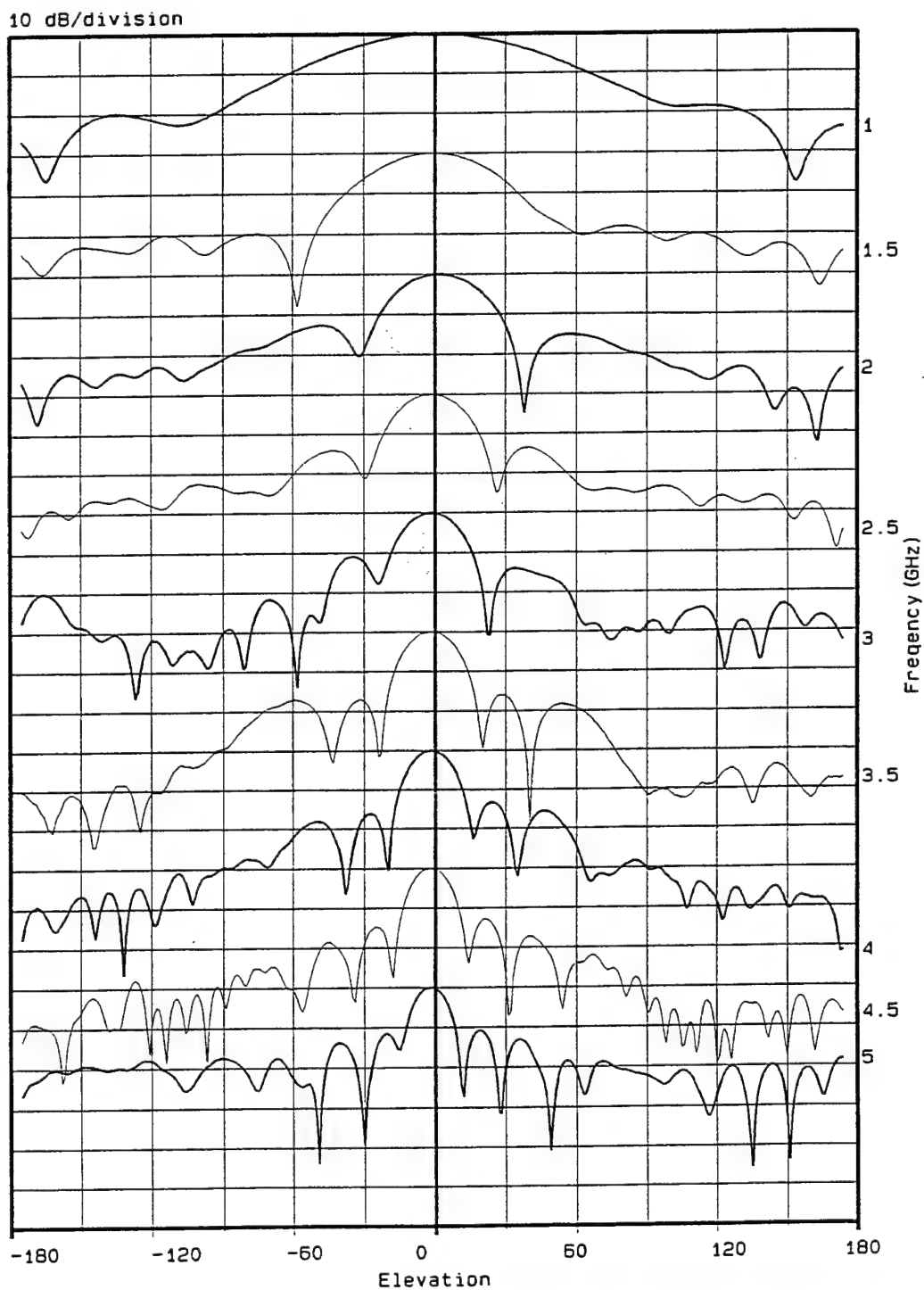


Figure 13(a) - Broadside E-plane radiation patterns for the array shown in Fig. 10.

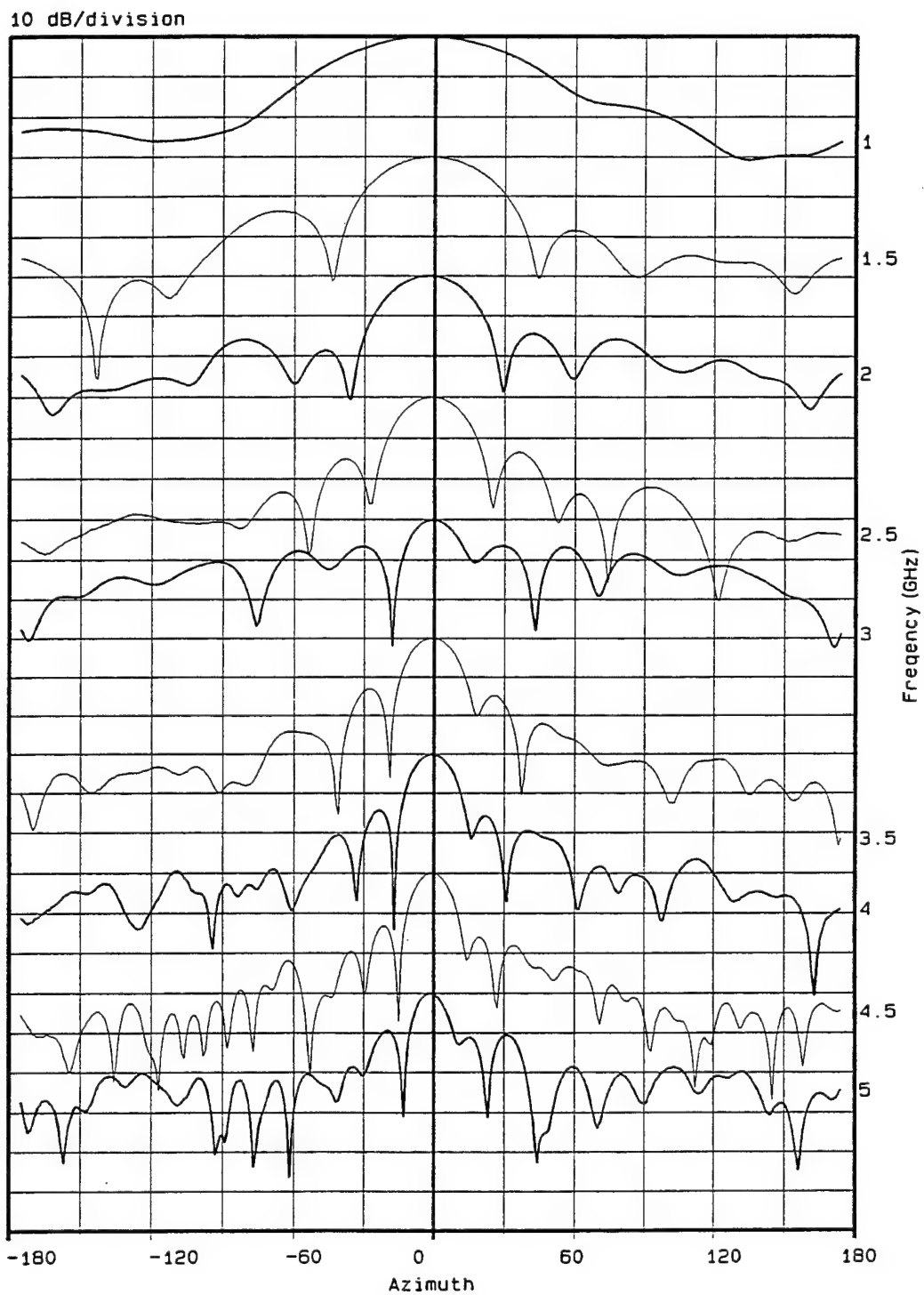


Figure 13(b) - Broadside H-plane radiation patterns for the array shown in Fig. 10.

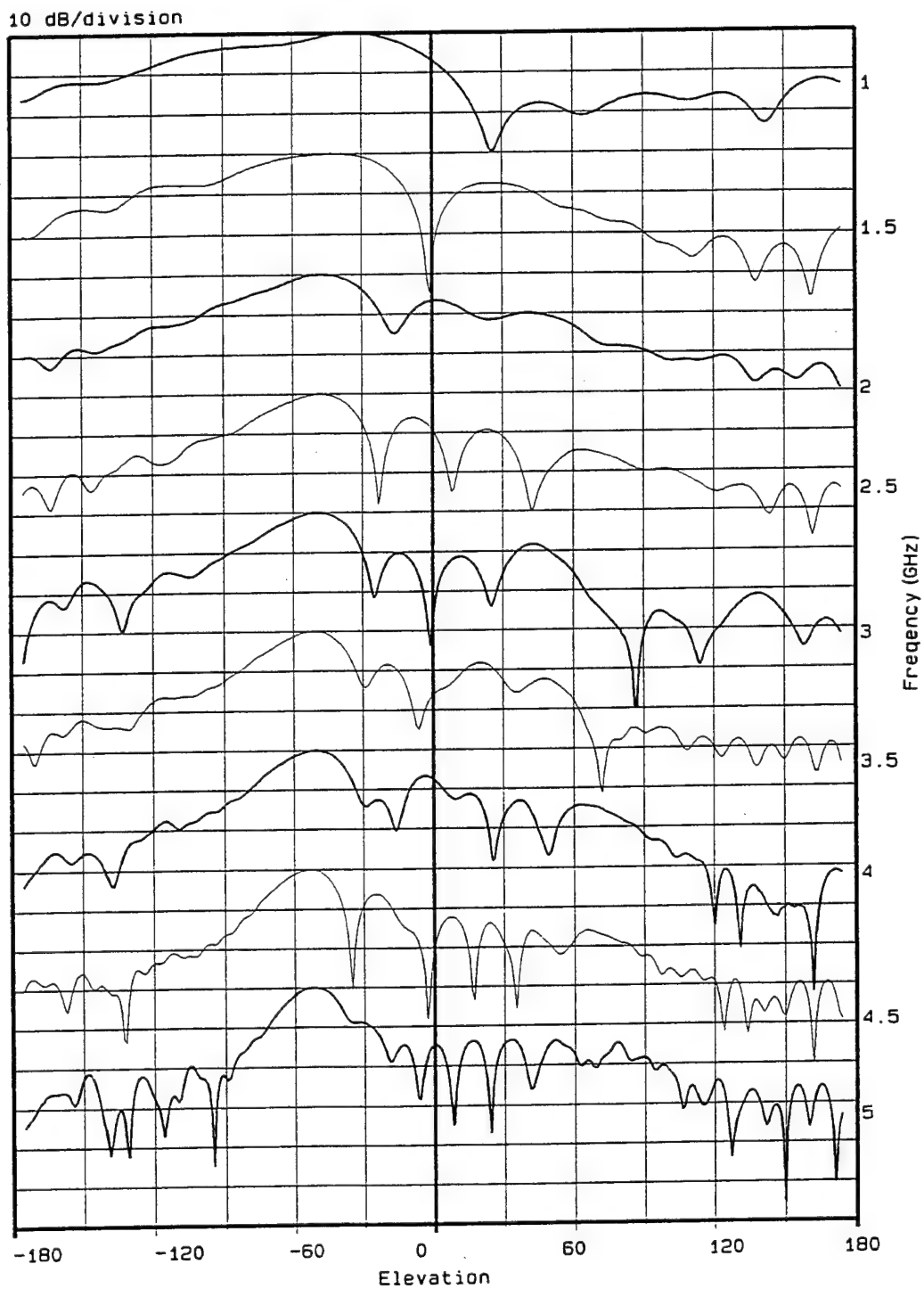


Figure 14(a) - 50° E-plane scanned radiation patterns for the array shown in Fig. 10.

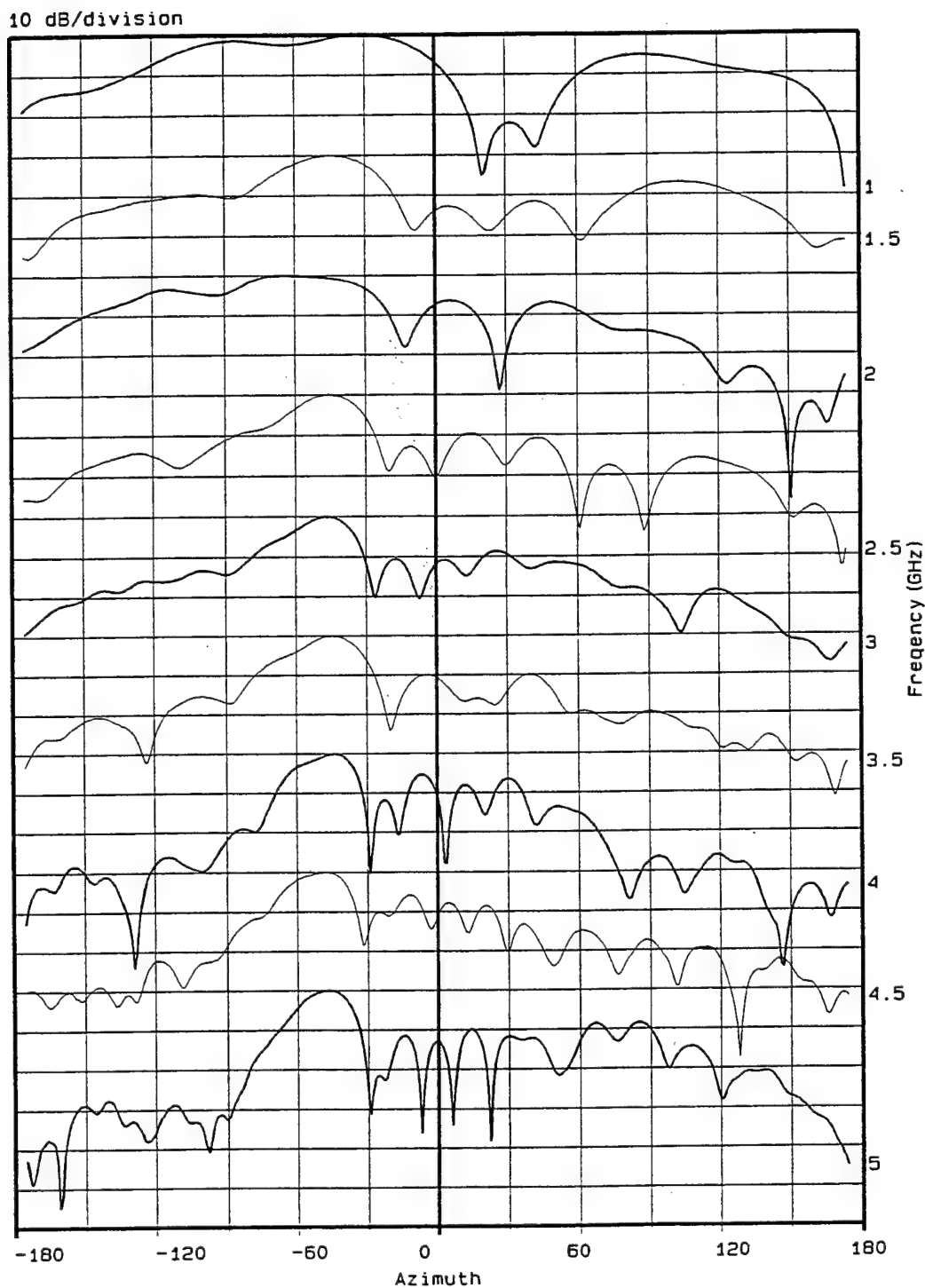


Figure 14(b) - 50° H-plane scanned radiation patterns for the array shown in Fig. 10.

AN AFFORDABLE SCANNING ARRAY USING A RADANT LENS

J.B.L. Rao, J.B. Evins, S.M. Brockett, M. Parent, J. Valenzi, D. Wilson
Naval Research Laboratory
4555 Overlook Avenue, SW
Washington, DC 20375

A.A. Moffat
Sachs Freeman Associates
1401 McCormick Drive
Largo, MD 20774

S. Krystofik, J. Maciel, V. Philbrook, F. Ziolkowski
Radant Technologies, Inc.
255 Hudson Road
Stow, MA 01775

Abstract: An affordable phased array for a ship self-defense experimental engagement radar is described. The array uses a hybrid approach by combining a slotted waveguide array with phase shifters at each column to provide scanning in the azimuth plane and a Radant lens placed in front of the slotted array to provide independent scanning in the elevation plane. The approach avoids using a phase shifter or a T/R module behind each radiating element and simplifies beam steering using row-column controls which reduce the phased array cost. The production cost of the proposed array is estimated to be less than one-third the cost of a similar sized array using a phase shifter or T/R module behind each radiating element. Recently, a 4'x8' Radant lens was procured from Radant Technologies, Inc. and placed in front of the existing (modified AN/TPQ-36) phased array. This paper reports on the results of this hybrid array.

1. Introduction

The Phased Array is one of the most versatile type of antenna used in radars aboard Naval ships. Each radiating element of a phased array is normally associated with a phase shifter or a T/R module where the element phase can be varied through

360°. The radiating elements are spaced nominally at a $\lambda/2$ spacing to avoid grating lobes. A typical phased array, with a 1° pencil beam, needs an aperture of at least $50\lambda \times 50\lambda$ requiring some 10,000 radiating elements and phase shifters. The complexity of the corresponding feed network can increase rapidly with the size of the phased array. The phase shifters (or T/R modules) and control circuitry along with the feed network account for the major hardware cost in a phased array antenna. A few years ago a study was made by NRL on ways to obtain two-dimensional scanning at low-cost. In that study, a hybrid approach of combining a slotted waveguide array in combination with a Radant lens was identified as a low-cost approach to a phased array which can meet the requirements of Ship Self-Defense [1]. Since then, a slotted waveguide array was assembled which was a modified version of a production series (AN/TPQ-36) built by Hughes Aircraft Company. The modified version used high-power phase shifters and a monopulse feed network, and can phase scan in the azimuth plane.

In 1995 a contract was awarded to procure a Radant lens from Radant Technologies Inc. The lens was delivered to NRL in June 1998. NRL added the lens to the front of the waveguide slotted array (modified AN/TPQ-36) to obtain scanning in the vertical plane. This paper presents the experimental results of this affordable hybrid phased array. The sponsor for the Radant program is ONR 311.

2. Modified AN/TPQ-36 Radar Antenna

The AN/TPQ-36 antenna consists of a stack of vertical slotted waveguide arrays each with a phase shifter to provide azimuth scanning. A TPQ-36 antenna was modified at NRL by procuring high-power phase shifters and a high-power monopulse feed network. A TPQ-36 array face was procured from Hughes Aircraft, high-power phase shifters were procured from Raytheon and a high-power monopulse feed network was procured from Westinghouse. Figure 1 is the modified AN/TPQ-36 antenna. NRL performed the integration and testing of the antenna. The resulting antenna has performed extremely well, as expected, to scan the beam in the azimuth plane. The details are documented in an NRL report [2].

3. Radant Lens

As stated earlier, the modified AN/TPQ-36 antenna can be used to scan the beam only in the azimuth plane. To scan the beam in elevation, a Radant lens has been procured from Radant Technologies, Inc. The Radant lens is a novel antenna, with a low-cost means of obtaining two-dimensional scanning by simply retrofitting it to the front of an existing one-dimensional scanning array, like the waveguide

slotted array.

The Radant lens reduces many of the fabrication problems that increase the cost and the transmission loss associated with the conventional implementation of a passive phased array - namely the discrete element and its phase shifter. The Radant lens eliminates all packaging, connectors, and transmission lines associated with the discrete phase shifters. It also reduces greatly the number of control circuits, drivers and connecting leads.

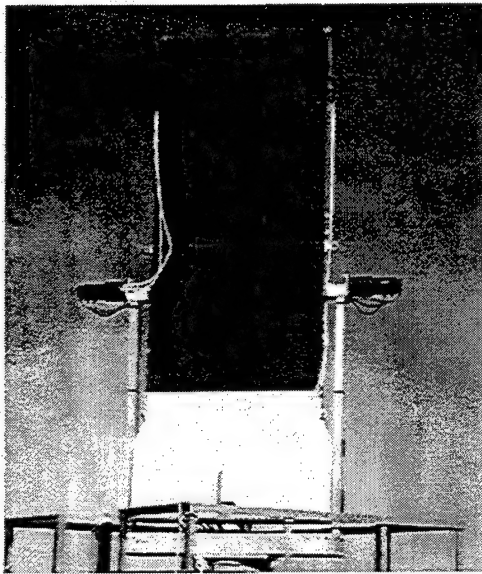


Figure 1. Modified TPQ-36 Antenna

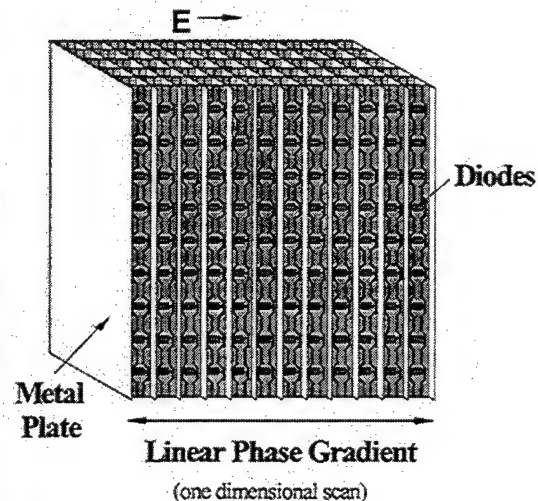


Figure 2. Radant lens concept

The basic principle on which the Radant lens operates has been demonstrated earlier by Radant Technologies, Inc. [3] under a contract to Rome Laboratory. The Radant lens concept is illustrated in Fig. 2. The lens is constructed from a set of parallel conducting plates. In between each set of plates is a series of dielectric support layers on which are two strips of metal cross connected by a set of diodes as shown in Fig. 3. The amount of metalization controls the amount of phase shift per dielectric layer. The operating principle of the Radant lens is that the phase shift through the lens changes when the diodes in one layer are turned on or off. The total phase shift results from selectively switching between the two diode states on each layer using a digital bias control circuit. In between the two parallel plates are 13 dielectric layers with diodes, which are used in combination to create a 4-bit bulk (i.e., column or row) phase shifter. The top view of one column of the lens is shown in Fig. 4. To construct a 4-bit phase shifter, three different types of layers, each with a different amount of metalization, is used to produce either a 11.25, 22.5, and a 45

degree phase shift. For example, to create a 112.5 degree phased shift, the 22.5 degree bit and 90 degree bit must be turned on. This is accomplished by turning on all the diodes on the first and second layers, activating the 22.5 degree bit, and also turning on all the diodes on the sixth, seventh, and eighth layers, activating the 90 degree bit. The set of thirteen layers was used to improve matching and minimize the resulting return loss.

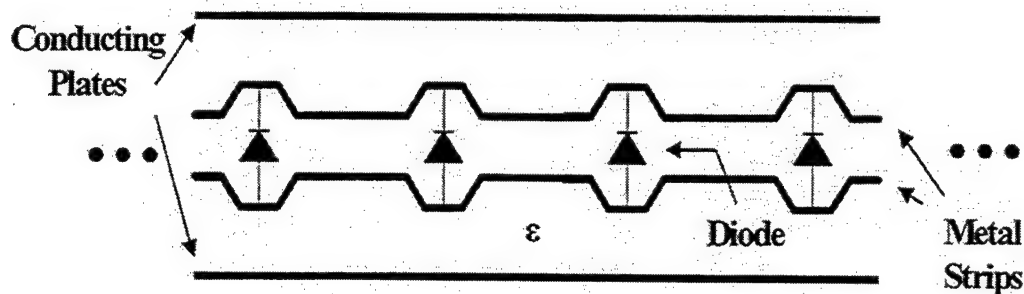


Figure 3. Dielectric support layer with diodes and metal strips between two conducting plates

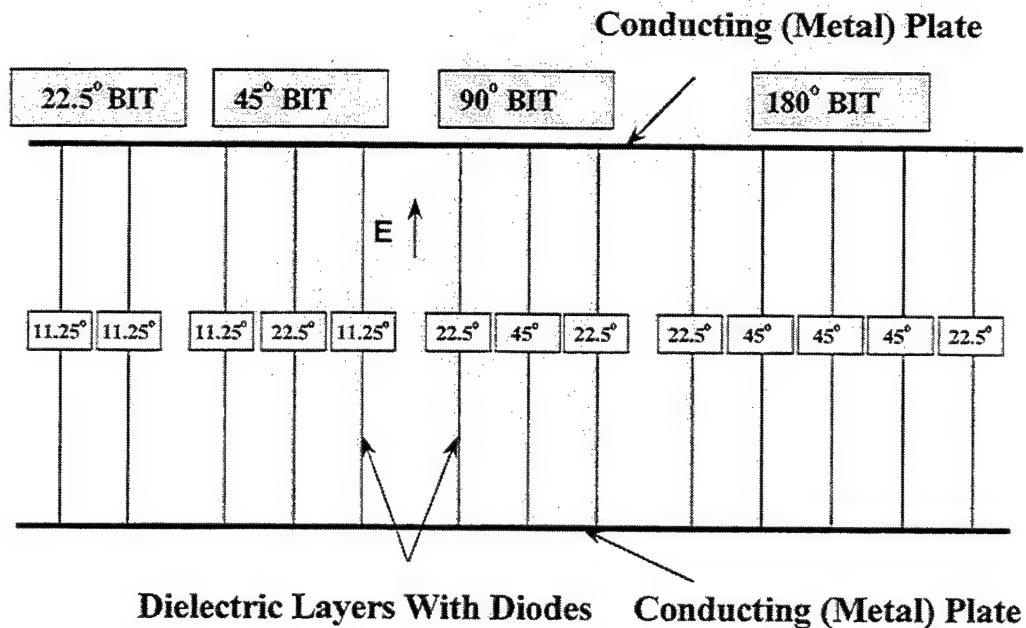


Figure 4. Top view of one column of the Radant Lens, illustrating 13 layers for a 4-Bit Phase Shifter.

The simplest configuration is an E-plane scanning lens in which beam scanning results from a linear phase gradient along the E-plane dimension. One Radant lens provides one-dimensional electronic beam scanning. By restricting the scan action of a lens to a single plane, a great simplification in the bias circuitry is achieved since the individual diodes need not be addressed independently. This reduces the complexity of the driver and facilitates its location exterior to the lens. Two-dimensional scanning can be achieved by cascading two Radant lenses or using one Radant lens in a hybrid configuration [4,5,6]. As stated before only the hybrid configuration is discussed in this paper. However, it may be of interest to note that the Radant lens technology is also being advanced in France by Thompson-CSF. They are using this technology in producing the RBE-2 radar for the French Rafale Fighter Aircraft. They are using a dual lens system with a polarization rotator to scan the beam in azimuth and elevation [7].

In 1995, a contract was awarded to procure a Radant lens in order to add it to the front of the slotted waveguide array to achieve two-dimensional scanning. A photo of the Radant lens in the final stage of construction is shown in Fig. 5.

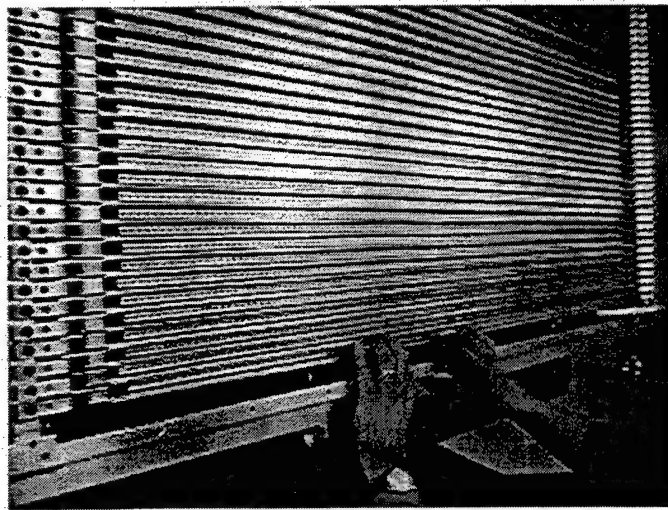


Figure 5. The Radant lens in final stage of construction.

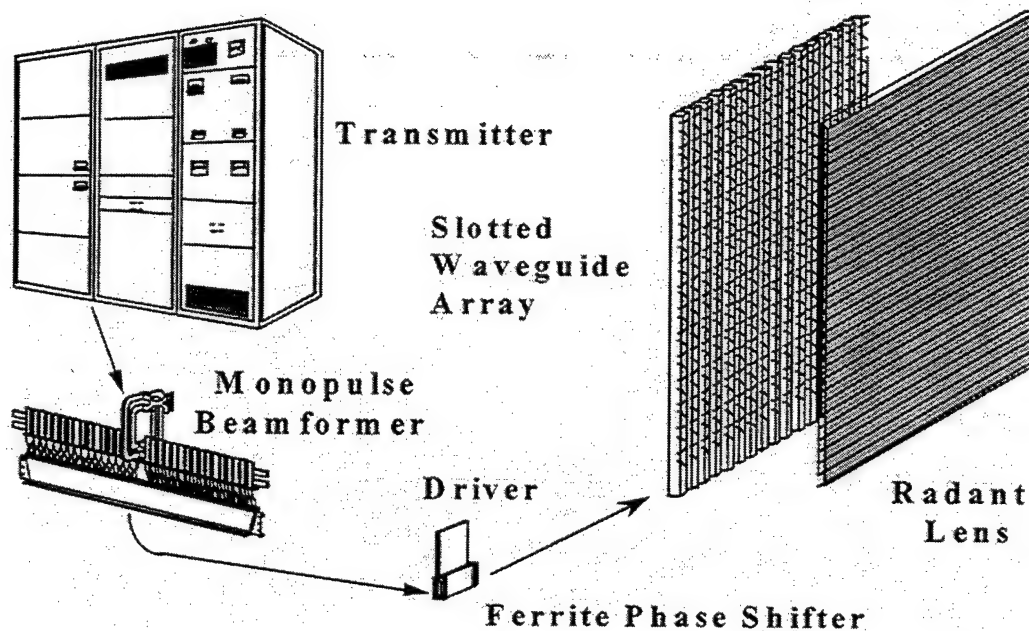


Figure 6. Radant lens with slotted waveguide array system.

Figure 6 shows the hybrid phased array configuration using a slotted waveguide array and a Radant lens in front of it. The slotted waveguide array with associated phase shifters is used to scan the beam in azimuth plane and the Radant lens is used to scan the beam in the elevation plane.

The procurement cost of a single developmental Radant lens is about \$3M. However, the production cost is estimated to be about \$1M. Combining the Radant lens with the previously procured slotted waveguide array and a transmitter will result in a production cost of the hybrid phased array of about \$3M. On the other hand, a phased array of the same size requires 12,000 phase shifters and drivers (or T/R modules). With an optimistic assumption of \$500 per phase shifter and driver (or \$1000 per T/R module), the total cost of a 12,000 element phased array will range from \$8M to \$14M. Therefore, a hybrid array with a Radant lens costs much less than a regular phased array and, hence, is an affordable phased array.

4. Theoretical Predictions

As stated before, each dielectric layer is made up of a dielectric substrate with two metalized strips interconnected by PIN switching diodes. The phase shift is accomplished by selectively setting forward or reverse biasing groups of diodes mounted on the dielectric layers. The amount of phase shift introduced by each layer

depends on the amount of metalization and the property of the diodes. The equivalent circuit model employs lumped elements (inductors, capacitors and resistors) to represent the metalization, the diodes, etc. The Radant Lens operation is modeled using these lumped element values. Three different layers, which gave 45° , 22.5° , and 11.25° phase shift, were designed and built. These three types of layers were used to create a model for the entire lens as illustrated by 13 layers in Fig. 4 for one column of the lens. The theoretically predicted transmission response for the full 13 layer lens is shown in Fig. 7a. The average normal incidence (0°) transmission is about -1.2 dB, with an absolute value of -1.1 dB at band center. To confirm the theoretical predictions, a group of five (5) early production phase shift modules (13 layers) were RF tested. These measured results are shown in Fig 7b.

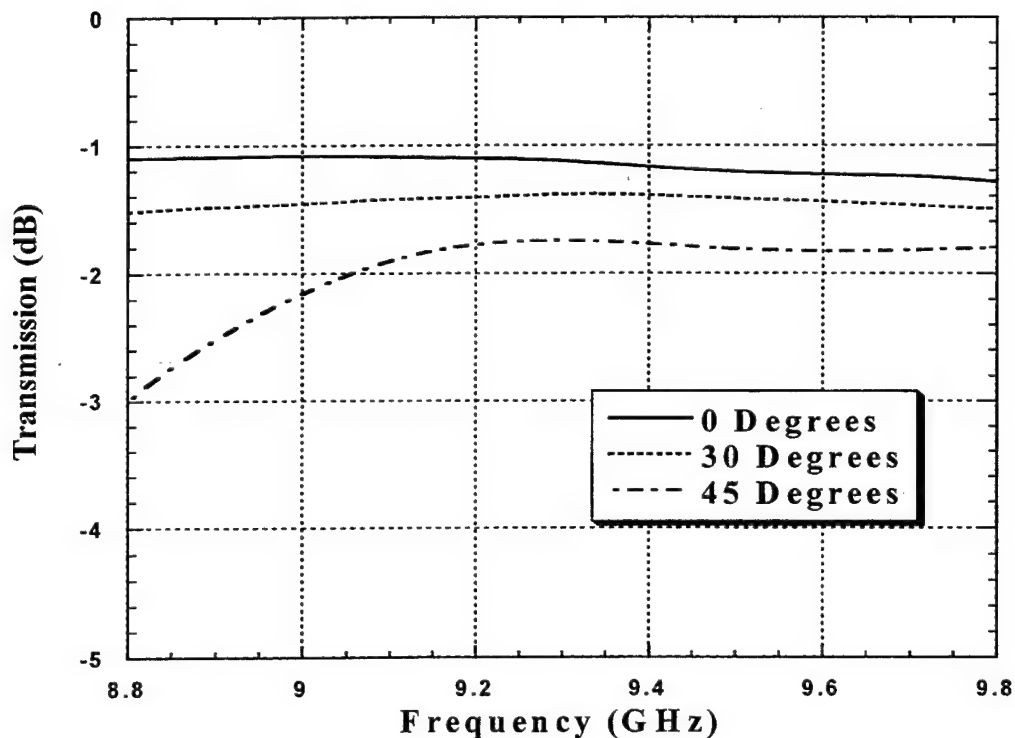


Figure 7a. Plot of model predicted full lens transmission response.

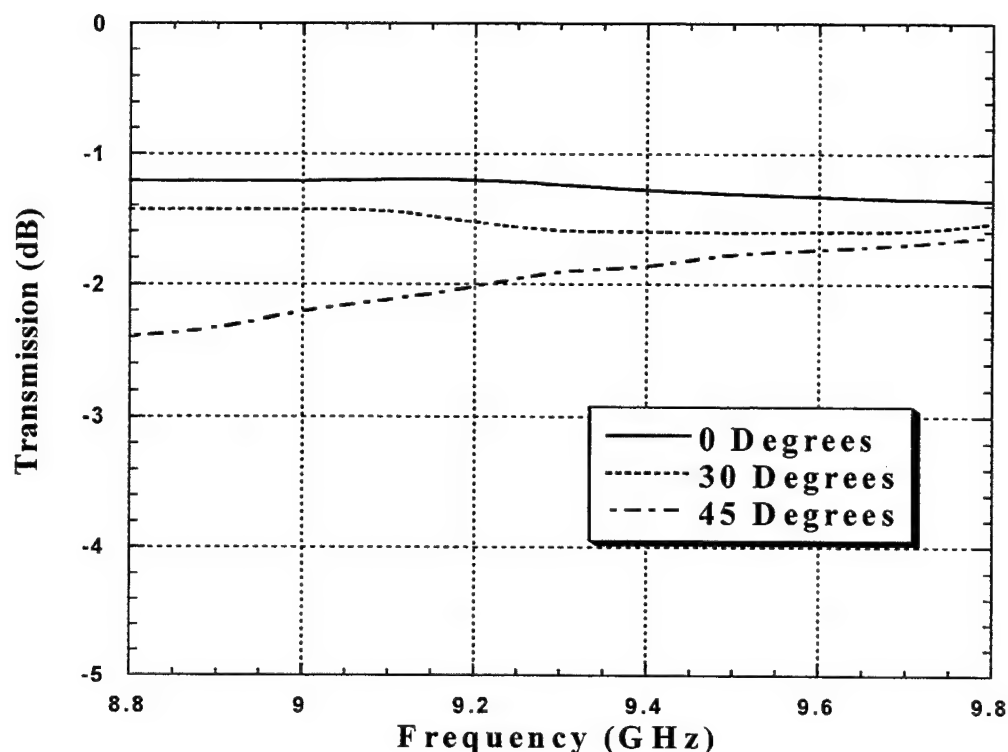


Figure 7b. Plot of transmission measurements taken on five (5) early production modules.

The normal incidence measurements indicated an average insertion loss of -1.2 dB. Within the uncertainty of measurement errors, these measurements agreed well with the theoretical predictions.

5. Experimental Results

Figure 8 shows the experimental setup of the hybrid phased array. It is shown here in the NRL Radar Division's compact range. Measurements of most interest were for the lens losses and the effect of the lens on antenna sidelobes. Therefore, gain and radiation patterns measurements were made with and without the Radant lens. In addition to these measurements, others were taken to calibrate the steering of the lens over the entire frequency band of interest (9.25 to 9.75 GHz). Data was collected in two sessions. First it was collected from the end of June through July

1998. After that time, the lens was repackaged and sent back to Radant Technologies, Inc. for further calibration and improvement. The lens was returned to NRL and final measurements and calibration were performed from the end of January to the middle of March 1999. The hybrid antenna system will be used at NRL's Chesapeake Beach Detachment as part of a 3D radar system.

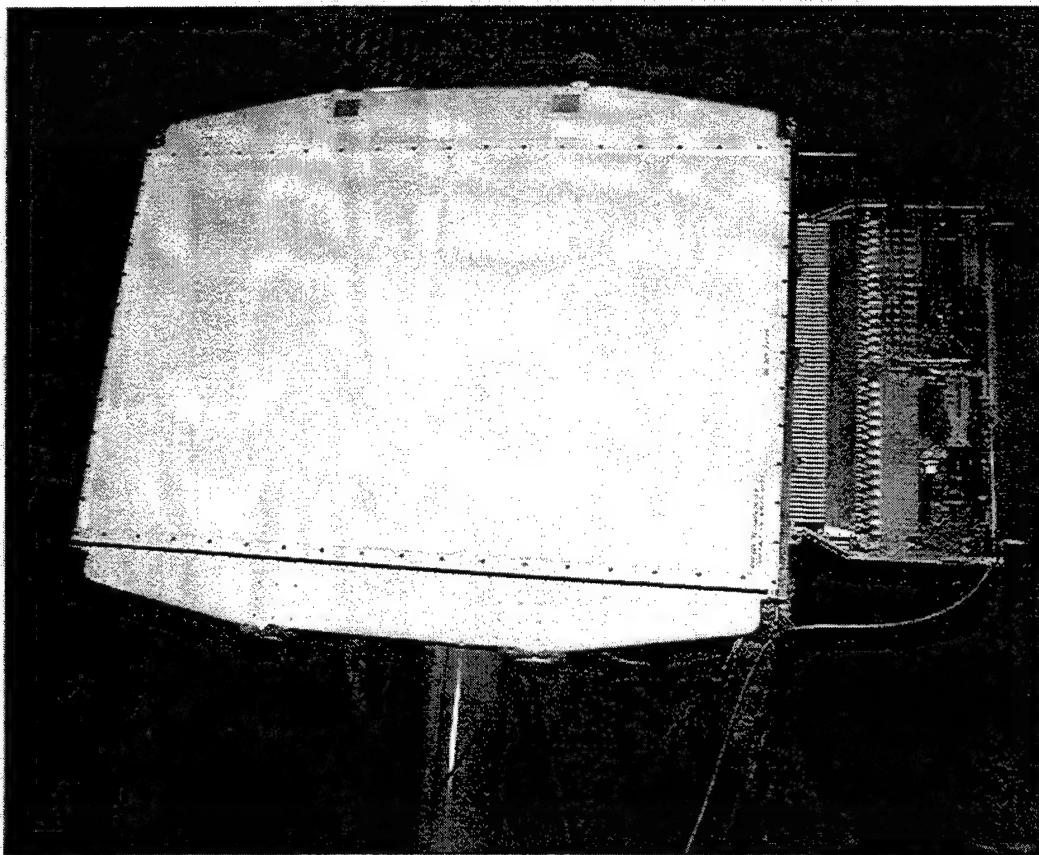


Figure 8. Experimental setup of the hybrid phased array in the compact range test facility. The light object is the Radant lens and the part shown at the back of the Radant lens and to the right is the lower segment of the slotted waveguide array.

Hundreds of antenna array patterns were collected, each one showed that the Radant lens has performed as expected, scanning the antenna beam only with small degradation in the antenna sidelobes. These conclusions are reached by comparing the antenna patterns of the slotted waveguide array by itself with the patterns for the slotted waveguide array with the Radant lens mounted in front of it. The patterns are shown in Figs. 9, 10 and 11. In Fig. 9, H-plane sum patterns for the slotted waveguide array only and the hybrid array are plotted on top of each other. In both

cases the frequency is at 9.25 GHz and the slotted waveguide array is steered to 0° . The Radant lens is powered off, putting the lens in state 15. In state 15, the diodes are all reverse biased, providing no beam steering and allowing the two patterns to line up. Care was taken to ensure that the main beams were peaked in the elevation plane for these azimuth patterns. Fig. 10 shows the difference patterns that are associated with the sum patterns shown in Fig 9. From figs. 9 and 10, it is readily seen that the Radant lens causes very little deterioration in the main beam and the sidelobes.

In fig. 11, a comparison of E-plane sidelobe levels is shown. The frequency is 9.5 GHz and the slotted waveguide array is scanned to 15° . The way this was done was to turn both antennas on their side and tilt the arrays back by 15° . In each case the beams were peaked and patterns were taken by rotating the array(s) about the vertical axis. In this plane there is a squint of 3.5° to 4.0° for each system, which happens because of the nature of the slotted waveguide array. There is also a 0.5° additional squint due to the non-linearities of the Radant lens. This, of course, causes the sidelobes to change. Notice that the highest sidelobe of the slotted waveguide is higher than the same sidelobe for the hybrid even with the loss correction. Notice that the sidelobe deterioration is small in the E-plane, but not quite as small as the H-plane. Not all patterns are as good as these examples, however the sidelobe levels are well within acceptable range for all patterns.

Fig. 12 illustrates the scanning capability of the Radant lens. In this plot, several over lapping patterns at 9.5 GHz are shown. These are E-plane patterns showing the lens ability to scan over large angles. In this example, the lens was scanned to 0° , $\pm 10^\circ$, $\pm 20^\circ$, $\pm 30^\circ$, $\pm 40^\circ$, and 45° . The main beams are not exactly at the correct angles due to the squint of the slotted waveguide array beam in this plane, which would be calibrated out when used with a radar system. Figs. 13 and 14 show E-plane patterns for two of the cases shown in Fig 12, the -30° (Fig 13) and 45° (Fig 14) scanned cases. For these two cases, no comparison pattern can be made to show how well it matches to the slotted waveguide only pattern. This, of course, is because the slotted waveguide array cannot scan to these angles. What is shown in these two patterns is that the relative sidelobe levels are reasonable and similar in level to the broadside cases, indicating that the Radant lens did not introduce large phase errors.

Now the transmission loss of the Radant lens is considered. This will be discussed from two main vantage points: The loss while scanning the beam and the loss while staring. In the staring mode, all diode phase shifters are set to the same state and the main beam does not change angle while passing through the lens (other

than due to small non-linearities). In the scanning mode, the main beam is steered away from broadside and this can only be accomplished with the diode phase shifters in various states. With the diode phase shifters in various state, there are different numbers of forward and reverse biased diodes. This results in a different loss than the staring state. In each mode, the loss was measured by taking the difference of the main beam peaks of the slotted waveguide array by itself and the hybrid array.

In staring state, there was no power applied to the Radant lens, which put all the diodes into state 15 or all diodes reverse biased. The loss for this case varied nearly linearly with frequency from 1.5 dB at 9.25 GHz to 2.5 dB at 9.75 GHz. In the scanning mode, the diode phase shifters states are somewhat random in appearance. With the Radant lens scanned to 20° , NRL measured a loss of 2.4 dB at 9.25 GHz, increasing linearly to 2.5 dB at 9.75 GHz. These losses are higher than the theoretical predictions. Radant Technologies, Inc. discussed the reasons for these higher losses[8] and provided ways to reduce them. In fact, Radant Technologies, Inc., since this lens was made, have constructed another smaller lens that has a loss of approximately 1 dB across the band.

6. Conclusions

An affordable hybrid phased array configuration is discussed. The hybrid configuration is made up of a modified AN/TPQ-36 antenna (a slotted waveguide array) and a Radant lens in front of it. The slotted waveguide array with the associated phase shifters at each column is used to scan the beam in the azimuth plane and the Radant lens is used to scan the beam in the elevation plane. Recently, a $4' \times 8'$ Radant lens was procured from Radant Technologies, Inc. for this purpose. Experiments were performed at Radant and then at NRL's compact range on this affordable hybrid array configuration to measure insertion loss, pattern distortion and scanning performance. Although the measured Radant Lens loss is a bit higher than the theoretically predicted loss, the Radant Lens performed well with good scanning properties, low radiation pattern distortion and low return loss. The major result of this development has been the successful demonstration of a low cost Radant lens, which is an electronically steerable antenna that could be employed for military and commercial application.

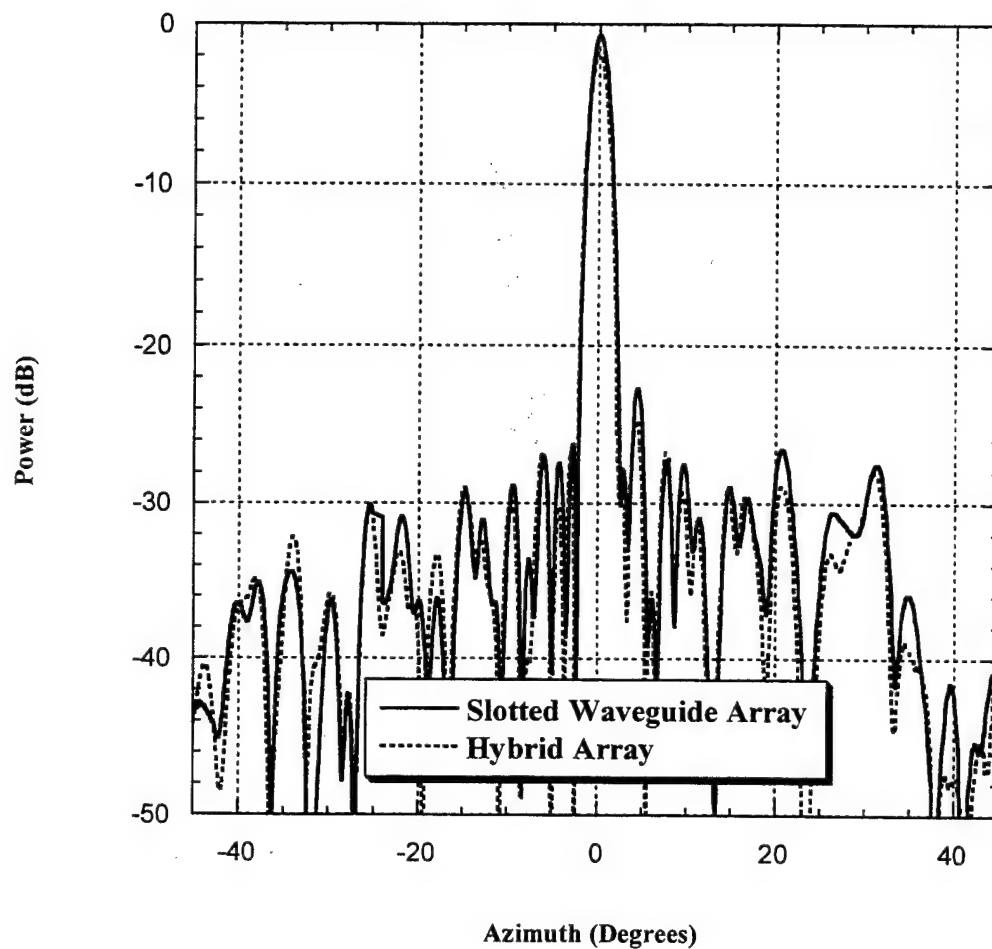


Figure 9. H-Plane sum channel patterns of slotted waveguide array only and hybrid array at 9.25 GHz.

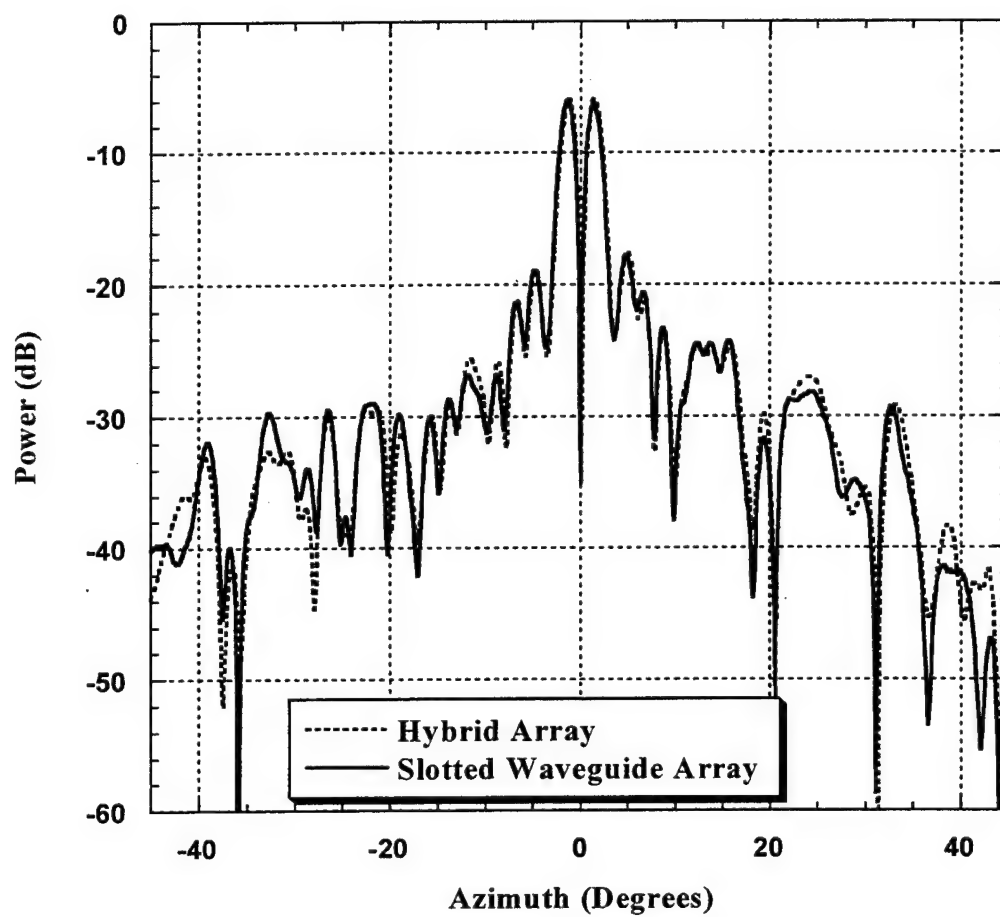


Figure 10. H-Plane difference patterns of slotted waveguide array only and hybrid array at 9.25 GHz.

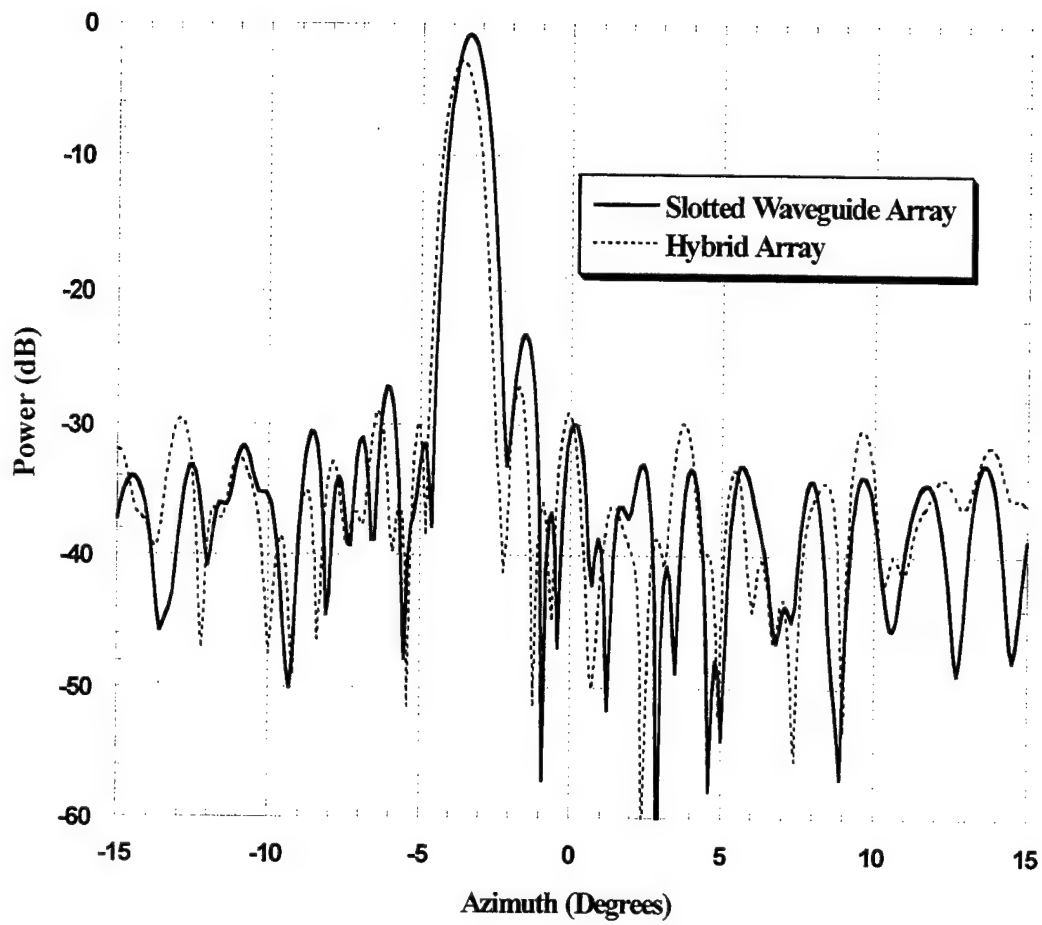


Figure 11. E-Plane patterns of slotted waveguide array only and hybrid array at 9.50 GHz.

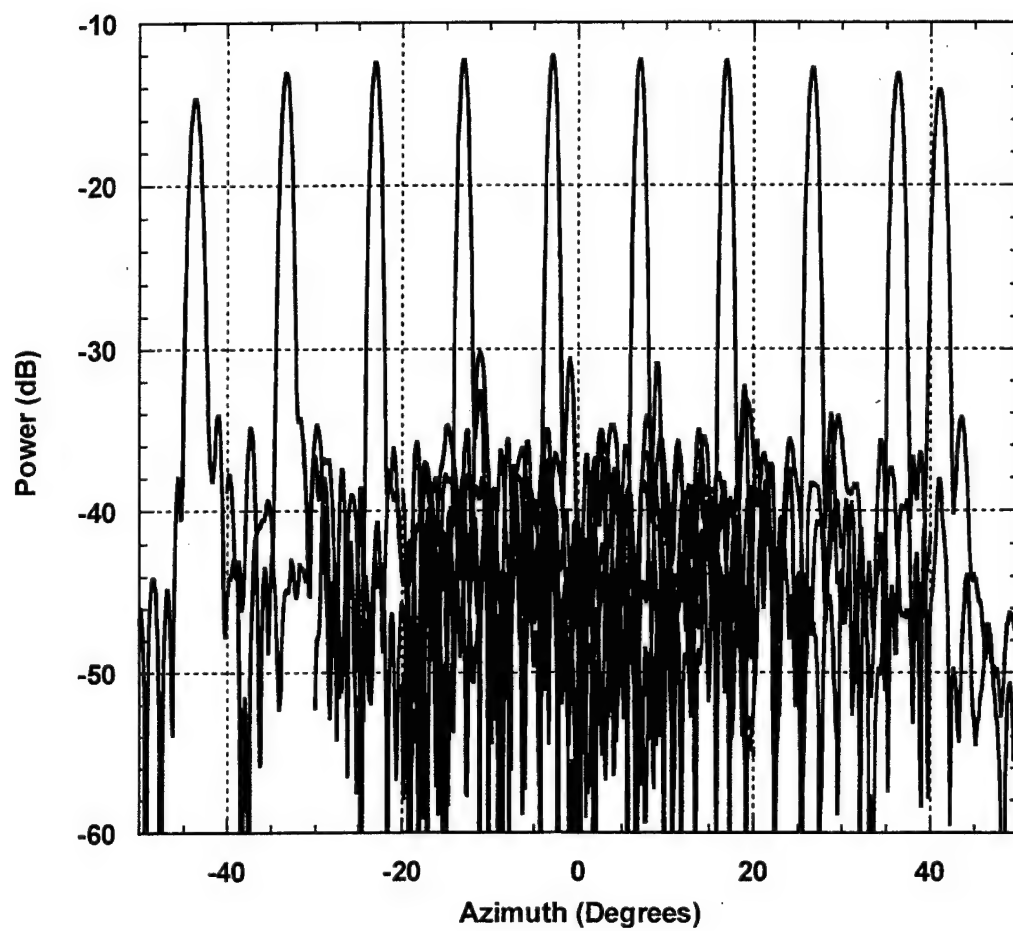


Figure 12. E-Plane patterns of hybrid array at various scan angles.

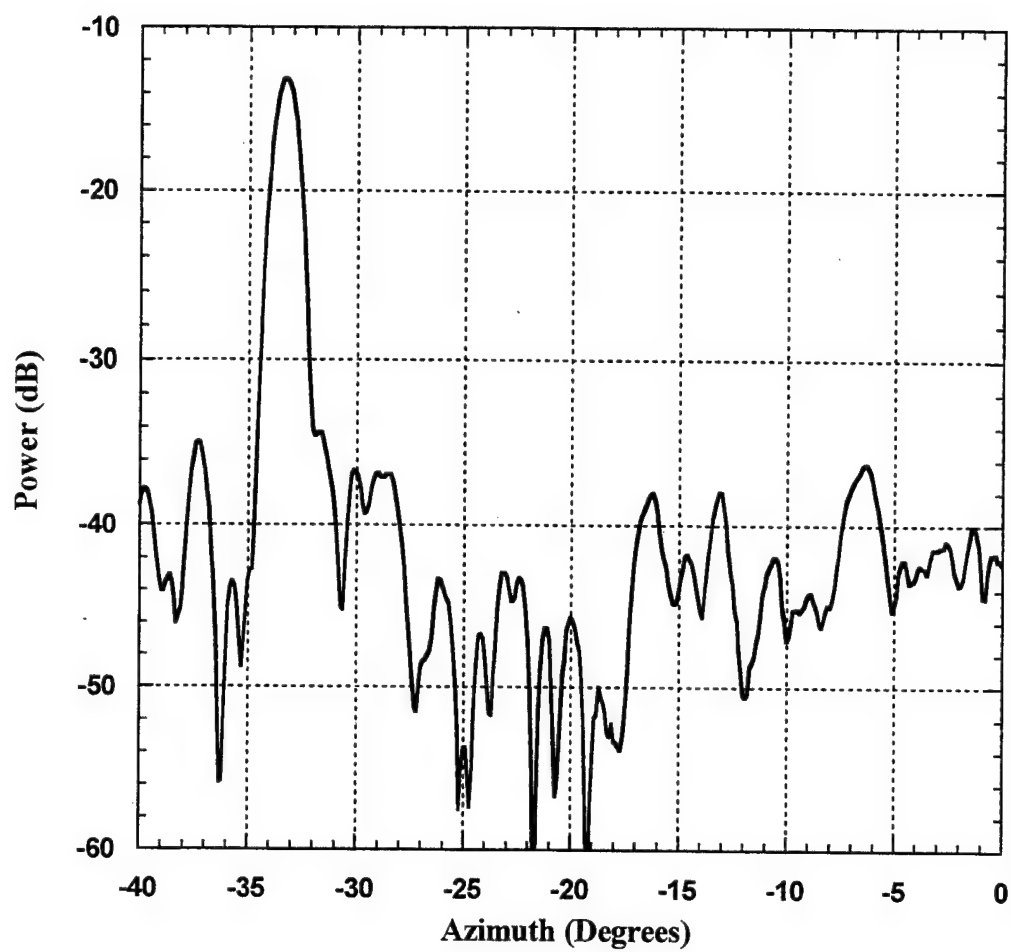


Figure 13. E-Plane pattern of the hybrid array scanned to -30°

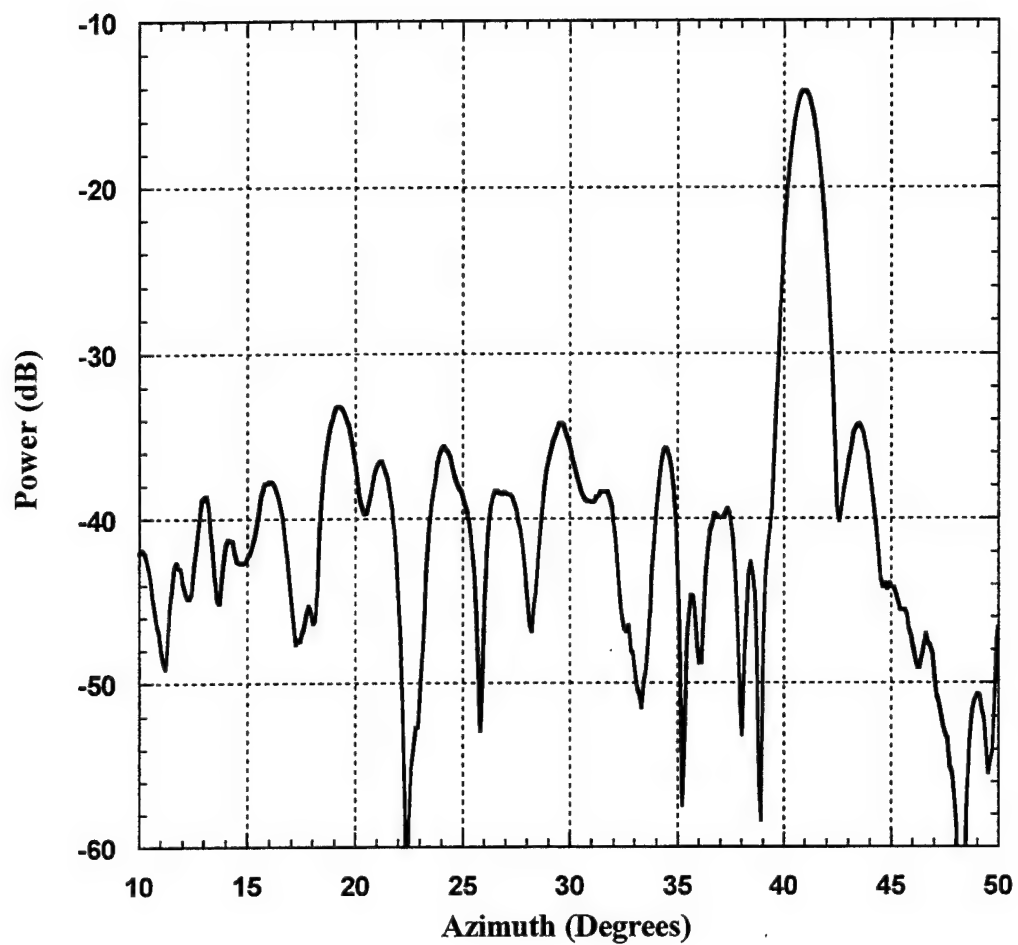


Figure 14. E- Plane pattern of the hybrid array scanned to 45°.

REFERENCES

- [1] J.B.L. Rao, T.C. Cheston and A.A. Moffat, "X-Band Phased Array Antenna Options for One and Two Dimensional Scanning", NRL Memo Report 6846, July 1, 1991.
- [2] J.B.L. Rao, T.C. Cheston, J.B. Evins, J.J. Alter, A.A. Moffat, and P.K. Hughes, "One-Dimensional Scanning X-Band Phased Array for an Engagement Radar", NRL Memorandum Report 7853, June 11, 1996.
- [3] Janice Leibinger, "Demonstration of Two Axis electronic Scanning by a Hybrid Radant-TM Lens Array", Final Technical Report, Rome Laboratory Report No. RL-TR-91-201, September 1991.
- [4] J.B.L. Rao, "Low Cost Phased Arrays", NRL Memo Report No. 7793, Washington, DC, November 24, 1995.
- [5] J.B.L. Rao, P.K. Hughes, II, G.V. Trunk, and J. C. Sureau, "Affordable Phased Array for Ship Self-Defense Engagement Radar", IEEE 1996 National Radar Conference, Ann Arbor, MI, May 1996.
- [6] J.B.L. Rao, G.V. Trunk, and D.P. Patel, "Two Low Cost Phased Arrays", IEEE 1996 International Symposium on Phased Array Systems and Technology, Boston, MA, October 1996.
- [7] J. Colin, "Phased Array Radars in France: Present and Future", 1996 IEEE International Symposium on Phased Array Systems and Technology, Boston, MA, October 1996.
- [8] Radant Technologies, Inc., "Electronic Scanning Lens for the NRL X-Band Engagement Radar Antenna", Final Technical Report, Contract No. N00014-95-C-2027, May 20, 1999.

MILLIMETER-WAVES RADIAL-LINE SLOT-ARRAY ANTENNA

Anatoliy A. Boryssenko
Scientific-research company "Diascarb",
P.O. Box 370, Kyiv, 253222, Ukraine,
E-mail: diascarb@public.ua.net

Abstract: The millimeter-waves radial-line slot array (RLSA) is perspective antenna for communications and radars due to high level of its performances achieved, as well as mass production opportunities by application of printed-circuit technology like for microstrip patch antennas. Both the theoretical and the experimental approaches to develop the millimeter-waves, 30-35 GHz band, linear-polarized, single-layered RLSA antenna will be presented. The theoretical consideration is aimed to predict antenna performances and develop relevant antenna design procedure while the experimental technique is employed for verification of theoretical concept as well as to estimate antenna's features can be achieved. The technological aspects of the millimeter-waves RLSA antenna creation will be considered here. Results of experimental investigations of the 50-200 mm diameter RLSA antenna in the 30-35 GHz band will be presented and discussed in this paper.

1. Introduction

A RLSA antenna has been proposed nearly 40 years ago [1] and became the subject of study as perspective antenna for direct TV satellite broadcasting and any other wireless communications since 1980 [2]. Undoubted preferable features of RLSA antenna include high efficiency and gain, easiness for handling and front-end installation etc. In contrast to commonly used parabolic antenna the RLSA antenna differs as low-profile, low-weight, and more-aesthetic one [3]. The millimeter-wave RLSA antenna presented here has additional advantages like portability and massive production opportunity. The last factor is achieved by employment of a printed-circuit technology for fabrication of antenna slotted-aperture due to its small-sized geometry in contrast to the X-band RLSA antenna. In another words, the millimeter-wave RLSA antenna can be manufactured like microstrip patch antennas while the manufacturing of the X-band RLSA antenna, which demands special labor technological mechanical operations when total production charges depends on number of slots produced directly [3].

There are some literature indications on the millimeter-waves RLSA antenna [4] but up to now the most studies are devoted to the X-band RLSA one. The millimeter-waves band, 30-35 GHz band, single-layered, linear-polarized RLSA antenna is under investigation in this paper. In contrast to the X-band (12GHz) RLSA antennas the millimeter-wave ones have additional benefits from technological point of view. The radiation characteristics, including pattern, antenna beam-width with 3-dB criterion, side-lobe level, gain factor, input VSWR (return-loss) are evaluated here by theoretical considerations based on model of slot in waveguide and matrix model involved slots' assembly forming antenna aperture. This theoretical model is simultaneously methodological foundation for a RLSA synthesis procedure to set exactly locations and dimensions of slots for obtaining the total performances required. Special attention has been paid to technological aspects to manufacture the millimeter-wave RLSA antenna prototypes as well to develop antenna feeding unit that should be preferable for front-end installation via a 7.2x3.4 mm (WR28) standard waveguide.

Some experimental research series have been performed to confirm the validity of the proposed theoretical concepts and to research experimentally some aspects of studied problems. Compact antenna range assembly based on the analog network analyzer has been employed. A good agreement between experimental and theoretical results has been obtained. Presented data result from considerable theoretical and experimental studies conducted by the author since 1990.

2. Problem Configuration

Fig. 1 shows the usual basic configuration of single-layered, linear-polarized RLSA antenna that is same in general features for the well-know X-band antennas [2,3] and millimeter-waves ones. Note that the millimeter-waves RLSA antenna has some construction peculiarities concerning implementation of its principal components like: 1) the radiating aperture formed by the upper plate of radial line with definite slot topology performed on dielectric substrate by etching process; 2) the lower plate of radial line served simultaneously as antenna construction base for its easy handling and installation; 3) antenna feeding unit included two transitions, i.e. 'rectangular guide - coaxial' and 'coaxial - radial line'. Shortly speaking, the RLSA antenna operates like a traveling wave antenna with gradually decaying outward wave, which starts from feeding point and excites consequently each partial linear-polarized radiator formed by pair of slots in common mode [2,3] (Fig. 2) to get linear polarization. An electromagnetic coupling between slots and radial outward wave produces definite amplitude-phase distribution of field over aperture resulted finally in some radiation performances obtained.

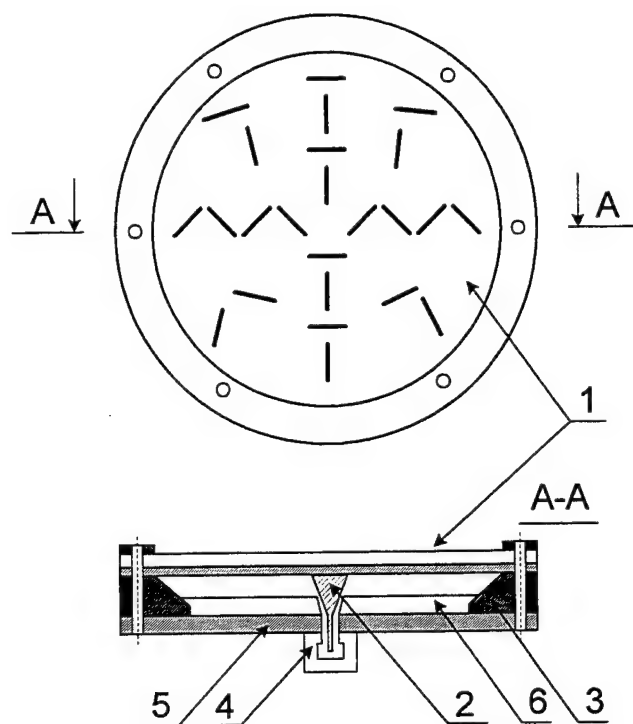


Fig. 1. Schematic presentation of the single-layered linear-polarized RLSA antenna with its principal elements: 1) upper radiating plate with slots on dielectric substrate with metallic thin sheet; 2) conical launcher of radial line; 3) matched edge load; 4) waveguide feeder; 5) antenna base and lower radial line plate; 6) slow-wave dielectric material.

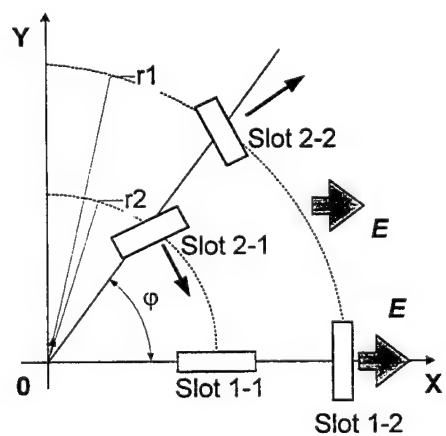


Fig. 2. Common slot geometry of linear-polarized RLSA antenna.

3. General Theoretical Consideration

3.1. Model of single slot

An equivalent electrical lumped-circuit model of single slot (Fig. 3) is starting point for the RLSA analysis [5]. This equivalent circuit with evident resonance features characterized by resonance frequency f_0 and quality factor Q [9] is shown in Fig. 3. The next step of analysis involves formal description of slot frequency behavior in a transmission line like in Fig. 4 for the TEM two-plate guide. Note that some correction of slot's length is necessary due to edge radiation effect.

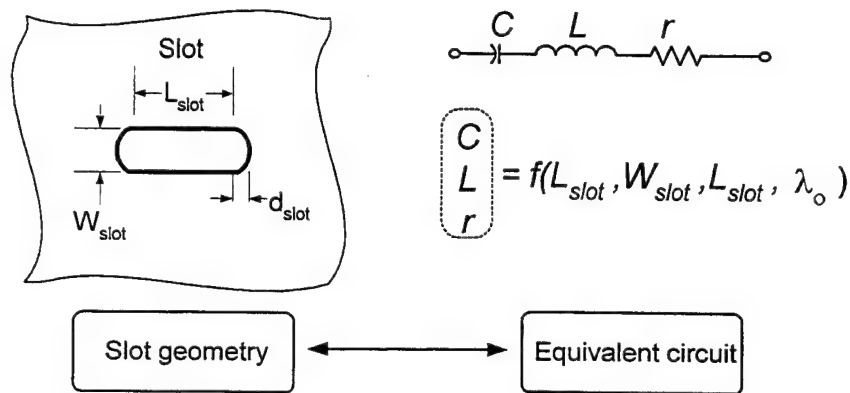


Fig. 3. Equivalent electrical lumped-circuit model of slot in thin metallic plate.

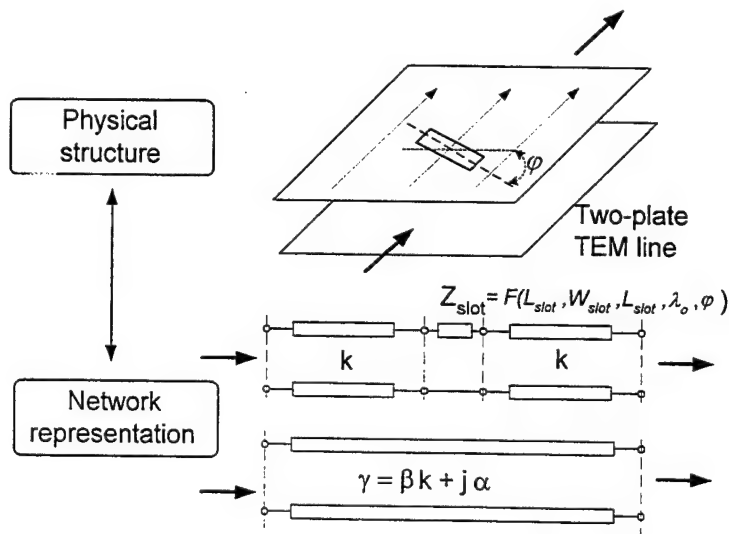


Fig. 4. Equivalent transmission line model of slot in the TEM two-plate guide.

It was established by the author that an approximated slot's analysis based on wave matrix model is productive in practice for considered problem. The basic idea implemented here is one that slot's influence on propagation features of waveguide fundamental mode, i.e. TEM mode in this case, can be outlined as modification of waveguide impedance and its wave propagation factor, which become frequency-dependent, i.e. disperse and complex [7].

3.2. Model of slots' assembly in radial line

Some specific properties of radial line [6] should be involved in study too. A radial line is treated here by its ringed-segment parts as shown conditionally in Fig. 5. Each segment is described by the T transmission matrix:

$$T = \begin{bmatrix} \frac{\exp(-j \cdot \beta \cdot d)}{\sqrt{1 + d / Ro}} & \frac{\exp(-j \cdot \beta \cdot d)}{\sqrt{1 + d / Ro}} \\ \sqrt{1 + d / Ro} \cdot \exp(-j \cdot \beta \cdot d) & 0 \end{bmatrix} \quad (1)$$

The T-matrix as any wave matrix for radial-line requires special cares concerning wave amplitude decreasing due to natural radial-wave outward propagation. Such formal approach is preferable thanks the fact that it allows inside framework of single mathematical model to compute all necessary values to characterize antenna internal features like return-loss and external one as radiation pattern and efficiency. In the radial-patch model proposed an amplitude-phase distribution of electromagnetic field over round aperture to achieve necessary radiation features is determined as superposition of all radial subsections (Fig. 5). In turn, amplitude-phase distribution of each subsection is determined by voltage drop on it that is difference between its input and output voltage for outward wave (Fig. 6). Frequency dependence of the T-matrix RLSA model gives possibilities to estimate antenna total frequency response in the operation frequency band.

In accordance to discussed model, the slot-disturbed aperture of radial line can be described via properties of equivalent transmission line that includes such factors like (Fig. 7): 1) slow-wave coefficient that modified effective wavelength in radial line and slots' spacing, 2) aperture coupling factor, i.e. leakage constants, which determines the effects of power take-off by slots from traveling outward wave that resulted in aperture field distribution, 3) phase of slot's voltage drop that is actual to maintain in-phase aperture field distribution. All these values are important for the aperture synthesis procedure considered above to obtain slotted aperture geometry for given pattern and radiation antenna requirements.

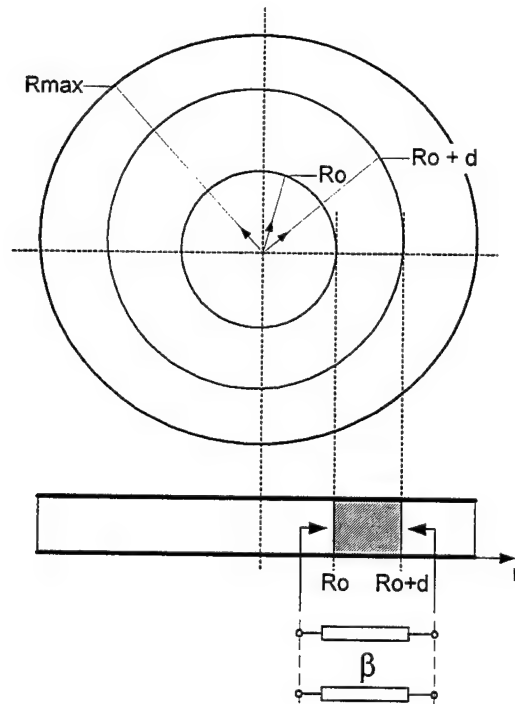


Fig. 5. Ringed segment of radial line for its presentation by transmission line model.

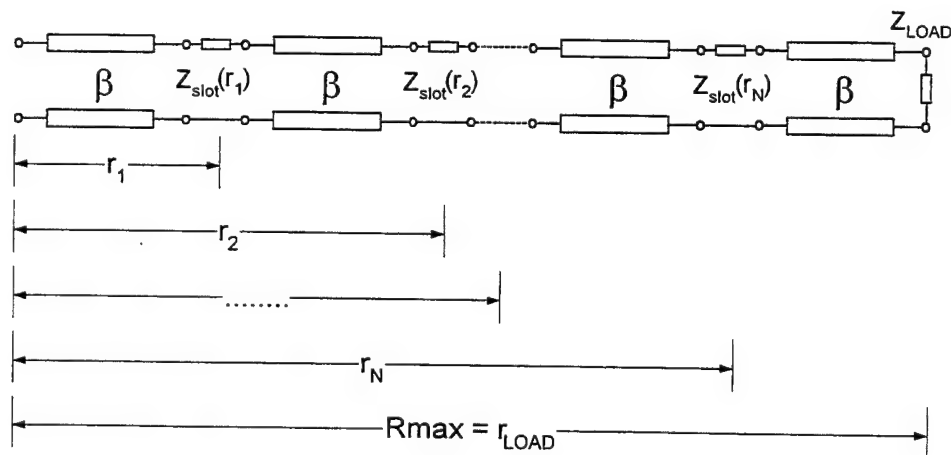


Fig. 6. Equivalent transmission line model of slots' assembly in the radial guide forming RLSA antenna aperture like quasi-periodic radial structure.

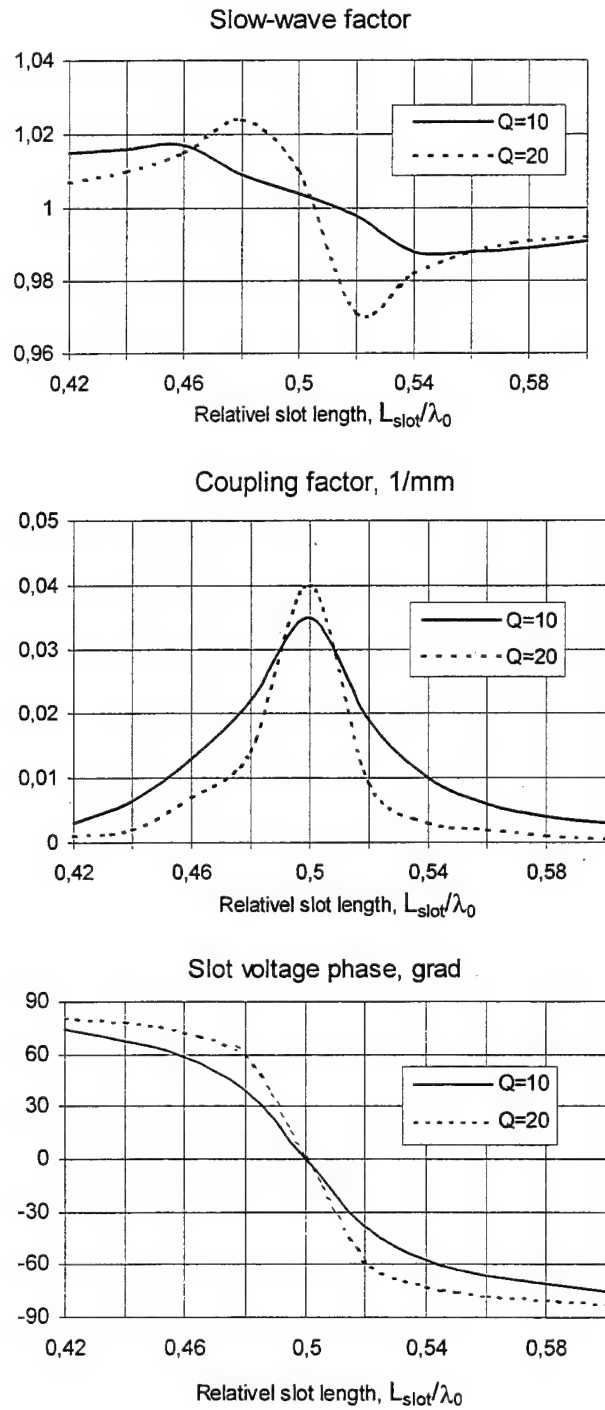


Fig. 7. Equivalent electrical features of slotted radial line where quality factor Q as parameter above is determined by slot geometry in Fig. 3 mainly.

4. CAD Synthesis Procedure

The developed synthesis procedure has implemented in the CAD-like software (Fig.9) to automate process of the RLSA antenna design. This software allows to design by iterations the slots' geometry to create mask of printed circuit technology for given set of antenna required performances. The RLSA antenna synthesis procedure includes the three main operationalization stages.

Firstly, a preliminary energy synthesis of antenna for chosen aperture amplitude field distribution $U(\mathbf{r})$ is accomplished that gives radial distribution of coupling factor $A(\mathbf{r})$ under assumption about in-phase aperture field distribution. At that there is some potential limits of the RLSA antenna efficiency shown in Fig. 8 that is similar to any traveling wave antenna when some optimal coupling factor exists due-to unavoidable trade-off between aperture efficiency affected by uniformity of aperture field distribution and antenna edge loading efficiency.

Next, slot geometry under requirement of grating lobe banning and in-phase aperture field distribution is determined based on taking into consideration all phase determined components in Fig. 7, i.e. slots' geometry, radial distance between them and slow-wave factor. Note that slots' length and spatial spacing is sufficiently non-uniform along radius of radial line. Finally, the matrix model of RLSA antenna offers estimating in the operation frequency band antenna gain and its aperture efficiency obtained, as well as antenna return-loss and total efficiency. At any synthesis stage the possibility to correct previous stages exists due to iterative nature of used design strategy with step-by-step or loop repetition to get finally a RLSA antenna mask.

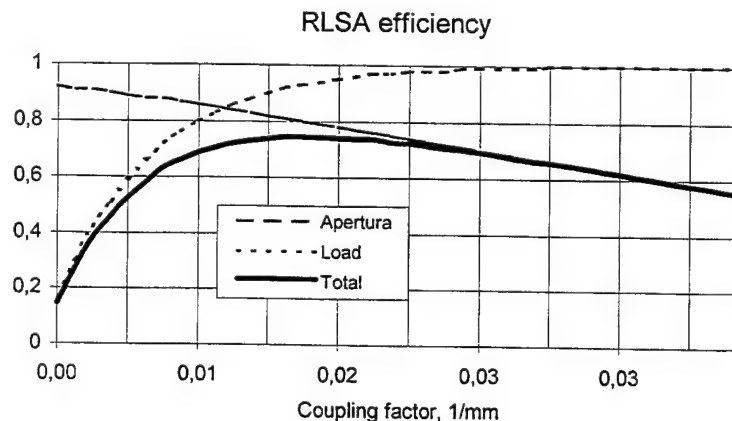


Fig. 8. Potential efficiency of the 200mm-diameter 32 GHz RLSA antenna with constant over aperture coupling factor.

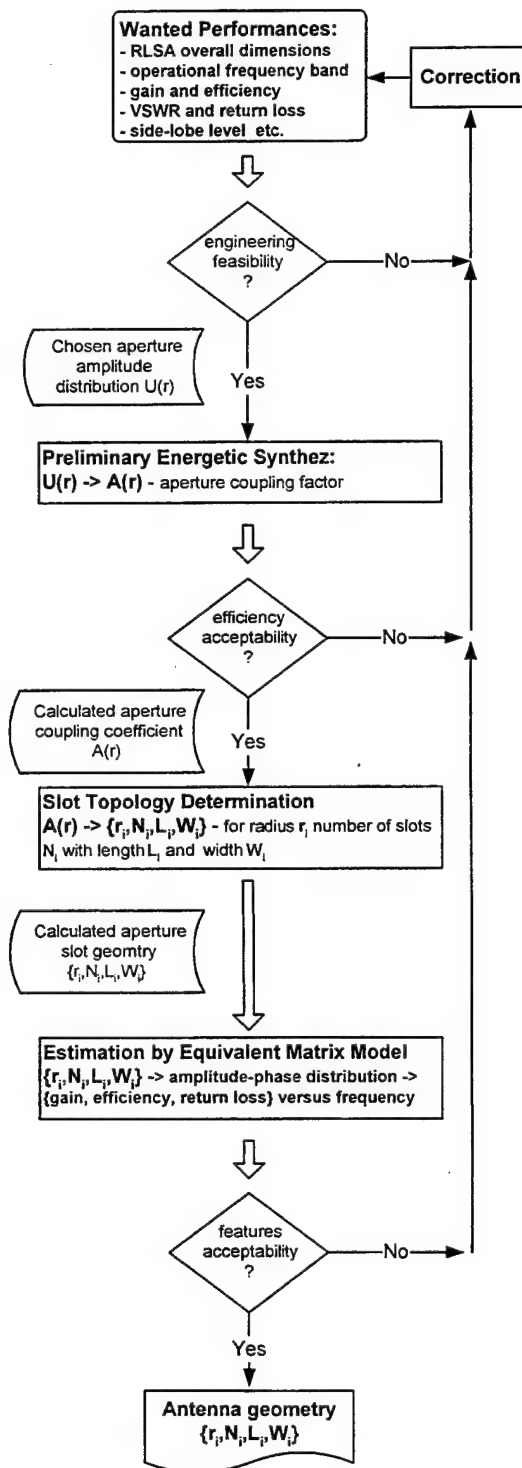


Fig. 9. Flowchart of the RLSA antenna synthesis procedure.

5. Some Technological Aspects of Antenna Prototype Manufacturing

As stated before, the millimeter-waves RLSA antenna has very attractive features due to its mass production opportunities, i.e. possibility to employ the printed-circuit technology like one for microstrip patch antennas and arrays. So, the upper slot-consisted plate of radial line (Fig. 1) can be fabricated by using mask produced by the CAD software in accordance with final antenna features required. The mask of slots' topology have been accomplished by computer laser jet printing on transparent film under control of special component of the CAD software. Later, the slotted antenna aperture can be fabricated by employment of common chemical etching technology with negative mask setting etc.

To accomplish the upper plate of RLSA antenna with complex slot topology, the thin foil-clad sheet-like dielectric materials with bonded copper 0.2 mm foil has been used. Both such low-frequency material applied in the 0.1-5 GHz frequency band mainly and more high-frequency, more expansive, fluoroplastic materials have been used by the author. Dielectric constant of used substrate materials have been estimated experimentally because corresponding figures have been known from references, at best, for low frequencies namely in some range that gives very large uncertainty, which is very critical aspect for proper RLSA antenna design. Same reasons are valid too for the slow-wave dielectric material used in the RLSA antenna to prevent grating lobes (Fig. 1). Moreover, any dielectric material have inherently a definite dispersion of its electrical properties that must be taken into consideration to estimate statistical dispersion of antenna final performances achieved, as well as manufacture tolerances for slots' position and their total geometry (length, width, shape).

In the presented investigations each example of RLSA antenna prototype has been designed for definite materials employed with electrical features estimated preliminary by applications of a special experimental technique shown in Fig. 10. This technique is based on estimation of dielectric constant and attenuation factor by measured values of resonance frequencies and quality factors in the reference low-coupled waveguide resonator (Fig. 10a), which enables its precise computing due to known exactly electrodynamics model (Fig. 10d) like one for slot slot-line (Fig. 10b) and dielectric H-guide (Fig. 10c) resonators.

For example, typical values of dielectric constant of high-frequency dielectric materials measured in the 30-34 GHz frequency band were about 3.75...3.80 with $\tan\delta \approx 5...6 \times 10^{-4}$ while the low-frequency materials have demonstrated 2.30...2.40 dielectric constant with $\tan\delta \approx 3...4 \times 10^{-3}$.

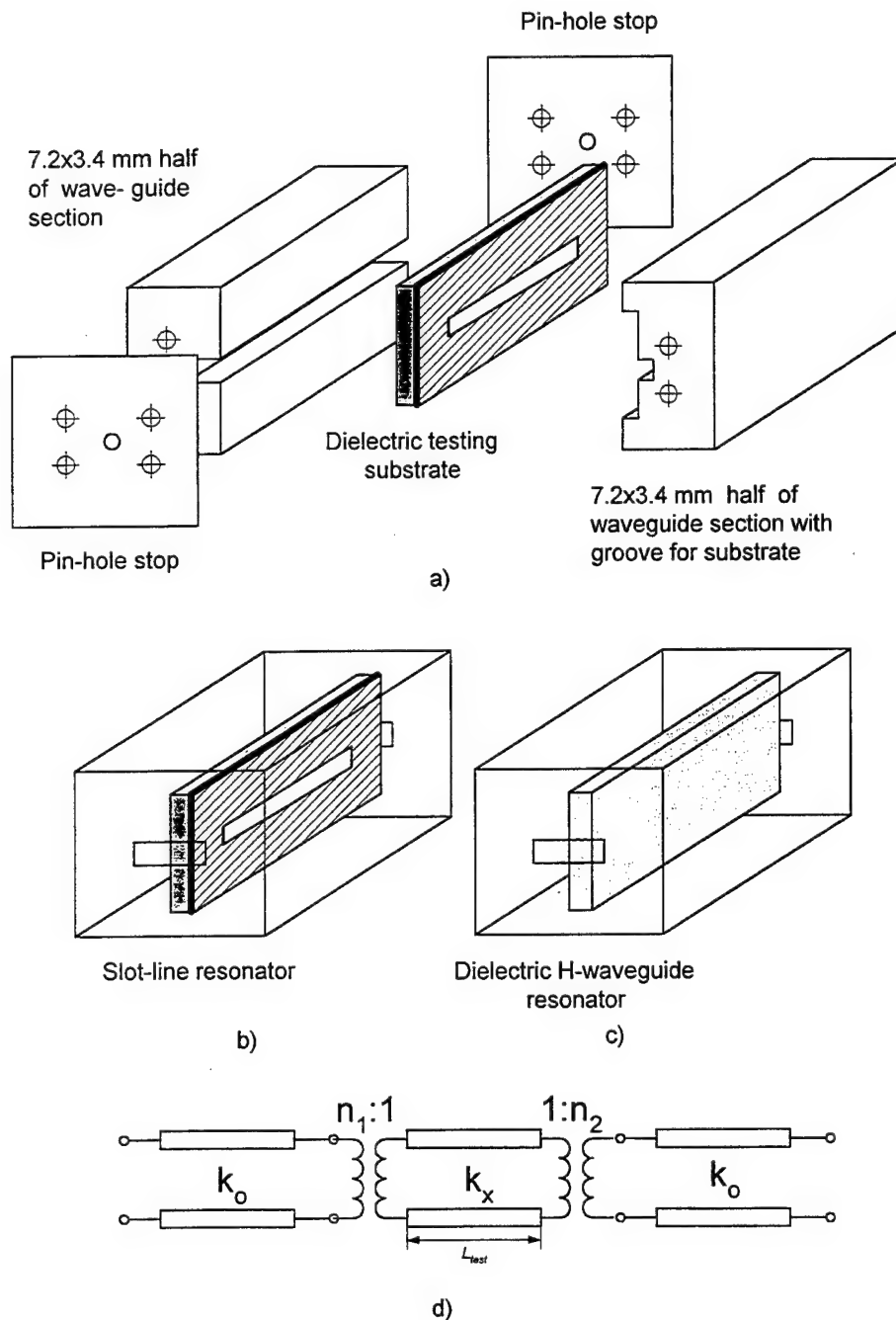


Fig. 10. Experimental studies to measure electrical properties of used dielectric materials: (a) method of low-coupled resonator in rectangular waveguide section, (b) slot-line resonator concept; (c) dielectric H-guide resonator method; (d) equivalent lumped-circuit for resonator computing.

6. Antenna Feeding

In contrast to the X-band RLSA antenna where feeding unit via coaxial line is employed [2-3], a standard waveguide feeding of 7.2x3.4 mm cross-section is preferable for the millimeter-waves RLSA antenna of the 30-34 GHz frequency band. So a some transition unit from rectangular waveguide to radial line is necessary. As results of studies conducted, a combined transition has been found more preferable for the millimeter-waves RLSA antenna. This transition consists of the first stage presented by a rectangular waveguide-coaxial line junction that connected with the next stage formed by coaxial-to-radial line transition.

Such combined transition has been implemented for antenna feeding. There are two constructive variants to implement the millimeter-waves RLSA antenna feeding via the standard 7.2x3.4 mm guide. These variants differ by position of input waveguide aperture in accordance to the main based plate of antenna (Fig. 1), i.e. with orthogonal orientation (Fig. 11b) where exciting probe is employed and parallel installation (Fig. 11a) with magnetic loop-like exciting elements. These both variants have been developed and tested experimentally. As for coaxial-to-radial line junction the two variants similar to ones studied before [2,3] have been employed: conductive conical-ended (Fig. 12a) and disk-ended capacitive (Fig. 12b) probes designed by electrostatic model with the following experimental revisions accomplished. Electromagnetic coupling between waveguide and coaxial line has been implemented by using planar printed circuits as in Fig. 12c-f, i.e. printed loops in Fig. 12c-d, and printed probes in Fig. 12e-f that is very attractive from manufacturing point of view in contrast to solid elements.

As seen in Fig. 12c-f some presented printed transition elements contain as well an additional circuit for return-loss compensation. The last is serious problem for linear-polarized RLSA antennas caused degradation of antenna total efficiency [3]. It is known that return-loss of such antenna seen by its feeding point is forced by in-phase summation of return waves produced by each radial set of slots spaced at half-wave distances. In this paper some improvement of antenna efficiency by mentioned above circuit has been achieved. Note that this solution is very preferable because it put into effect by compact millimeter-waves printed circuit imbedded in a feeding waveguide of the RLSA antenna.

Total performances of the RLSA antenna feeding unit can be investigated by its equivalent electrical circuit presented in Fig. 12g that consists of all discussed above components, including return-loss compensation circuit [8].

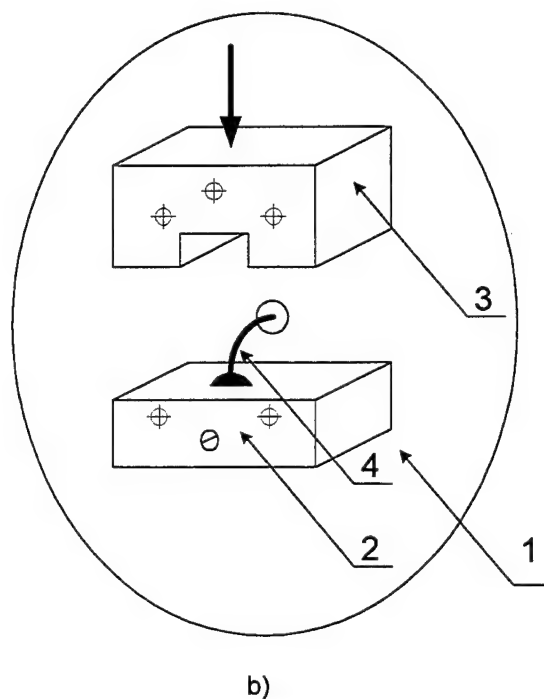
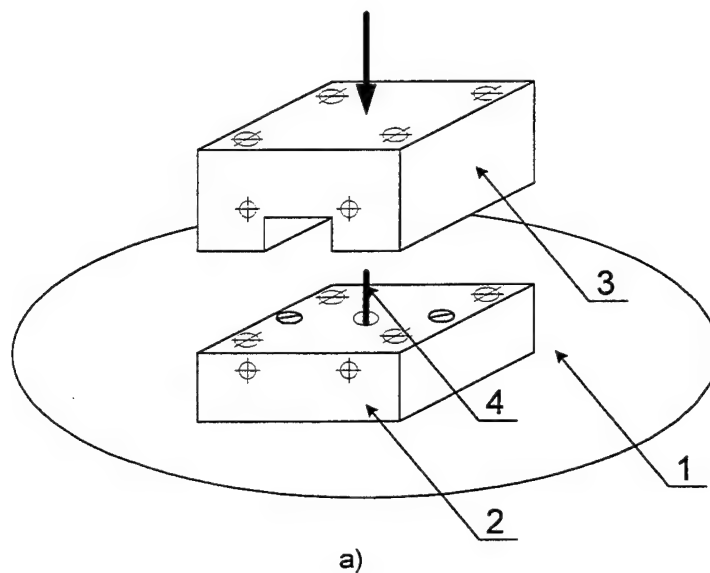


Fig. 11. Constructive variants to implement the millimeter-waves RLSA antenna feeding via the standard 7.2x3.4 mm guide: (a) orthogonal position of feeding waveguide in accordance to main based plate of antenna with exiting probe, (b) parallel position of feeding waveguide with exciting loop where 1- antenna base, 2&3 - waveguide half-sections, 4 - waveguide exciting element (probe or loop).

7. Experimental Measurement Set-up

The special experimental measurement assembly has been developed (Fig. 13). This assembly includes the analog network analyzer for the 26-39 GHz frequency band as base elements with 7.2x3.4 mm waveguide interconnections. The two antennas, i.e. the reference horn antenna and the RLSA antenna under experimental investigation are implemented both in testing waveguide transmission line with free-space wireless section. The distance between antennas is of about 8 meters and antennas have studied in the Frenel zone partially. So real gain magnitude should be a little more than measured one for the far-region of antenna operation that employed commonly. The measurement assembly has been installed in ordinary laboratory room, not special anechoic chamber. Only the reference or the testing RLSA antenna has back-installed special sheets of electromagnetic adsorber to minimize interference scattering. There is also a mechanical beam steering units with possibility to set elevation and azimuthal position of antenna in the range $0 \pm 90^\circ$ to estimate radiation pattern. Notice the presented compact millimeter-wave antenna measurement assembly is used now for millimeter antenna laboratory teaching course on the Radioengineering Department of the Kyiv Polytechnic Institute, Ukraine.

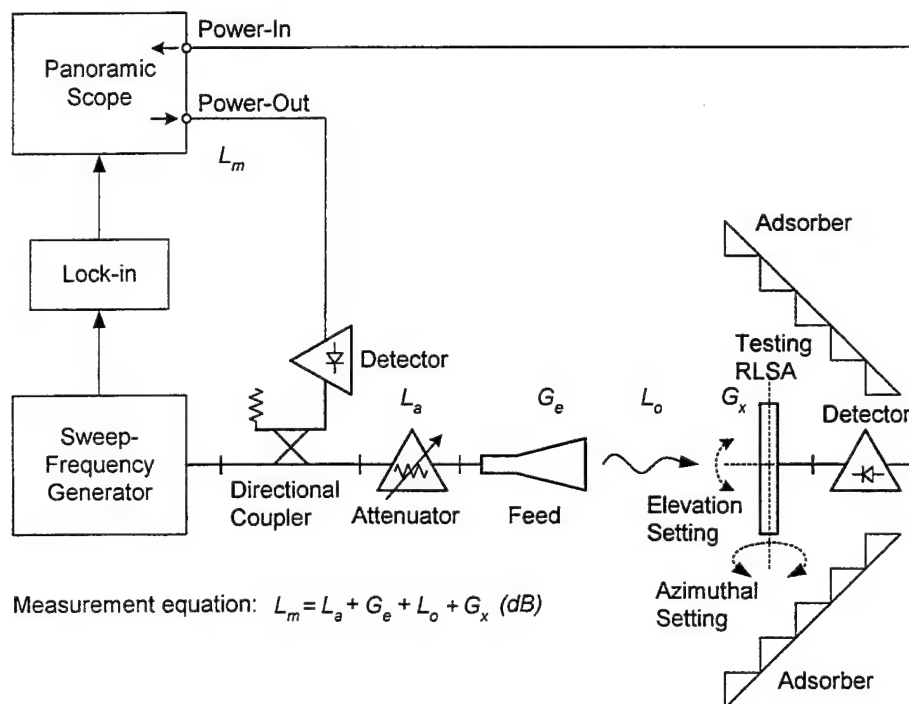


Fig. 13. Measurement assembly to examine millimeter-waves RLSA antenna.

8. Experimental Studies

A set of the 50-200 mm diameter linear-polarized RLSA antennas has been developed by the author due to the proposed theoretical model discussed above. These antennas has been designed by the CAD software, which implements the presented above synthesis procedure with antenna mask as final result. Later, the radiating aperture of the experimental prototype RLSA antennas have been fabricated by the printed-circuit technology and those antennas have been tested in the compact antenna measurement assembly (Fig. 13). Fig. 14 shows one of the 200 mm diameter RLSA antennas for the 32-34 GHz operation frequency band where etched slots are located on the back side of dielectric substrate with single-side metallic foil conductor, which forms antenna aperture. Note that slots are visible on the antenna front in transparent mode in Fig. 14. Additionally same antenna is shown from its front in Fig. 15 and rear side in Fig. 16 where antenna waveguide feeder is visible. The two side views of this antenna with holder are presented in Figures 17 and 18 enabled estimating its unique low-profile property.

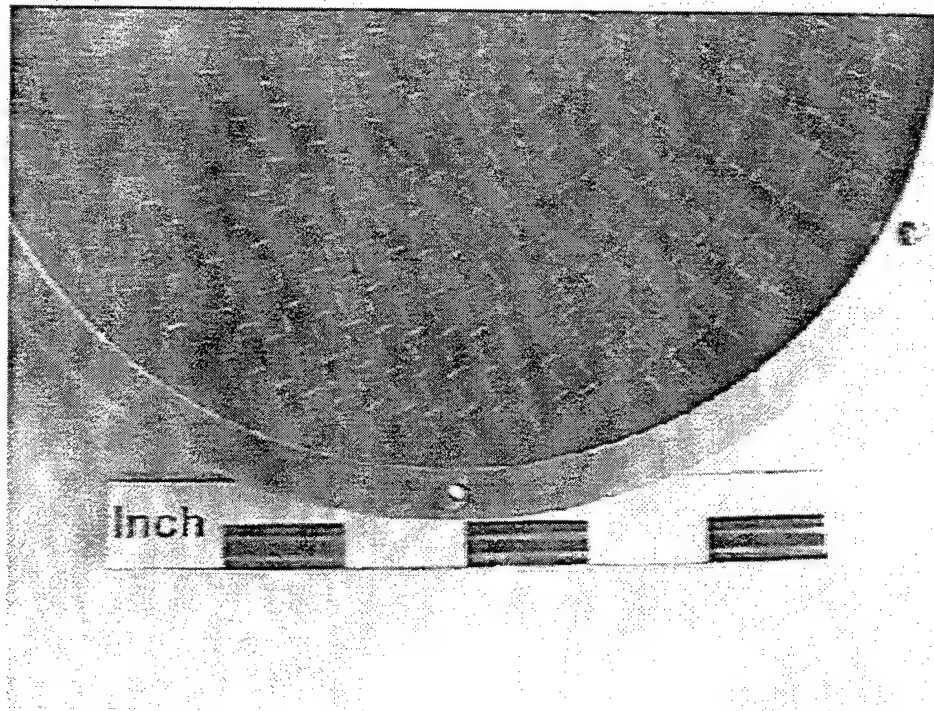


Fig. 14. Fragment of the front of the 200 mm diameter RLSA antenna where etched slots are located on the back side of dielectric substrate, which forms antenna aperture.

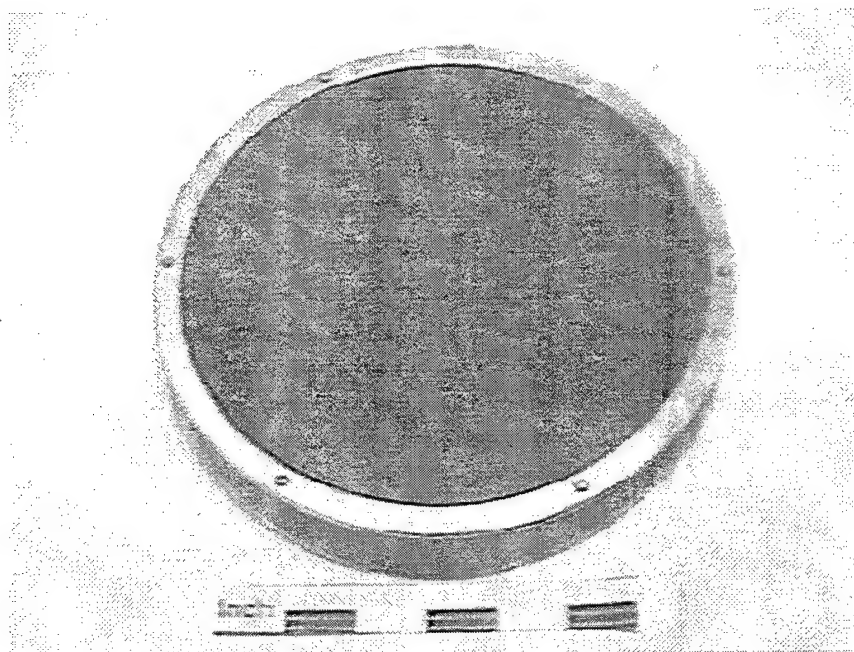


Fig. 15.

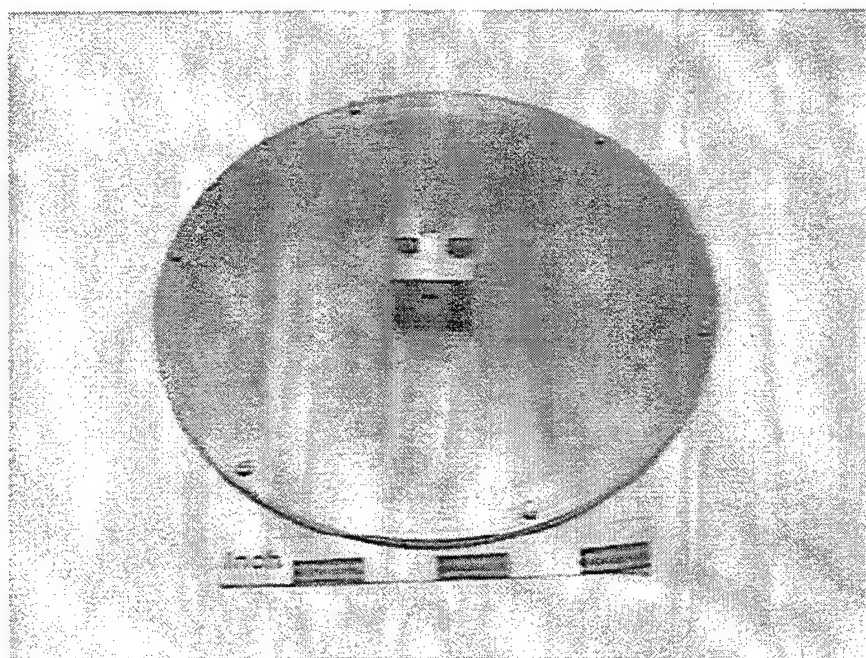


Fig. 16.

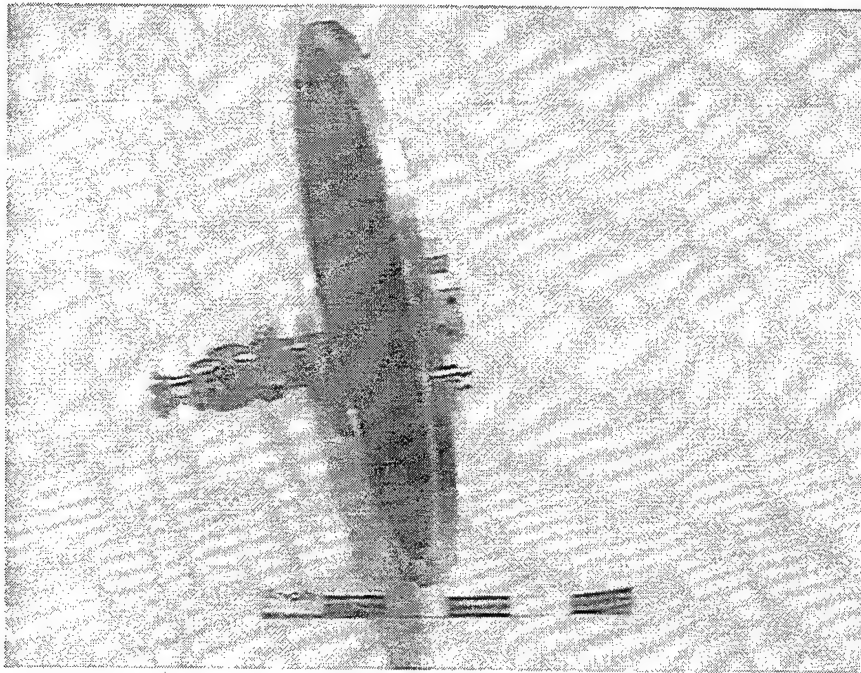


Fig. 17.

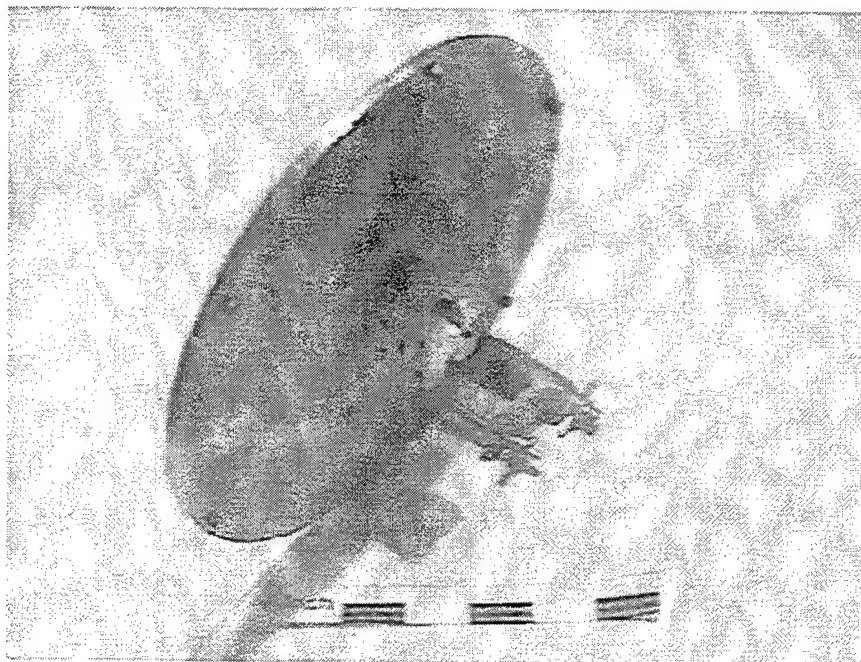


Fig. 18.

Antenna's gain factor and VSWR versus operation frequency, both the theoretical and the experimental ones, are shown in Fig. 19 for the millimeter-waves, 200 mm diameter, linear-polarized RLSA antenna where seen a moderate discrepancy between theory and experiment. The gain and VSWR are within 10% of the theoretic values. It is apparent thanks acceptable level of antenna performances achieved that developed theoretical models and their implementation in the synthesis procedure give available design accuracy under condition of exactly known dielectric constant of used materials. The last requires necessary measurement operations to get such data (Sect. 5).

Another kind of antenna features resulted from employment various aperture field distribution and design strategies is depicted in Fig. 20 for the low- and high-frequency dielectric materials used for aperture fabrication (Sect. 5). Data in Fig. 20 demonstrates that employment of a low-frequency material with more dielectric loss has some positive feature to improve return-loss. There is some interest generalization concerning decreasing of antenna return-loss that can be achieved by application of losses material for creation of the antenna upper plate. As it found [3] that using of low conductive metal, i.e. aluminum instead of copper, gives some improvement of linear-polarized RLSA return-loss due to additional attenuation produced by non-perfect conductor. Note that in both cases total decreasing of antenna efficiency due to attenuation effect in the upper plate material is lower than one forced by return-loss factor. And resulted antenna efficiency and its gain factor is better (+ 3-5 dB) in contrast to situation when more perfect material used and return-loss effect is expressed strongly.

From Fig. 19 and Fig. 20, it is found that the frequency bands where antenna demonstrates high gain and low VSWR magnitudes are tightly coupled thanks to the antenna feeding used with circuit for return-loss improvement (Sect. 6). This is peculiarity of the presented RLSA antenna in contrast to known variants with simple feeding unit via coaxial-to-radial junction [2,3].

The key moment of antenna design is to ensure necessary amplitude distribution over antenna aperture for given its total performances. In order to get high magnitude of antenna efficiency, as well as low level of antenna side-lobes, other types of aperture field distribution than uniform one are required. This design problem has optimal solution taking into consideration of all discussed above aspects. Fig. 21 demonstrates measured by special millimeter-waves probe an amplitude distribution of aperture field where computed magnitudes of aperture efficiency (AE) used as curve's parameter. It has been observed that optimal features of antenna is reached with non-uniform distribution.

Typical experimental pattern of the 200 mm diameter RLSA antenna in the electric plane with side lobe-level of about -22 dB is shown in Fig. 22. For this pattern about 2.5° beam width at -3dB pattern level has been obtained. The cross-polarization component measured was approximately -18dB for this antenna.

Fig. 23 represents the results of experimental studies to measure gain factor of the RLSA antennas with various diameters ranged from 40 to 195 mm as well as theoretical curve for gain of in-phase radiating round aperture with 100% and 30% efficiency factors. As seen in Fig. 23, efficiency of the RLSA antenna with diameter that is less or equal to 150 mm is not preferable. So the considered 200 mm diameter RLSA is optimal. At the same time, for some applications small-sized RLSA can be useful due-to plane aperture, low-profile features and opportunities of its conformal implementation. These features are very competitive in contrast to horn antennas of same diameter.

9. Discussions and Conclusions

A millimeter-waves linear-polarized RLSA antenna has been studied theoretically, numerically and experimentally in this paper. Total gain factor achieved is about 32 dB that corresponds of 60% aperture efficiency in the operation frequency band of about 31-33 GHz. The effect of return-loss that is principal for such antennas is estimated here by VSWR value, which is about 1.11-1.15 in the 1-1.5 GHz frequency bandwidth. Results that illustrate the accuracy of developed synthesis procedure were being presented.

For comparison, the measured pattern performances (gain, beam-width) and efficiency of RLSA are better, than ones for a horn antenna with/without dielectric lens, and slightly worse, than for parabolic reflector antenna. For example, the presented 200 mm diameter RLSA demonstrates 60 % efficiency, 30-32 dB gain in the 31-32 GHz being planar structure with low-profile features and high mass production opportunities due to printed circuit technology employed.

Some oscillating features of RLSA performances in Fig. 19 and Fig. 20 result from non-uniform slots features above aperture due to used design strategy that based on homogenous slot distribution over aperture. It seems reasonable to make some generalization of the design strategy that should be based on consideration of advanced theory of antenna synthesis, which is similar to classical theory of filter synthesis [8] in some features when preferable approximation for antenna gain and WSVR versus frequency band can be employed.

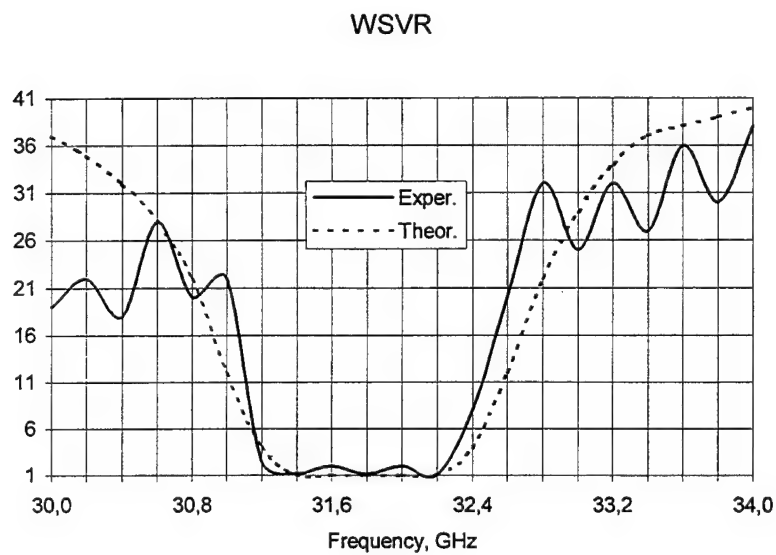
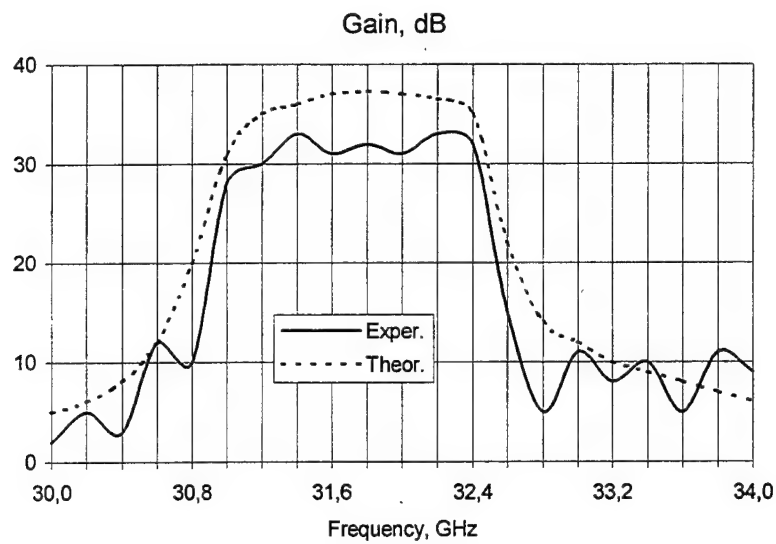


Fig. 19. Theoretical and experimental gain and VSWR of the 200 mm diameter RLSA antenna versus operation millimeter-waves frequency band that demonstrates tight coupling between theory and experiment.

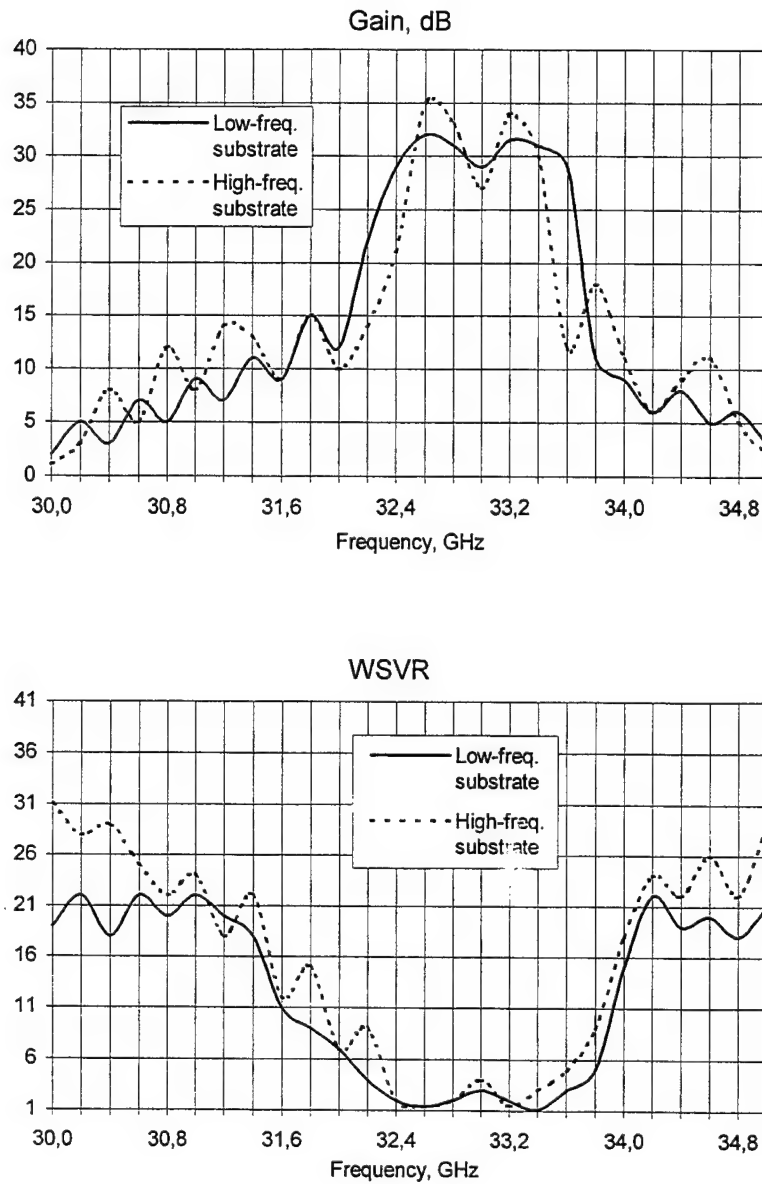


Fig. 20. Experimental values of gain and VSWR of the 200 mm diameter RLSA antenna versus operation millimeter-waves frequency band with the low- and high-frequency dielectric materials.

Aperture amplitude distribution

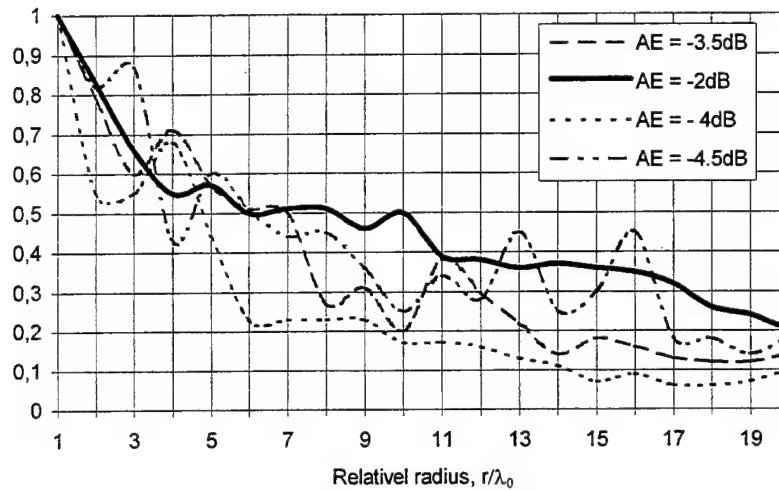


Fig. 21. Experimental amplitude distribution of aperture field of the 200 mm diameter RLSA antenna for some set of aperture efficiency (AE) implemented for definite operation frequency of antenna with features in Fig. 19. Solid-line curve (AE = -2dB) corresponds to the 31.2-32.4 GHz operation band.

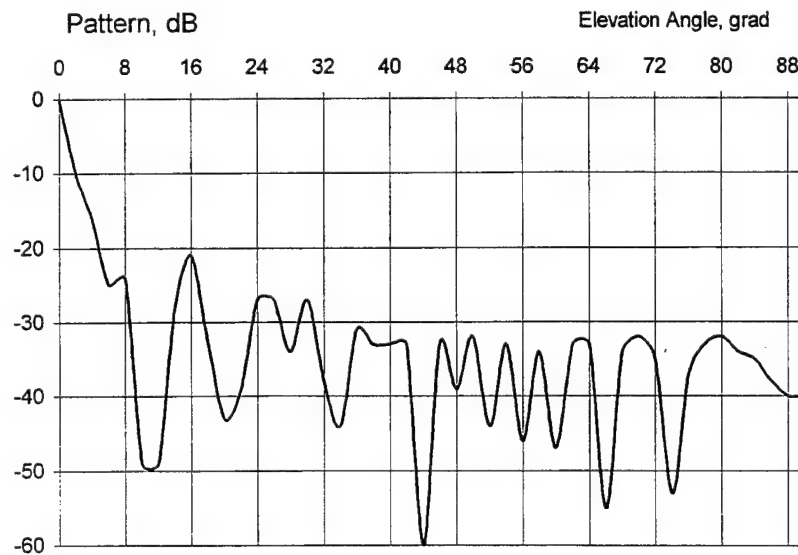


Fig. 22. Measured pattern of the 200 mm diameter RLSA antenna in the electric plane with side lobe-level of about -22 dB.

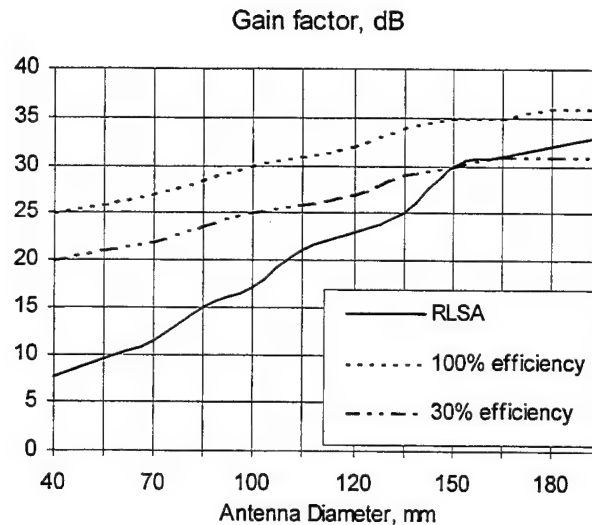


Fig. 23. Experimental gain factor (solid line) of the RLSA antennas in the 32 GHz frequency band with various diameters of aperture ranged from 40 to 195 mm. There are as well here reference curves for 100% and 30% efficiency for radiating round aperture of same diameter.

Let note that presented above results have been obtained by using approximated theoretical models with some heuristic reasons mainly due to inherent complexity of presented problems from electrodynamics point of view when analyzed radiating systems is formed by tremendous amount of radiating slots with their excitation by traveling wave inside radial-line disturbed by slots in turn. So synergy effect is dominant here that demands special care, as well as developing of more exact electromagnetics model to take into consideration effects of slot's mutual connection via internal waveguide high-mode electromagnetic fields and external radiated ones.

The influence of tolerances of the slot width, slot length, geometry and properties of dielectric substrate (coating) on radiating characteristics should be investigated by statistical simulation technique like the Monte-Carlo method.

In general, one can point out that RLSA antenna have common features with antennas formed by frequency selective surfaces (apertures) and RLSA antenna is very similar to those antennas by its exterior, as well as radiation features. So some generalized aspects of those problem can be taken into considerations also including conformal antenna implementation etc.

Asknolodgement

The author would like to think Dr. M. Ando, the Tohoky Institute of Technology University, Japan for his inestimable help due to copies of his papers concerning the X-band RLSA antenna, which were being given to the author. This paper was stimulated by discussions of its subject via Internet with Dr. M. Bialkowsky, University of Queensland, Australia.

References

- [1] K.C. Kelly. "Recent Annular Slot Array Experiments", *IRE National Convection Records*, vol. 5, pp. 144-151, March 1957.
- [2] M. Ando, T.Numuta, J. Takada and N.Goto. "A Linearly Polarized Radial Line Slot Antenna", *IEEE Trans. Ant. Propagat.*, vol. 36, pp. 1675-1680, December 1988.
- [3] P.W. Davis, M.E. Bialkowski. "Linearly Polarized Radial-Line Slot-Array Antennas with Improved Return-Loss Performance", *IEEE Ant. Propagat. Magazine*, vol. 41, pp.52-61, February 1999.
- [4] M. Ando, J. Hirokawa, T. Yamamoto, A. Akiyama, Y. Kimura, N. Goto. "Novel Single-Layer Waveguides for Mass-Producible Millimeter Wave Arrays", *Proc. of Int. Symp. Electromagnetic Theory*, pp. 229-231, 1998.
- [5] J. Takada, M. Ando, N. Goto. "An Equivalent Circuit of a Slot in Radial Line", *IEICE Trans.*, vol. E 74, pp. 2922-2928, September 1991.
- [6] J. Takada, M. Ando, N. Goto. "Suppression of Reflection from Slots in a Linearly-Polarized Radial Line Slot Antenna", *Proc. of IEEE Ant. Propagat. Int. Symp.*, pp. 1342-1345, 1991.
- [7] R.A. Collin, *Foundations of Microwave Engineering*, McGraw-Hill, New York, 1964.
- [8] J.L. Altman, *Microwave Circuit*, Van Nostrand, New York, 1964.
- [9] S. Ramo, J. Whinnery, J. van Duzer, *Fields and Waves in Communications Electronics*, J.Wiley and Sons, New York, 1984.

An Implementation of a 0.5 to 2.0 GHz Circular 360 Degree Direction Finding Antenna

T. R. Holzheimer
Raytheon Systems Company
Aircraft Integration Systems
P. O. Box 6056
Greenville, Texas 75403

Abstract:

A Circular 360 degree direction finding (DF) antenna was previously presented at the 1995 Antenna Applications Symposium illustrating the capabilities of a novel antenna implementation. Data was presented illustrating the accuracy of the DF antenna over a full 360 degree field of view (FOV) and over the operational band of 2 to 18 GHz. This paper presents the results for the 0.5 to 2 GHz version of this antenna. A comparison in mechanical and electrical characteristics are presented.

The new 360 DF antenna is larger, which reflects in the lower frequency of operation as compared to the previously reported version. However, the angle of arrival (AOA) accuracy is similar to the 2 to 18 GHz version at approximately 0.75 degrees RMS. The biggest problem encountered was the size required for operation at the 0.5 GHz frequency. A comparison is discussed against a standard linear interferometer operating in the same frequency band. Performance issues are discussed as related to installation on mechanical structures.

The results shown will illustrate the frequency scaling of this design. Certain problems will be discussed, that affected the DF antenna and prevented the performance at the 0.5 degree RMS AOA accuracy levels.

1.0 Introduction:

Several high accuracy direction finding (DF) antennas have been described in numerous papers and textbooks over the

years.[1] A high accuracy (0.5 degrees RMS), 2 to 18 GHz, 360 degree azimuthal direction finding antenna was described and presented previously at the Antenna Applications Symposium in 1995. In general, most DF arrays use low gain elements such as spirals and dipoles. There are interferometers made using medium gain horns for the elements. These type of elements are implemented in linear interferometers and full 360 degree azimuthal field of view DF systems. A comparison between linear interferometers and the high accuracy DF antenna was presented in the previously reported results.

In providing a full 360 degree azimuthal field of view the typical DF array consists of a circular array where the earliest types were designed using low gain omnidirectional elements. Subsequent investigators then looked at using directional antennas in circular arrays and assessed them for use in DF implementations. Many different types of elements and beamformers have been used such as flared notch radiators and N-element Butler matrix. Mixed polarizations have also been investigated with varying degrees of success requiring today's easily acquired high speed computers. Derivations and explanations of the synthesis used to produce AOA from a circular array has been previously reported and will not be repeated here.

A lower frequency version of the DF antenna is described in this paper. The frequency range of this 360 degree circular DF antenna is 0.5 to 2 GHz. The desired AOA accuracy was 0.5 degrees RMS which was identical to the original 2 to 18 GHz version of the circular DF antenna.

The circular DF arrays investigated in this paper are of the simultaneous modal phase type. Figure 1 illustrates the different phase modes which follow periodic functions of 360 degrees, i.e., $N \times 360$ degrees, where N is the modal phase

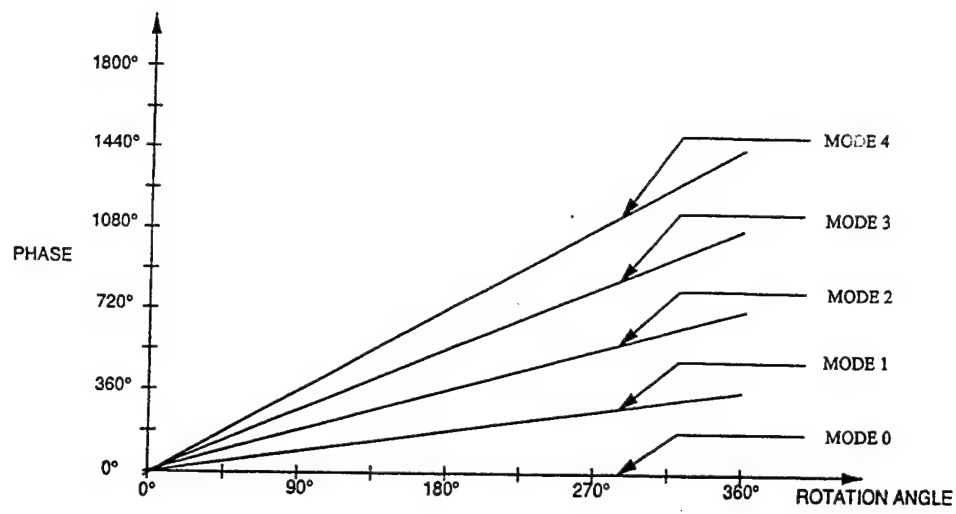


Figure 1. Modal Phase versus Rotation Angle

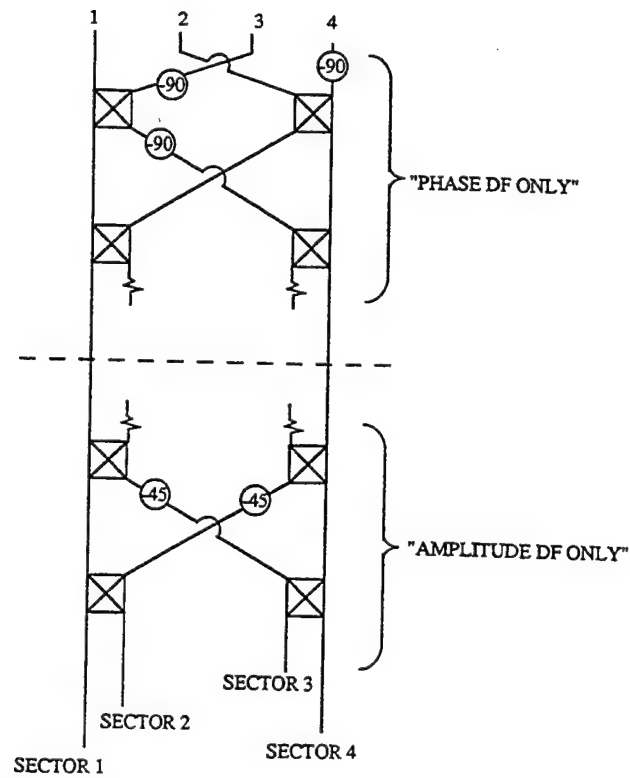


Figure 2. Phase Only versus Amplitude Only DF

order. They are phase only DF arrays but not amplitude only DF arrays. The phase modes are set up using a modeformer which can be a Butler matrix and/or a circular Rotman lens where the modal phases are all existing simultaneously. The Butler matrix is quasi-frequency independent while the Rotman lens is linearly dependent on frequency. An additional network is required beyond the basic phase modeforming network in order to provide amplitude DF which is illustrated in Figure 2. The RMS AOA is derived by differencing the two simultaneous modal phases which results in an azimuthal angle.

Measurements were collected and analyzed using phase information only and then both phase and amplitude information combined. The readily available amplitude information raised the issue of whether using this information, in addition to the phase information, could increase the AOA accuracy.

2.0 Design of the Circular DF Array

The design of this circular DF antenna is covered under United States patent pending. [2] This design uses commercial off the shelf hardware that basically consists of elements and modeformers. The interelement spacing is kept less than a half wavelength in order to minimize higher order mode phase distortion, provide a compact and light weight design, and provide a full 360 degree azimuthal field of view. This concept was arrived at in two steps and is reported in the previous paper. [1] The basic electrical concept was verified with a 4 element circular array and then with powers of two, and for modeformer simplicity, an 8 element array was designed and fabricated in order to meet the less than 1 degree RMS AOA accuracy goal. Pertinent specifications are listed in Table I.

Table I. Goal Specifications.

Frequency Range: 0.5 to 2 GHz minimum
Element Gain: 7.5 dBli minimum
Polarization: Dual Linear as minimum
Field of View: Azimuth - 360 degrees
 Elevation - +/- 30 degrees minimum
RMS AOA Accuracy: 1 degree maximum
Ambiguity Rate: less than 5%
Unambiguous Data Rate: greater than 90%
Signal to Noise Ratio: 8 dB minimum

The 0.5 to 2 GHz circular DF antenna was implemented with 8 elements in order to meet the power of two beam forming requirements. The modeformer used is an 8 X 8 Butler matrix which provided phase modes 0, 1, +/- 2, and +/- 3. The beamformer limited the frequency range to 0.5 to 2 GHz. Figure 3 illustrates the 8 element DF array. The actual array that was built and tested is shown in Figure 4. Data was acquired over the 0.5 to 2 GHz frequency range.

3.0 Performance of the Circular DF Array

Measured data were collected on every usable phase mode port from 0.5 to 1 GHz in approximately 0.6 MHz steps and 1 to 2 GHz in approximately 1.2 MHz steps both over 360 degrees of azimuthal field of view. Four phase pairs or differential phases were then constructed. A phase calibration table was also constructed. A residual 6.1 degree (one sigma) phase pair tracking error was used as typical for a post calibrated, wide-bandwidth, phase-discriminating receiver. Residual 11.1 degree (one sigma) phase pair tracking error was also used for comparison and verification of the analysis. The 11.1 degree data is not included in this paper due to page limitations. An Raytheon Systems Company proprietary algorithm was then invoked using a metric in order to determine the AOA accuracy.

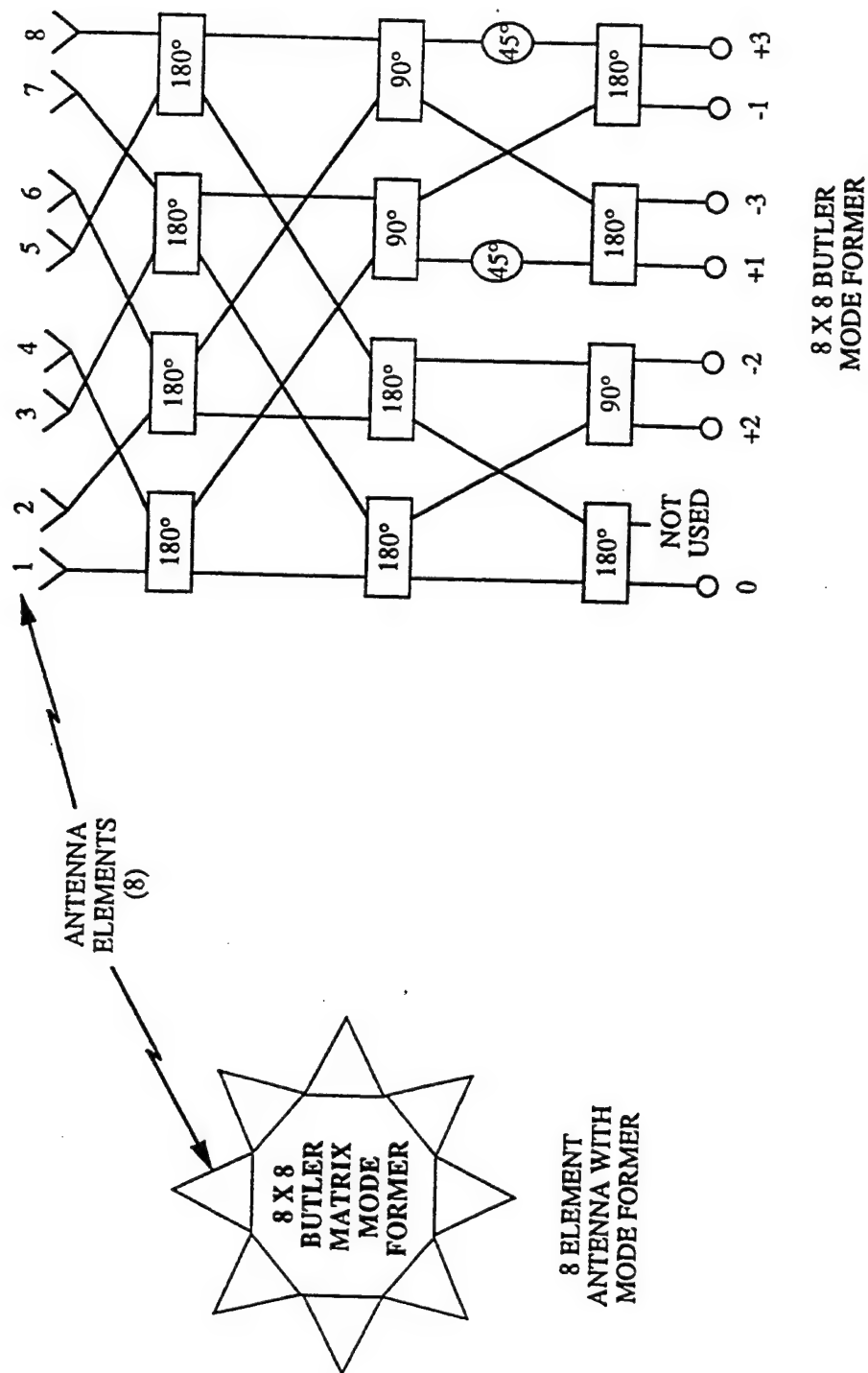


Figure 3. 360 Degree Eight Element DF Antenna

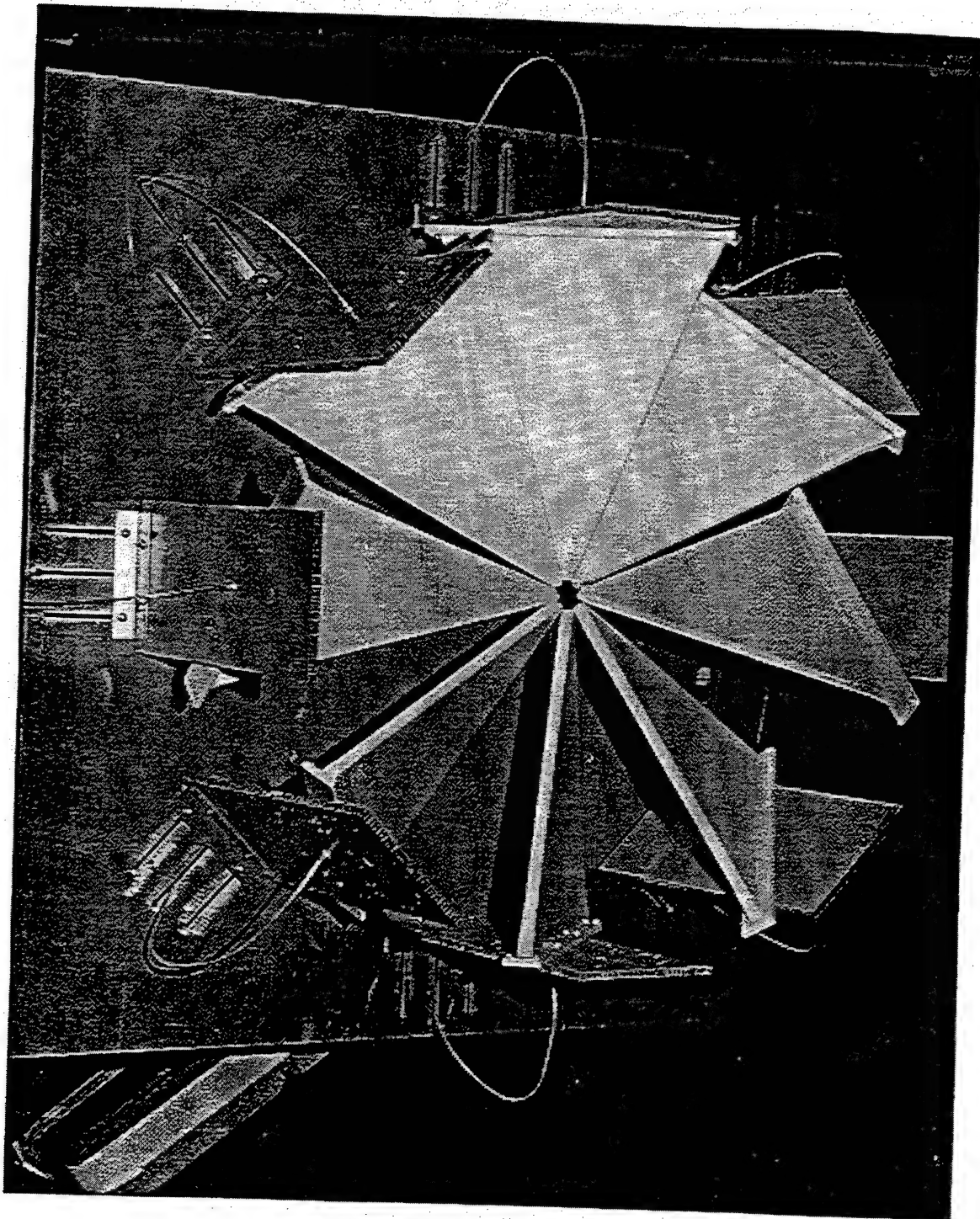


Figure 4. View of Low Band 360 Degree Eight Element DF Antenna

It was recognized, as has been reported, that a perfect array with no coupling could provide a full unambiguous 360 degree azimuthal field of view. However, it is also recognized that in a realistic situation and installation that ambiguity rate and RMS AOA accuracy are driven by element spacing and signal to noise ratio as in a linear interferometer. The close spacing of the elements which increases the coupling between elements and the non-ideal cardioid radiation pattern of the elements cause the additional error sources and differences from the perfect array. Tradeoffs are made that affect all of the above. Based on the preceeding, criteria were determined for specifying a DF system whether it be a circular DF Array or a linear interferometer. They are listed in Table II.

Table II. Required DF System Specifications.

1. RMS AOA over Frequency.
2. Unambiguous Data Rate over Frequency.
3. Untagged Ambiguity Rate over Frequency.
4. RMS AOA Accuracy over Signal to Noise Ratio.
5. Unambiguous Data Rate over Signal to Noise Ratio.
6. Untagged Ambiguous Data Rate over Signal to Noise Ratio.

Good data is labeled as Unambiguous Data Rate, while bad data are Untagged Ambiguity Rate. This says that based on use of proprietary algorithms and calibration, data can be made more accurate and false AOA's can be minimized and identified. This has been shown in the previous paper for the circular DF array operating over the 2 to 18 GHz frequency range. [1]

Measurements were made with the circular array elements in the linear and slant linear polarization configurations and collected with the transmitter oriented in the linear, slant linear and cross-polarization cases. This type of DF antenna

typically uses only the phase information in determining AOA due to the fact that the amplitude has large variations over frequency and angle. Figures 5 through 7 show the phase and amplitude variation versus AOA for four different modes of the circular array beamformer at 2 GHz. The figure 5 amplitude data is scaled by a factor of 100 to fit on the plots and shows large variations. Figure 5 shows that phase follows the different phase slopes expected for each mode with the ripple showing the addition of phase errors inherent in the system. Figure 6 illustrates contour plots of estimated AOA versus true AOA. In this case the correct AOA is along the diagonal and anything off diagonal is an ambiguity or false AOA. Figure 7 adds an additional third axis for ambiguity rate illustrating the desired ambiguity rate of less than 5%.

The data from figures 8 through 11 uses phase information only and disregards any information that can be derived using the amplitude information. The data from figures 8 and 9 shows the RMS AOA accuracy and ambiguity rate over the 1 to 2 GHz frequency range for a co-polarized signal and a slant 45 degree polarized signal. The co-polarized signal AOA accuracy is maximum at 0.9 degrees and 1.8 degrees for slant 45 degrees. The average AOA accuracy for the co-polarized signal is approximately 0.7 degrees, and for the slant 45 degree signal is approximately 1.4 degrees. The ambiguity rate is approximately 22% (ambiguity rate times 100% on all plots) for the co-polarized signal and approximately 48% for the slant 45 degree signal. The average ambiguity rate for the co-polarized signal is approximately 5 % and for the slant 45 degree signal is approximately 10%. The data from figures 10 and 11 shows the RMS AOA accuracy and ambiguity rate over the 0.5 to 1 GHz frequency range for the co-polarized signal and the slant 45 degree polarized signal. The co-polarized signal AOA accuracy is maximum at approximately 1.52 degrees and 1.47

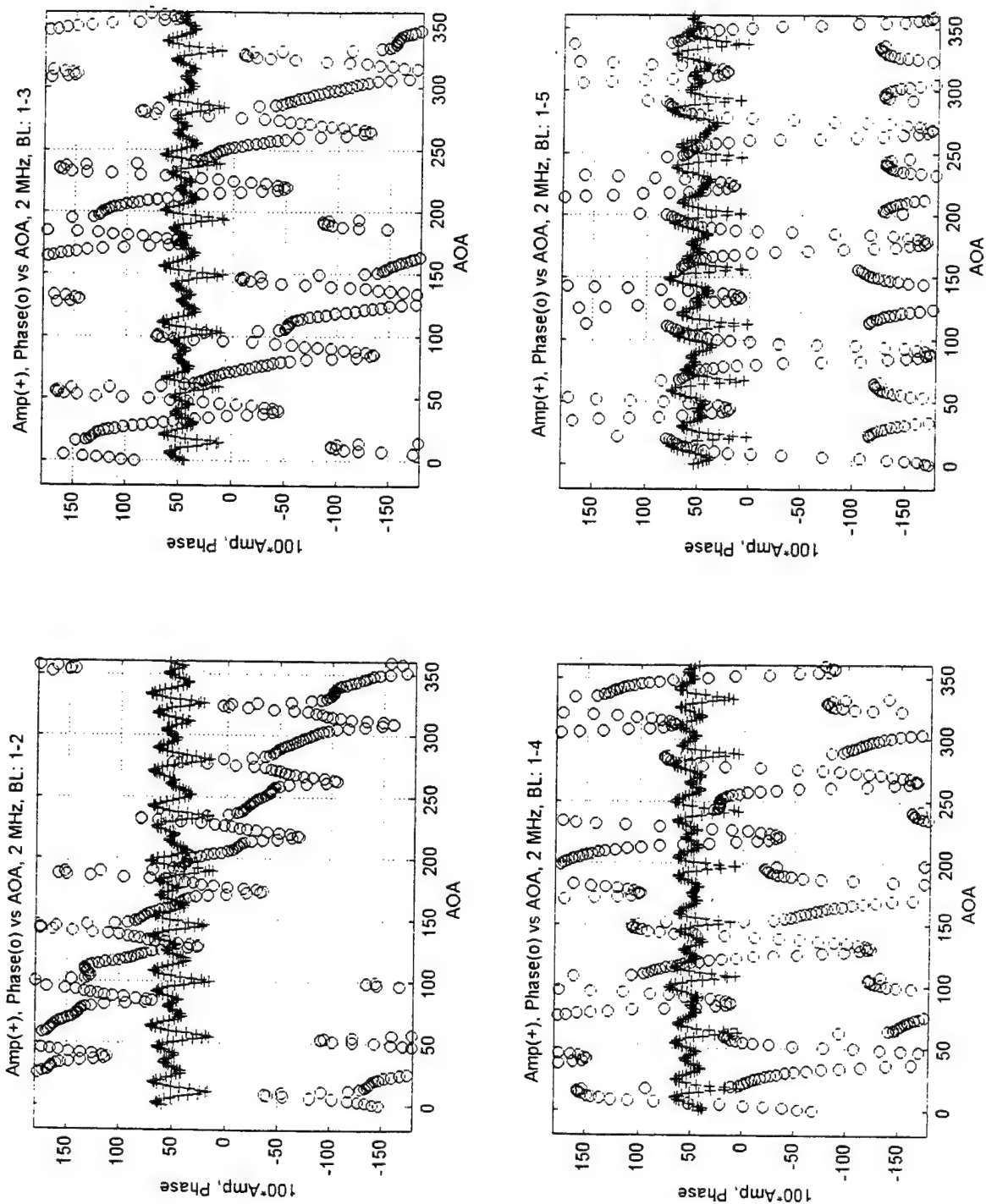


Figure 5. Amplitude and Phase variation versus AOA for four different DF Antenna Modal Outputs at 2 GHz

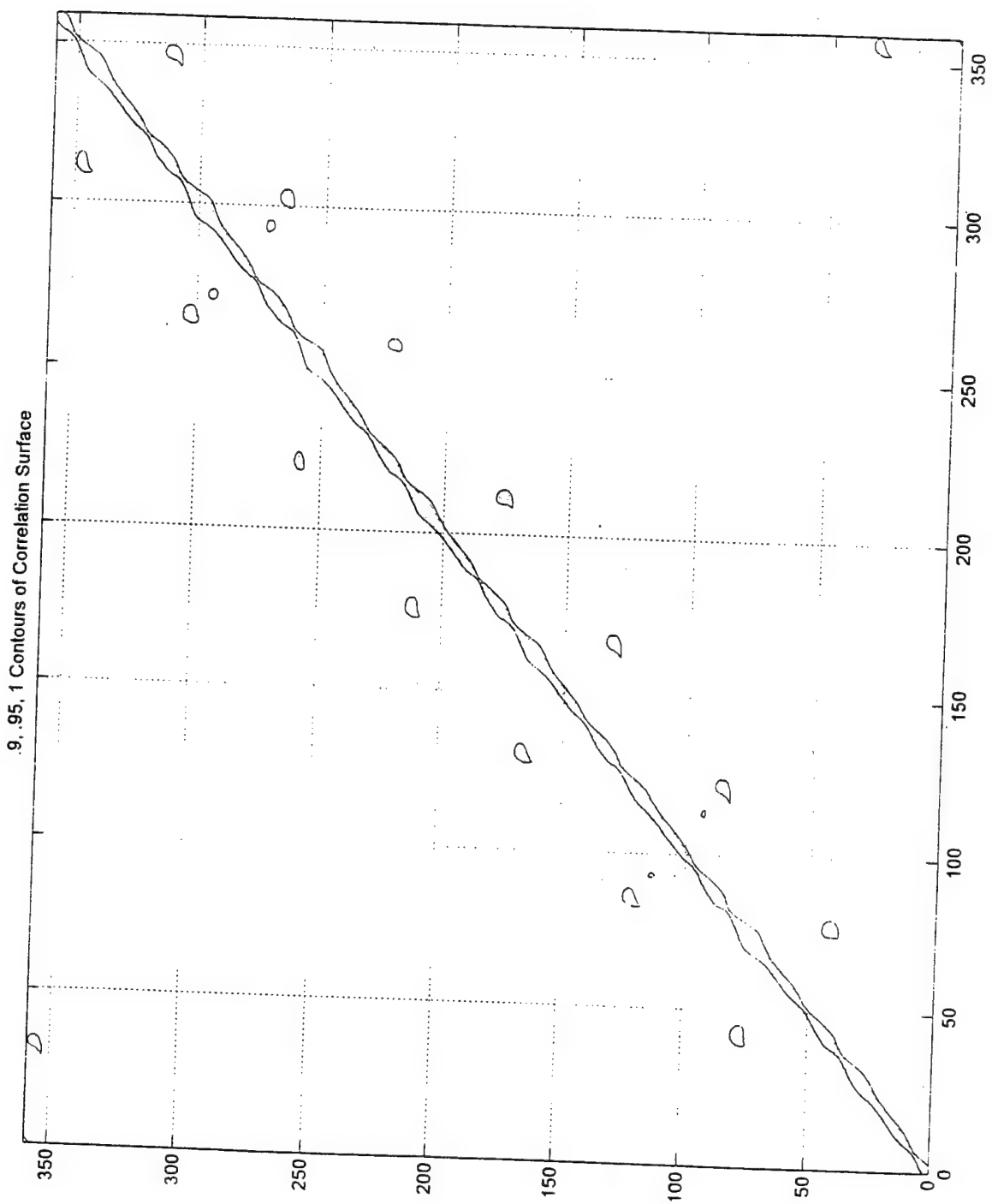


Figure 6. Contour Plot of Estimated AOA versus True AOA at 2 GHz

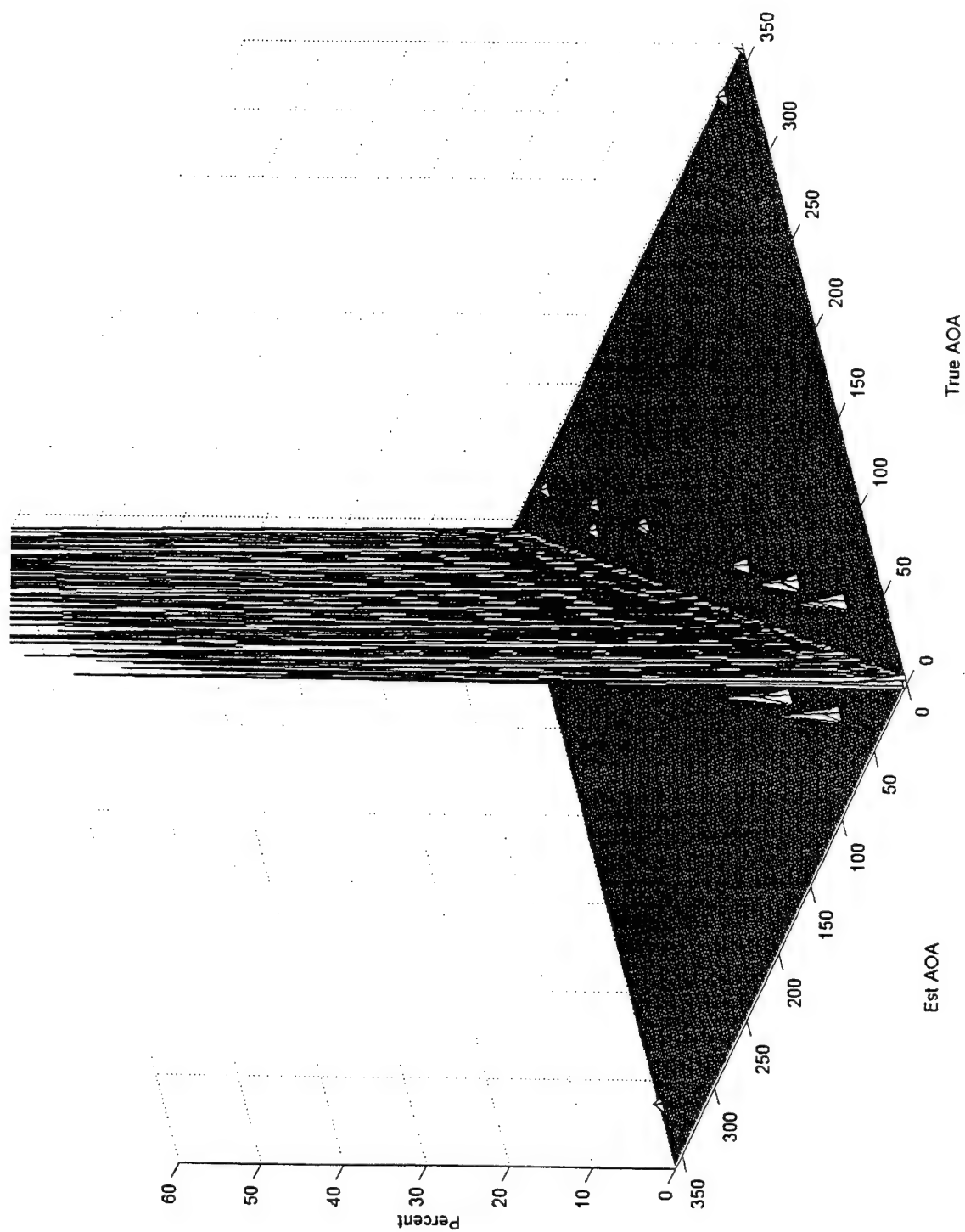


Figure 7. Plot of Ambiguity Rate versus Estimated and True AOA at 2 GHz

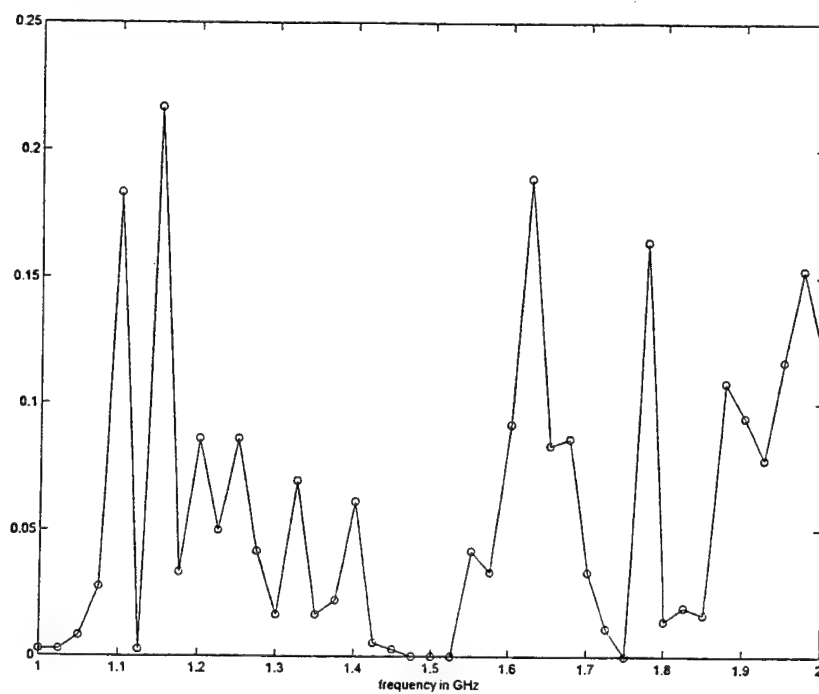
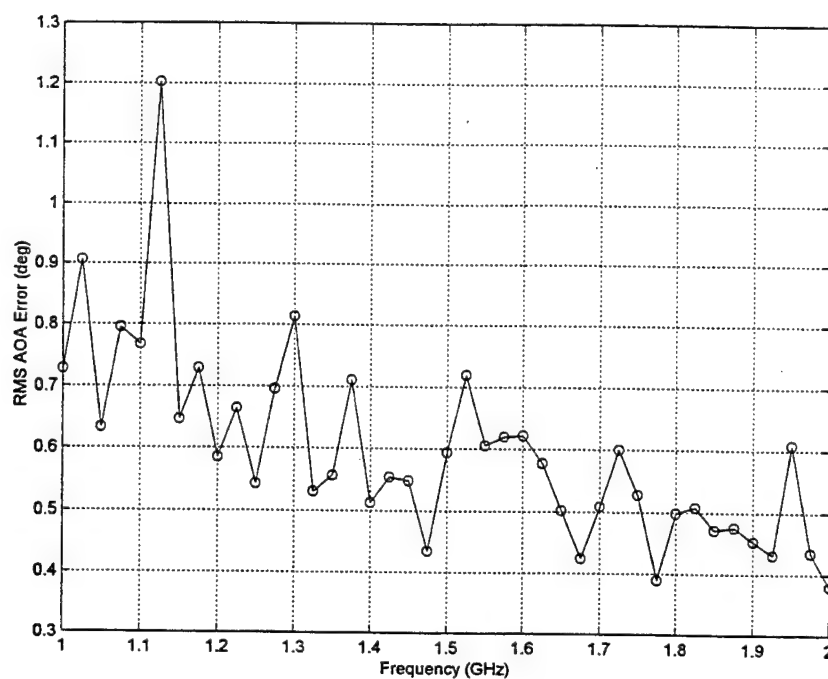


Figure 8. Co-polarized, RMS AOA and Mean Ambiguity Rate over 1 to 2 GHz, for DF antenna using Phase only

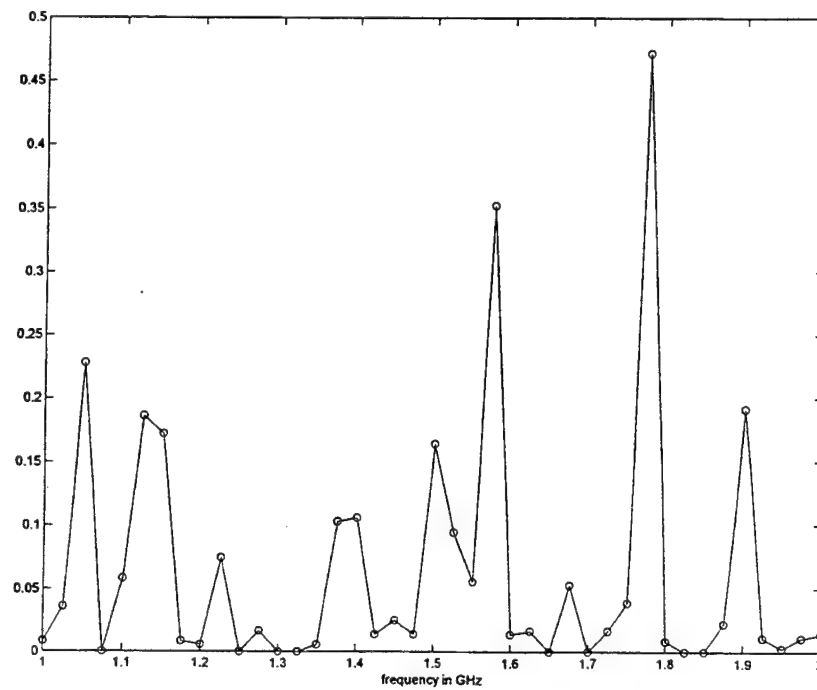
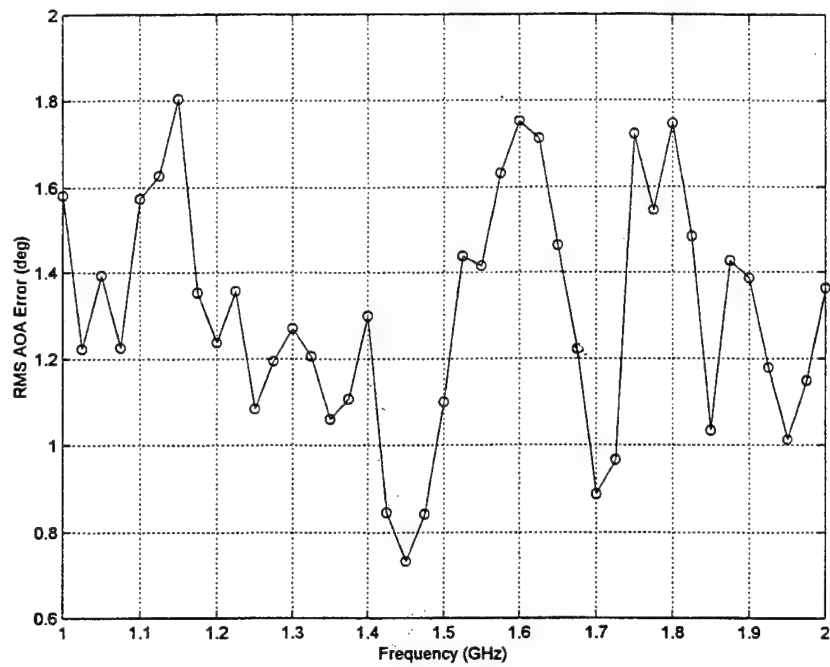


Figure 9. Slant 45 degree, RMS AOA and Mean Ambiguity Rate over 1 to 2 GHz, for DF antenna using Phase only

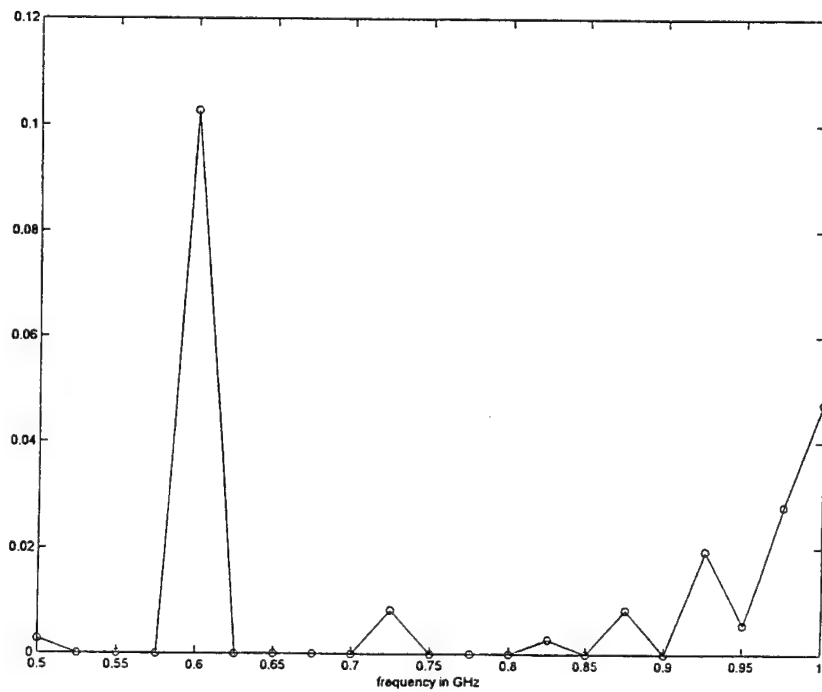
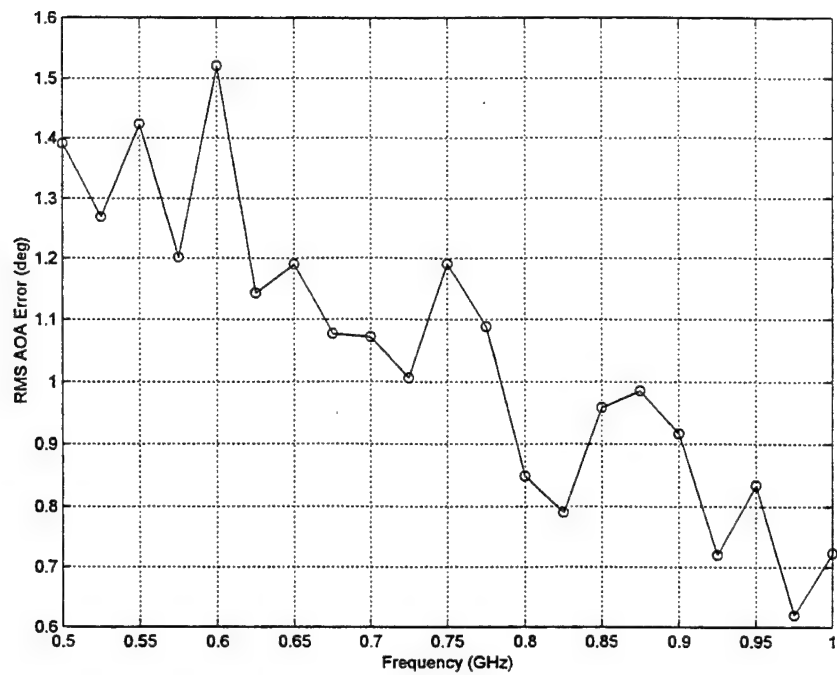


Figure 10. Co-polarized, RMS AOA and Mean Ambiguity Rate over 0.5 to 1 GHz, for DF antenna using Phase only

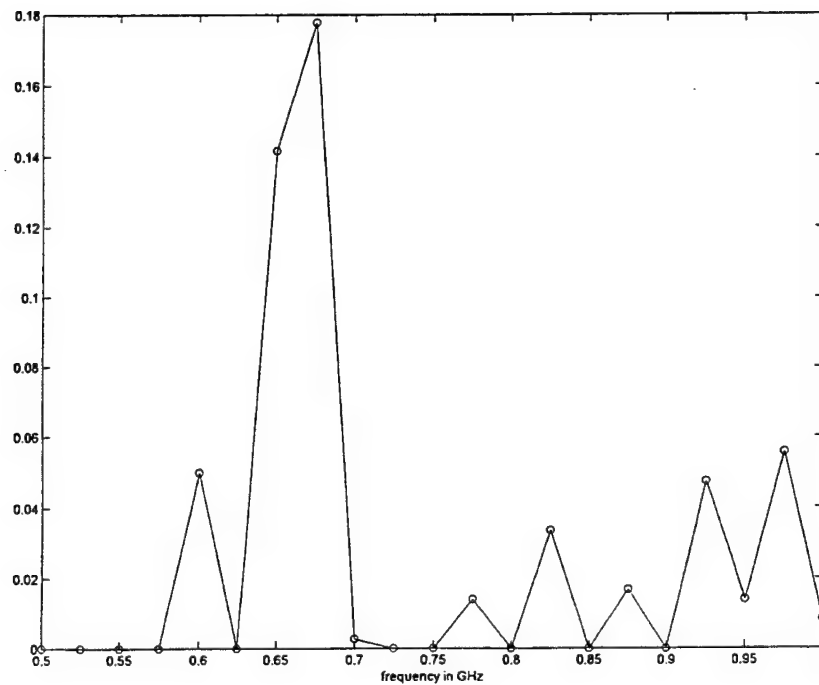
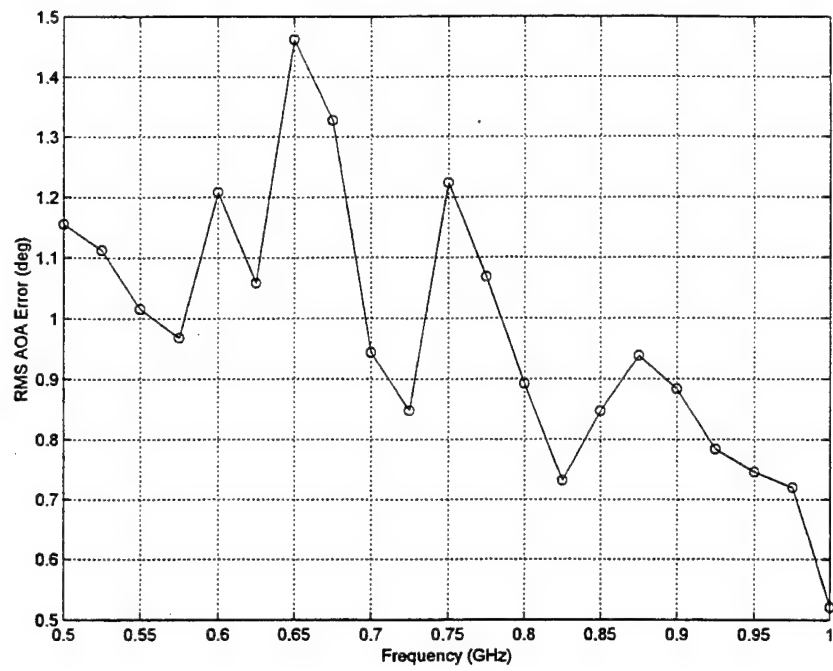


Figure 11. Slant 45 degree, RMS AOA and Mean Ambiguity Rate over 0.5 to 1 GHz, for DF antenna using Phase only

degrees for the slant 45 degrees signal. The average AOA accuracy for the co-polarized signal is approximately 1.1 degrees and for the slant 45 degree signal is approximately 0.9 degrees. The ambiguity rate is approximately 10% for the co-polarized signal and approximately 17.8% for the slant 45 degree signal. The average ambiguity rate for the co-polarized signal is approximately 1% and for the slant 45 degree signal is approximately 4%. This data does not meet the goal of 1.0 degree AOA accuracy using phase information only.

The data from figures 12 through 15 use both phase and amplitude information in order to increase the AOA accuracy. The data from figures 12 and 13 shows the RMS AOA accuracy and ambiguity rate over the 1 to 2 GHz frequency range for the co-polarized signal and the slant 45 degree polarized signal. The co-polarized signal AOA is maximum at 0.66 degrees and 0.71 degrees for slant 45 degrees. The average AOA accuracy for the co-polarized signal is 0.42 degrees, and for the slant 45 degree signal is 0.47 degrees. The ambiguity rate is approximately 6.8% (ambiguity rate times 100% on all plots) for co-polarized signal and approximately 4.3% for slant 45 degree signal. The data of figures 14 and 15 shows the RMS AOA accuracy and ambiguity rate over the 0.5 to 1 GHz frequency range for the co-polarized signal and the slant 45 degree polarized signal. The co-polarized signal AOA is maximum at approximately 1.2 degrees and 1.38 degrees for slant 45 degrees. The average AOA accuracy for the co-polarized signal is 0.88 degrees and for slant 45 degree signal is 0.94 degrees. The ambiguity rate is approximately zero or very small for the co-polarized signal, and approximately 2.7% for slant 45 degree signal. This data meets the goal of less than 1.0 degree AOA accuracy using phase and amplitude information.

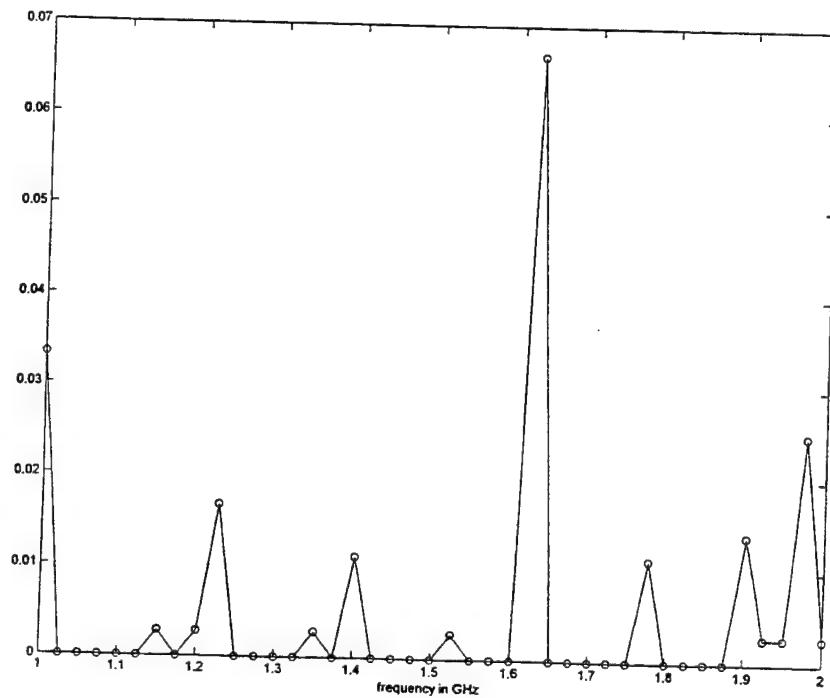
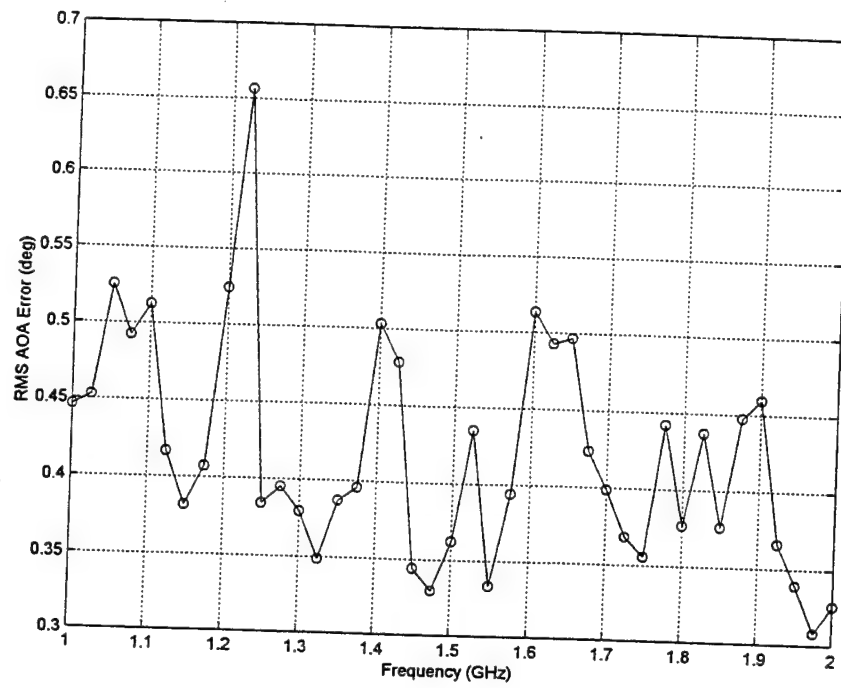


Figure 12. Co-polarized, RMS AOA and Mean Ambiguity Rate over 1 to 2 GHz, for DF antenna using Phase and Amplitude

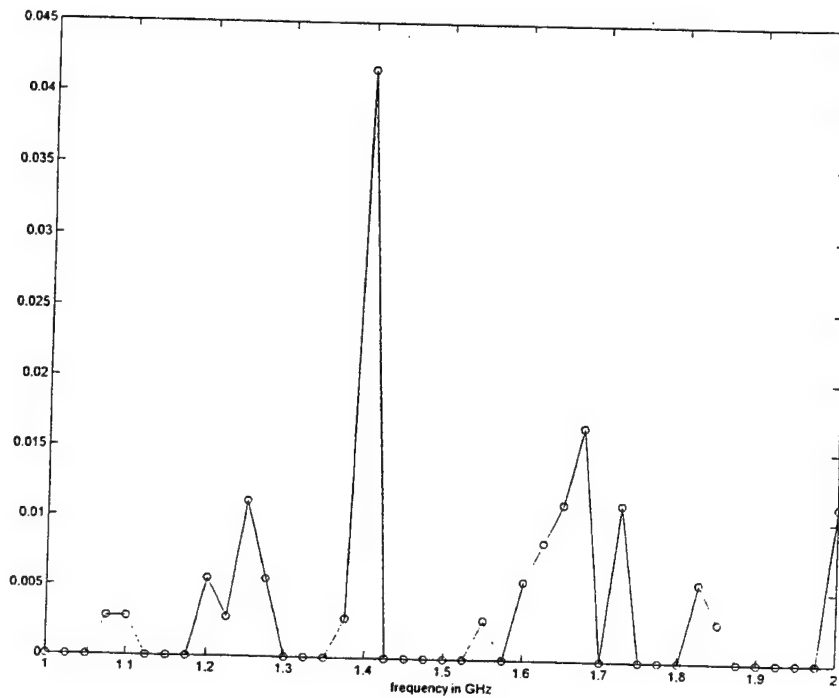
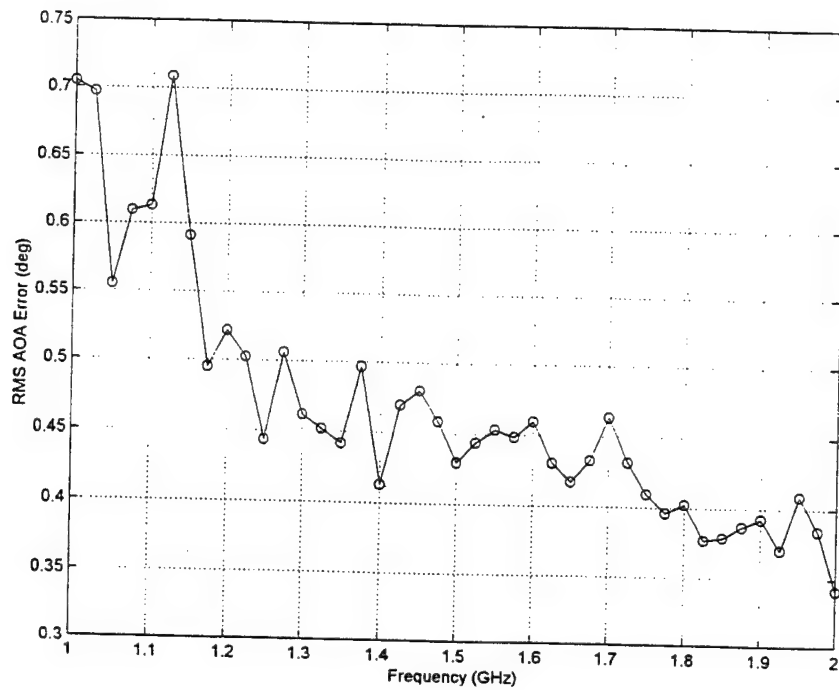


Figure 13. Slant 45 degree, RMS AOA and Mean Ambiguity Rate over 1 to 2 GHz, for DF antenna using Phase and Amplitude

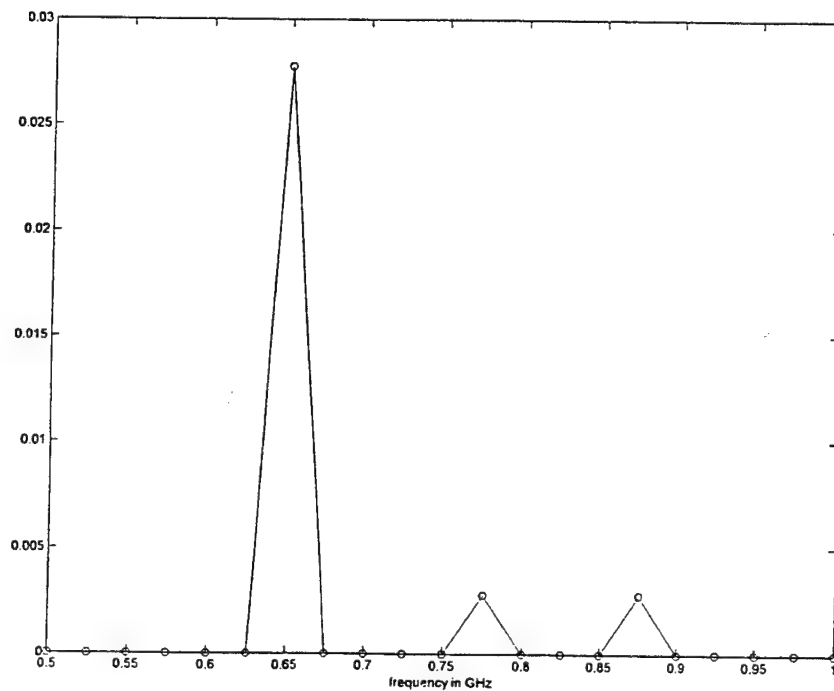
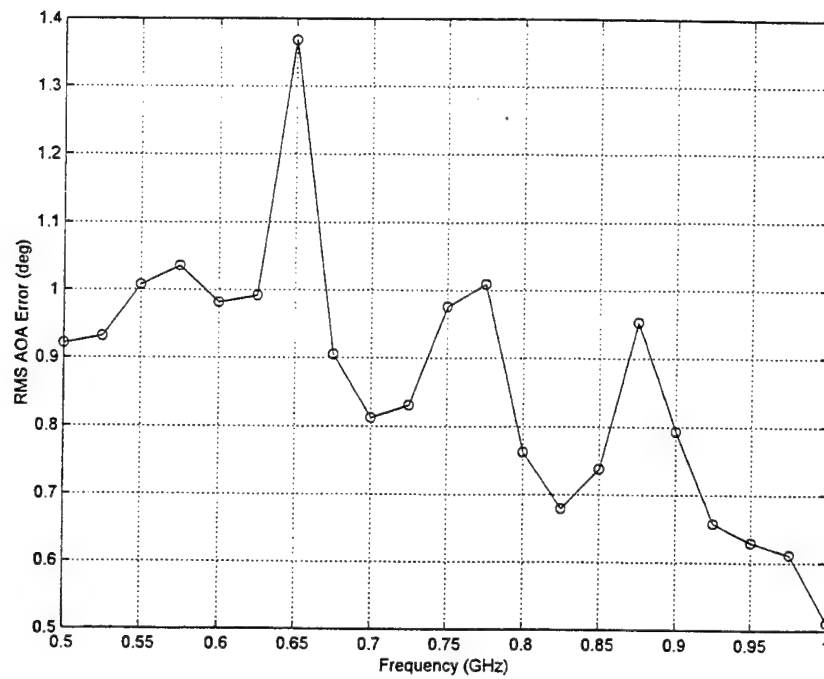


Figure 14. Co-polarized, RMS AOA and Mean Ambiguity Rate over 0.5 to 1 GHz, for DF antenna using Phase and Amplitude

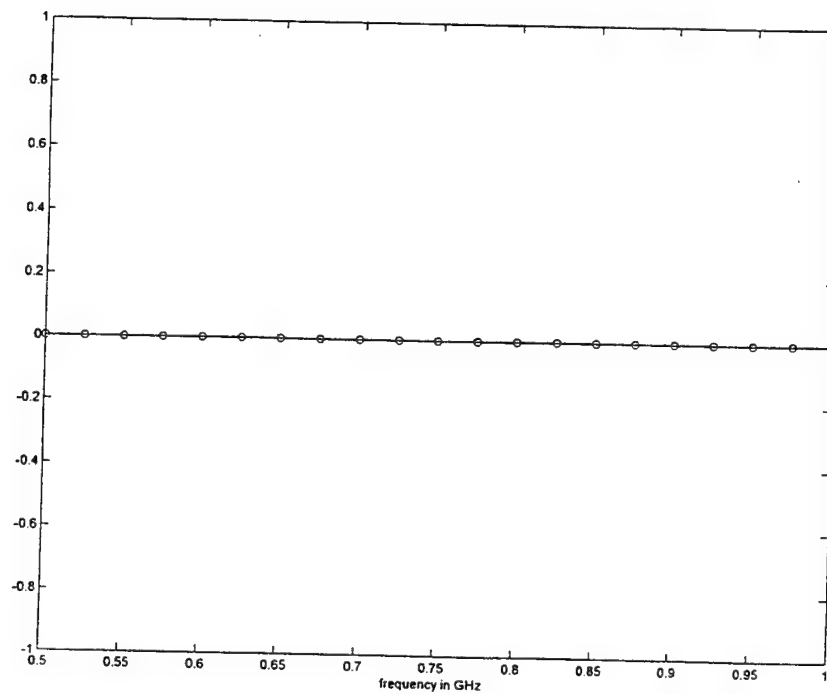
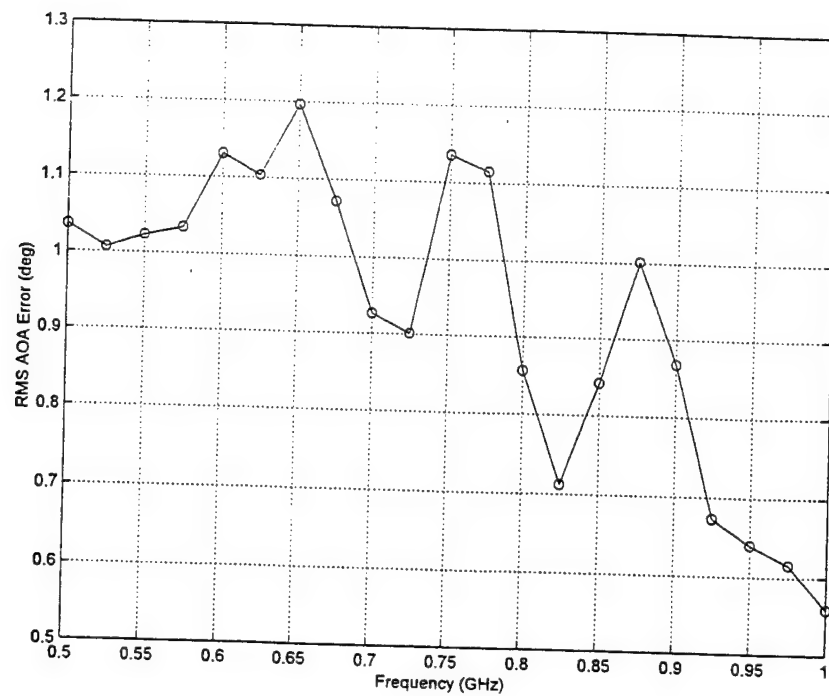
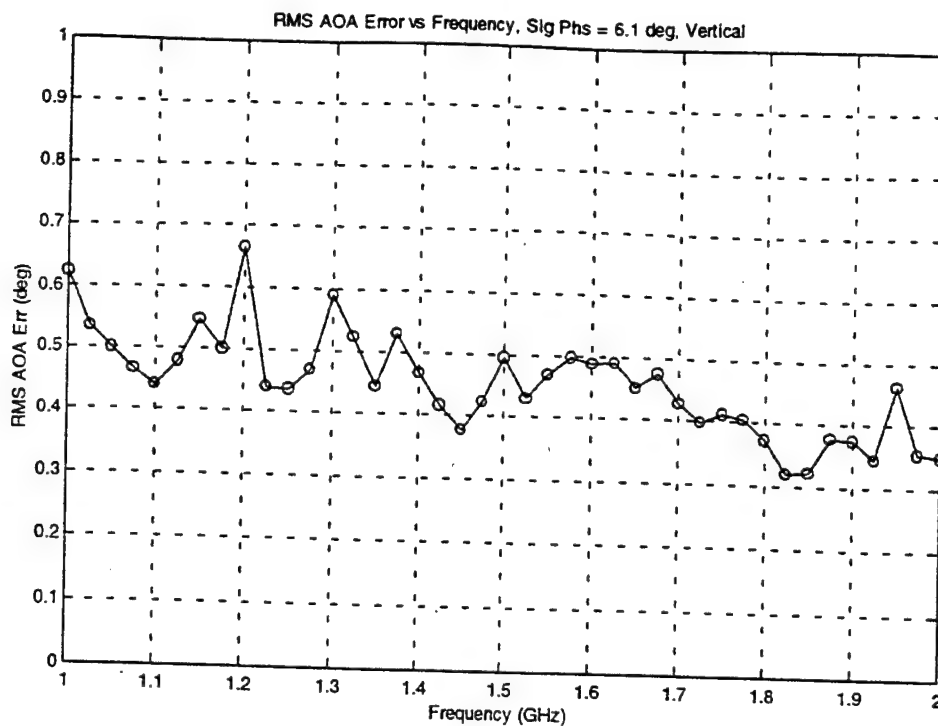


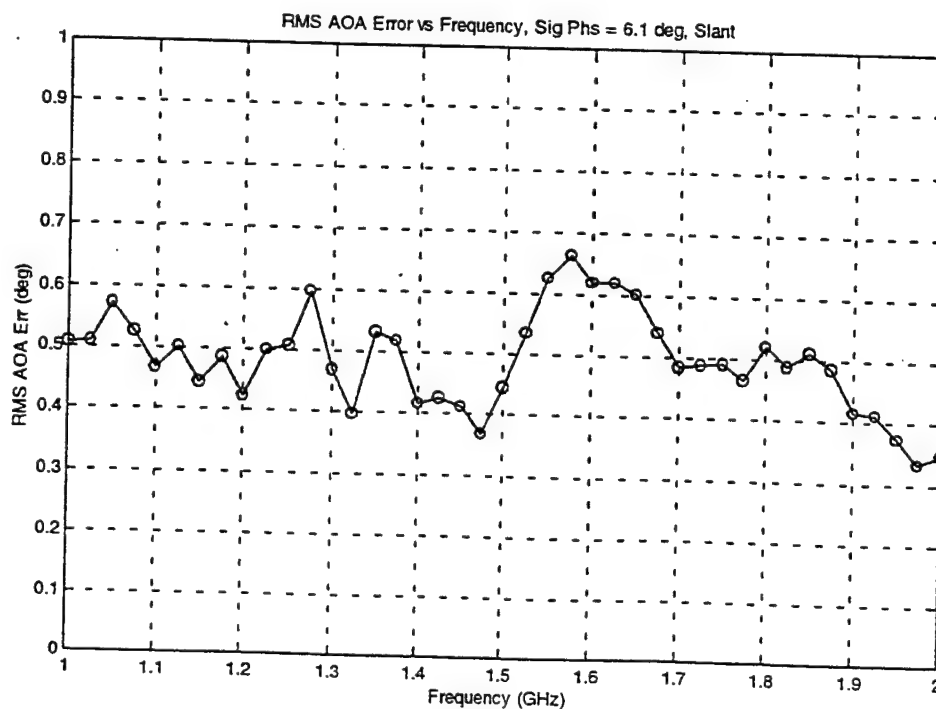
Figure 15. Slant 45 degree, RMS AOA and Mean Ambiguity Rate over 0.5 to 1 GHz, for DF antenna using Phase and Amplitude

The 0.5 to 2 GHz data discussed above was generated using the circular DF antenna configured as shown in figure 4. This structure used single polarization elements due to cost constraints that prevented acquisition of dual polarized elements. In looking at the measurements reported previously, dual polarized elements had been used and extremely accurate results were obtained. Based on this, we then went back to the previous array and measured the 1 to 2 GHz DF accuracy, using the same beamformer shown on the antenna shown in figure 4.

All parameters, such as residual phase error for the measurements and data analysis were the same. Figures 16 through 21 are plots of the data collected and analyzed. Figure 16 shows the RMS AOA accuracy versus frequency for both reception of a linearly polarized (vertical) and a slant 45 degree polarized signal. The RMS AOA accuracy for the linearly polarized case was of 0.67 degrees maximum with an average of 0.46 degrees. The RMS AOA accuracy for the slant 45 degree polarized case was 0.65 degrees maximum with an average of 0.50 degrees. A plot was made to see how the SNR changes with RMS AOA error. Figure 17 shows that 20 dB SNR results in 0.5 degrees RMS AOA accuracy, for essentially one pulse. Figure 18 shows a residual phase error, or one sigma phase error, versus SNR of 6.1 degrees at 20 dB SNR for a single pulse. Figure 19 shows ambiguity rate versus frequency from a SNR of 5 dB to 29 dB in 3 dB steps. The second curve shows that 8 dB SNR results in an average ambiguity rate of approximately 5% with a maximum of 7.5%. Figure 20 shows an average ambiguity rate versus SNR where approximately 4.8% ambiguity rate results for an 8 dB SNR. Figure 21 shows RMS AOA accuracy versus frequency where the residual phase error has been increased to 11.1 degrees. Again, SNR curves range from 5 dB to 29 dB in 3 dB steps. At 14 dB SNR, also 11.1 degree residual phase error, the average RMS AOA accuracy averages approximately 1.0 degree.



RMS over frequency = 0.46 deg for the vertical case



RMS over frequency = 0.50 deg for the slant case

Figure 16. Vertical and Slant 45 RMS AOA over 1 to 2 Ghz using dual polarized 1 to 18 GHz elements

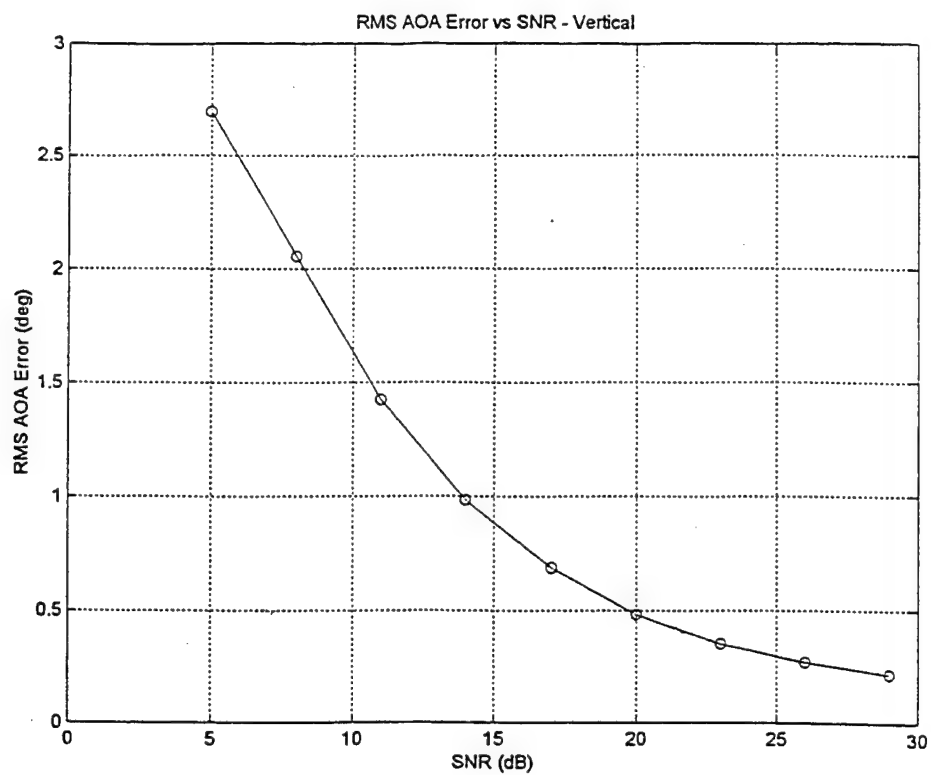


Figure 17. RMS AOA Error versus SNR (dB)

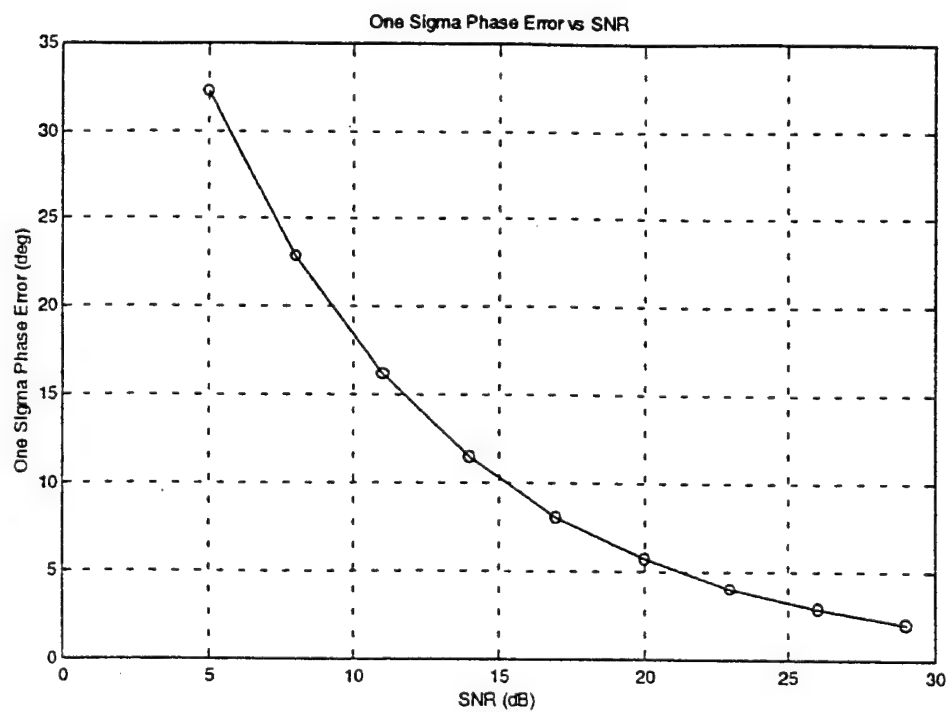


Figure 18. One Sigma Phase Error Versus SNR (dB)

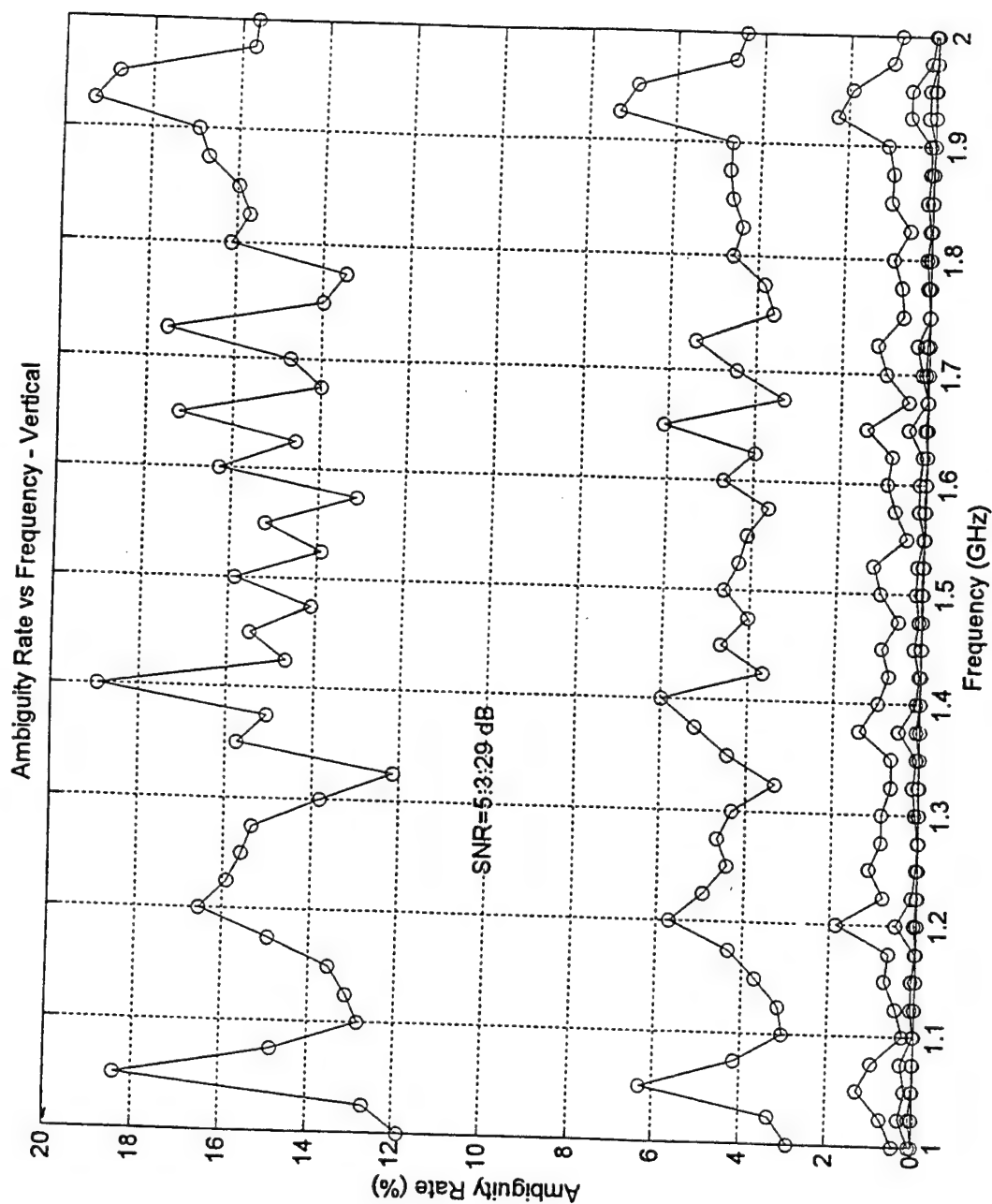


Figure 19. Ambiguity Rate versus Frequency, Vertical Polarized Signal, 1 to 2 Ghz Using Dual Polarized Elements

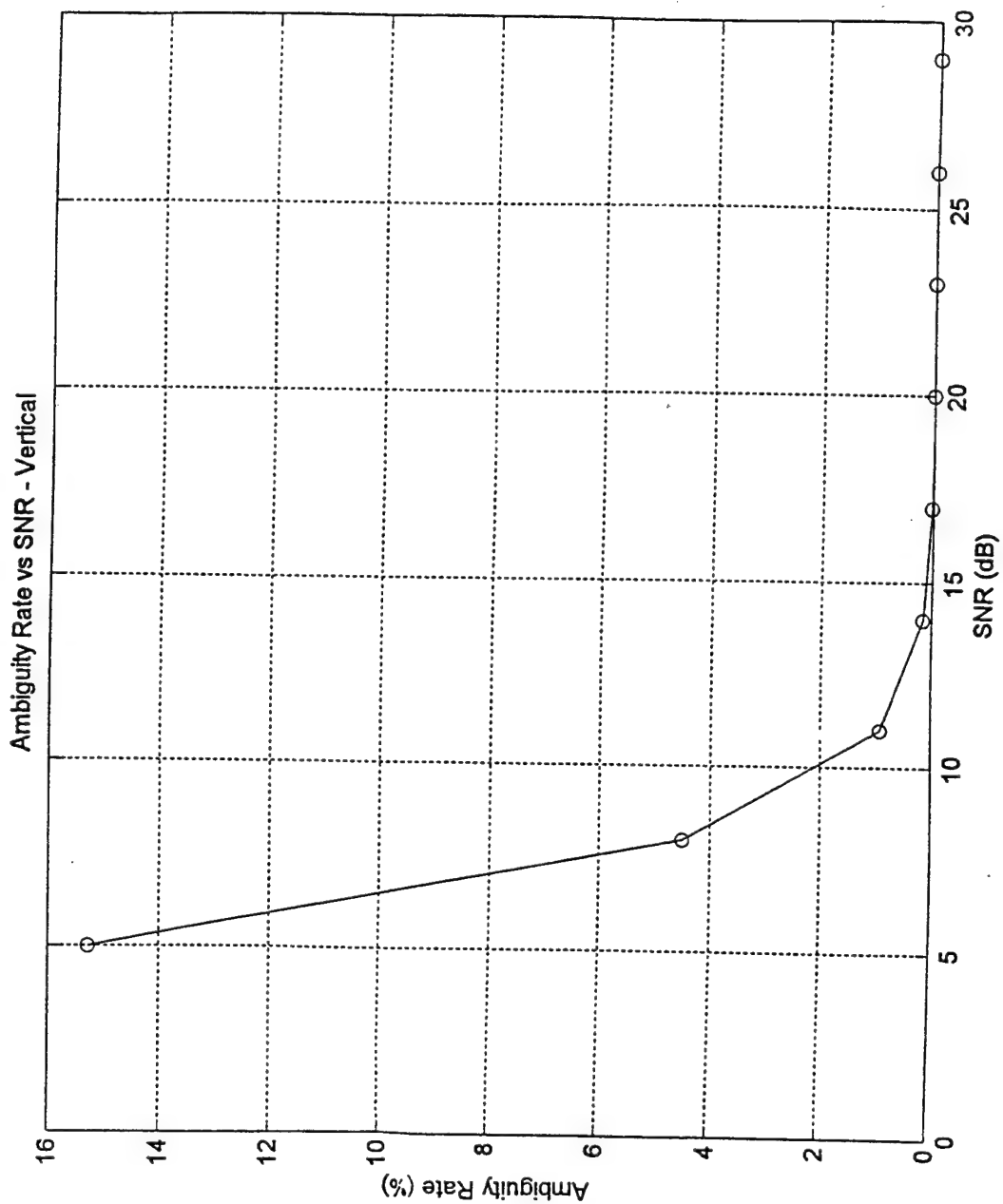


Figure 20. Ambiguity Rate versus SNR (dB), Vertical polarized Signal, Using Dual Polarized Elements

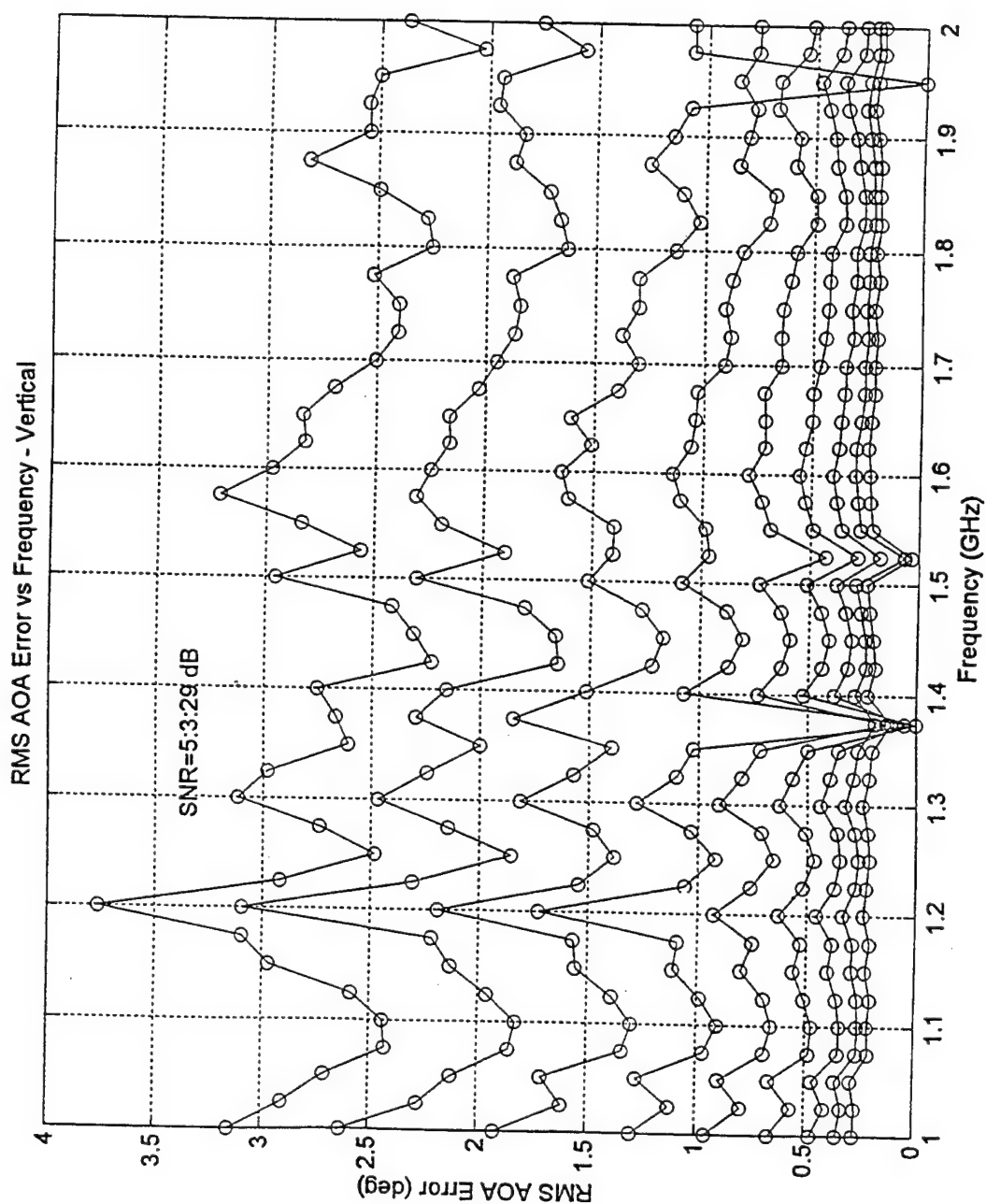


Figure 21. RMS AOA Error versus Frequency, Vertical Polarized Signal, 1 to 2 GHz, Using dual polarized Elements

This data suggests that the elements used in the 2 to 18 GHz circular DF antenna, now used in the 1 to 2 GHz frequency range, are much closer matched to each other in phase and amplitude. These elements track each other closer than the elements used in the 0.5 to 2 GHz antenna.

The size of the high accuracy 0.5 to 2 GHz Circular DF array was 40 inches in diameter by approximately 16 inches in height. The size of the 1 to 2 GHz circular DF antenna, which actually is a 1 to 18 GHz DF antenna, is still 24 inches in diameter and approximately 8 inches in height.

The data presented shows RMS AOA accuracy of 0.71 degrees approximated on the high side to 0.75 degrees. This was done to account for additional variations in noise over the 0.5 to 2 GHz frequency range.

A generic 4 or 5 element linear interferometer would have the typical specifications illustrated in Table III. The linear interferometer has elements spaced at judiciously selected multiples of half wavelengths. This is used for comparison to the circular DF array. The assessment is that the linear interferometer is an extremely high accuracy AOA antenna over a limited field of view.

Table III. Generic Linear Interferometer specifications.

Frequency Range: 0.5 to 2 GHz
Element Gain: 0.0 dBi minimum
Polarization: Single
Field of View: Azimuth - +/- 60 degrees
 Elevation - +/- 45 degrees
RMS AOA Accuracy: 0.6 degrees maximum
Ambiguity Rate: less than 0.1%
Signal to Noise Ratio: 8 dB minimum

The real estate required to install an linear interferometer is greater than that required for a circular DF array. The size of the high accuracy circular DF array was 40 inches in diameter by 14 inches in height.

4.0 Implementation Issues

In all configurations of apertures evaluated, a Butler beamformer is desired since it is simultaneous, quasi compact, and already exists. Low Noise amplifiers should be installed to overcome the insertion loss incurred through the Butler matrix. Filters can be added to keep out-of-band interference minimized. Available COTS Butler matrix (beamformer), switches, LNA's and filters should be used in the actual installations. Using COTS available hardware is the most cost effective implementation.

The low noise amplifiers used must be evaluated and adjusted in order to optimize and maximize sensitivity, and 2nd and 3rd order spur free dynamic ranges, based on the requirements of the installation.

Calibration is extremely important for providing accurate AOA especially at and below 1 GHz. Structural interactions will exist. This needs to be considered in the measured modal phase data, based on the installation requirements. The calibration data is used to take out known sources of systematic phase bias errors such as interference from other structures.

With regard to specifications, it is extremely difficult to specify the DF array separately from the DF processor. The reason is that both are intertwined in determining AOA accuracy and sensitivity of a system and are highly reliant

on the proprietary algorithms and calibration techniques that are utilized.

The light weight and simplicity of this design allow for endless installations in ground based, mobile and airborne systems. Different frequency bands of operation are presently being prototyped using a multitude of different dual polarization elements. A new Raytheon Systems Company coaxial antenna, United States Patent Pending, is being used in a new DF antenna which will result in a 12 inch diameter and height of 6 inches operating over the 2 to 18 GHz frequency band. [3]. Other designs have been designed for operation to and including 60 GHz and as low as 400 MHz.

5.0 Conclusion

Raytheon Systems Company has developed a 360 Degree Azimuth DF antenna using COTS hardware. It was designed to operate from 0.5 to 2 GHz with a goal of 1.0 degree RMS AOA accuracy. An antenna prototype has been tested and evaluated using proprietary algorithms, resulting in a maximum 0.71 degree RMS AOA accuracy with an average of approximately 0.5 degrees. This antenna is approximately 40 inches in diameter and 14 inches in height. It is dual linearly polarized with two polarization configurations possible. The ambiguity rate meets the maximum requirement of 5% from high SNR to a low SNR of 8 dB. Normal operation is in the 14 to 20 dB SNR range.

This aperture installation is also expected to save weight due to a simplified mounting structure. The antenna aperture has higher gain that translates into larger detection range.

In all configurations of apertures, a Butler beamformer is recommended since it is simultaneous, quasi compact, and

already exists. The performance of the proposed aperture is better than the specified goals.

Implementation issues were addressed with regards to using COTS hardware. Sensitivity improvements to overcome Butler matrix insertion loss were discussed with regard to appropriate situational selection of amplifiers and filters. Calibration was also addressed as a means of increasing accuracy and accounting for known error sources.

The basic circular DF array design is easily scaled to other frequency bands that are being prototyped. Due to the light weight and simplicity of this antenna, installations are essentially endless for different ground based, mobile, and airborne systems. A 12 inch diameter, 2 to 18 GHz DF antenna is presently under construction.

6.0 References:

- [1] T. R. Holzheimer, "High Accuracy DF Antenna Using COTS Hardware," Antenna Applications Symposium, Monticello, Illinois, pp 11-1 to 11-30, 20-22 September, 1995.
- [2] T. R. Holzheimer, "360 Degree DF Antenna," Patent Pending, 20 November, 1998.
- [3] R. H. Jaeger, T. R. Holzheimer, et al., "Coaxial Cavity Antenna," Patent Pending, 20 October, 1998.

**SOURCE SEPARATION OPERATING ON A SET OF COLLOCATED
ANTENNAS : THEORY AND
APPLICATION IN THE H.F. BAND (3-30 MHz)**

C. Le Meins*, Y. Erhel**, L. Bertel* and F. Marie*

* : Laboratoire Structures Rayonnantes / Radiocommunications
UPRES-A CNRS 6075 Université de Rennes 1
35042 RENNES-Cedex France

** : Centre de Recherches des Ecoles de Coëtquidan
56381 GUER-Cedex France

Abstract : Source separation is a subject of great interest for numerous applications, among which is the improvement of the coherence bandwidth in digital transmissions. In this paper, a spatial filtering method based on the knowledge of collocated antenna's responses is proposed to reach this goal. The applications are related to the HF band (3-30 MHz). The performances of the method are compared with those of a well known second order blind technique. Both theoretical and experimental results are presented to illustrate this new technique.

1. Introduction

Source separation can be set up with different techniques. Most of them use antenna arrays whose sensors are spatially distributed. Signal filtering requires an estimation of the steering vectors, which can be achieved in two different ways : estimating the angles of arrival (AOA) or resorting to a blind technique.

Recently, a method of direction finding has been developed which operates on an heterogeneous array [1], that is to say an array made up of different antennas. The classic MUSIC algorithm is applied, resorting however to a particular expression of the normalized steering vector and assuming that a reliable model yields the complex directional responses of the sensors. Experimental validations have been carried out in the H.F. band, demonstrating for example that a 3-D direction finding can be achieved with a linear array provided it is heterogeneous [2].

This technique is extrapolated to a system made up with different collocated antennas : the space diversity is then replaced by the diversity of the antenna responses. A convenient choice of the antennas geometry minimizes their mutual coupling while optimizing their diversity. It has been successfully tested in direction finding with broadcast transmitters more than 700 km away [3].

The possibility of separating the multiple sources which are induced by the ionospheric channel is examined in this paper, resorting to two different methods :

- the first one estimates the steering vectors whose components are the antenna responses computed for the AOA of each path, and then applies spatial filtering using the classic least mean square method. Such a technique had been applied in 1986 using a tripole antenna [4] ; however, the direction finding algorithm was not fully efficient because of the small number of sensors.

- the second one is a blind technique [5, 6] for which the knowledge of the antenna responses is not necessary.

This paper presents the vectorial signal model used and some theoretical as well as experimental results using these two techniques.

2. Signal model including propagation and antenna effects

2.1. The scalar model

The general model of propagation for HF links (3-30 MHz) is based on optical geometry. If the transmitted signal is assumed to be in the following form :

$$e(t) = m(t) \cdot e^{j\omega_0 t} \quad (1)$$

where $m(t)$ represents the modulation of the signal and ω_0 is the carrier angular frequency, the received signal, for narrow band and for the k^{th} mode of propagation, can be expressed as [7, 8] :

$$s_{rk}(t) = A_k \cdot m(t - \tau_{gk}) e^{j\omega_{rk}(t - \tau_{pk})} \quad (2)$$

where A_k is the attenuation related to the k^{th} mode, τ_{gk} is the group delay corresponding to the k^{th} mode, ω_{rk} is the received angular frequency including the Doppler shift, τ_{pk} represents the phase delay for the considered mode.

2.2. The field-signal relations in HF propagation

Maxwell equations induce a dispersion equation from which the phase indexes (for the O and X modes) and the polarization relations can be defined. At the exit of the ionosphere (at an altitude of about 90 km) the polarization relations are given by the limit relations of Budden [9].

Let us consider a receiving antenna. In a general form, the electric field related to an incoming wave is expressed as a three component vector $E(t)$; hence the signal $s(t)$ at the output of an antenna can be expressed as a vectorial product :

$$s(t) = M \cdot E(t) \quad (3)$$

Where M is a matrix which characterizes the antenna response.

Since the components $E_1(t)$, $E_2(t)$ and $E_3(t)$ of the electric field can be written in the following form according to the polarization relations :

$$E_1(t), \quad E_2(t) = a E_1(t), \quad E_3(t) = b E_1(t) \quad (4)$$

the signal can be expressed as :

$$s(t) = (M_1 + aM_2 + bM_3) \cdot E_1(t) \quad (5)$$

The scalar term $E_1(t)$ contains all the propagation effects as developed in section 2.1.

If the coefficients of M are function of the directions of arrival (azimuth and elevation) the notion of antenna diversity can be introduced ; on the other hand if a and b are function of the directions of arrival, a polarization diversity can be defined. In general this dependence will be noted $M(\theta)$ or $a(\theta)$ and $b(\theta)$. In the HF band these two forms of diversity must be considered : the coefficients of M

are related to the type of antenna and the a and b terms depend on the angle between the geomagnetic field and the direction of propagation of the wave [10].

This expression is generally written in a compressed form as [3] :

$$s(t) = F(\theta) \cdot E_1(t) \quad (6)$$

The $F(\theta)$ complex function is named the antenna response function. It can be obtained from physical laws [10, 11] or with the help of simulations [12]. The ground effect in the area of the sensor can be included in the computation of the $F(\theta)$ function [10]. In the HF band this function is also related to the geographic characteristics of the considered link [10].

23. The vectorial model

The inhomogeneity and the anisotropy of the ionosphere induce multipath and multimode propagation. The formula mentioned above for a receiving antenna can also be applied for a transmitting antenna ; thus, a general expression for the received signal can be written as :

$$x_{ri}(t) = \sum_k A_k \cdot G_{lk} \cdot F_{ik} \cdot m(t - \tau_{gk}) e^{j\omega_{rk}(t - \tau_{pk})} + n_i(t) \quad (7)$$

where k identifies the paths, G_{lk} is the complex function of the transmitting antenna l and F_{ik} is the complex function of the receiving antenna i . A_k characterizes the attenuation of the wave corresponding to the k^{th} mode, $n_i(t)$ is additive noise.

If the type of the transmitting antenna is unknown, the received signal can be simplified as :

$$x_{ri}(t) = \sum_k B_k \cdot F_{ik} \cdot m(t - \tau_{gk}) e^{j\omega_{rk}(t - \delta_k)} + n_i(t) \quad (8)$$

In this case, B_k and δ_k take into account the effects of propagation and the effects of the transmitting antenna via the complex value of G_{lk} .

For an array of NC collocated antennas the vectorial expression of the received signal becomes :

$$x_{ri}(t) = \sum_{k=1}^{ns} F_{ik} \cdot s_{rk}(t) + n_i(t) \quad i = 1, \dots, NC \quad (9)$$

where :

- $s_{rk}(t)$: is the signal relative to the k^{th} mode,
- ns : is the number of modes.

24. Example of signals obtained with collocated antennas

A collocated antenna array system (figure 1) has been set up in the field station of the University of Rennes (Monterfil, lat : 48° 03' N, long : 2° 00' W). It includes seven active antennas (3 loops, 1 vertical dipole, 2 inverted V, 1 XYZ antenna) connected to seven coherent receivers [13]. These receivers can operate with a very narrow bandwidth (10 Hz) or with a 3 kHz bandwidth, in order to analyze carrier signals or modulated narrow band signals.

Figure 2 shows an example of the received carrier signals, plotted over 50 seconds, at the output of the receivers in the case of a Skelton (United Kingdom)-Monterfil link. Figure 3 represents simulated signals for the same link under similar propagation conditions. The envelopes of the carrier signals appear to be decorrelated, as expected according to the previous relations.

3. Source separation operating on a set of collocated antennas

The vectorial expression of the data at the output of the antennas can be written in the following form :

$$X(t) = A(\theta) \cdot S(t) + N(t) \quad (10)$$

where :

- $X(t)$ denotes the observation vector obtained on the collocated antennas,
- $S(t)$ is the signal vector corresponding to the different modes,
- $A(\theta)$ represents the steering vector matrix,



Figure 1 : Collocated antennas

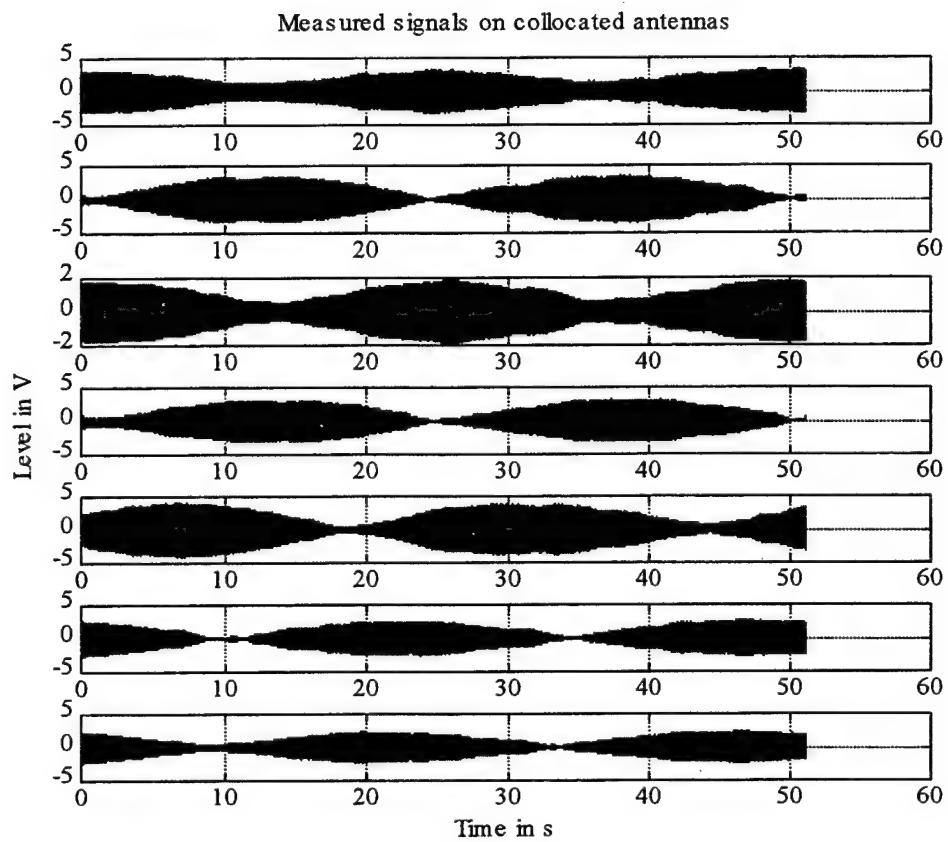


Figure 2 : Measured signals on collocated antennas

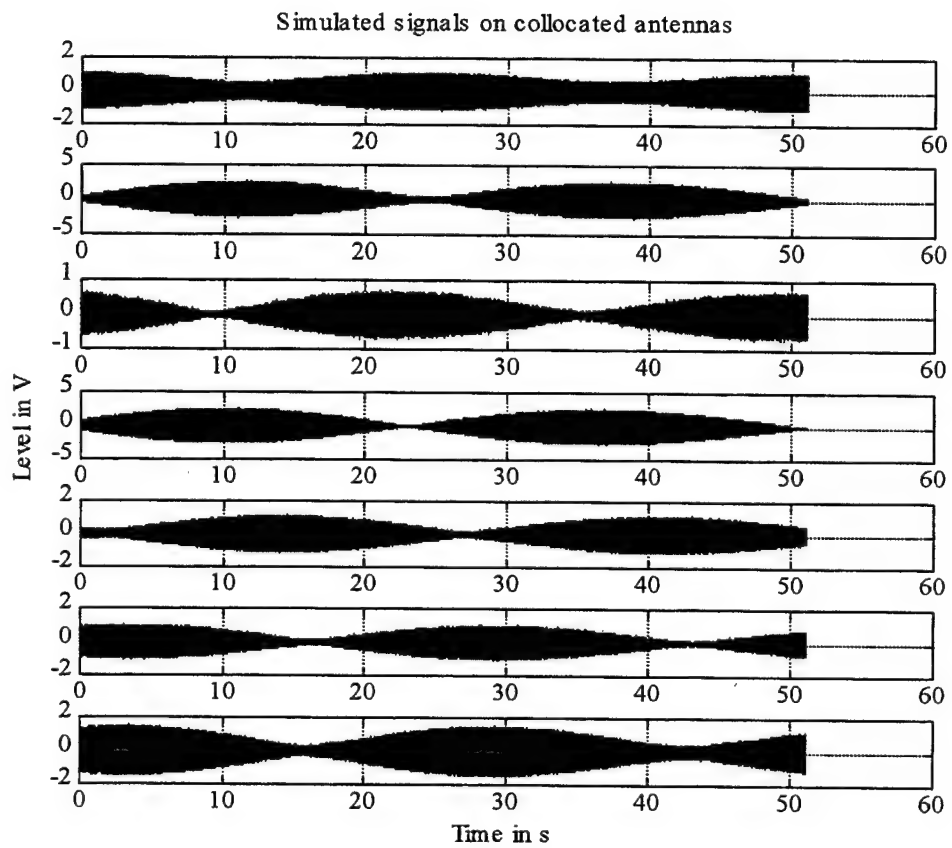


Figure 3 : Simulated signals on collocated antennas

$N(t)$ is an additive noise vector. The components of this vector are assumed to be temporally and spatially white, zero-mean, and independent of the signal vector components.

The goal of the filtering is to determine the $S(t)$ vector from the measurements $X(t)$. The main difficulty is to estimate the steering vectors defined by the matrix $A(\theta)$. In the context of a collocated antenna array, the components of $A(\theta)$ are the functions $F_i(\theta)$.

31. Determination of the directions of arrival

An original method to determine the directions of arrival has been proposed and tested experimentally [13, 14]. It is based on the knowledge of the antenna responses. This technique has been mapped on heterogeneous arrays and on collocated arrays. The array manifold depends not only on the geometry but also on the directivity function of the sensors.

Under these conditions, it becomes feasible to find the directions of arrival with a small array aperture, and even with collocated antennas for which the phase center is the same for all the sensors. The theory of these techniques is developed in the references.

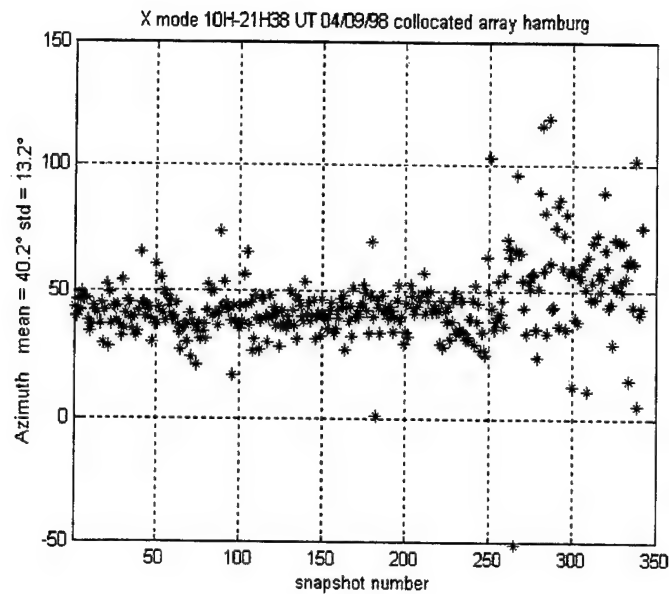
As an illustration, figure 4 shows the variations of the estimated azimuth for both O and X modes over approximately 11 hours for a European link (Hamburg (Germany)-Monterfil) obtained with the collocated antenna array. In this application the MUSIC algorithm is applied. The computation of the pseudo-spectrum is done using steering vectors related to the normalized antenna responses [14].

This technique includes the computation of two pseudo-spectra related to both O and X modes and consequently the determination of the angles for these two modes of propagation.

32. Source separation

The general processing algorithm is shown on figure 5. Initially, the components of matrix $A(\theta)$ are estimated ; then a spatial filter is realized by applying the least mean square method to these estimated values. Then the observed signals on the collocated antennas are spatially filtered to achieve source separation.

• **X mode** :



• **O mode** :

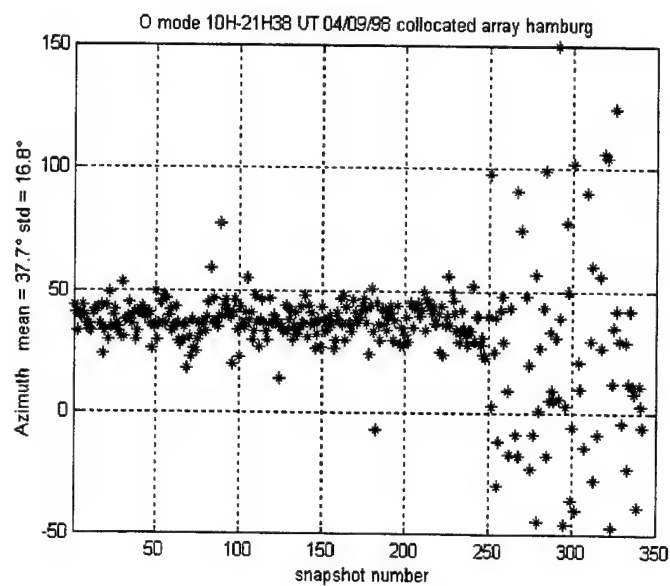


Figure 4 : Direction finding results for the Hamburg-Monterfil link

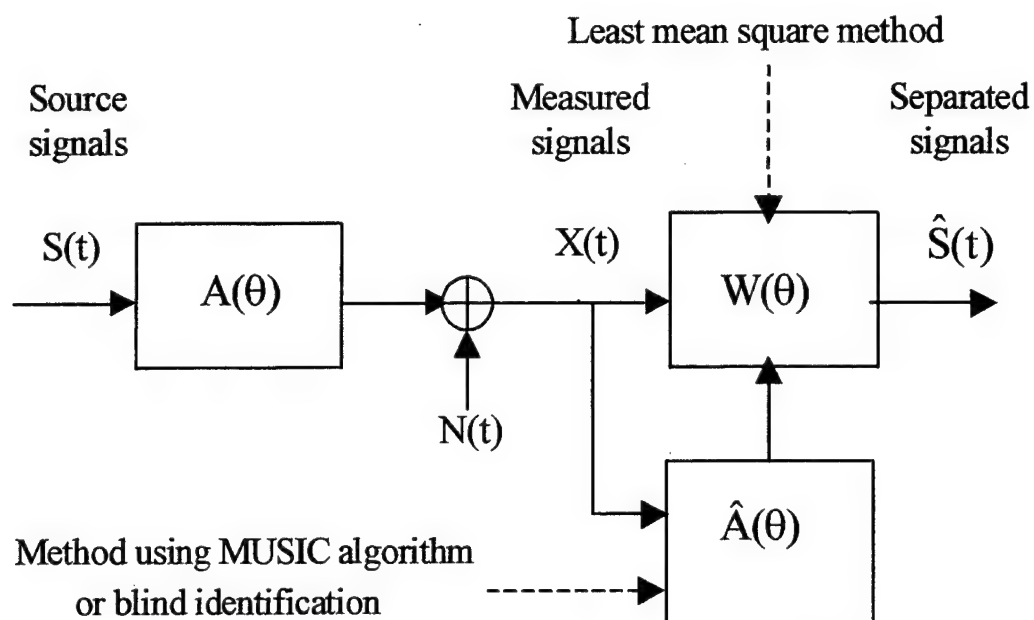


Figure 5 : Filtering algorithm

The mathematical expression of the estimated signals is :

$$\hat{S}(t) = (\hat{A}(\theta)^* \cdot \hat{A}(\theta))^{-1} \cdot \hat{A}(\theta)^* \cdot X(t) \quad (11)$$

or

$$\hat{S}(t) = W(\theta) \cdot X(t) \quad (12)$$

where $W(\theta)$ is the optimum filter to minimize the quadratic error. The * sign denotes the conjugate transpose.

In this paper, two methods are presented to estimate the components of matrix $A(\theta)$:

- for the proposed method the terms of matrix $A(\theta)$ are the values of the antenna responses computed from the estimated AOA (resorting to the MUSIC algorithm),
- for the blind method, a classic second order identification is applied to the signals, assuming that the powers of the signals related to the different modes vary independently in time. For this method the knowledge of the antenna responses is not necessary and cannot be deduced from the algorithm.

To compare these two methods, simulations were carried out for the two different bandwidth measurements with data given in table 1.

	Very narrow band	Narrow band
IF Frequency	5 Hz	30 KHz
Frequency sampling	160 Hz	40 KHz
Acquisition time	51.2 s	204.8 ms
Emitter	Skelton (UK)	Hamburg (G)
Frequency	12.095 MHz	10.101 MHz
Modulation	AM	AFSK
Bandwidth	10 Hz	3 KHz
Ground range	723 km	1070 km
Geometrical azimuth	-5°	47°

Table 1 : Measurement configurations

The antenna responses are computed by the NEC2D software which takes into account the ground effect and the coupling between the antennas.

In the signal model, a differential Doppler shift and a differential time delay are introduced. The Doppler is related to the angle of elevation deduced from measurements [7].

Figure 6a shows the simulated signals on the seven antennas. Figure 6b represents the Eigen values of the data covariance matrix, showing in this case that two modes are present (as introduced in the simulation). The figures 6c and 6d represent the two pseudo spectra, for the O and X mode, obtained with the MUSIC algorithm, from which the angle of arrival can be estimated. The filtered signals obtained with the two methods are plotted on figures 7a and 7b.

In this case where no errors are generated in the simulation in the antenna functions, it can be seen that the proposed spatial filter seems to reduce considerably the time fading of the signals. In addition the determination of the differential Doppler shift gives the expected result (figure 7c and 7d).

Figures 8 and 9 are related to the case where errors of phase and amplitude, on the antenna responses, are introduced in the processing. Consequently, the performances of the proposed method are reduced. If the errors are too important (more than 20% on the relative amplitude and 20° on the phase), the blind method becomes more efficient as it does not need the knowledge of the antenna responses.

For 3 KHz band signals the blind method seems to be more efficient if the product bandwidth by differential time delay is large enough. Currently the blind algorithm assumes the signals to be decorrelated. However, additional studies should be done before a reliable conclusion is drawn.

Three experimental results are listed in this paper.

The first one is related to the case of very narrow band analysis. Figures 10 and 11 show that the proposed spatial filter gives better performances than the blind technique. The differential Doppler shifts extracted from the filtered signals are coherent for the two methods, which give similar results. The opposite signs are due to different classifications of the signals for the two methods.

The second one, shown in figures 12 and 13, involves signals which were acquired some minutes later. The time fading period is larger than in the first case, indicating a stronger correlation. Under this condition, the blind separation method appears inefficient, whereas the proposed spatial filtering method keeps on giving satisfying results confirmed by the Doppler shift estimation.

For transmission of modulated data (figures 14 and 15), the proposed spatial filtering method seems to be more efficient ; this can be due to a strong correlation coefficient. The spectra of the different signals are typical of the AFSK modulation (figures 15c and 15d). The differential time delay is correctly determined with the proposed method while the value seems to be false for the blind method (figures 15e and 15f).

4. Conclusion

The feasibility of source separation based on an array of collocated antennas has been demonstrated. Experimental measurements show that the proposed technique may give better results than the tested blind technique. However, this new method must be tested on more links before being implemented operationally.

This method could also operate in other frequency bands and for other applications such as for mobile radio operating in the UHF band.

The design of a collocated antenna array induces some new aspects in antenna definition. Indeed, the direction finding method and the spatial filtering processing depend on the phase antenna responses which are usually not taken into account in system designs.

5. Acknowledgements

The authors wish to thank the French department of defence for its support regarding the financing of the experimental direction finding systems through contracts n° 95-059 and n° 95-066.

6. References

- [1] Y. Erhel, D. Lemur and L. Bertel, "H.F. radio direction finding operating on an heterogeneous array of active antennas". *10th I.C.A.P. Conference, Edimburg (U.K.)*, April 14-17, 1997.
- [2] Y. Erhel, A. Edjeou, L. Bertel, "Contribution of the polarization diversity in H. F. direction finding systems", in *Proceedings of the SPIE's 1994 International Symposium*, 24-29 july 1994, San Diego, USA.
- [3] Y. Erhel and L. Bertel, F. Marie "A method of direction finding operating on an array of colocated antennas". *1998 IEEE/APS/URSI/International Symposium, Atlanta, 21-26 june 1998*.
- [4] L. Bertel, J. Rojas-Varela, "Antennes HF adaptées à la polarisation des signaux reçus : exemples de résultats " *J.I.N.A., Nice*, 1986
- [5] A. Souloumiac, "Blind source detection and separation using second order non stationarity " *I.C.A.S.S.P.95*, pp 1912-1915, 1995.
- [6] J. F. Cardoso, E. Moulines, A. Belouchrani, " A blind separation technique using second-order statistics. *IEEE Transactions on Signal Processing*, 45(2), 434-444, 1997
- [7] : L. Bertel, P. Parion, D. Lemur, " Model of narrow band signal used in ionospheric high frequency (3-30 MHz) channel ", (in french) *Journées d'études SEE 96, communications numériques en présence de multi-trajets*, Paris, France 28-29 mars 1996.
- [8] : S. Salous, L. Bertel, " Analysis of propagation effects on UHF mobile radio signals", *Proceedings of PSIP'99 conference*, Paris, January 1999
- [9] : K. G. Budden, "Radio waves in the ionosphere", *Cambridge University Press*, 1988
- [10] : L. Bertel, J. Rojas-Varela, D. Cole, P. Gourvez, " Polarization and ground effects on H.F. receiving antenna patterns " , *Annales Télécom*, september 1989.

[11] : D. Lemur, P. Parion, A. Edjeou, L. Bertel, " Propagation effects on phase and amplitude of H.F. antenna response ", *Ionospheric Effects symposium IES 96*, 7 Mai 1996.

[12] : D. Lemur, A. Edjeou, L. Bertel, "H.F. active loop antennas response ", *IEE Antennas and propagation conference, (ICAP)*, Edinburg, April 1997.

[13] : F. Marie, L. Bertel, D. Lemur, Y. Erhel, "Comparison of HF direction finding experimental results obtained with circular and collocated antenna arrays", *Ionospheric Effects Symposium 99*, Alexandria, 3-6 May 1999, USA.

[14] Y. Erhel and L. Bertel, "A method of direction finding operating on an heterogeneous array". *9th Eusipco Conference, Rhodes*, September 8-11, Greece, 1998.

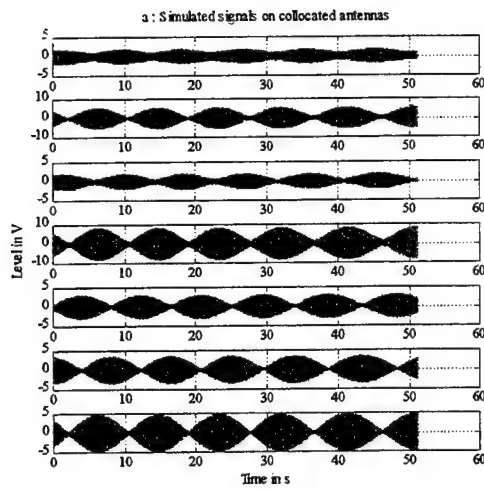


Figure 6a

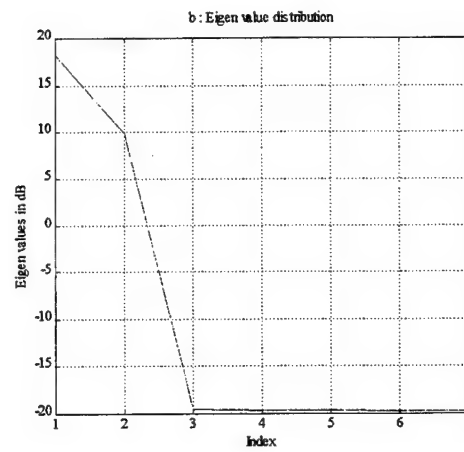


Figure 6b

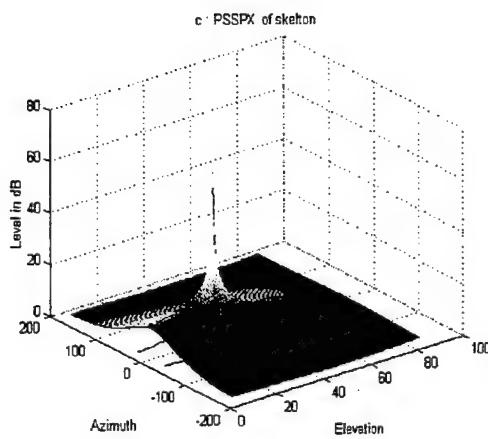


Figure 6c

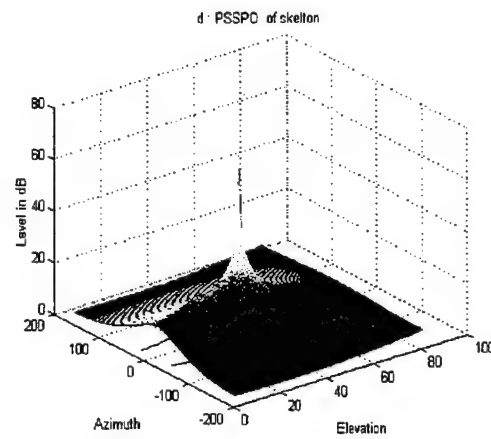


Figure 6d

Figure 6 : Simulated results

The configuration is : 1 X mode ($\tau_{g1} = 4.0$ ms, $El_1 = 30^\circ$, $\Delta P_1 = 1.1$) and 1 O mode ($\tau_{g2} = 4.5$ ms, $El_2 = 40^\circ$, $\Delta P_2 = 0.9$). There are no antenna response errors ; $\Delta\Psi(\text{Fik}) = 0^\circ$ and $\Delta M(\text{Fik}) = 0\%$.

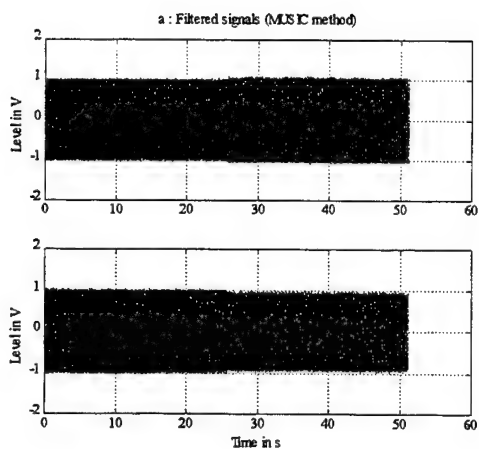


Figure 7a

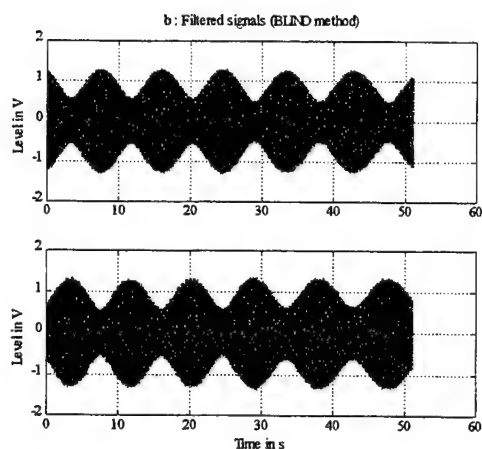


Figure 7b

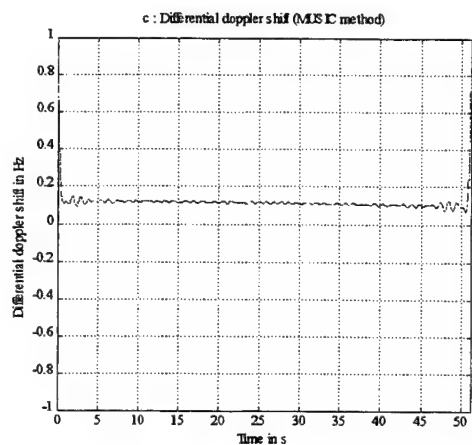


Figure 7c

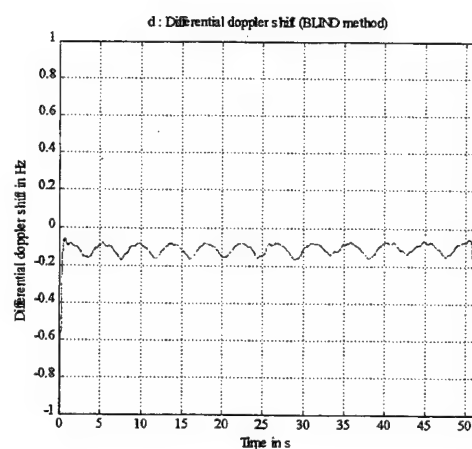


Figure 7d

Figure 7 : Simulated results

The estimated modes are : 1 X mode ($Az_1 = -5^\circ$, $El_1 = 30^\circ$) and
1 O mode ($Az_2 = -5^\circ$, $El_2 = 40^\circ$).

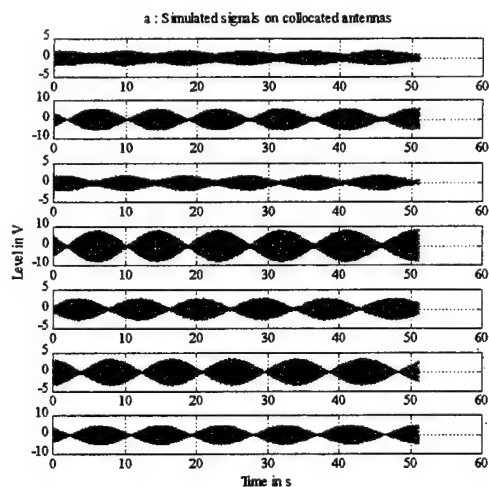


Figure 8a

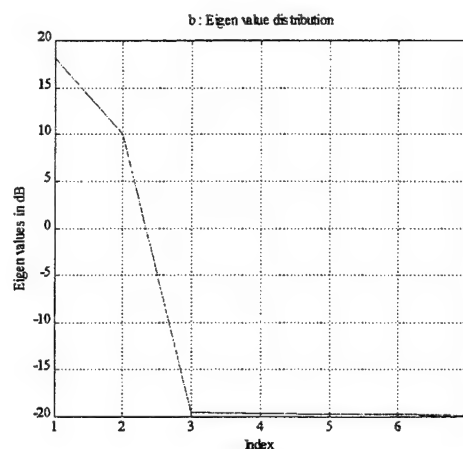


Figure 8b

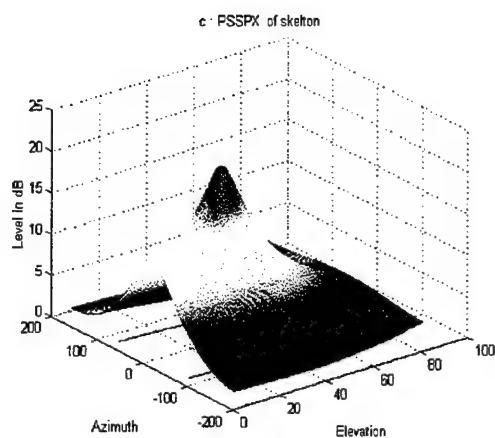


Figure 8c

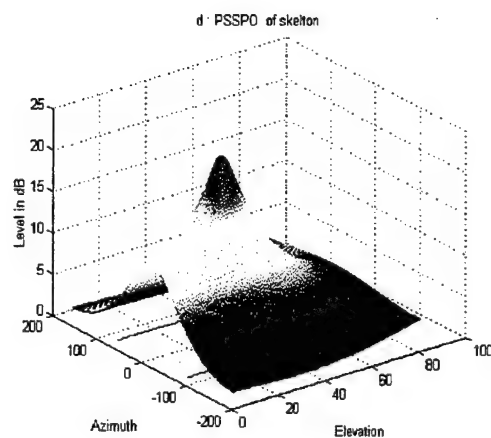


Figure 8d

Figure 8 : Simulated results

The configuration is : 1 X mode ($\tau_{g1} = 4.0$ ms, $El_1 = 30^\circ$, $\Delta P_1 = 1.1$) and 1 O mode ($\tau_{g2} = 4.5$ ms, $El_2 = 40^\circ$, $\Delta P_2 = 0.9$). The antenna response errors are : $\Delta\Psi(\text{Fik}) = \pm 10^\circ$ and $\Delta M(\text{Fik}) = \pm 10\%$.

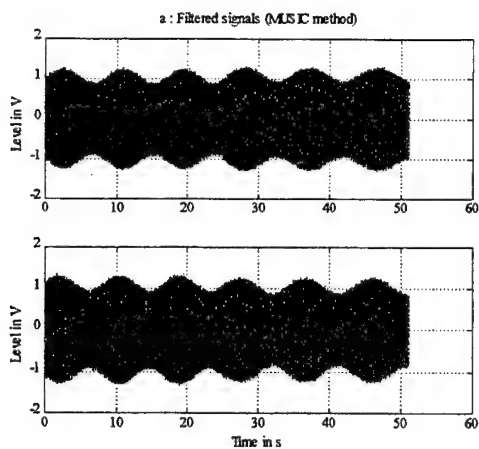


Figure 9a

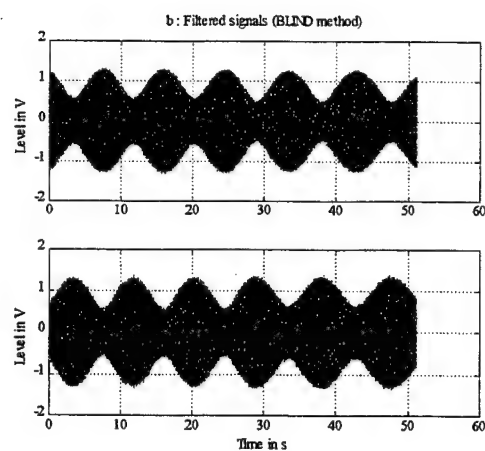


Figure 9b

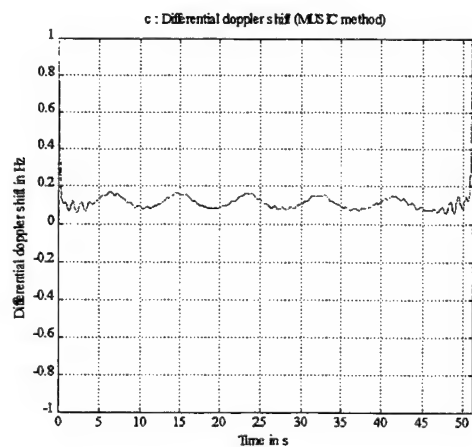


Figure 9c

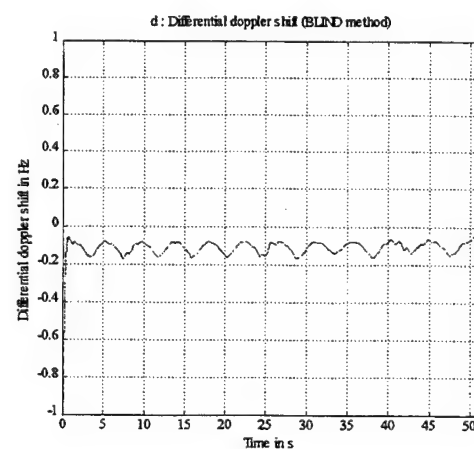


Figure 9d

Figure 9 : Simulated results

The estimated modes are : 1 X mode ($Az_1 = 1^\circ$, $El_1 = 33^\circ$) and
1 O mode ($Az_2 = -1^\circ$, $El_2 = 33^\circ$).

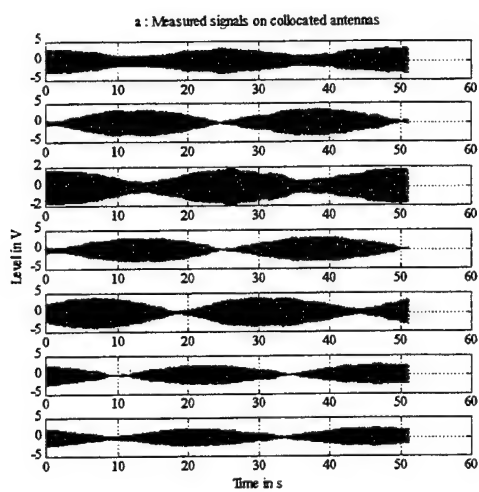


Figure 10a

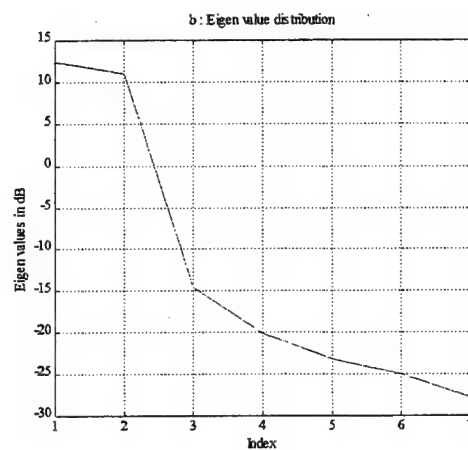


Figure 10b

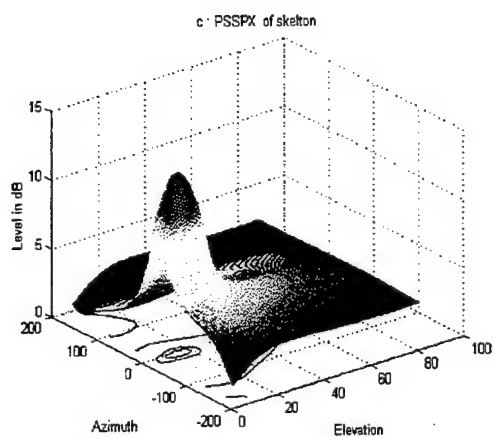


Figure 10c

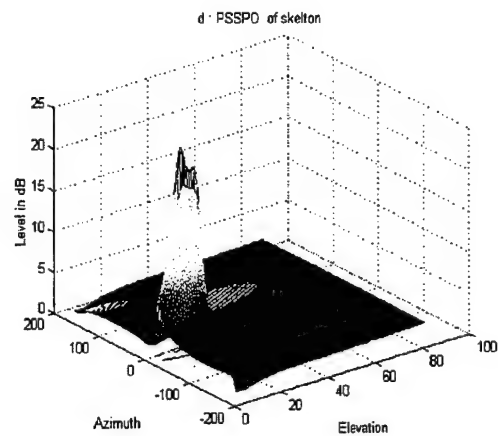


Figure 10d

Figure 10 : Experimental results for the Skelton-Monterfil link.

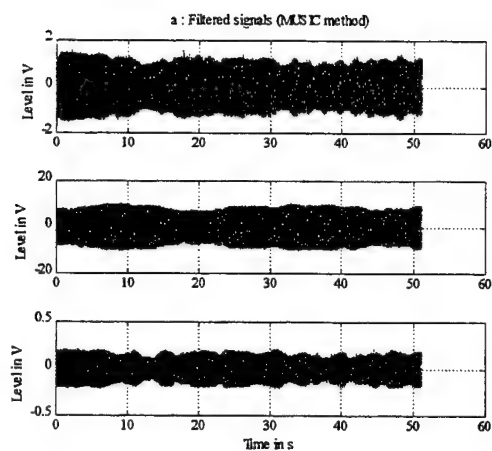


Figure 11a

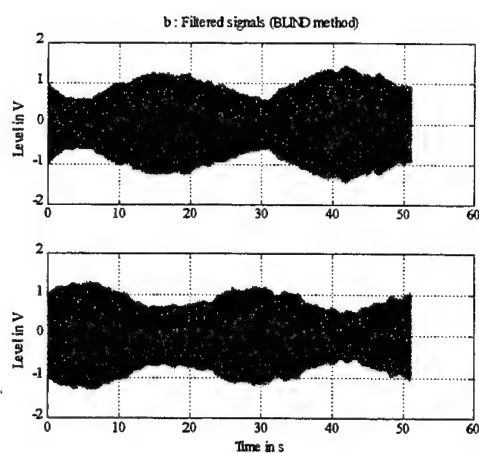


Figure 11b

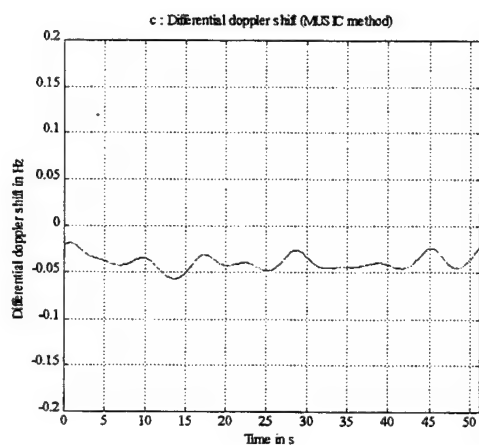


Figure 11c

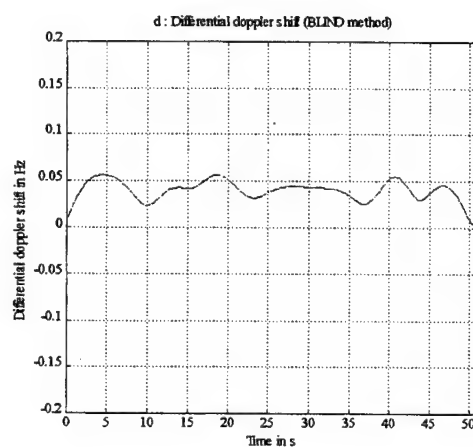


Figure 11d

Figure 11 : Experimental results for the Skelton-Monterfil link.

The estimated modes are : 1 X mode ($Az_1 = -4^\circ$, $El_1 = 15^\circ$) and
2 O modes ($Az_2 = -5^\circ$, $El_2 = 14^\circ$, $Az_3 = -5^\circ$, $El_3 = 20^\circ$).

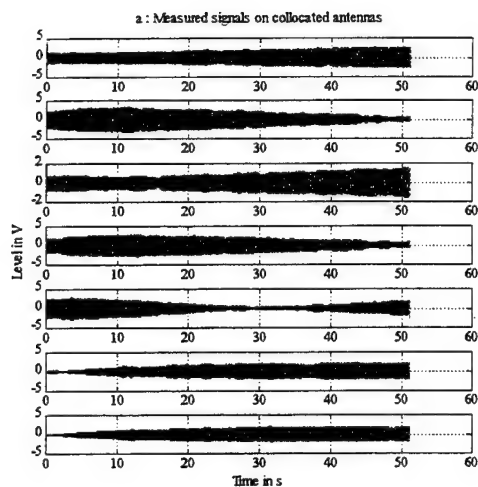


Figure 12a

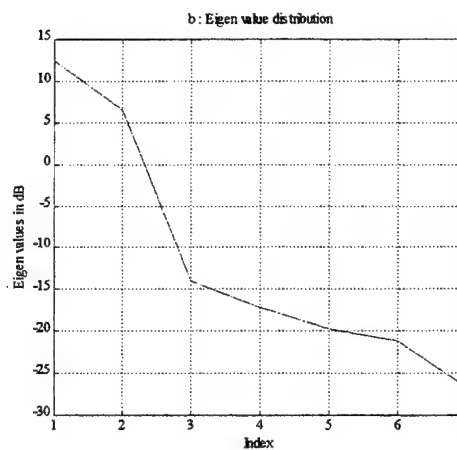


Figure 12b

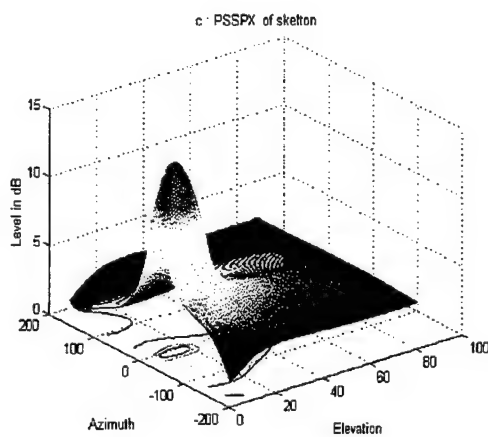


Figure 12c

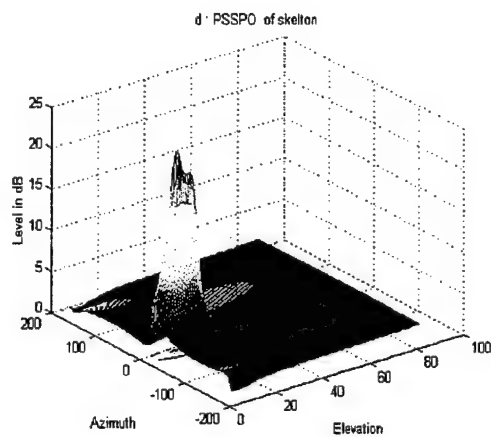


Figure 12d

Figure 12 : Experimental results for the Skelton-Monterfil link.

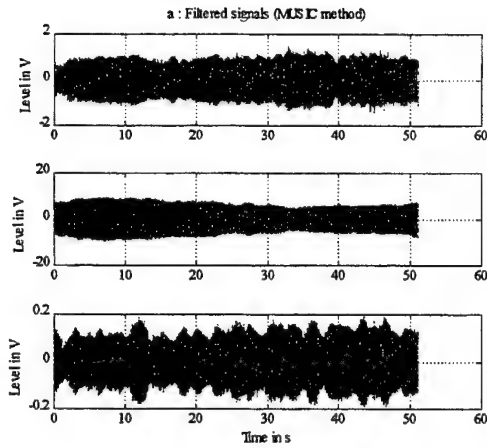


Figure 13a

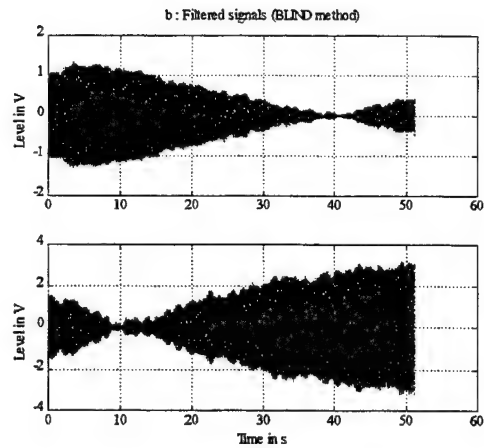


Figure 13b

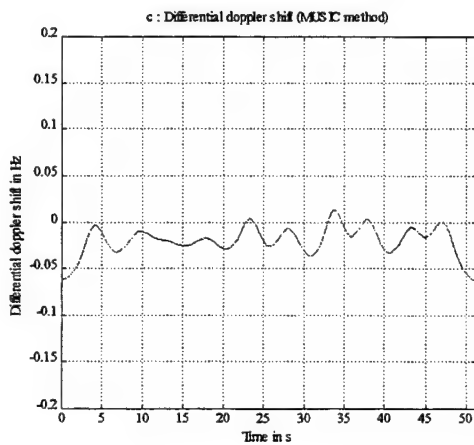


Figure 13c

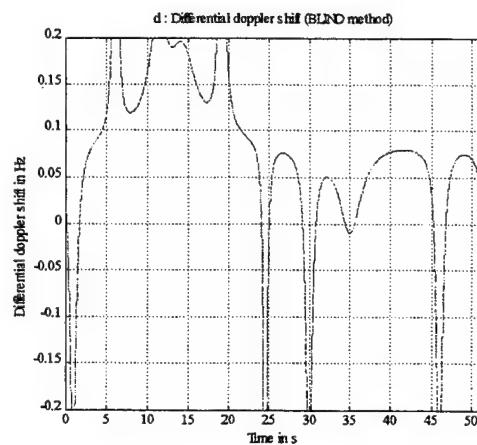


Figure 13d

Figure 13 : Experimental results for the Skelton-Monterfil link.

The estimated modes are : 1 X mode ($Az_1 = -5^\circ$, $El_1 = 14^\circ$) and
2 O modes ($Az_2 = -6^\circ$, $El_2 = 14^\circ$, $Az_3 = -6^\circ$, $El_3 = 20^\circ$).

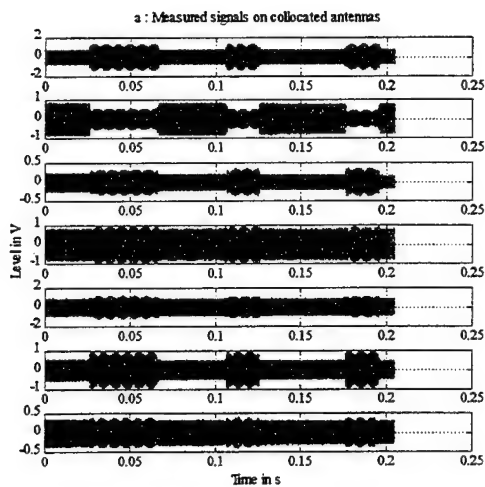


Figure 14a

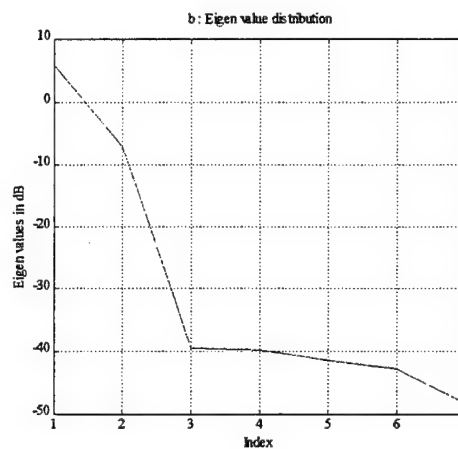


Figure 14b

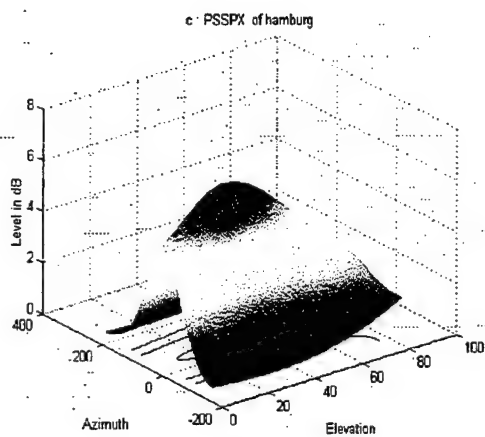


Figure 14c

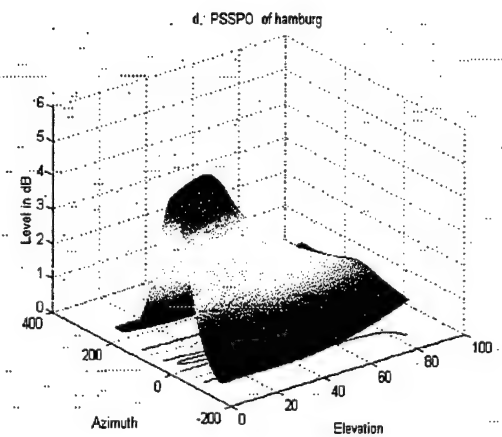


Figure 14d

Figure 14 : Experimental results for the Hamburg-Monterfil link.

The estimated modes are : 1 X mode ($Az_1 = 42^\circ$, $El_1 = 32^\circ$) and

1 O mode ($Az_2 = 30^\circ$, $El_2 = 18^\circ$).

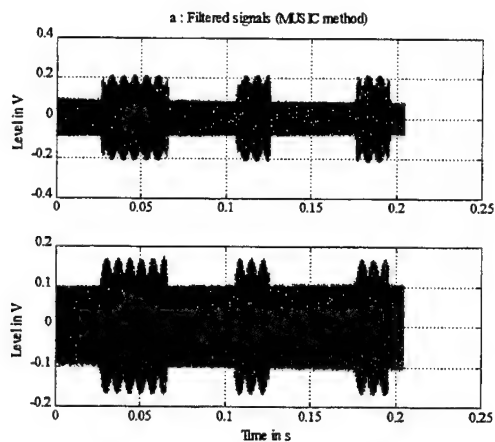


Figure 15a

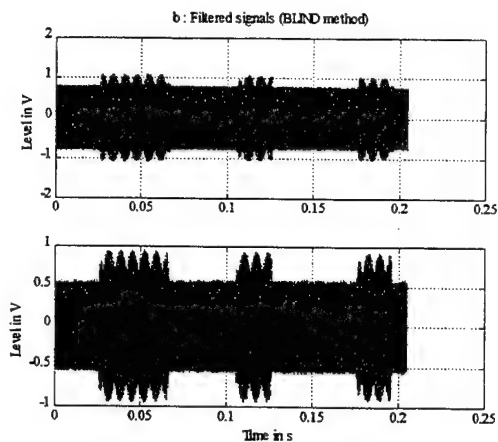


Figure 15b

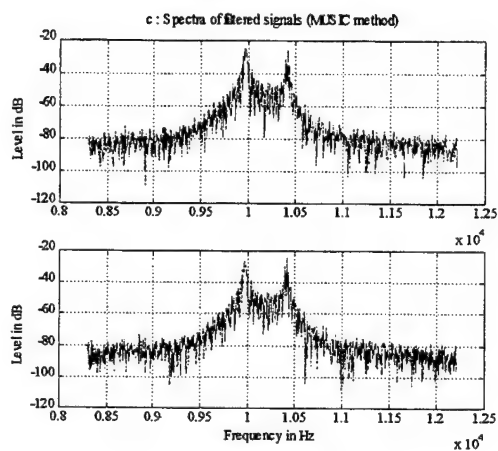


Figure 15c

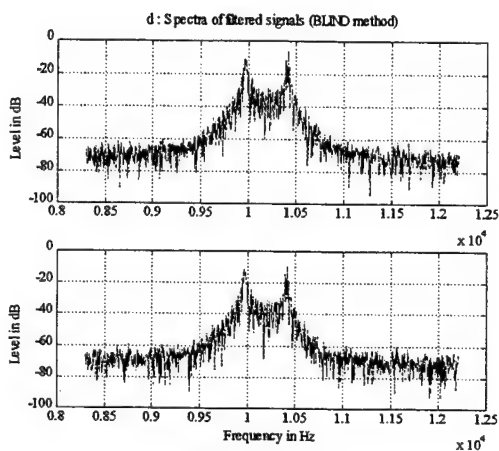


Figure 15d

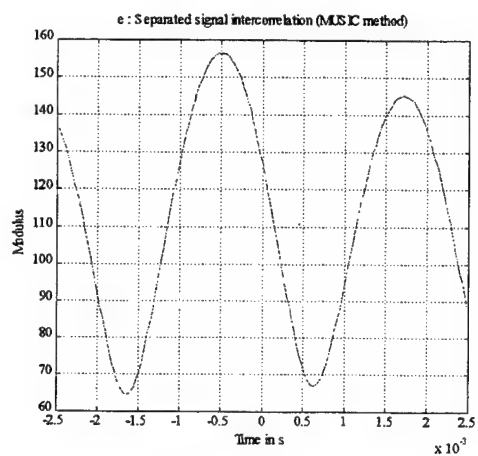


Figure 15e

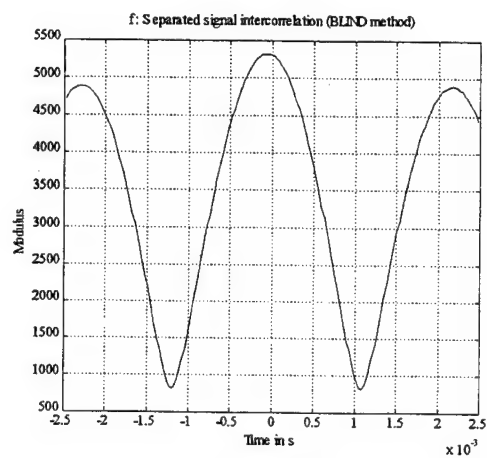


Figure 15f

Figure 15 : Experimental results for the Hamburg-Monterfil link.

STUDY OF AERIAL TARGET RADAR RECOGNITION BY METHOD OF BACKSCATTERING COMPUTER SIMULATION

Ja. D. Shirman, Kharkov Military University (Ukraine, Kharkov)

S.A. Gorshkov, Military Academy of Belarussia Republic (Belarussia, Minsk)

S. P. Leshenko, Kharkov Military University (Ukraine, Kharkov)

V. M. Orlenko, Kharkov Military University (Ukraine, Kharkov)

Abstract: A definite experience of the computer simulation of concrete aerial radar target's backscattering is accumulated for centimeter and decimeter wavebands. On this base a number of the radar recognition problems has been studied, namely: simulation of aerial target's signatures; simulation of recognition signal processing; peculiarities of backscattering and signature simulation in case of time-extended signals. Use of designed simulation methods in R&D of radar systems unconnected with recognition is briefly discussed in conclusion.

1. Introduction

Radar Recognition Versions are widely discussed now. However, it's difficult to compare them numerically without using various target backscattering data.

The possibilities of **physical simulation** of backscattering [1-3] are limited. It's very hard to simulate the variety of characteristics, orientations and positions of a large number of targets, for the time-extended signals especially.

Uptodate computer simulation of backscattering isn't simple also. The programs have to take jointly into account:

- **Electrodynamics** of backscattering of **various** real radar targets in **various** orientations and positions;
- Variety of **probing signals**;
- Existence of target **moving parts**;
- Peculiarities of **target motion** in calm and turbulent **atmosphere**.

Nevertheless, the computer simulation is **worthwhile**. It can **substitute expensive natural experiments** in the initial steps of the recognition system R&D [2- 5].

2. Methods and results of Backscattering Computer Simulation

Our program approximately simulates the centimeter and decimeter wave reflections from the "shining" elements, now of 11 none-stealth aerial targets. These targets are:

- Airplanes Tu-16, B-52, B-1B, Mig-21, F-15, Tornado, An-26;
- Helicopter AN-64;
- Cruise missiles ALKM, GLKM;
- Decoy-missile with the Luneberg lens reflector in the nose part.

The description of target's airframe is performed on the basis of its **drawing**. The target surface is considered as conductive. It is divided into **elementary surfaces**, separated by **limiting planes** (Fig. 1). The following surfaces or their parts are attributed as elementary:

- Straight or bended wedges;
- Double curved surfaces;
- Cone, truncated cone, cylinder, torus, ogive, plate etc.

Total number of such surfaces N depends on the target type and varies in the limits of 60-200.

The **shade effects** and **mirror reflection effects** are taken into account.

In Fig. 1 the following **coordinate systems** using in calculations are shown:

- Radar system with origin at the point O_{radar} ;
- Target system with origin at the point O_{target} ;
- Local systems with origins at the points O_i ($i=1, 2, \dots, \Lambda$).

Precise coordinate recalculations allow taking into consideration **various orientations** of targets and their regular and random **motions of all kinds**.

Reflected signals are calculated by **superposition of reflections** from separate unshaded "brilliant" elements. Equations of Fig. 2 account:

- Signal **space-time and polarization transformations**;
- **Receiver matched intrapulse processing**.

Polarization matrices $A(\vec{r}_i)$ for "brilliant" element majority are introduced on the basis of known theoretical results of physical optics, geometrical and physical diffraction theories [6-8]. The experimental results are also used for description of some of them (pilot cabins etc.) [2-4].

Simulation program has "Windows"- type design as it is shown in Fig. 3 and Fig. 4. The "windows" allow to bring the following initial data in:

- Target type;
- Initial target range, flight velocity and orientation (course, pitch and roll angles);
- Type and bandwidth of probing signal modulation;
- Kinds of polarization in transmission and reception;
- Existence and parameters of the target rotating parts;
- Existence and parameters of interaction between the "target and turbulent atmosphere".

3. Backscattering Computer Simulation and Recognition Problems

Backscattering Computer Simulation simplifies the solution of many of Recognition Problems. It ensures the reasonable choice of:

- Alphabets of target classes or types;
- Recognition Signatures and their combinations;
- Probing Signals;
- Decision Rules;
- Rational Tolerances for Radar Subsystems (Antennas, Feeders, Transmitters, Receivers, Processors).

Backscattering Computer Simulation can be used for Study of Recognition both of Target Classes and Target Types. We've been using it mainly for Study of Target Class Recognition (in reference to Multipurpose Radar with the short Time of "Radar- Target" Contact). Target Type Recognition is now also being studied.

4. Simulation of Aerial Target Radar Signatures

Simulation technique been developed is sufficiently universal. It can be used in radiation of various Signals: Narrowband, Multifrequency and Broadband. There is ensured simulation of different Target Signatures:

- Radar Cross Sections or their averaged values for various signals;
- Other Polarization Matrix Elements;
- Secondary (Turbine and Propeller) Modulation Spectrums;
- Fluctuation Correlation Factors of two or more Reflected Signals on near carrier frequencies via frequency detunings;
- Fluctuation Correlation Matrices on various Frequencies and kinds of Polarization;
- Target Range Profiles which are obtained in the broadband radar owing to high range resolution;
- Target Range-Polarization Profiles which are obtained in broadband radar owing to
- whole Polarization Transmission and Reception or
- transmission and only Amplitude Reception on Different kinds of Polarization;
- Target Range-Frequency Images which are obtained in broadband radar owing to supplementary frequency resolution realized due to a definite increase of "radar-target" contact time;
- Target Azimuth-Range Images which are obtained in broadband radar owing to a considerable increase of "radar-target" contact time;

Examples of simulated Distributions of Amplitudes of Narrowband Signals reflected by the targets of various types are shown in Fig. 5. Let us notice that reliable Cross Section experimental data we had for only one target. Disagreement of its simulated and experimental Values made 0...2,5 dB for the majority of aspect angles [2, 4].

Examples of simulated Secondary Modulation Spectra of turbo-jet, turbo-prop and helicopter targets for wavelength of 5 cm and pulse repetition frequency of 12 kHz are shown in Fig. 6 (see also [9,10] about Secondary Modulation Spectra variants, which also can be simulated).

Example of Fluctuation Correlation Factor dependencies of Reflected Signals on near carrier

frequencies via their frequency detuning is shown in Fig. 7 (see also [1] about their use and, more generally, about the use of Fluctuation Correlation Matrices on various Frequencies and Polarization).

Examples of simulated **Range Profiles** of various targets are shown in Fig. 8. Let us notice that the **real Target Profiles** had been observed for the first time on our Chirp Radar with 70 MHz Bandwidth in 1963-1964 [11-12] and repeatedly obtained then on other modified radar models.

So, in 1980 the **Amplitude Range-Polarization Profiles** including Cross-Polarization ones have been observed. See also [13-15] about range profiles, and [2,16] about range-polarization profiles.

Example of simulated Range-Frequency Image is shown in Fig. 9 for the plane An-26 observed at aspect angle of 30° . Range scale in Fig. 9 is vertical, and frequency scale is horizontal. On a level with plane length and structure (the nose part *N*, the tail part *T*) such image shows the position of rotating propellers *P*, one of which is shaded here on a half [4].

Example of simulated **Azimuth-Range Image** of the B-52 plane obtained during a single-shot "radar-target" contact by the prolonged pulse burst is shown in Fig. 10. See also [17-20] about such image's variants, which also can be simulated.

5. Simulation of recognition processing: correlation procedures and their generalization

Simulation has been carried out with **obligatory evaluation of decision quality** [2, 21].

Various **Decision Rules** (Bayessian, Nonparametrical, and Neural) and various **Recognition Signatures** have been simulated. The main attention was given to recognition on the basis of **Single Range Profile Signature** and of its **Combinations** with other Signatures.

On the basis of Bayessian Decision Rule the **Approximate Correlation Sum Method** was introduced (it was considered also in [15]). This Method requires **Formation of Standards for Target Profile Subclasses**. Decision about Subclass isn't delivered but it ensures delivering the Decision about Target Class. Such method was justified in our 1986-1987 nature experiment.

Introduction of **Subclasses** is conditioned by the **Changeability** of Range Profiles, as it is explained in Fig. 11. Three rows of simulated Range Profiles of TU-16, MIG-21 planes and ALKM cruise missile are shown in small 0.1° aspect angle change from row to row. The change of large target Range Profile (left column) can be noticed, although aspect change of 0.1° itself can't be noticed.

Distinguished sectors of target aspect angle in surveillance radar are great enough (about $10-20^\circ$). The **classes of Target Range Profiles** given their Changeability and Recurrence were divided therefore in **Subclasses** in number up to 3- 10.

A definite idea about the **Range Profile Simulation Quality** can be obtained from comparison of its results with limited 1986-1987 experimental results. Let us notice that correlation of simulated Target Range Profiles with 3 Standards produced from experimental Range Profiles comes to $0.88...0.97$.

The Correlation Sum Method was generalized from the positions of Bayessian Statistics to use **Supplementary Signatures**. This generalization [22] led to **Additive Inclusion of Supplementing Independent Signatures** (of trajectory, Radar Cross Sections, etc.), see also [2, 21].

So, Recognition of $M=4 \dots 6$ target classes was simulated in use of chirp signal of 70 MHz bandwidth. Simulation was realized for $N=1 \dots 5$ of independent "radar-target" contacts, Bayesian and nonparametrical decision rules, and various signature combinations.

Simulated **Probabilities of Target Class Misrecognition** via input signal-to-noise ratio are shown in Fig. 12, separately for various numbers N of independent "radar-target" contacts. This example is related to correlation recognition by the range profile:

- For alphabet of $M=4$ classes of targets (large, middle, small, small – decoy with Luneberg lens);
- For total number of target types equal to 8;
- For number of Standards equal to 3 for each class;
- For use of one supplementing Signature – total Radar Cross Section measured in wideband operation.

Obtained simulation results **have been agreed** with the limited results of 1986-1987-experiment.

Let us notice, the peculiarity of our investigation regarding to known of Hudson and Psaltis [15] consisted in the choice of **study goal**.

Simulation was carried out so as to introduce the recognition into surveillance radar supplemented by chirp exciter and **minimally disturb the main narrowband service**.

6. Simulation of recognition processing: neural network robust learning, special bayessian procedures

As an important direction of the following study we consider the simulation

of recognition by means of **Neural Networks**. A block diagram of such a network [1, 23, 24] is shown in Fig. 13 (AN-artificial neurons). Example of "windows" used in simulation is shown in Fig. 14.

The study progress [25] has shown a need for Neural Network **Learning**, which is **Robust to various interfering factors**. They are:

- Presence of additive noise with unknown level;
- Partial uncertainties of target range and orientation.

The important **Principles of Neural Network Robustness Provision** confirmed in recognition simulation turned out to be:

- Learning in Near to Real Work Conditions;
- Increasing the Number of Neural Network Hidden Elements [25].

Experimental three layer Neural Network (Fig. 14) has been learned to recognize $M=4$ classes of targets probing by chirp signal of 70 MHz bandwidth. Neural Network consisted of 64 elements in the input layer, 200 elements in the hidden layer and 4 elements in the output layer.

All the **Range Profiles were re-counted** on a certain **rated range**. Accordingly the **Noise Levels** were re-counted. Re-counted Range Profiles and Noise Levels were applied onto Neural Network in both operations: learning and recognition.

Neural Network Learning was carried out by presentation of 720 Range Profiles and corresponding Noise Levels for various:

- Target types and classes;
- Aspect angles (in a sector of aspect angle ambiguity);
- Ranges (in a small interval of range ambiguity);
- Signal-to-Noise Ratios (in interval of 17-50 dB).

Neural Network Performance Test was carried out by presentation of 3200 of such Range Profiles with corresponding Noise Levels in condition of $N=1$ "radar-target" contact. **False Recognition Probabilities reduced in half** comparatively to **Correlation Sum Method** with **Approximate Standard Formation**.

At present the **Special Bayesian Methods** are simulated on a level with Neural Network and Correlation Sum Methods to ensure effective recognition of both **class and type of targets**. They are accounted on remembering of expected statistical distributions and presume **significant increase of a priory information volume being remembered**.

7. Peculiarities of backscattering and signatures in use of extended in time signals

Together with Chirp Signals the Signals with **Spectrum Synthesis -Slow Stepped Frequency (SSF)** Signals [13] were simulated. Due to growth of signal duration the significance of the following **disturbance factors** has been increased:

- Target motion's fluctuations caused by the atmosphere turbulence [4, 5];
- Signal's secondary modulation caused by fast rotation of target elements.

So, the **Wind Gust** of turbulent atmosphere act on a flying target. If the signal duration is less than one second, the simple linear differential equations and linear models of target motion can be used [26].

Fig. 15 clarifies the idea of **simulating both the Wind Gusts transverse to target motion and the Target Yaws** caused by them. There are shown:

- Generators of white noise and linear dynamic elements of second order with characteristics $K_{WG}(p)$. They simulate 3 co-ordinate components of **Wind Gust vector** in atmosphere;
- Dynamic element of zeroth order. It evaluates the **Wind Gust vector component transverse to the target velocity vector**. It re-counts then this component **into an angle deflection** of target movement direction relative to wind direction;
- Output dynamic element $K_{TY}(p)$

of second order, simulating the **Target Yaw**.

There are in the output element accounted:

- Action on the target of the **Aerodynamic Torque** caused by wind;
- Existence of the Target **Inertia Moment**;
- Pilot or autopilot efforts smoothing the yaw;

Longitudinal Wind Gust action is accounted by our model in addition to **Transverse Wind Gust** action.

According to simulation results obtained on the basis of SSF signals of 80 MHz bandwidth, storm weather begins to influence on Range Profiles if signal duration exceeds 50–60 ms [4, 5]. Decrease of target altitude increases the weather factor influence.

Fig. 16 explains the weather and altitude factor influences on the signal. The Range Profiles are simulated:

- For target flights in calm atmosphere at altitude 10 km;
- For target flights in storm atmosphere at altitude 1 km.

As pre-cited example shows, it is desirable to join the use of Time-Extended Signal with simulation of weather condition.

Degree of **Secondary Modulation** influence on processing quality depends on the ratios of the target rotating element dimensions to wavelength, on the observability of the rotating elements, and also on the signal duration. Influence of Secondary modulation on the Range Profile for targets having propellers (helicopters, propeller planes) may be basic.

8. Conclusions

As it was shown by examples, **Backscattering Computer Simulation** essentially expands possibilities of investigations of **Aerial Target Recognition Systems**.

Method and programs of Backscattering Computer Simulation can be used also in R&D of classical detection and tracking radar systems. From the detection position there is noteworthy recent critical discussion [27] of classical Swerling Backscattering Statistics in AES Transactions, February 1997. Here also (see pp. 718-719 by S. L. Jonston) an intention appeared of **new models' looking for**. Study of secondary modulation and other backscattering nonstationary effects on target's tracking also leads using the new models.

Therefore, we suppose that **Backscattering Simulation Programs** will be repeatedly created, edited and gradually improved in Radar R&D interest as **new experimental data** will be repeatedly accumulated.

Our Simulation Programs we consider as a **definite step** in this direction.

9. References

- [1] I. Jouny, F. D. Garber, S. Anhalt, "Classification of Radar Targets Using Synthetic Neural Networks", IEEE Trans. Aerosp. Electron. Syst., vol. AES-29, pp. 336-344, April, 1993.
- [2] Ja. D. Shirman, S.A. Gorshkov, S. P. Leshenko, G. D. Bratchenko, V. M. Orlenko, "Aerial Target Radar Recognition Methodes and their Simulation", Zarubeghnaja radioelektronika- Uspehi sovremennoi' radioelektroniki, pp.3-63, November 1996 (in Russian).
- [3] S. A. Gorshkov, " Experimental and Rated Methods of Secondary Radiation Performance Evaluation", in Handbook " Electronic Systems: Construction Foundations and Theory", Ja. D. Shirman, ed., pp.153-179, Moscow, Makvis, 1998 (in Russian).
- [4] Ja. D. Shirman, S. P. Leshenko, V. M. Orlenko, "Aerial Target Backscattering Simulation and

their use in radar recognition engineering", Vestnik Moskovskogo Gosudarstvennogo Tehnicheskogo Universiteta imeni N. E. Baumana, "Radioelektronika", pp. 14-25, 1998, No. 4 (in Russian).

[5] V. M. Orlenko, S. P. Leshenko, G. D. Bratchenko, Ja. D. Shirman, "Signal-trajectory "Program Enveloping" of the secondary radiation model, "Electromagnitny'e volny' i elektronny'e systemy", vol. 4, pp.38 – 43, March 1999 (in Russian).

[6] Proc. IEEE, vol. 53, August 1965, Special Issue.

[7] Proc. IEEE, vol. 79, May 1989, Special Issue.

[8] G. T. Ruck, D. E. Barrick, W. D. Stuart, C.K. Krichbaum, Radar Cross-Section Handbook New York: Plenum Press, 1970.

[9] M.R. Bell, R.A. Grubbs, "JEM Modeling and Measurement for Radar Target Identification", IEEE Trans. Aerosp. Electron. Syst., vol. AES-29, pp.73 - 87, January 1993.

[10] E. Piazza, "Radar Signals Analysis and Modellization in the Presence of JEM Application to Civilian ATC Radars", IEEE AES Magazine, pp. 35-40, January 1999.

[11] J. D. Shirman, V. B. Almazov, V. N. Golikov, V. I. Gomofov, D. A. Zurski', A. P. Krivelev, "On the First Super-wideband Radar Investigations in Soviet Union", Radiotekhnika i elektronika, vol. 36, pp. 96-100, January 1991 (in Russian).

[12] J. D. Shirman, "Resolution and Suppression of Signals", pp.129-134, Moscow: Sovetskoe Radio, 1974 (in Russian).

[13] D. H. Wehner, "High Resolution Radar", Norwood: Artech House, 1987.

[14] C.R. Smith, P.M. Goggans, "Radar Target Identification", IEEE Ant. Propagat. Magaz., vol.35, pp.27 – 38, April 1993.

[15] S. Hudson, D. Psaltis, "Correlation Filters for Aircraft Identification from Radar Range Profiles", IEEE Trans. Aerosp. Electron. Syst., vol. AES-29, pp. 741-748, July 1993.

[16] N. Chamberlain, E. Walton and E. Garber, "Radar Target Identification of Aircraft Using Polarisation – Diverse Features", IEEE Trans. Aerosp. Electron. Syst, vol. AES-27, pp. 58-66, January 1991.

[17] B. D. Steinberg, "Microwave Imaging of Aircraft", Proc. IEEE, vol. 76, pp.1578-1592, December 1988.

[18] R.B. Perlov, B. D. Steinberg, "Automatic Stereo Processing of High Resolution Radar Imagery", IEEE Trans. Aerosp. Electron. Syst., vol. 33, pp. 696-720, July 1997.

[19] V. C. Chen, S. Quian, "Joint Time –Frequency Transform for Radar Range-Doppler Imaging", IEEE Trans. Aerosp. Electron. Syst, vol. AES-34, pp. 486-499, April 1998.

[20] Y. Wang, H. Ling, V. C. Chen, "ISAR Motion Compensation Via Joint Time-Frequency

Technique", IEEE Trans. Aerosp. Electron. Syst, vol. AES-34, pp. 670-677, April 1998.

[21] S. A. Gorshkov, Ja. D. Shirman, "Classification in active radar with passive response and in passive radar", in Handbook "Electronic Systems: Construction Foundations and Theory", Ja. D. Shirman, ed., pp. 668-688, Moscow: Makvis, 1998 (in Russian).

[22] Ja. D. Shirman, "About some Algorithms of Object Classification by a Set of Features", Radiotekhnika i Elektronika, vol. 40, pp.1095-1102, July 1995 (in Russian).

[23] P.J. Werbos, "Backpropagation Through Time", Proc. IEEE, vol. 78, pp. 1550-1561, October 1990.

[24] Parallel Distributed Processing, D. Rummelhart, J. McClelland, ed., vol. 1, Cambridge MA, MIT Press, 1988.

[25] V. M. Orlenko, J. D. Shirman, "Neural-computer recognition in hindering factors accounting", Elektromagnitny'e volny i elektronny'e systemy', vol. 4, 1999 (in Russian, in print).

[26] Yu. P. Dobrolenskii', "Dynamics of Flight in Disturbed Atmosphere", Moscow: Mashinostroenie, 1969 (in Russian).

[27] S. L. Johnston, P. Swerling, X. Xu, P. Huang, "Target Fluctuation Models for Radar System and Performance Analysis", IEEE Trans. Aerosp. Electron. Syst., vol. AES- 33, Part two, pp. 696-720, February 1997

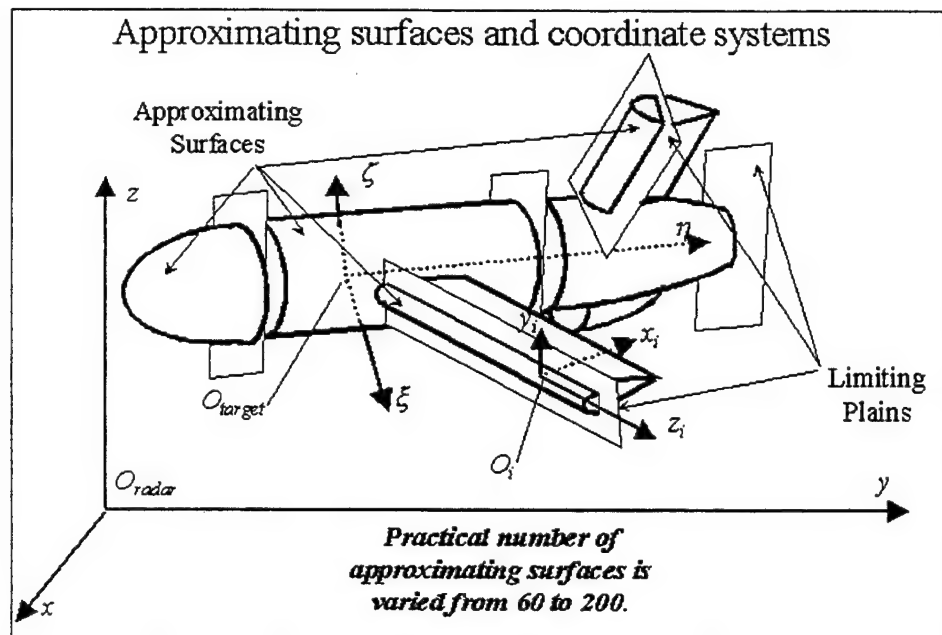


Fig. 1

Calculation of Backscattering in case of Intrapulse Processing

$$\mathbf{X}(t) = \sum_{i=1}^N \mathbf{A}_i(\bar{\mathbf{r}}^o) \bar{\mathbf{S}} U(t - 2\bar{\rho}_i(t)\bar{\mathbf{r}}^o/c) e^{-j4\pi f_0 \bar{\rho}_i(t)\bar{\mathbf{r}}^o/c},$$

$$X(t) = \bar{\mathbf{S}}_0 \mathbf{X}(t),$$

$\mathbf{X}(t)$ and $X(t)$ - signals receiving by two channels and single channel;

$\bar{\mathbf{S}}$ and $\bar{\mathbf{S}}_0$ - polarization vectors of transmitting and receiving antennas in the target direction;

$\bar{\mathbf{r}}^o$ - unit vector of incident wave;

$\bar{\rho}_i(t)$ - coordinate vector of the i -th local reflector phase centre in the radar system;

$\mathbf{A}_i(\bar{\mathbf{r}}^o)$ - polarization matrix of i -th local reflector;


$U(t)$ - complex amplitude of the signal processed in the receiver;

f_0 - carrier frequency;

N - number of local reflectors

Fig. 2

Initial data entering



Target type

☒ Secondary modulation considering

FMS ☐ Frequency band (MHz)

Weather condition

Course (180 dg. - attacking)

Altitude (meters)

Flight (observation) time (s)

Initial range (km)

Velocity (km/h)

Pulse repetition frequency (Hz)

Wavelength (sm)

Pulse number of FMS

Fig. 3

Radar

ENTERING THE PARAMETERS OF RADAR PROBING SIGNAL

Kind of signal

☒ Bell chirp pulse
☐ Rect. chirp pulse
☐ Rect. pulse

Displaying mode

☒ uninterrupted
☐ stepped
☐ don't display

Recording mode

☐ don't record
☒ record all samples
☐ record central sample only

Polarization

Pulse duration (mks)

Bandwidth (MHz)

Range gate (m)

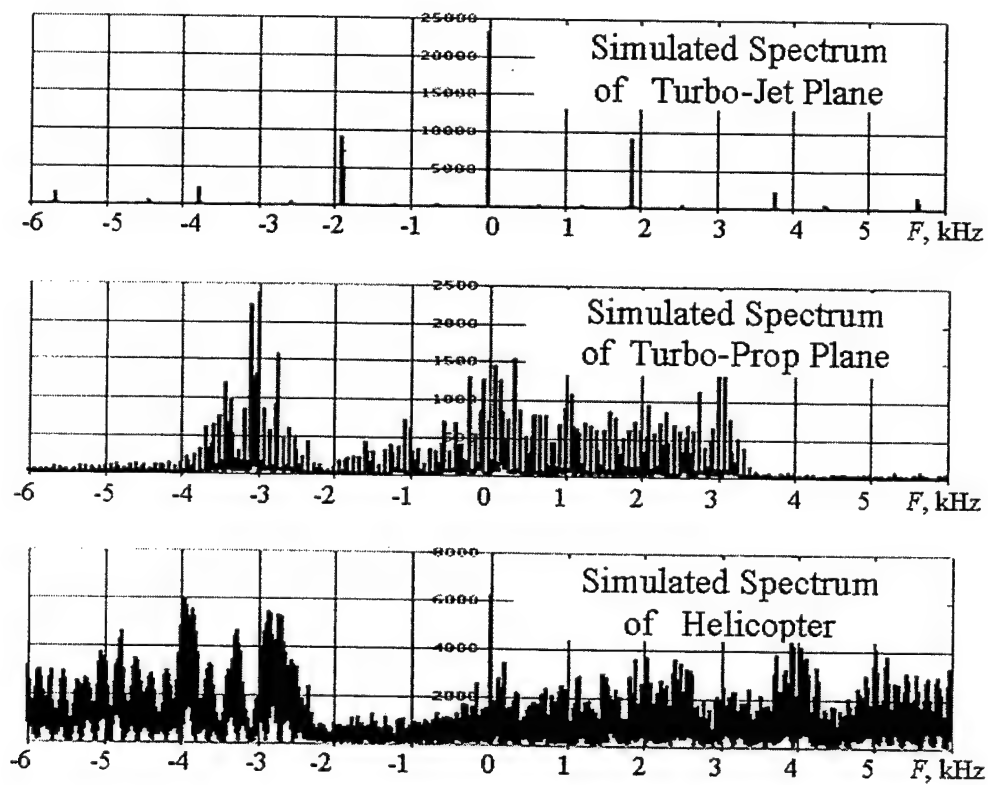
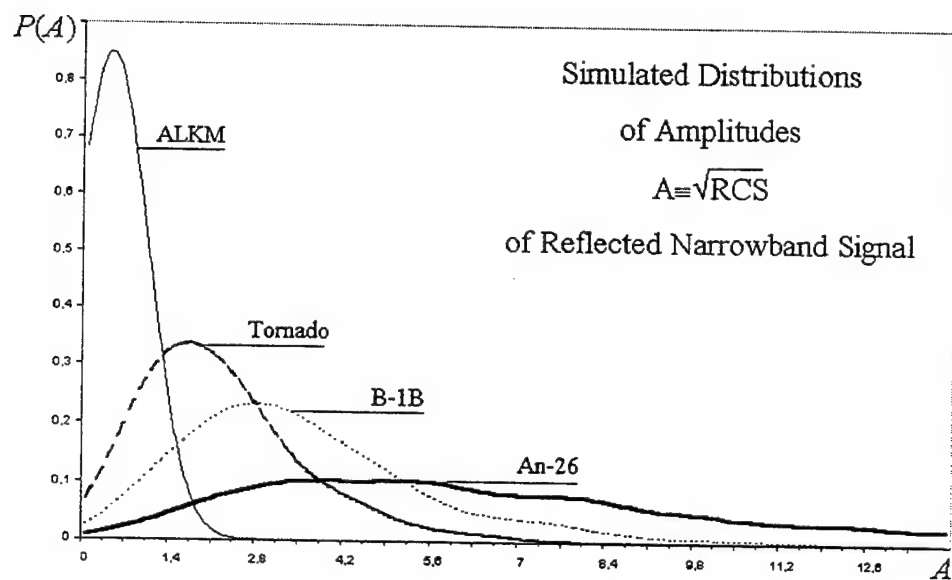
Range sampling step (m)

Sample number

☒ Tracking mode

Backscattered signal calculation progress

Fig. 4



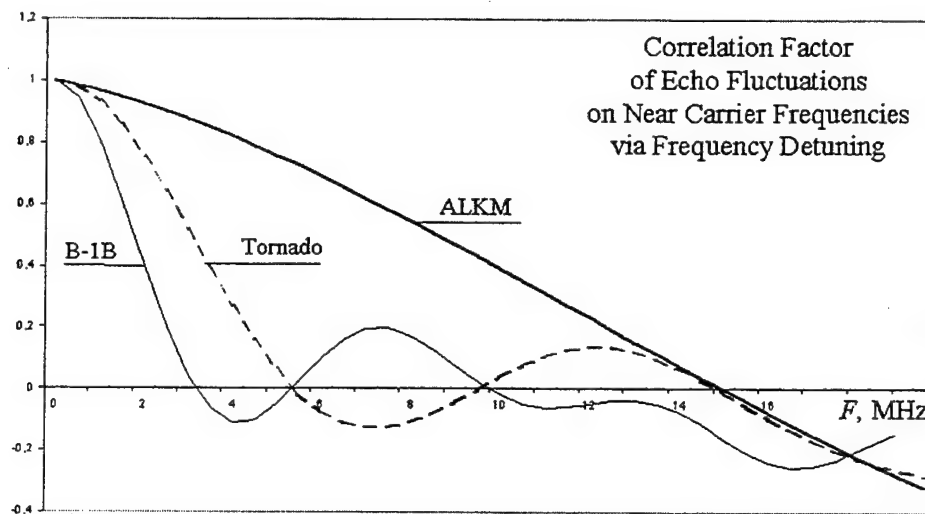


Fig. 7

Simulated Range Profiles for:
Bandwidth $B=80$ MHz; Wavelength $\lambda=10$ cm; Aspect Angle $\alpha \approx 10^\circ$.

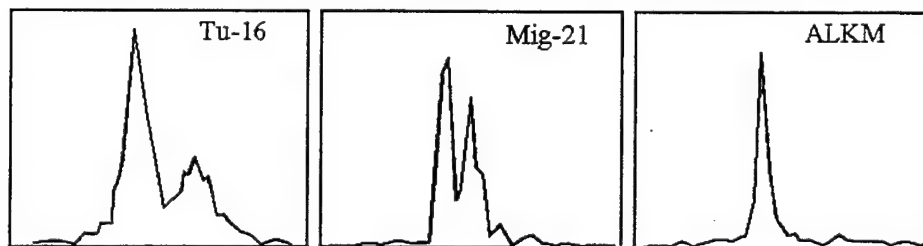


Fig. 8

Simulated Range-Frequency Image of An-26

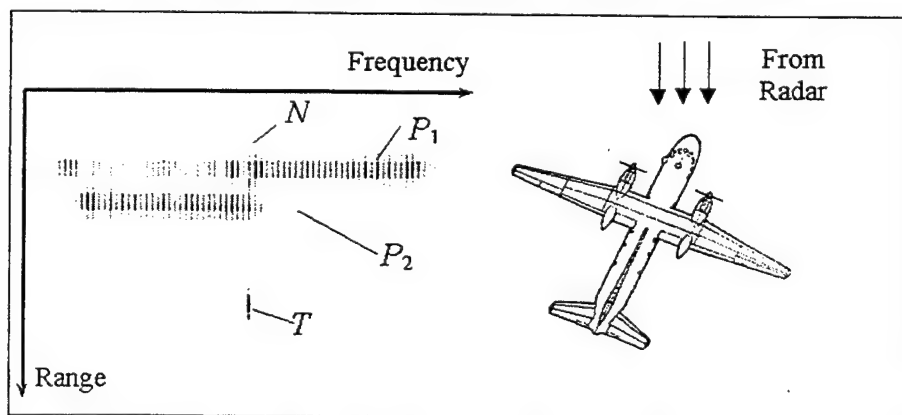


Fig. 9.

Simulated Range-Azimuth Image of B-52 Plane

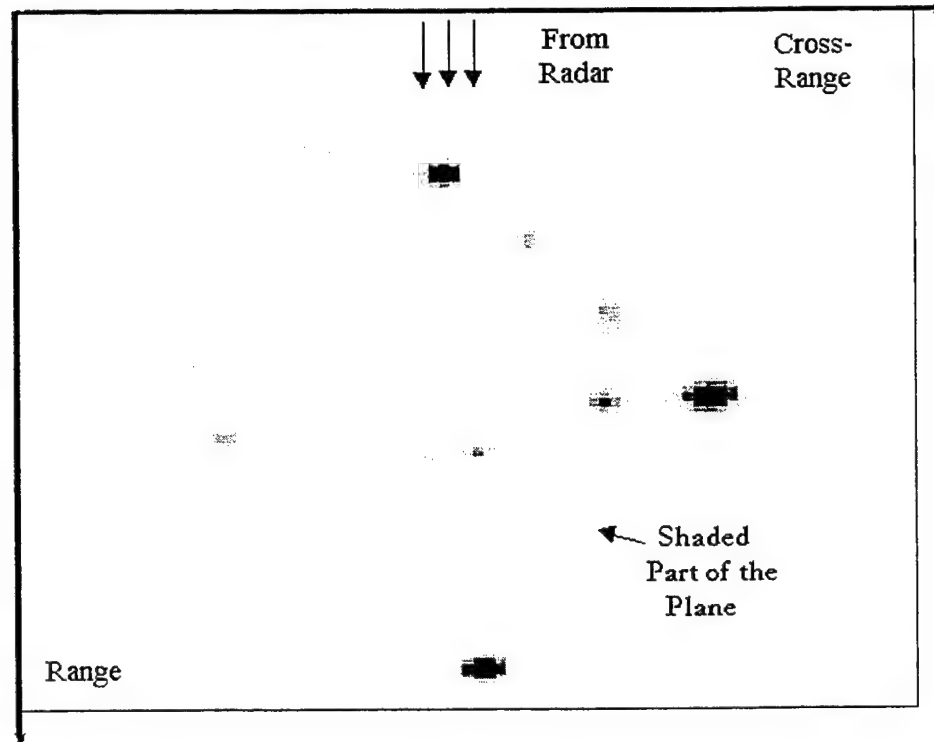


Fig. 10.

Simulated Range Profiles ($B=80$ MHz, $\lambda=10$ cm) for Aspect Angles α , $\alpha+0,1^\circ$ and $\alpha+0,2^\circ$.

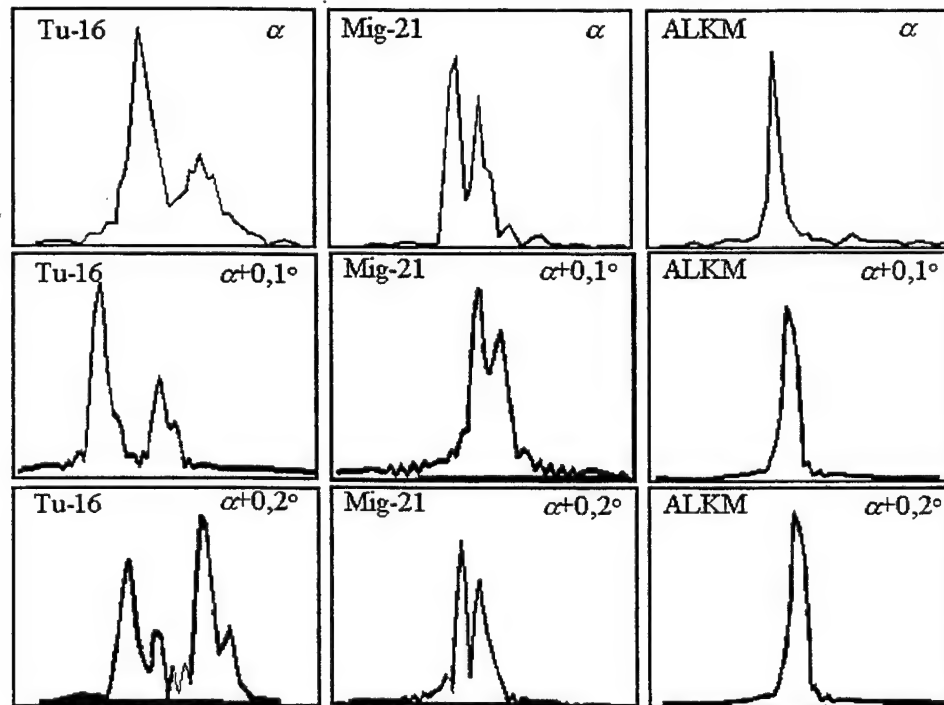


Fig. 11

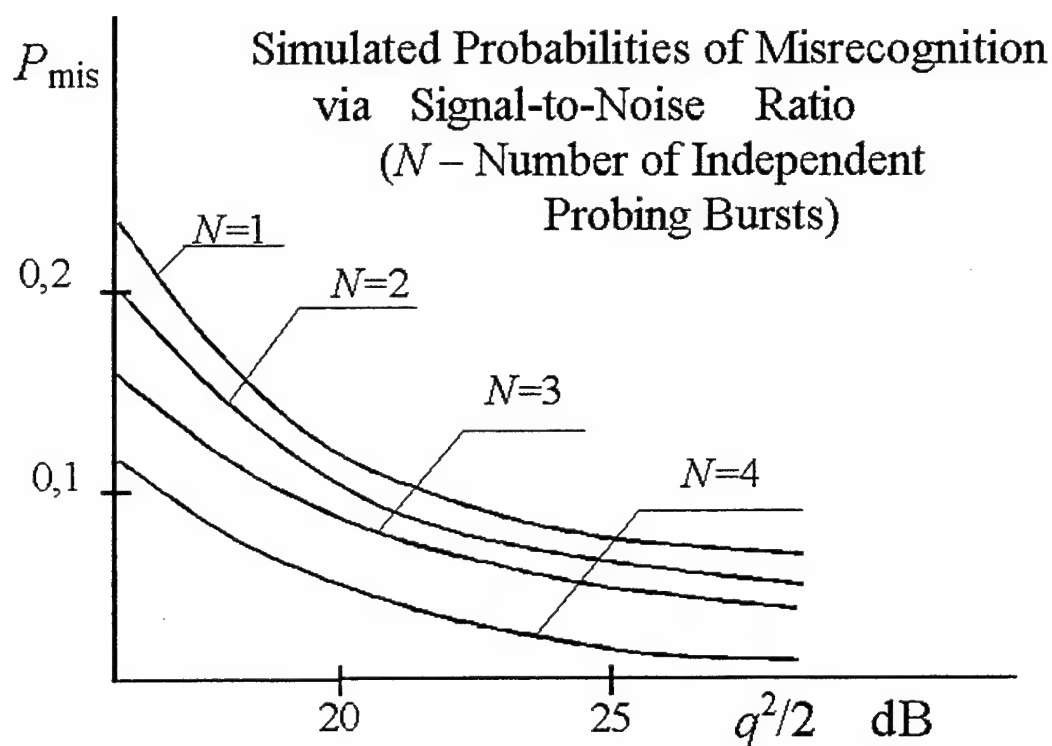


Fig. 12

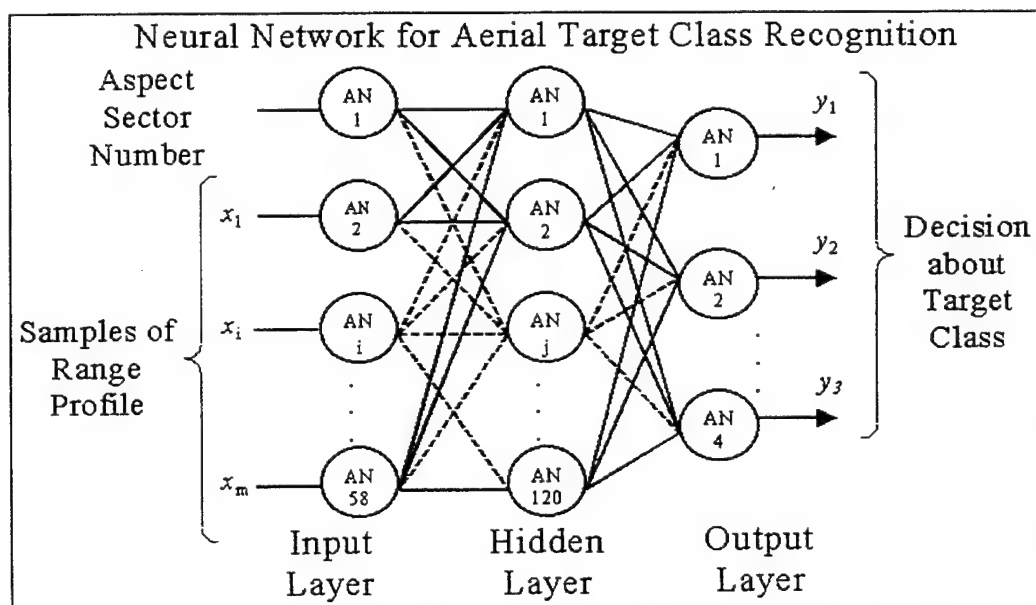


Fig. 13

Example of Neural Network "Windows"

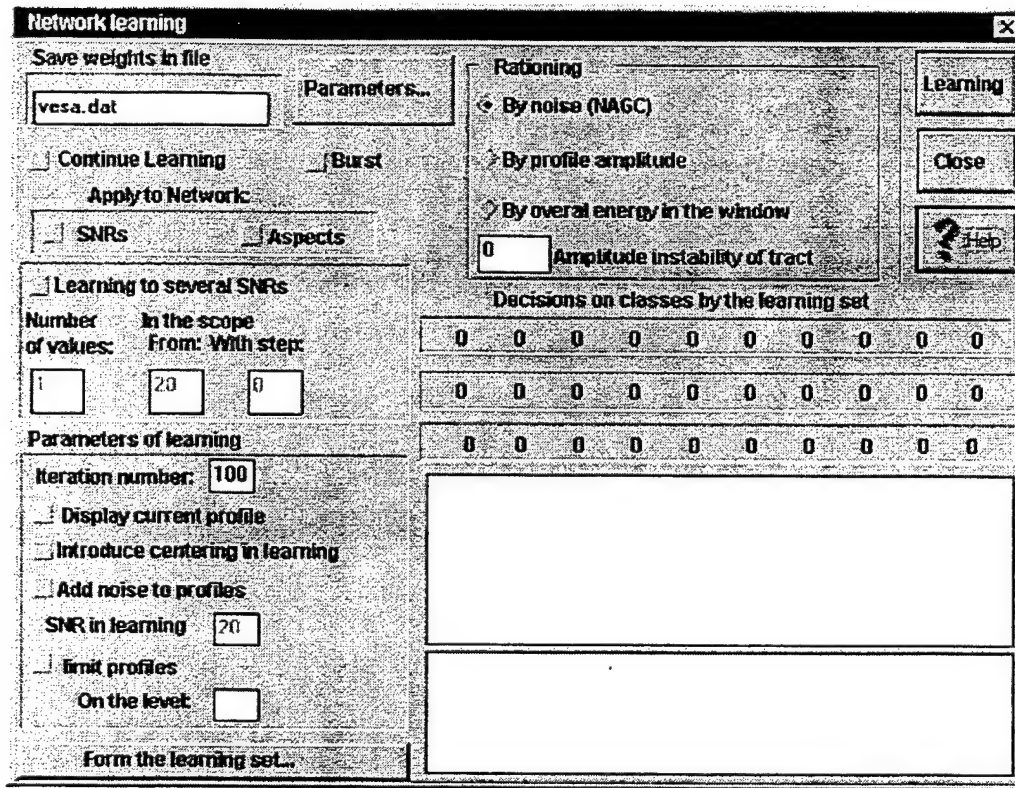


Fig. 14

Principle of Transverse Wind Gusts (WG) and Target Yaws (TY) Simulating

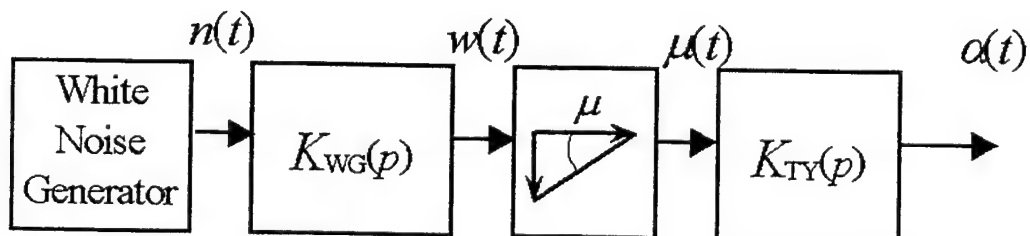
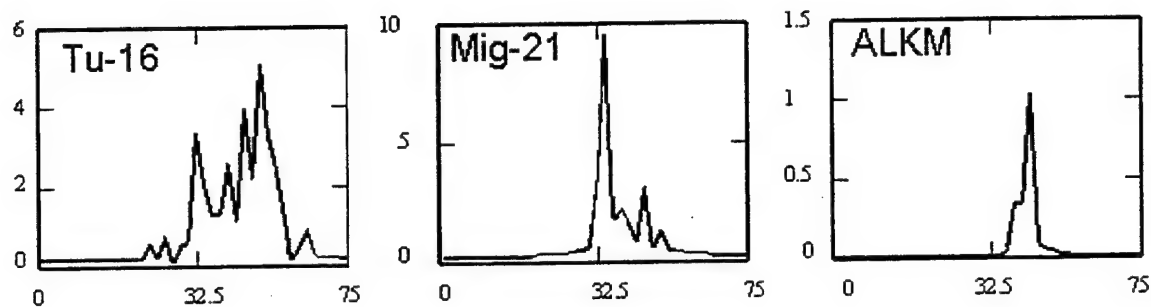


Fig. 15

Simulated Range Profiles for the Low Step-Frequency Signal
($T_s=60$ ms, $B=80$ MHz)

In Calm Weather, $H=10$ km



In Storm Weather, $H=1$ km

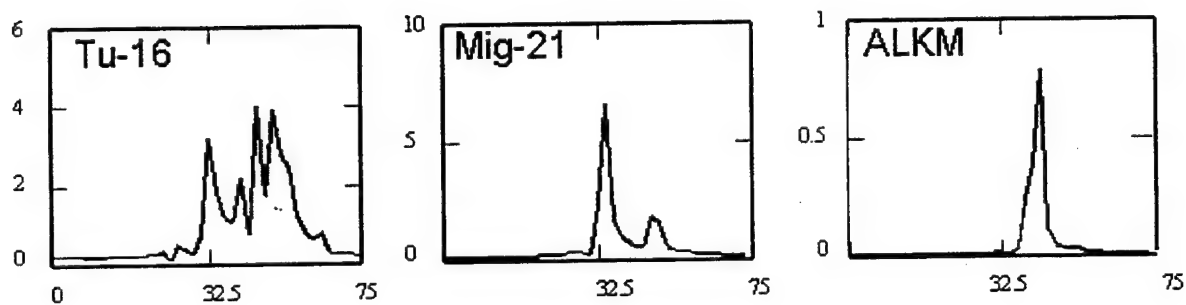


Fig. 16

RADAR TRACING OF STEALTH TARGETS IN THE BACKGROUND OF INTENSIVE MULTIPLE JAMMING

Y.N.Sedyhev

Kharkov Military University

Sq.Svobody, 6. 310043 Kharkov. Ukrain tel/fax: (38) 0572-430740

1. Abstract: The features of adaptive antenna array (AAA) applications active-passive bistatic radar (BSR) for target observation in the background of intensive multiple interference are considered. The concept of complete information interaction between BSR channels is proposed. It is shown that multiprocessor AAA with various types of adaptation are the key and common element of signal space-time processors. The approach to there problem solution is a combined usage in AAA of analog devices developed with the use of new low-noise wideband microwave technologies and digital systems of signal processing and data storage. As an example, the applicability of low-noise parametric circuits with correlation feedback for creating multi-channel AAA with signal processing at microwave frequency is discussed.

2. Introduction.

Possibilities of modern methods and means of electronic counter measures essentially limit the use of different-purpose radars reduction of due to expense of radar cross-section and application of high-intensity multiple interference. For ground-based radars the number of sectors of suppression increase due to re-reflections from dominating local subjects which are nearby receiving positions. Radar energy potential increase under these conditions is inefficient.

At the same time it is necessary to bear in mind that possibilities of jamming means are also limited by their energy resource and are localized in a small space volume as against radar observation zone. This circumstance, at least theoretically, shows that preservation of radar information capabilities can be achieved by increasing spatial selectivity and localization of interfering radiation sources.

Multisite radar systems with optimal processing of space-time fields generated by signals scattered on targets and produced by interfering radiation sources in the limits of their spatial coherence possess these properties [1,4,11]. In our opinion, the efficiency of using such systems under multiple interference conditions can be achieved by complex application of active and passive radar methods under strict accomplishment of principle of information

complementation and possibly complete use of energy of all radiation sources for obtaining coordinate information on targets and radiation sources (RS).

The information complementation principle assumes that radar observation zones of active and passive radar channels coincide, the character of space surveillance by antenna systems MSR is matched in the direction of probing signal radiation, and takes into account parallax in the directions of interfering signal arrival into receiving points. Probing signal parameters must stimulate jamming, spectrum width and action time of which would allow to obtain an acceptable location accuracy of their sources by goniometric-difference range-finder method with small measuring bases.

In this case spatial coherence in MSR is almost always guaranteed what gives the opportunity to detect covered interference and targets by the coherent compensation in main antenna beams [1].

Besides, under small bases the problems of data interchange between positions at all stages of signal and coordinate information processing, required for MSR functioning, are simplified [1,3].

3. The concept of constructing signal processors of bistatic radar with adaptive antenna arrays.

To define the requirements to active and passive radar channels of MSR it is expedient to consider characteristic features of radar observation in bistatic radar (BSR) consisting of two active radar with independent space survey in the plane of azimuth (Θ) and range (R) and independent reception of echo signals (Fig.1). In effective optimal aperture signal processing in AAA of each radar there is no influence of interfering signal reception over sidelobes and after combining target information radar observation capabilities are limited only by the regions of intersection of each active radar suppression sectors. The number of such regions is m_i^2 (m_i is the number of interference sources (IS)) and under multiple interference conditions it reduces an observation area. For unambiguous determination of RS coordinates it is necessary to measure the difference times of arrival of interfering signals from non-coordinated sources to reception points by base-correlation method $\Delta\tau_i$ (range difference ΔR_i) for which it is necessary at the opposite points of BSR to introduce an additional receiving system and to ensure signal interchange for correlation coherent processing in each radar. Fig.1 also shows that the problem of interference high suppression in main beam of each radar has solution under angular selection of each IS and simultaneous observation of it by specially selected beams of BSR adaptive antennas. It is evident that coherent interference compensation in main beam requires multichannel coherent signal exchange between receiving points. However its application solves the problem of covered target detection under multiple interference and, in addition, offers scope for "quiet" (secret) observation of targets in electromagnetic fields of any radiation sources [1].

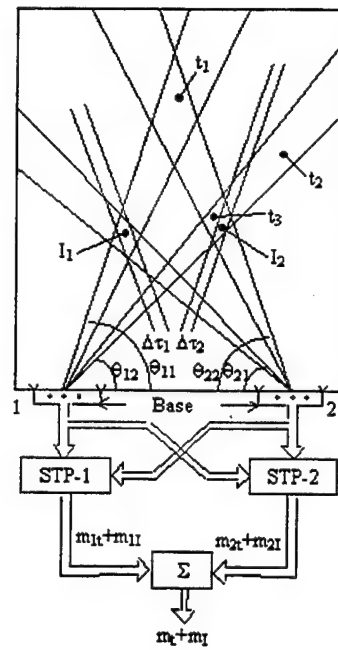


Fig. 1. Coverage sector of BSR with space coherence.

I – interferences; t – targets.

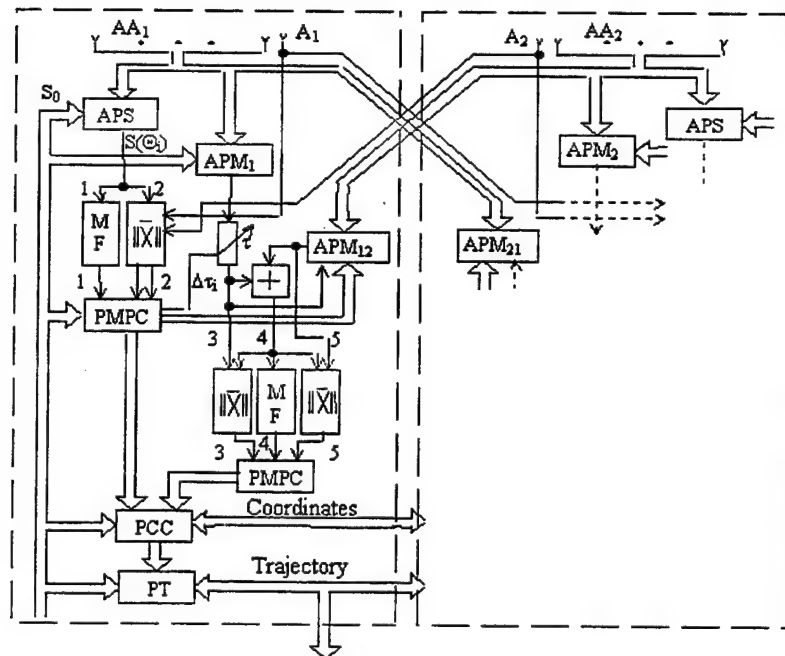


Fig. 2. Concept of information interaction of BSR channels with AAA in reception point.

APM – adaptive processor of the mainlobe; APS – adaptive processor of the sidelobes; MF – matched filter; PMPC – Processor of Measured Parameter Calculation; PCC – Processor of Coordinate Calculation; PT – Processor of Trajectory; $\|X\|$ – Matrix Correlator;

The presented justification is based on our knowledge in the field of theory and technology of multisite radar systems, adaptive antenna arrays [1-14]. It enables to represent the structural scheme of space-time processing processors of BSR with AAAs and to define peculiarities of data exchange between processors of the three information channels inside each radar and between them (Fig.2).

The main and key processor elements are adaptive antenna arrays with number of channels N which is more than the number of interference sources m_i ($N > m$). Additional weakly directed reference signal antennas A_1, A_2 ensure functioning passive location channels with matched space survey by each BSR. Estimates of primary measurement of azimuth Θ and difference in signal arrival times $\Delta\tau_i$ for each interference source ($\Theta_i, \Delta\tau_i$) are the original ones for measuring co-ordinates RS_i and formation of the reference signal in the third channel, the one of coherent compensation of spatially selected interference in the main beam with the help of processor APM_1 . For this, the vector of beam control $S(\Theta_{i1})$ in processor APM_1 and vector $S(\Theta_{i2})$ in processor APM_{12} are being formed.

The interference source signals received by antennas AA_1, AA_2 and adjusted in time ensure self-focusing AA_2 at their processing in processor APM_{12} (Fig.2).

Here echo signal of the covered target in the main beam acquires an additional time delay what is necessary to take into account when estimating coordinates and identifying targets.

Finally, the signals of selected source with known coordinates in reference to covered target can be considered as the probing ones and differences in time of signal arrival to reception points and in sum

Doppler shift for coordinate measurement by sum-goniometric method can be used. For this purpose into the third channel circuit matrix correlation filter processor intended to serve for measuring bases IS_i-AA_1, IS_i-AA_2 , are to be introduced. The proposed concept of interaction of three BSR information channels was verified experimentally at the model with the use of 8-channel AAA of gradient type and matrix correlation measurers for noise signal delays ensured signal processors with spectrum width up to 20 MHz and coherent processing time up to 10^{-3} s. As compared to Fig.2, the model scheme is simplified at the cost of time division of operation modes of the two AAA adaptive processors. Coherent signal data exchange at the base up to 1000 m occurred over cable and optic-fiber communication lines. Radiators simulating echo signals and interference were placed fixedly in a far zone of receiving antennas.

The displays with direction finding characteristics of non-adaptive AA and AAA are shown in Fig.3 (a, b, c).

AAA responses under the action of one, two and three interference sources with interference/noise ratio in a channel 15-20 dB illustrate the high quality of angular selection and the opportunity of unambiguous estimation of IS signal arrival direction. Fig.3 (d - l) illustrates the results of signal and

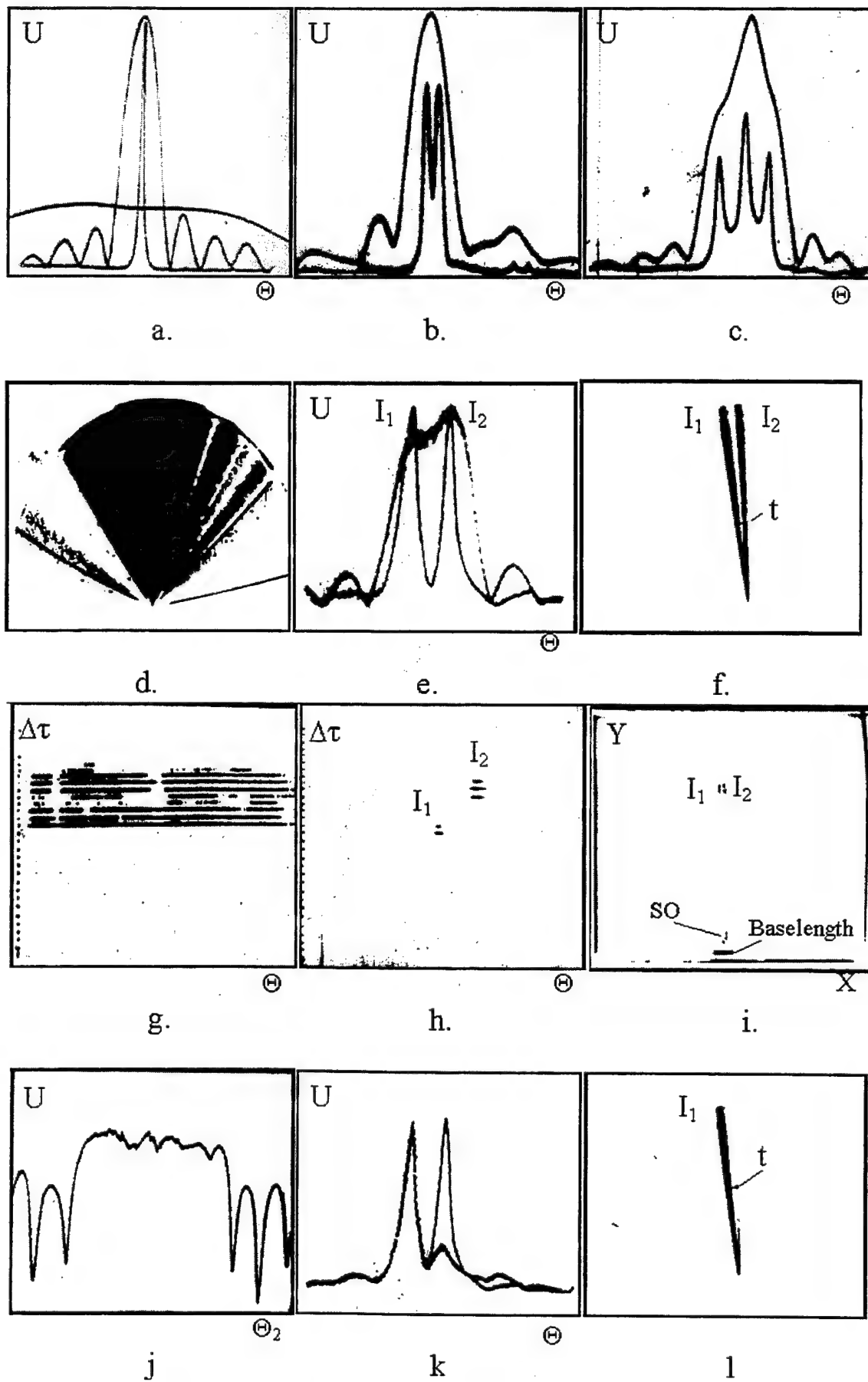


Fig.3. Interaction information channels of BSR with AAA.

interference processing of BSR information channels. In Fig.3 (d, e, f) the efficiency of echo-channel interference protection under the action of two ISs with angular separation close to AA beam width (echo-signal is observed between bearings at IS, , I_i are interference sources, t is the target (Fig.3 f)) is shown. Fig.3 (g, h, i) represents the functioning of passive radar channel with AAA in the same interference situation for non-adaptive AA and AAA. The use of AAA in passive channel allows more accurate combined estimation both of angular position and delay time of selected IS (Fig.3 h) and obtaining complete coordinate information at one measuring base (Fig.3 i)(display scale is determined by the baselength, SO is clutter from the surface objects).

The introduction of measured parameters Θ_i , $\Delta\tau_i$ into devices of forming reference signals ensuring self-focusing of AAA of the second receiving point (Fig.3 g, k) permits to detect the target covered by interference in the main beam (Fig.3 l). The presented investigation results indicate the perspectivity of proposed principles of constructing BSR (MSR) on the basis of interaction between information channel signal processors and AAA. However, the complete technical reliability under multiple interference conditions requires the development of new lines of investigations and technological principles of constructing AAA multichannel processors.

One of such directions combines the advantages of analog low-noise wideband microwave devices with the possibilities of modern microprocessor technology for constructing AAA with signal processing at microwave frequency.

4. AAA Adaptation method in AAA for microwave signal processing

For the last forty years the works on the theory development and practical application of adaptive arrays and antennas have been going on [6,7,8,11]. Optimal processing of signals against the background of a stationary noise produced by non-correlated point sources of active interference with the accuracy up to α scale factor corresponds to a multichannel weight processing according to the Wiener filter algorithm:

$$W = \alpha R^{-1} \cdot S_0, \quad (1)$$

where W is the weight factor vector; S_0 is the space vector of an expected signal in the antenna aperture providing the main beam formation; R^{-1} is the inverse correlation matrix of interference and internal noise received in N partial receiving channels with dimensions of $N \times N$.

Signal weight summation at $N > M$ (where M is the number of interference sources) (1) maximizes the signal/ interference plus noise ratio (SNIR) minimizing the signal loss in the main beam and forming reception zeros in the directions to the interference sources by the coherent compensation of their signals.

$$q_0 = S_0^* \cdot W = S_0^* \cdot R^{-1} S_0, \quad (2)$$

where $*$ is the Hermitian transpose. For AAA with identical channels the module of the complex coefficients of the interchannel correlation outside the main diagonal R^{-1} depends on the total interference power/noise ratio and can be obtained like follows as

$$\rho = |\dot{\rho}| = \sum_{i=1}^m h_i / \sum_{i=1}^m h_i + 1, \quad h_i = \frac{P_i}{P_n} = \frac{\sigma_i^2}{\sigma_n^2}, \quad (3)$$

where σ_i^2, σ_n^2 are the variances of the interference and noise, respectively.

For a quantitative estimation of the weight summation results we use the methods of reducing Hermitian matrices to the diagonal form through non-multiple eigenvalues and projection matrices [6,7].

$$\begin{aligned} R = \sum_{i=1}^{m+1} \lambda_i P_i; \quad P_i \cdot P_k &= \begin{cases} 1 & i=k, \\ 0 & i \neq k; \end{cases} \quad f(R) = \sum_{i=1}^{m+1} f(\lambda_i) P_i, \\ \lambda_1 \geq \lambda_2 \dots \lambda_m, \quad \lambda_{m+1} &= \lambda_{m+2} = \dots \lambda_N. \\ \sum_{i=1}^N \lambda_i &= N, \quad m+1 = \mu.. \end{aligned} \quad (4)$$

Thus, the relation (2) is transformed to the following form:

$$q_0 = \sum_{i=1}^{m+1} \frac{1}{\lambda_i} S_0^* P_i S_0. \quad (5)$$

From (4) and (5) it follows that if $m=1$ and the array main beam position $S(\Theta)$ is changed, the value q_0 can vary over a wide range from

$$q_{0\max} = \frac{N}{1-\rho} \quad \text{to} \quad q_{0\min} = \frac{N}{1-\rho + N_p} \approx 1,$$

at Rayleigh resolution of m ($N > m$) sources of equal power

$$q_{0\min} = \frac{N}{1-\rho + N_p / m} \approx m,$$

and, therefore, a potential gain of aperture processing varies over a range of

$$\frac{q_{0\max}}{q_{0\min}} = \frac{N}{m(1-\rho)}. \quad (6)$$

From (6) it follows that the efficiency of broadband multiple interference aperture processing depends on receiving channel characteristic identity ($\lambda_N = 1-\rho$ determines limiting possibilities of the coherent compensation) as well as on receiving channel redundancy in relation to the number of interference sources.

The degree of the modulus of the correlation coefficient approximation in real receiving channels, including array line-source feed, to (3) is criterion of integral estimation of the adaptation algorithm efficiency and technological perfection of processing equipment.

The quality of aperture processing is defined by the accuracy of setting the amplitude-phase distribution (APD) reduced to the antenna aperture. At the same time, the most of the known adaptation methods and devices provide weight summation at intermediate frequency or in digital processors after analog-to-digital conversion of signals at the outputs of multistage receiver's [7]. In evaluating channel identity it is necessary to account both external and internal statistics of the antenna system. The identity difficulties increase with strengthening the requirements to a dynamic range of input signals and their relative broadbandness $\Delta f_s/f_0$. As applied to the use of digital methods it takes the form of the capacity of representing signals in the digital form and digital processor rapidity.

Besides, it is necessary to take into account additional quantization noise, which unlike internal noise cannot be considered as non-correlated one. It influences both the value of SNR and the accuracy of the weight vector calculation.

To estimate the advantage in (6) it is necessary to take into account that an equivalent value of correlation coefficient modulus decreases due to non-identities of non-linearities of the amplitude (ρ_{\approx}), amplitude-phase and phase-frequency ($\rho_{\Delta(\alpha,\varphi)}$) responses of receiving channels, differences of signal interchannel delay \hat{R}^{-1} up to weight adder ($p_{\Delta\tau}$). Besides, errors in estimates of the inverse correlation matrix \hat{R}^{-1} or the weight vector \hat{W} in (1) also result in reduction of $\hat{\rho}$ proportional to $\rho_{\Delta W}$. Thus,

$$\hat{\rho} = \rho \cdot \rho_{\approx} \cdot \rho_{(\alpha,\varphi)} \cdot \rho_{\Delta\tau} \cdot \rho_{\Delta W} < \rho. \quad (7)$$

From (7) it follows that for obtaining potential gains of the aperture optimum processing the operation of interference coherent compensation should be carried out in analog form in a broadband low-noise coordinated path at low signal level. In this case

$$\rho_{\Delta\alpha}; \rho_{(\alpha,\varphi)}; \rho_{\Delta\tau} \approx 1; \quad \hat{\rho} = \rho \cdot \rho_{\Delta W}. \quad (8)$$

For quantitative estimates at arbitrary arrangement of interference sources and using the estimated values of \hat{R} and \hat{W} while processing we can use the following relations for SNIR at the processor output [11,14].

$$\hat{q}(\Theta) = \frac{(S_{\Theta}^* \hat{R}^{-1} S_{\Theta})^2}{S_{\Theta}^* \hat{R}^{-1} R R^{-1} S_{\Theta}} = \frac{(S_{\Theta}^* \hat{W})^2}{W^* R W}, \quad (9)$$

or, in accordance with (4)

$$\hat{q}(\Theta) = \left(\sum_{i=1}^m \frac{1}{\lambda_i} S_{\Theta}^* P_i S \right)^2 / \left(\sum_{i=1}^m \frac{\lambda_i}{\lambda_i} S_{\Theta}^* P_i S \right). \quad (10)$$

It is obvious that the relation \hat{q}/q_0 defines the total losses of processing.

$$K_1(\Theta) = \frac{\hat{q}}{q_0} \leq 1.$$

In the absence of adaptation $\hat{R} \rightarrow I$ and SNIR at the output

$$q_{na}(\Theta) = \frac{N^2}{S_{\Theta}^* R S_{\Theta}}. \quad (11)$$

and the relation $q(\Theta)/q_{na}(\Theta)$ defines a relative advantage if using non-adaptive PAA. Thus, its directivity pattern is determined by the Fourier transform for $W(\Theta_i)$

$$q(\Theta) = \dot{S}(\Theta) W(\Theta_i). \quad (12)$$

At all variety of adaptive AAA algorithms two basic methods of the weight vector calculation are used:

- the method of direct determination of the correlation matrix by signal samples at the output of N-channel receiver with subsequent calculation of the weight vector in the digital form [6,7,9];
- the gradient method with N-channel negative correlation feedback (CNF) minimizing the noise at the output and forming in the stationary mode the vector of the form [6,7]:

$$w = (I + \beta R)^{-1} S \approx \frac{1}{1 + \beta} R^{-1} S; \quad \beta \gg 1,$$

where β is the amplification factor in a feedback circuit; I is the identity matrix.

Both the direct and gradient methods require much time for estimates of weight vector and large amplitudes of signals even if at one of correlator inputs. The direct method is practically non-realized at $N > 2$ when using analog technologies, while the gradient methods admit both analog and digital realizations [11].

The advantage of the direct method is the opportunity of producing optimum amplitude-phase distributions in AAA aperture for signal reception from any direction in a scanning sector. However, they do not work in the real time. The period of data updating affects essentially the errors of the weight vector calculation, which depend on the time of interference stationary and reduce $\rho_{\Delta W}$. In the practical application of direct methods it is necessary to take into account substantial computational expenses.

The process of adaptation in gradient methods goes in real time and provides high calculation accuracy of the weight vector, though for one direction only; transients limit the speed of space scanning in a multichannel system with CNF. Besides, in the digital calculation of the weight vector and coherent weight summation the broadbandness is limited by the internal performance of digital elements. Therefore, in weight summation of analog signals at SHF it is proposed to search reasonable trade off in combinations of direct and gradient methods, optimizing their contribution to the accuracy of the weight vector calculation ($\rho_{\Delta \omega} \rightarrow 1$), stabilization and reduction of transient time by the long-duration storage and updating information on \hat{R}^{-1} or $\hat{W}(\Theta_i)$ for the pre-adaptation and fast correction of the weight vector for the direction of a useful signal arrival $S(\Theta_i)$.

The fulfillment of the listed conditions results in AAA structure which, to our mind, is versatile for a variety of applications and is given in Fig.4.

In the circuit of a linear AAA from the outputs of N -channel low-noise amplifier (LNA) with a pre-selector limiting a processing band, the low-level signals are applied to a weight adder. Through N -channel amplifiers-converters with ANGK the same signals are applied to multipliers of a multi channel correlators of two processors: of direct calculation of interference matrix and gradient one.

Their dimensions are shown on the vector signal arrows. The vector sum of the weight vector estimates of two processors \hat{W}_d and \hat{W}_g providing more accurate amplitude-phase distribution $\hat{W}(\Theta_i)$ corrected by the gradient processor in the real time is applied to the weight adder control inputs.

Thus, the discrepancies of calculating the weight vector $\hat{W}_d(\Theta_i)$ appearing due to finite time of action and non-stationary of interference are removed and the equalization of levels of various intensity interference provides a essential reduction of the transient time in a multichannel processor with CNF (Fig.5).

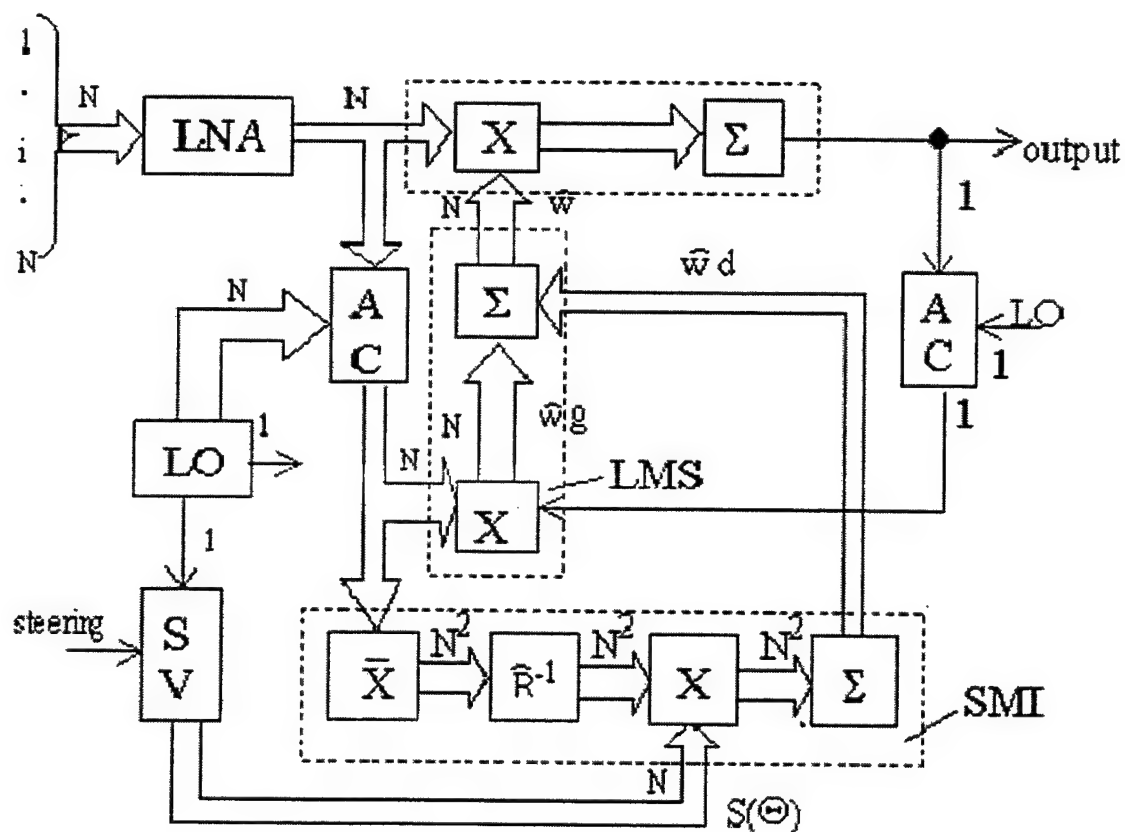


Fig. 4. Structural scheme of microwave weighting AAA signal processing.

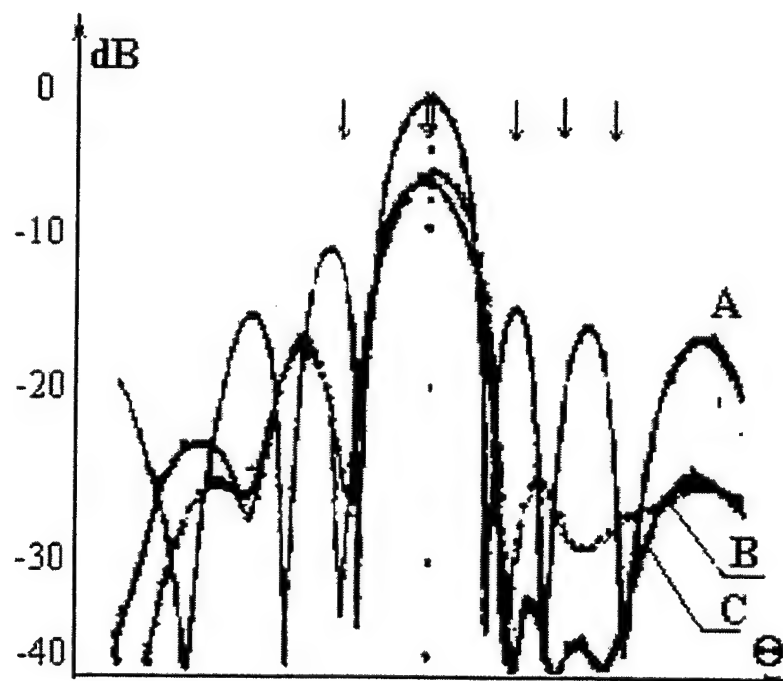


Fig. 5. Experimental patterns of 8-channel AAA.
(A-linear AA, B-SMI-method, C-SMI+LMS method)

It should be noted that when constructing multichannel adaptive PAA with relative broadbandness of up to 10% the redundancy of the number of summing channels has to be not less than 2-3. Gradient processor stability in a dynamic range is of special difficulty here. Its digital realization can require clock frequency of ADC (analog-to-digital converter) up to 0,5...1 GHz or division of total bandwidth into subchannels. The design of precision weight multipliers with low noise in various microwave ranges is not of less difficulty. However, the use of modern microwave technologies enables not only to solve these problems but also to provide the construction of steady-state analog multichannel gradient processors with the weight vector calculation at high frequency. It can be achieved by using the properties of coherent parametric circuits with correlation feedback at non-linear reactances in adaptive antenna arrays.

5. Application of gradient parametric processors

The block-diagram of parametric processor for coherent weight summation is shown in Fig.6.

The basis of each adaptation channel is a parametric non-regenerative converter (Fig.7). At one of the combination frequencies of converter (ω_0) a narrowband integrating filter is tuned. This provides a parametric connection only between correlated components of exciting signals in channels and the sum of signals, converted to the frequency of summation filter (ω_Σ) with the aid of the reference signal vector components at frequency (ω_0). Under the condition of smallness of the signals at the frequencies ω_0 and ω_Σ , $|U_s| \gg |U_0|$ and $\omega_s + \omega_\Sigma = \omega_0$, oscillations, proportional to interchannel correlation coefficients, i.e. the weight vector components, are excited in the narrow-band filter. Inverse conversion of these oscillations through a modulated reactance provides a closure of negative correlation feedback and interference coherent compensation in the filter F_Σ with the voltage differing from the initial oscillation by a factor of $(1-\beta\rho/(1+\beta))$.

Non-linear capacities of parametric diodes (Fig.6) are modulated by a signal set at the carrier frequency received by the array elements and amplified by a low-noise amplifier with AGCN to a desired level

$$\dot{U}_s^{(i)} = \sum_{k=1}^m \dot{U}_{sk} e^{j\varphi_k(i-1)} + U_{sn}, \quad (13)$$

which can be represented as the sum of correlated and non-correlated components

$$U_s^{(i)} = U_{s1}^{(i)} + U_{s2}^{(i)}. \quad (14)$$

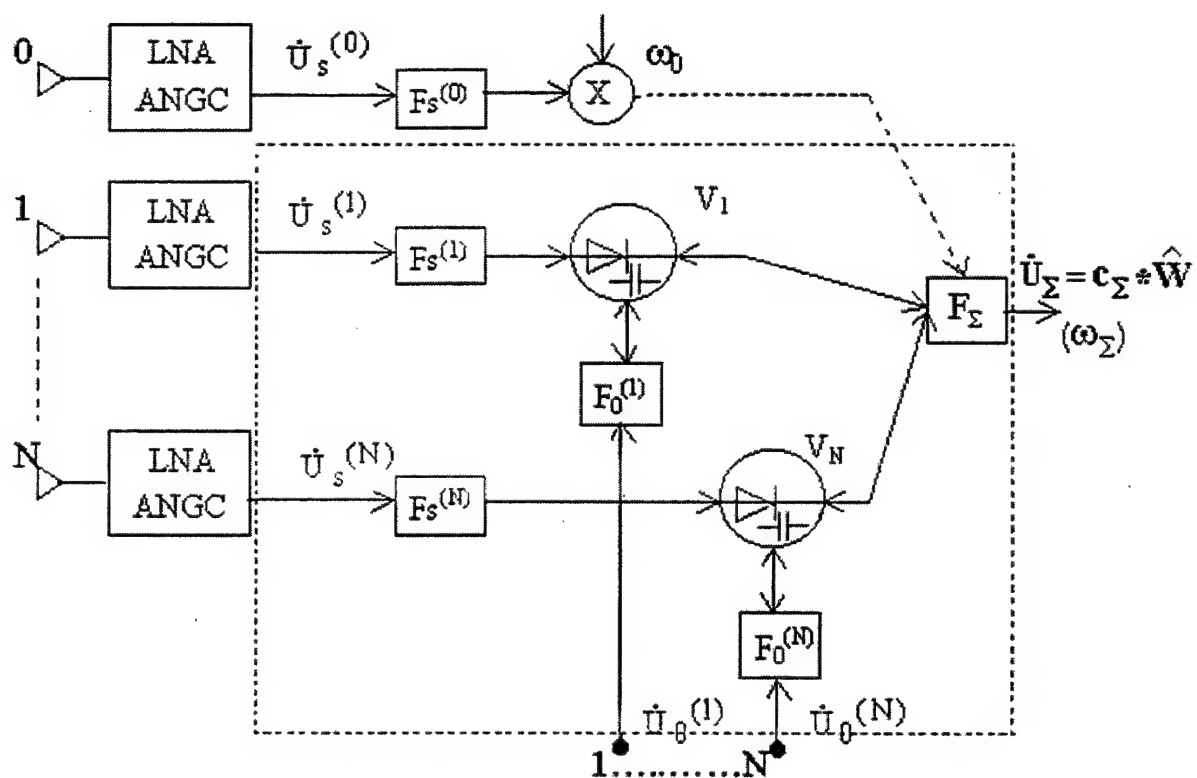


Fig. 6. Structural scheme of AAA with the adaptive parametric microwave processor.

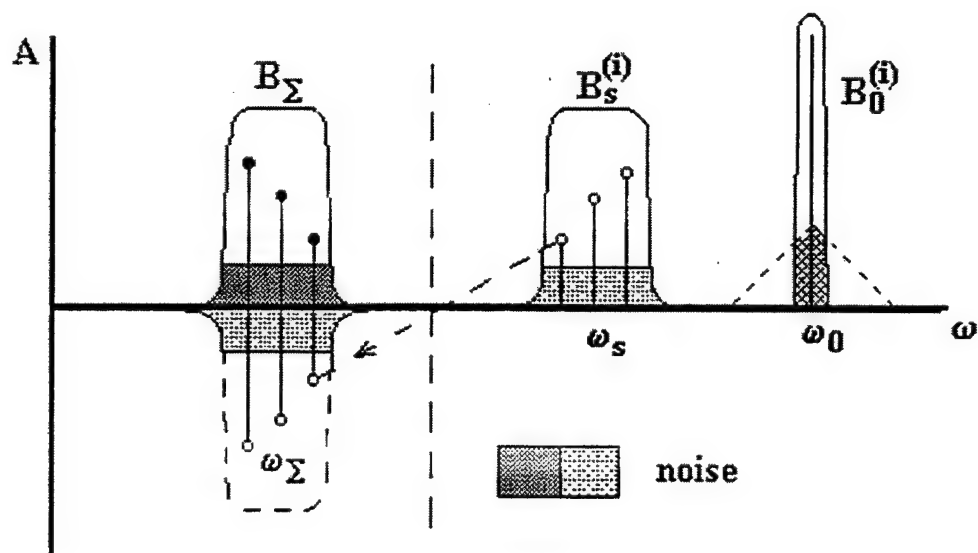


Fig. 7. Frequency diagram of the parametrical converter with a negative CFB.

Assuming that interference sources radiate Gaussian signals we suppose:

$$\overline{U_{s1}^* U_{s2}} = 0 \quad \overline{U_s^{(i)} U_s^{*(i)}} = \sigma_s^2, \quad \rho_{il}^2 = \frac{\overline{U_s^{(i)} U_s^{(l)}}}{\sigma_s^2}. \quad (15)$$

Correlation feedback availability enables to represent the i -th non-linear capacity of the circuit in terms of a superposition of a constant component and two variable components $\dot{C}_{11}^{(i)} = \alpha \dot{U}_{s1}^{(i)}$, $\dot{C}_{12}^{(i)} = \alpha \dot{U}_{s2}^{(i)}$, where α is the slope of varicap capacity change.

In this case the analysis of gradient processor characteristics reduces to the analysis of the linear multi port properties (Fig.8).

The scattering matrix S_s and the transfer operator T accounting for multi channel circuit linearity (coherence) can be obtained through its inverse normalized matrix of conductances Y_0 :

$$S_s = I - 2\eta' Y_0^{-1} \eta'', \quad (16)$$

$$T = I - S = 2\eta' Y_0^{-1} \eta'' = 2\eta' \frac{\|a_{ij}\|}{|Y_0|} \eta'.$$

Here, η', η'' are the diagonal matrices of conductance's raised to the power 1/2 correcting for the losses in passive circuits of reference signal sources at the frequency ω_0 and the load frequency ω_Σ ;

$\|a_{ij}\|$ is the matrix consisting of algebraic complements of transposed matrix Y_0 , $|Y_0|$ is the matrix Y_0 determinant, I is the identity matrix.

The matrix Y_0 in Fig.9 relates the correlated and non-correlated signal components in receiving channels and signals of reference signal and load ω_Σ . Since the coupling between frequency components through a narrow-band filter-integrator is possible only for correlated components, the normalized conductance matrix consists of four block matrices: two identity matrices at the principal diagonal (I_{N+1} и I_N) and coupling coefficient matrices Y_{12} , Y_{21} of dimensions $N*(N+1)$ and $(N+1)*N$, respectively.

If the signal from a separated channel is applied to the general adder then the total size I_{N+1} increases by one and becomes equal to $(2N+2)*(2N+2)$. In this case the reference signal has the form of $S_0 = (1, 0, 0 \dots 0)$ and AAA operates as an interference compensatory [11,12].

The rows $\{y_{11}^{(i)}\}_{N+1}$ in Y_{12} and the column $\{y_{11}^{*(i)}\}_{N+1}$ in Y_{21} ensure coherent summation of correlated signals at the frequency ω_Σ and diagonal coefficient matrices in blocks Y_{12} and Y_{21} take into account non-coherent summation of thermal noise, which is proportional to the components of the weight vector. The coefficients Y_{12} , Y_{21} for the equivalent circuit in Fig.8 have the following form:

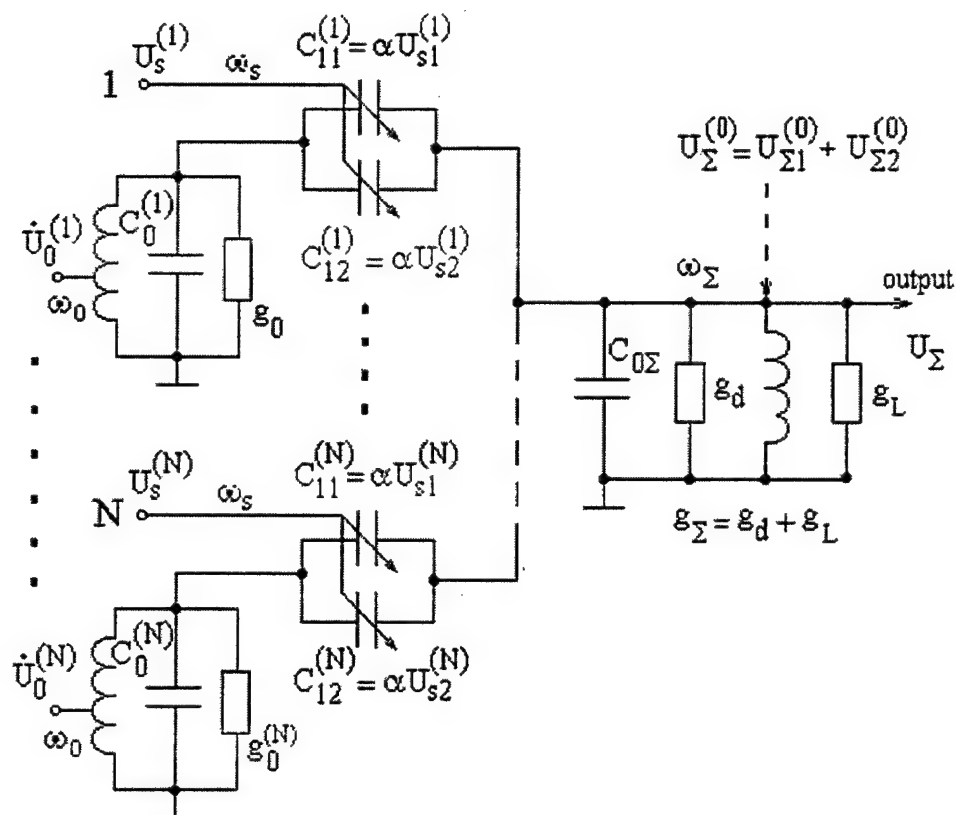


Fig. 8. Equivalent APP circuit.

	$U_{\Sigma 2}^{(0)}$	$U_{\Sigma 1}$	$U_{\Sigma 2}^{(1)}$	$U_{\Sigma 2}^{(2)}$	$U_{\Sigma 2}^{(N)}$	$U_0^{(1)}$	$U_0^{(2)}$	$U_0^{(N)}$	
$Y_0 =$	1	0	0	0	0	0	0
	0	1				$y_{11}^{(1)}$	$y_{11}^{(2)}$	$y_{11}^{(N)}$
ω_{Σ}			1			$y_{12}^{(1)}$	0	0
				1		0	$y_{12}^{(2)}$	0
	0			1	0		$y_{12}^{(N)}$
	0	$y_{21}^{*(1)}$	$y_{22}^{*(1)}$	0	1	0	0
ω_0		$y_{21}^{*(2)}$	0	$y_{22}^{*(2)}$		0	1	0
	0	$y_{21}^{*(N)}$	0	$y_{22}^{*(N)}$	0	0	1

Fig. 9. Normalized matrix of conductances.

$$y_{11}^{(i)} = \frac{j\omega_{\Sigma}\alpha\dot{U}_{s1}^{(i)}}{(g_0 * g_{\Sigma})^{1/2}}, \quad y_{12}^{(i)} = \frac{j\omega_{\Sigma}\alpha\dot{U}_{s2}^{(i)}}{(g_0 * g_{\Sigma})^{1/2}},$$

$$y_{11}^{*(i)} = \frac{j\omega_0\alpha\dot{U}_{s1}^{(i)}}{(g_0 * g_{\Sigma})^{1/2}}, \quad y_{12}^{*(i)} = \frac{j\omega_0\alpha\dot{U}_{s2}^{(i)}}{(g_0 * g_{\Sigma})^{1/2}},$$

where g_0, g_{Σ} are resonance conductance of summing (ω_{Σ}) and integrating filters, respectively.

Using the rules of the block matrix determinant calculation it is possible to find the determinant, eigenvalues of matrix Y_0 and the transfer operator in a stationary mode providing for averaging in integrating filters for identical channels:

$$\det|Y_0| = I_{N+1} |I_N - \overline{Y_{12} Y_{21}}| = |I_N + \|\beta \cdot \dot{\rho}_{ij}\||. \quad (18)$$

$$\text{где } \beta = \frac{\omega_0 \omega_{\Sigma} \alpha^2 \sigma_s^2}{g_0 g_{\Sigma}};$$

$$\text{where } \dot{\rho}_{i,j} = \dot{\rho}^*_{i,j} = \left(\frac{U_{s1}^{(i)} U_{s1}^{*(j)}}{\sigma_s^2} \right)^{1/2}, \quad (19)$$

$$i, j = 1 \dots N.$$

$$|\dot{Y}_0 - I_{2N+1} \lambda| = |I_{N+1} (1 - \lambda)| * |I_N (1 - \lambda) + \|\beta \cdot \dot{\rho}_{ij}\|| = 0. \quad (20)$$

From (18,20) it is seen that the properties of the multichannel parametric circuit under consideration is determined by the correlation matrix of input signals at the input and by the feedback depth. The normalized conductance matrix Y_0 has $N+1$ multiple roots $\lambda=1$ and, therefore, its rank is determined by the rank of the correlation matrix.

The transfer operator in a stationary mode to within the coefficients $1/1+\beta$ and the losses in circuits of an exciting signal source and a load is determined by the estimated value of the inverse correlation matrix

$$T = \eta' \hat{R}^{-1} \eta'' = \sum_{k=1}^m \frac{1}{\lambda_k} \eta' P_k \eta''. \quad (21)$$

Here its minimum eigenvalue is

$$\lambda_{\mu} = \lambda_N = 1 - \frac{\beta}{1+\beta} \rho \quad (m < N).$$

Thus, under the action of the reference signal $S_0(\Theta)$ for reflected wave in a load circuit at the frequency ω_{Σ} $B=TS_0$. The power transfer coefficient in view

of (17), (19) and the frequency scale factor $\sqrt{\omega_\Sigma/\omega_0}$, when converting the reference signal U_0 to the frequency ω_Σ in parametric converter, is equal to

$$K_{p, \text{opt}} = \frac{B^* B}{S_0^* S_0} = \frac{1}{N} \cdot \frac{\omega_\Sigma}{\omega_0} \cdot \frac{\beta^2}{(1+\beta)^2} \cdot \left[\sum_{k=1}^m \hat{\lambda}_k^{-1} S_0^* \eta' P_k \eta'' S_0 \right]^2. \quad (22)$$

In the absence of interference $\hat{\lambda}_N = 1 + 1/\beta$ and

$$K_{p, \text{opt}} = N \cdot \frac{\omega_\Sigma}{\omega_0} \cdot \frac{\beta^2}{(1+\beta)^2} \cdot \eta'_0 \cdot \eta''_\Sigma, \quad (23)$$

$$\eta'_0 \cdot \eta''_\Sigma = \left[S_0^* \eta' P_k \eta'' S_0 \right]^2,$$

which corresponds to the coefficient of internal noise power transfer in the N-channels non-regenerative frequency converter accounting for losses in filters. The relation's (22) within to a constant multiplier coincides with the numerator of expression (10) and at $\beta \rightarrow \infty$ with the relations (1), which points to an adequacy of the multi channel parametric circuit and the gradient adaptive aperture-processing algorithm.

6. Estimation of the influence of the correlation feedback depth on losses of the aperture processing

The losses in signal processing at the output of AAA (Fig.6) at the finite value of β can be obtained from (1), (9) and (10):

$$K_L = \frac{\bar{q}}{q_0} = \frac{(S_0^* \hat{R}^{-1} S_0)^2}{(S_0^* \hat{R} R S_0)(S_0^* R^{-1} S_0)} = \frac{\left(\sum_{k=1}^m \frac{1}{\hat{\lambda}_i} S_0^* P_i S_0 \right)^2}{\left(\sum_{k=1}^m \frac{\lambda_i}{\hat{\lambda}^2} S_0^* P_i S_0 \right) \left(\sum_{k=1}^m \frac{1}{\lambda_i} S_0^* P_i S_0 \right)}. \quad (24)$$

For one interference source from (4) is follows:

$$\lambda_1 = 1 - \rho + N\rho; \quad \lambda_N = 1 - \rho; \quad \hat{\lambda}_1 = \frac{1 + \beta \lambda_1}{1 + \beta};$$

$$\hat{\lambda}_N = \frac{1 + \beta \lambda_N}{1 + \beta};$$

$$S_0^* P_1 S = N F^2(\varphi - \varphi_0); \quad S_0^* P_N S = N [I - F^2(\varphi - \varphi_0)];$$

$$\text{where } F^2(\varphi - \varphi_0) = \left[\frac{\sin \frac{N}{2}(\psi_0 - \psi)}{N \sin \frac{1}{2}(\psi_0 - \psi)} \right]^2$$

is the value of normalized AAA pattern depending on angular distinctions in directions of signal and interference arrived. Then the value of K_L is equal to:

$$K_L = \frac{[\hat{\lambda}_N F_{01}^2 + \hat{\lambda}_1 (1 - F_{01}^2)]^2}{[\hat{\lambda}_N^2 \lambda_1 F_{01}^2 + \hat{\lambda}_1^2 \lambda_N (1 - F_{01}^2)]^2} \cdot \frac{\lambda_1 \lambda_N}{[\lambda_N F_{01}^2 + \lambda_1 (1 - F_{01}^2)]} \leq 1. \quad (25)$$

Since $\lambda_N \ll \lambda_1$, $\hat{\lambda}_1 = \frac{1 + \beta \lambda_1}{1 + \beta}$; it can be shown that the value K_L is minimum (losses are maximum) at $F_{01}^2 = 0.5$, which corresponds to the action of the interference coming from the direction corresponding to the half-width of AAA pattern. In this case

$$K_{L \min} = \frac{N \beta^2 (1 - \rho)}{1 + N \beta^2 (1 - \rho)}. \quad (26)$$

For m resolvable radiation sources

$$K_{L \min} = \frac{N \beta^2 (1 - \rho)}{m + N \beta^2 (1 - \rho)} = \frac{\frac{N}{m} \beta^2 (1 - \rho)}{1 + \frac{N}{m} \beta^2 (1 - \rho)}. \quad (27)$$

From (27) we can make an important conclusion that losses of the weight vector estimation because of the CNF finite depth can be compensated by the redundancy of the number of channels with respect to the number of interference sources.

The simplicity of adaptive elements enables to construct multistage parametric processors [5].

7. Adaptation elements of parametric processors

The adaptation element (AE) in APP is an electric circuit in the form of a series connection of the non-linear reactance and high-Q filter. Possible variants of AE circuits are shown in Fig.10.

The main task in selecting AE consists in ensuring the CNF depth, which is obtained from (18) and can be expressed through the equivalent filter Q-factors Q_0 and Q_Σ .

$$\beta = \frac{\omega_0 \omega_\Sigma \alpha^2 \sigma_s^2}{g_0 g_\Sigma} = a^2 Q_0 Q_\Sigma,$$

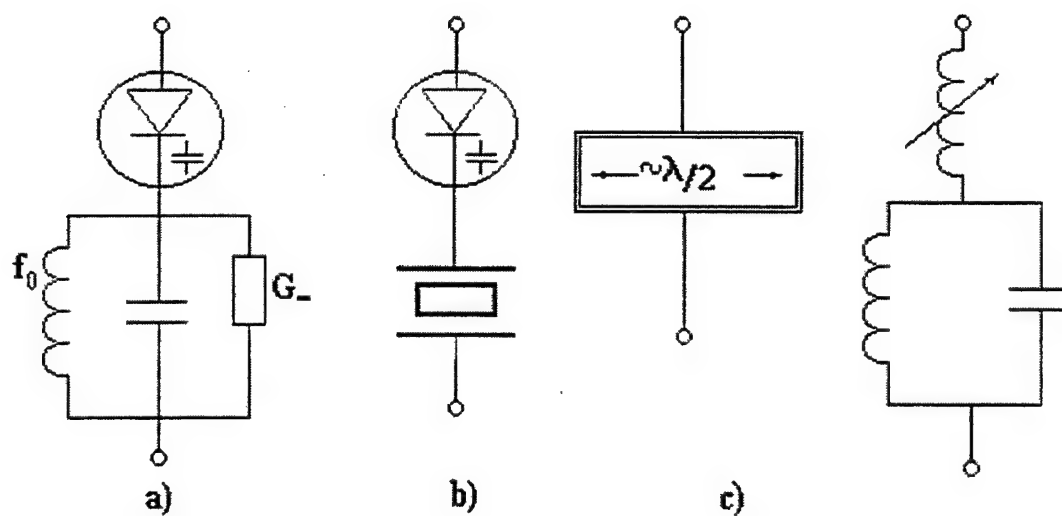


Fig. 10. Adaptive elements.

Frequency, Mhz			CFB	Number of channels	Number of stage	Time of estimations	Accuracy of estimations	Type AE
f_{Σ}	f_0	f_s	β	N	n	t_{MKC}	$\hat{\lambda}_N$	B
64	17	47	50	2	1	20	$5 \cdot 10^{-3}$	B
54	17	37	10^4	2	3	10	$5 \cdot 10^{-4}$	B
41	11	30	5000	4	2	50	10^{-3}	B
3000	90	2910	>100	2	1	2-4	$5 \cdot 10^{-3}$	a, B
490	90	400	>100	4	1	2-4	$4 \cdot 10^{-3}$	B

Fig.11

where a^2 is the square of the modulation parameter of AE non-linear capacity, which is equal to

$$a^2 = \frac{\alpha^2 \sigma_s}{C_0 C_{0\Sigma}},$$

where $C_0, C_{0\Sigma}$ are filter average capacities at the frequencies ω_0, ω_Σ , respectively.

Q-factor $Q_\Sigma \approx 10 \dots 20$ is determined by the spectrum width of processed signals and for existing varactors for obtaining $\beta \gg 100$ it is quite promising to use high-Q resonators at volume and surface acoustic waves (Fig.10 b). When constructing microwave AE, conventional filters with tunnel-diode regenerative amplification have been effectively used (Fig.10 a).

The use of resonators based on the super-conduction phenomena (Fig.10 c) makes it possible to ensure Q-factor up to 10^6 - 10^7 in the microwave range. The film superconducting resonator having features both of the nonlinear inductance and filter, can be used as AE connecting the filters at the frequencies ω_s and ω_Σ and operates at super low levels of input signals. [13].

It is also interesting to use nonlinear reactance's on superconductor-insulator-superconductor structures.[13]

AE simplicity enables to construct multi-layered receiving systems for multichannel adaptive processors by using modern microwave technologies. As in the case of [10], the dimensions of a receiving adaptive structure will not exceed the aperture ones.

The tabulated results (Fig.11) show the possibility to obtain a sufficiently high accuracy of the weight vector calculation in APP at the interference level in each channel up to - 30dB. Here the technical realization in various frequency ranges depends on availability of a corresponding nonlinear reactance's and possibility of technical implementation of high-Q filter-integrators.

8. Conclusion.

The results presented in the report indicate the perspectivity of using BSR with multichannel combination of radio signals and their subsequent coherent space-time processing. The use of AAA in signal space-time processors ensures combined processing of echo signals and IS signals, target-oriented information exchange between active and passive radar channels.

Besides, the realization of information complementation principle opens the way of constructing feasible information conveyers and complete using electromagnetic field energy in the BSR frequency band for secret observation of covered targets near interference sources. For stable radar observation of such targets under multiple interference of high intensity the multichannel AAA must be used with a high control accuracy, optimal amplitude-phase distribution in BSR antenna aperture, combining the advances of analog low-

noise microwave technologies and the possibilities of microprocessor techniques. The adaptive parametric processors on non-linear reactivities with low inner noise has such properties.

The advanced theory of such systems permits to reduce calculations of multichannel processors of AAA space processing to calculations of multichannel linear electric microwave circuits and to develop devices which will not exceed aperture dimensions.

Many problems of BSR practical realization associating with communication link characteristics for multichannel exchange of coherent signals and processing data in information channels are not touched up in the report. Everybody knows that this is an actual problem but they are not the subject of discussion at this symposium.

9. Acknowledgements.

The author is grateful for long-term collaboration in developing works of this area to professors Kobzev A.V., Kondratenko A.P. and Khachaturov V.R.

10. References

1. W.S.Chernyak, Fundamentals of Multisite Radar Systems. Gordon and Breach Science Publishers.1998.
2. K.Milne "Principles and Concepts of Multistatic Surveillance Radar" Proc. IEEE, Inter.Radar Conf. "Radar 77". London 1977.pp 66-71.
3. G.Retzer " A. Concept for Signal Processing in Bistatic Radar" Proc. IEEE 1980. Inter.Radar Conf. - Arlington. Va. – 1980 pp. 88-93.
4. V.V.Karavaev, N.F. Sazonov. Statistical Theory of Passive Location. Radio i Svyaz. Moscow, 1987. (in Russian)
5. Y.N.Sedyshev. V.R. Khachaturov. "Adaptive Antenna Arrays with Microwave Signal Processing" Proc. 3 th Inter Conf. an Antenna Theory and Technigues ICATT-99. Sevastopol 1999 (in Ukrain).
6. A.A. Pistolcors, O.S. Litvinov , Introduction to the adaptive arrays theory, M.: Nauka, 1991 (in Russian).
7. Hudson J.E. Adaptive array principles, L. Peregrinys, 1981.
8. Pat.3202930 US. -Intermediate frequency sidelobe canseller, P.W. Howells.Pabl.24.0865
9. R. Nitzberg, "Computational precision requirements for optimal weights in adaptive processing", IEEE Trans. Aerospace and Electron.Syst., 1980 Vol.16, N4, pp.418-425.
10. P. Jarmuszewski, Y.Shen, C.Laperle, J.Livta, "Four-Element Integrated Receiver Array for Digital Beemforming", URSI RADIO SCIENCE MEETING, June 19-24, 1994. Program and Abstracts the University of Washington Seattle, Washington. p.186.
11. J.D. Shirman et al. , Handbook on radio electronic systems /J.D. Shirman ed. pp. M.: MACVIS, 1998.

12. Yu.N. Sedyshev et al., The transceiver devices of the radio engineering systems P.2, /Yu.N. Sedyshev ed., Kharkov, MREA, 1992.
13. V.F. Kravchenko, A.B. Kazarov, "The surface impedance superconductors and its application in the physics and engineering" // FRE, № 11, 1997.
14. Yu.N. Sedyshev, A.V. Kobzev, "The applicability of multichannel parametrical correlation filters for signal processing", Voprosy radioelektroniki, Radar series, №16, pp. 64-69, M., 1969 (in Russian).

DESIGN OF ULTRA WIDE BAND ANTENNAS FOR THE DETECTION OF BURIED OBJECTS

N. Verneuil, A. Bourdillon

Laboratoire radiocommunications/structures rayonnantes
Université de Rennes 1, Campus de Beaulieu
35042 RENNES Cedex, FRANCE

Abstract: The use of circularly polarized frequency-independent antennas for the detection of buried plastic and metallic anti-personnel mines is analyzed in the context of step frequency radar (SFGPR). It is shown that the dispersive behavior of the antennas can be corrected by using a simulated impulse response. The leakage signal mainly due to the antenna cross-coupling and to the wave reflection at the air-ground interface is then considered for several ground moisture, and solutions are suggested to reduce it and thus to enhance the signal to clutter ratio.

1. Introduction

The problem of plastic antipersonnel-mines detection is difficult because the mines are of low contrast with their surrounding media and they are buried at shallow depth (some centimeters) below the ground surface [1]. Thus, radar systems need ultra wide bandwidth to separate in the time domain the leakage signal due to the antenna cross-coupling and the ground surface reflection from the mine signal. Generally radars do not have such a wide bandwidth and special efforts must be made at the antenna design level to reduce the leakage signal which is usually strong as compared to the weak signal of the mine.

The use of equiangular spiral antennas with opposite polarization sense in transmission and reception could be a solution to decrease the cross-coupling while enabling the mine detection. Indeed, the backscattered fields of a body-of-revolution plastic mine buried near the ground interface have no cross-polarization component [2], meaning that there is no matched component in circular polarization. However, these antennas are dispersive and probably difficult to correct in the time domain. As we are using a step frequency ground penetrating radar (SFGPR) [3] we have chosen to process the antennas effects in the frequency domain.

2. Antenna description

Two arms planar equiangular spiral antennas have been designed and built with a 500 MHz starting operating frequency. The arm's edges are loaded to reduce current reflections causing ringing effects and to extend the bandwidth in comparison with the external dimensions (the diameter of the antenna is 30 cm). Figure 1 shows a side view of one antenna. The backward radiation is limited by an absorbing layer and a metallic plate. The antenna is excited at its center via a microstrip Marchand's balun performing a 2:1 impedance transformation [4]. The antenna and the balun are etched on a FR-4 epoxy substrate.

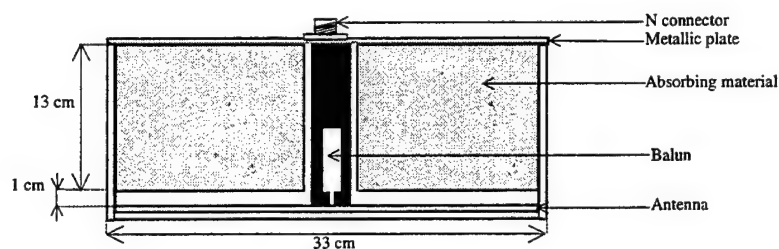


Figure 1 – Side view and dimensions of one antenna.

Radiation patterns and axial ratio have been measured in an anechoic chamber between 1 GHz and 2 GHz. The radiation patterns presented in figure 2 show the reduction of the backward radiation which improves for increasing frequencies.

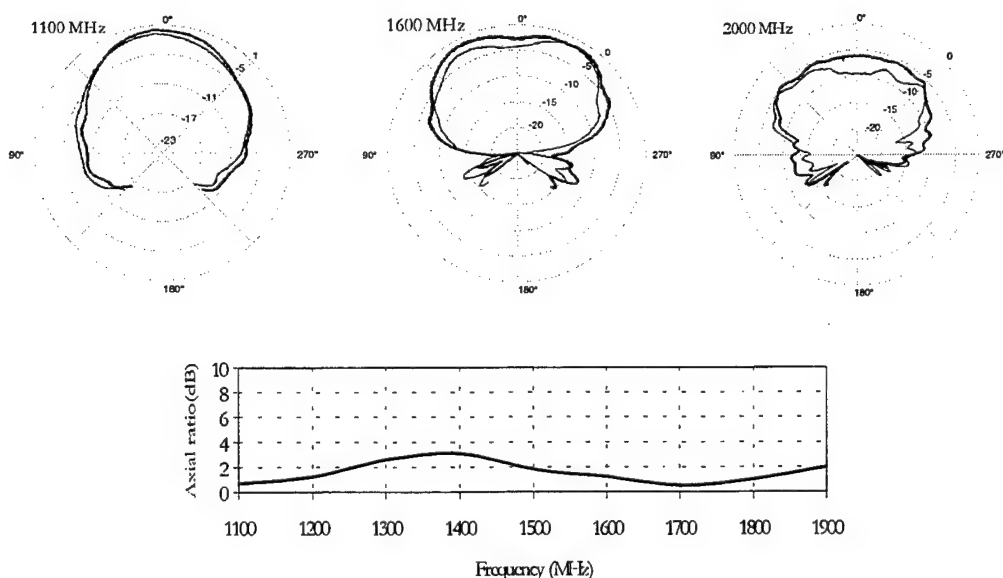


Figure 2 – Radiation pattern measured at three frequencies, *E* component (bold) and *H* component (regular). Axial ratio versus frequency in boresight.

This may be due to the finite size of the metallic plate and the attenuation profile of the absorbing material. A good symmetry is observed between the vertical and the horizontal components and a quasi circular polarization is radiated with an axial ratio better than 3 dB. The gain in circular polarization is about 0 dB at 1.1 GHz, -3dB at 1.6 GHz and it decreases rapidly above 1.95 GHz. The cutoff frequency of the antenna is fixed by the matching bandwidth limits of the balun. Finally, the operating band of the antenna is [500 MHz –2 GHz].

3. Impulse response and antenna correction

Equiangular spiral antennas are frequency independent. However, they are characterized by a phase dispersion which can introduce ringing effects and losses in radar range resolution. Such an antenna can be used in ground penetrating radar applications only if it is possible to correct this dispersion effect. If one antenna complex frequency response is $H(f)$, the inverse filter with $1/H^2(f)$ response is applied to all the step frequency radar measurements. Here, the assumption is made that both transmitting and receiving antennas are identical.

Hence, the main difficulty is to estimate $H(f)$. As we found that measurements do not give good results, we have used antenna simulations to obtain $H(f)$. The antenna has been modeled with a wire approximation model and the far field components were computed using the NEC2D electromagnetic code. Figure 3 shows the circularly polarization frequency response simulated and the phase dispersion is clearly highlighted. However, the simulation doesn't take into account the ground influence on the antenna response.

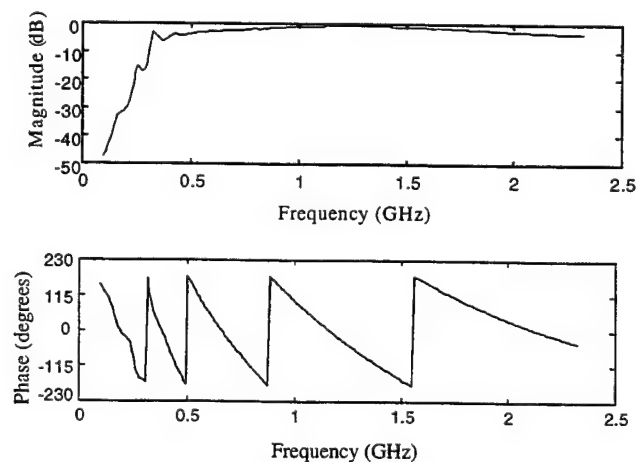


Figure 3 – Simulated magnitude and phase versus frequency of the antenna response.

To analyze the effects of phase dispersion, simulations of the step frequency radar in the [500 MHz-1900 MHz] have been performed taking into account the antenna response. Figure 4-a shows a radar profile calculated for an hypothetical experiment with a perfectly conducting plate buried at 32 cm deep in a non-dispersive soil with an effective permittivity equal to 4. It is observed that antenna dispersion produces a of 3 nanoseconds offset in time delay, a loss in range resolution and finally an increase of ringing lobes.

A similar scenario has been measured to compare with the previous case and to validate the antenna response. A radar profile in a dry sandy soil is presented on figure 4-b. A pit filled with 40 cm of sand (200 cm long, 50 cm wide and 60 cm deep) is used for the experiment. The target is a metallic plate buried at 17 cm. Antennas are placed 10 cm over the ground surface and spaced of 36 cm from their center such that the target time range corresponds to a depth of about 32 cm in a monostatic configuration.

It is observed that the target echo is shifted in time delay by 3 nanoseconds and the range resolution is degraded. The simulated response has been applied to obtain the corrected profile. This last one is very similar to the original step frequency radar simulation of figure 4-a without antenna effects, except a small time range offset of one nanosecond which can be explained by the mechanical uncertainties of the measurement bench. However, parasitic echos due to the bottom of the pit and of the air soil interface make the ringing lobe correction efficiency difficult to estimate.

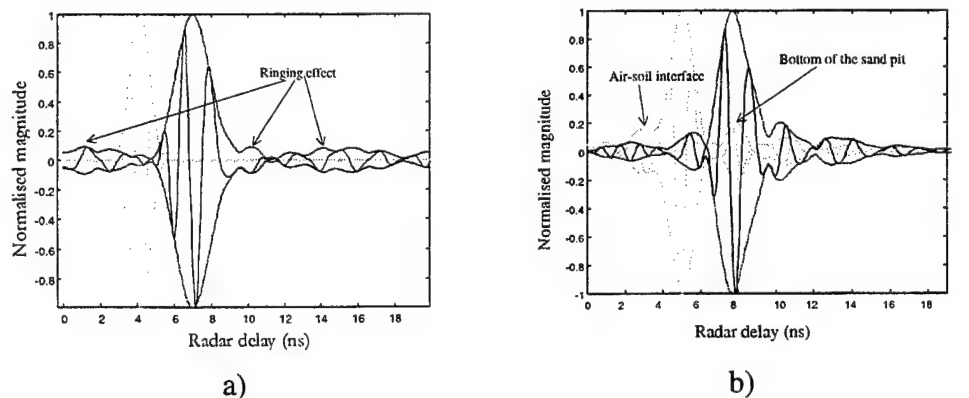


Figure 4 – a) Simulated radar profile without antenna effects (black) and with antenna effects (gray). **b)** Measured radar profile without antenna correction (black) and with antenna correction (gray).

4. Leakage signal reduction

The antenna efficiency in the buried anti-personnel mines detection is determined by the level of the leakage signal which is due to the antenna cross-coupling and to the reflection on ground surface. An analysis of this signal is proposed in figure 5 from measurements with the antennas placed 10 cm over the ground. The leakage signal and the bottom of the sand pit signal are separated in the time domain using a radar time delay profile.

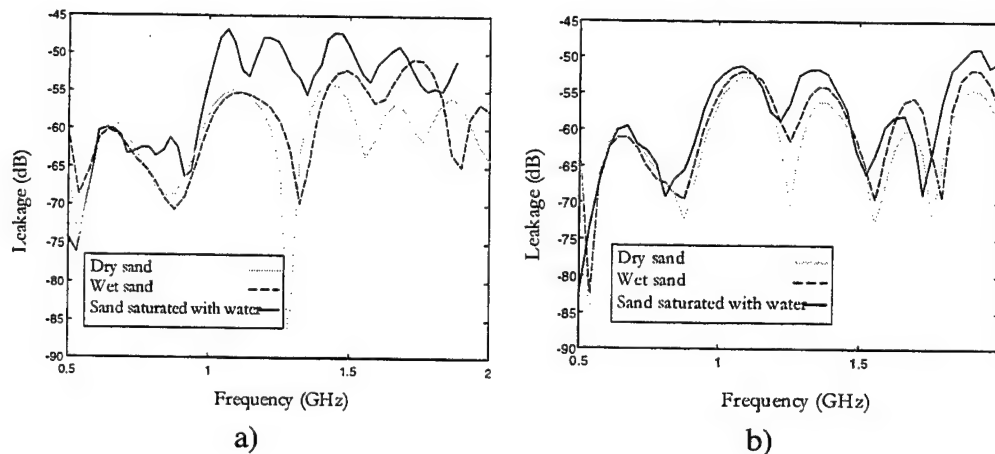


Figure 5 – a) Leakage signal versus frequency for antennas parallel to the ground surface. **b)** Leakage signal versus frequency for antennas with a tilt angle of 10°.

Figure 5-a shows the evolution of the leakage signal for different ground moisture when antennas are parallel to the ground surface. A cross-coupling isolation around 60 dB is achieved. The specular reflection concerns mainly the highest frequencies of the band (over 1 GHz) and its sensitivity with the ground moisture is observed. Indeed, the reflection level increases by 5 dB at 1.5 GHz for a wet sand, and by 10 dB at 1 GHz for a sand saturated with water. Hence, we can expect a limitation in mine detection efficiency in wet soil.

To overcome this problem, antennas have been mounted with a 10° boresight angle with respect to the vertical, resulting in a 80° incidence on the ground surface. Figure 5-b shows that the leakage signal has decreased by about 5 dB in dry sand above 1.3 GHz. An increase of only 5dB is noticed for a sand saturated with water. To verify the interest to use tilted antennas in terms of signal to clutter ratio, measurements are presented on figure 6 when antennas are slid over the ground surface with a plastic mine and a metallic mine buried at 3 cm. The curves represent the power versus distance along the horizontal measurement axis at the mine depth radar range bin.

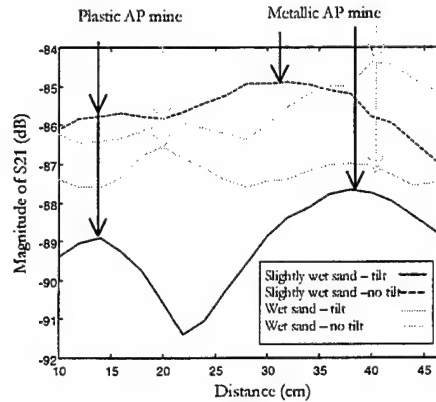


Figure 6 – Power measured at mine depth radar range bin when antennas incidence angle is 90° and 80° for a slightly wet sand and a wet sand.

The general effect of the tilt is to reduce the clutter level by about 5 dB in slightly wet sand and 2 dB in wet sand. An improvement of the signal to clutter of about 2 dB is observed when antennas are tilted. It is observed that plastic mines return more power when the soil is wet than when it is dry. Indeed, the plastic mine RCS is strongly dependant of the soil-plastic contrast.

5. Frequency selection for AP mine detection

Even with a tilt angle, the signal to clutter ratio is too small to achieve a good detection. The total frequency band has been decomposed in three sub-bands of 500 MHz to analyze the frequency dependence in the mine detection process.

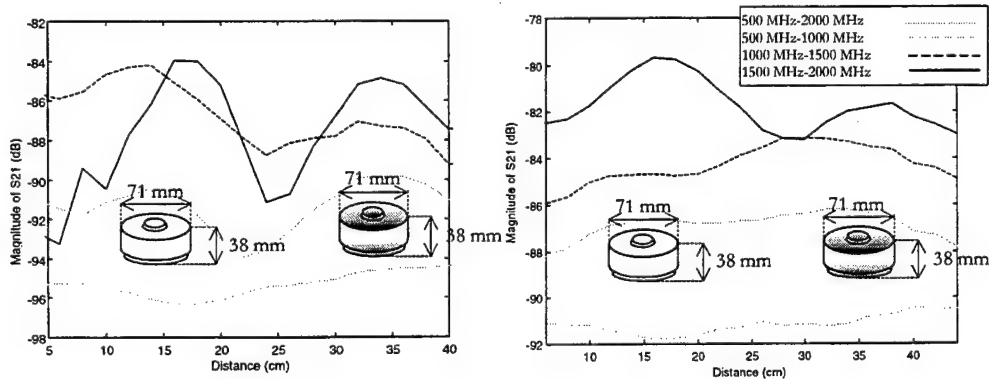


Figure 7 – Power measured at mine depth radar range bin for several frequency band in a dry sand (left) and in a wet sand (right).

Figure 7 shows the power returned along the horizontal axis at the mine depth radar range bin for a plastic and a metallic AP mine in a dry and a wet sand for several operating frequency bands.

The measurements show that the mines return more energy in the [1500 MHz-2000 MHz] frequency band and a signal-to-clutter ratio of 8 dB in dry sand and 4 dB in wet sand is achieved in this band. The leakage signal is stronger at higher frequencies, especially in the [1000 MHz-1500 MHz] frequency band. The leakage is the smallest between 500 MHz and 1000 MHz but the targets return very few energy at these frequencies. Finally, the poor detection results with the whole frequency bandwidth can be explained by the role of each sub-bands.

Figure 8 represents two ground penetrating radar images for a plastic and a metallic mine with antennas placed 10 cm above the ground, with a 10° tilt angle and for the [1500 MHz-2000 MHz] operating frequency band.

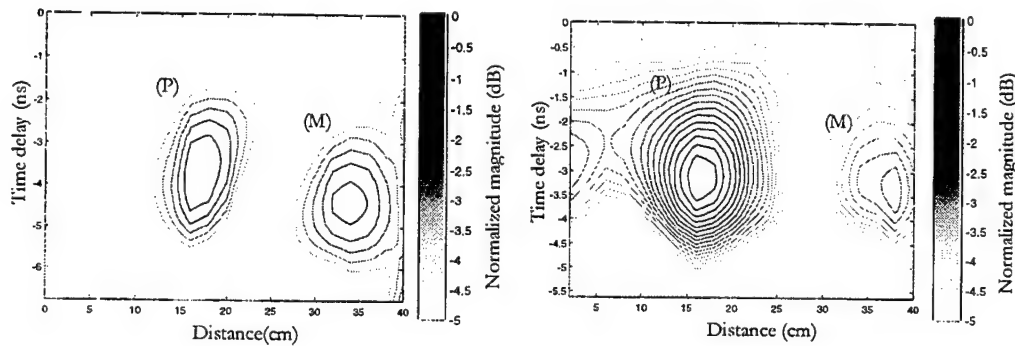


Figure 8 – Radar images of a plastic mine (P) and a metallic mine (M) in a dry sand (left) and in a wet sand (right).

The mines appear clearly on the images. The air-soil interface and antenna cross-coupling echo is more than 5 dB below the mine's level in the case of the dry soil and it just begins to rise on the wet sand radar image.

6. Conclusion

Equiangular spiral antennas have been built and used in the [500 MHz – 2000 MHz] for the detection of buried anti-personnel mines with a step frequency ground penetrating radar. The dispersive effect of the antennas has been characterized with simulations and then applied to radar profiles with success. It is shown that a 10° tilt angle reduces the reflection on the ground surface by about 5 dB but this is not enough to provide a satisfactory signal-to-clutter ratio. At last, a frequency sub-band analysis shows that the best results are obtained between 1500 MHz and 2000MHz. Finally, a clutter-to-signal ratio of 8 dB in dry sand and 4 dB in wet sand has been obtained for the plastic mines.

7. References

- [1] *Second International conference on the detection of abandoned land mines*, Edinburgh, UK, 12-14 October 1998.
- [2] L. Carin, N. Geng and al., "Ultra-Wide-Band Synthetic-Aperture Radar for mine field Detection", *IEEE Antennas and Propagation Magazine*, Vol. 41, N°1, pp. 18-33, February 1999.
- [3] A.P. Freundhorfer, K. Iizuka and al., "Step-frequency radar", *Journal of Applied Physics*, N°58, pp.2572-2583, 1984.
- [4] R. Bawer, J.J. Wolf, " A Printed Circuit Balun for Use with Spiral Antennas", *IRE Trans. on microwave Theory and Technology*, pp. 319-325, May 1960.

ULTRA-WIDE BAND IMPULSE ANTENNAS FOR SUBSURFACE RADAR APPLICATIONS

Anatoliy Boryssenko, Vladislav Tarasuk
Scientific-research company "Diascarb",
P.O. Box 370, Kyiv, 253222, Ukraine,
E-mail: diascarb@public.ua.net

Abstract: The impulse antennas operate in transient non-stationary mode demands special cares in contrast to common antennas with sinusoidal excitation. At the same time, such impulse antennas applied in high resolution videopulse subsurface (ground-penetrating) radar should be functioned near a border between two media with quite different electrical properties. As a rule, the lower dielectric half-space under radar antenna is its strong disturbance factor that in turn causes serious modification of total radar performances. Both the theoretical and the experimental approaches will be employed for those antenna investigations. The theoretical studies to simulate impulse antennas are based on developed approximated approaches originated from simplest monopole antenna. The experimental technique includes a set of impulse antenna prototypes, transmitter and receiver electronics, as well as other electronics and software components for time-domain antenna testing. The final goals of presented studies involves estimation of impulse antenna performances with unavoidable influences of sounding medium and minimization of such negative effects on all possible stages like antenna design, in process of radar antenna operation and post-processing of radar data registered.

1. Problem Background

Subsurface (ground-penetrating) radars of the 50 MHz - 5 GHz operation frequency band are at present a rapidly growing smart technology of remote noninvasive sensing and imaging applied to study the Earth interior regions, as well as other opaque media like rocks, brick and concrete, snow, vegetation and so forth [1]. In order to achieve high spatial resolution in radars, ultra-wide band (UWB) sounding signals are used implemented in time-domain region by videopulse signals (signals without frequency carrier or nonsinusoidal signals [2]), which form by shock excitation of antennas. UWB features of radar signal can be implemented in frequency domain (FD) also by frequency synthesis of a short-

pulse but this case is not considered here. Subsurface radar antennas with impulse excitation in TD are subject of presented studies.

It is certain that radar antennas are ones of the key, critical for some cases, component of radar's equipment determined the main system features like performance factor, receiver-operating-characteristics [3] etc. In contrast to common radar in free-space, radars discussed should operate near a border of the two half-spaces "air medium - subsurface medium" like shown conditionally in Fig. 1. Such radar arrangement causes serious, stochastic as a rule, perturbation of antenna's features due to homogenous sounding medium and its rough surface, as well as complex modes of wave propagation and scattering.

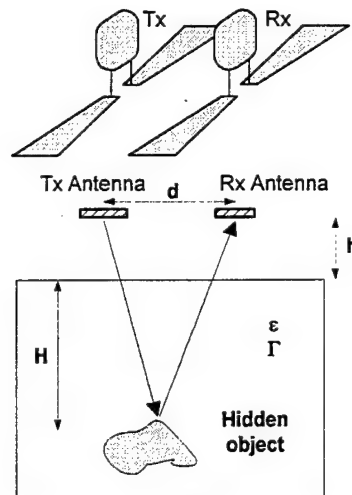


Fig. 1. Common subsurface radar arrangement in bistatic mode with spatially-diversity of transmitting (Tx) and receiving (Rx) antennas to study hidden structure of lower uniform medium with dielectric constant ϵ and attenuation factor Γ where buried object is located and should be detected.

In spite of the large amount of works on impulse antennas and similar TD topics [4-7], the authors have not be able to locate any research where consideration of problem was preferable for own research and design practice due to complexity of theoretical approaches based on complex mathematical models and computer simulation techniques. This paper is devoted to obtain simple general models of impulse antennas in TD with clear physical picture of events to apply for wide range of problems connected with application such antennas in subsurface radars. Developed antennas and other equipment employed for experimental verification are presented and discussed in this paper as well as results of testing obtained.

2. Basic Aspects of Studied Problem

2.1. Time-domain studies versus frequency-domain one

Let note that waveform transformation due to inherent physics of transient electromagnetics [1,5,10,11] is principal moment of impulse UWB antenna operation. So TD approaches should be more adequate for estimating performances of such antennas in contrast to FD studies while from general point of view a impulse response in TD and a complex spectral frequency response in FD are mathematically equivalent. As for complexity of problems under consideration some heuristic methods seems reasonable to apply them for antenna design in TD due to more evident physical meaning.

2.2. External antenna operation modes

There are the three possible positions of subsurface radar antenna near a sounding opaque medium. These settings differ by criterion how strong effects of antenna performances modification by medium are expressed. The first usual operation mode is one that radar antenna is laid directly on surface and strongly disturbed by it. This mode can be called "stand-on" or an applicator mode and it is preferable due to better coupling between antenna and subsurface medium arises from focusing effects of dielectric constant difference. At the same, such mode is unfavorable because effects of random rough-surface perturbation and influence of vegetation. Antenna hanging over searching area at short distance [9] is specific for the second mode that can be called as "stand-over" mode, which is applied, for example, in hand-held demining subsurface radars. This antenna setting is less sensitive to impact of medium but with more scattering effect when signal crosses a border between two media. And the last third mode is characterized by such distance between antenna and medium when antenna features are not disturbed by sounding half-space that can be titled as "stand-off" mode. Due to inherent large diameter of foot-print of impulse antenna, a strong background scattering takes place in this mode demanding special cares at the system algorithm level. It seems reasonable here to analyze firstly the third mode without influence of sounding media on antenna performances and later with such effect because there are some principal aspects of TD impulse antennas, which are common for all modes.

2.3. Internal antenna operation modes

A some classification of operation modes of impulse antennas can be based on the features of their excitation. The last is determined by impedance matching of both the arms of antenna achieved like in Fig. 2 for a simplest monopole antenna. Let note that matching of opened end of antenna is provided by lumped or distributed

resistive loading while matching of antenna terminal port is put into practice by special transmitter/receiver microwave electronics circuits used. The single- and double-passing modes are used only for subsurface high-resolution radars because UWB features can be achieved in these ways while multiple passing produces signal stretching in time or equivalent spectrum contraction. In fact, multiple-passing excitation or standing-wave mode is stationary operation mode of sinusoidal excitation antennas. Notice resulted waveform in the single-passing mode is determined by initial signal waveform and antenna features while in the two-passing mode antenna is key wave-forming element. It is evident that due to impossibility of ideal antenna matching its real operation is always characterized by presence of multiple-passing excitation born so-called antenna ringing [1].

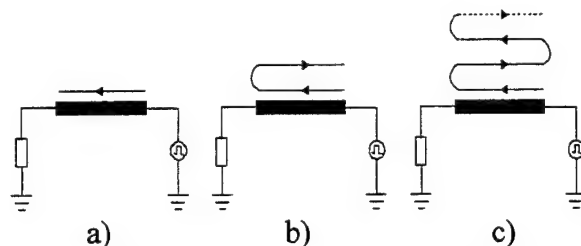


Fig. 2. Excitation modes of impulse monopole antenna due to its matching: a) single-passing or traveling-wave, b) double-passing, c) multiple-passing.

2.4. Geometrical structures of antennas under investigation

Fig. 3 shows the basic configurations of antennas applied for subsurface impulse radars. These antennas are symmetrical center-feed ones. The dipole and bow-tie antennas studied in detail throughout this paper are preferable for operation in the stand-on mode while a TEM-horn like antenna is preferred in stand-over and stand-off modes. At the same time, dipole and bow-tie antennas can operate in the single- and double-passing excitation modes discussed above while horn antenna is more preferable in the single-passing or traveling-wave excitation mode. Real antenna geometry has, as a rule, more complex structure than one in Fig. 3 forced by application of reflector, shielding and other design approaches to improve antennas performances like demonstrated later in sections 5 and 6.

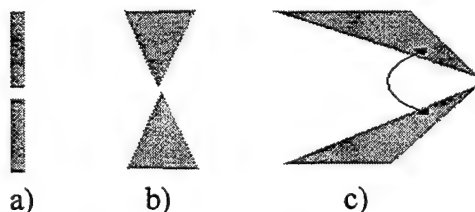


Fig. 3. Commonly used in subsurface radar impulse antennas with central feeding: a) dipole antenna; b) bow -tie antenna; c) TEM horn-like antenna.

3. Antenna Research Strategy

3.1. Free-space antenna operation

Let consider firstly the main regularities that are common for UWB impulse antennas with shock excitation, which operate in the free space. Such regularities are valid for antenna behaviour near a border between two dielectric half-spaces too. At the same time, those regularities are quite different to ordinary antennas with sinusoidal excitation:

- 1) working features of impulse (videopulse) antenna are determined by transient behavior implemented in act of short-time shock excitation;
- 2) shock excitation of transmitting antenna is due to impulse driving source while receiving antenna is excited by an incident impulse electromagnetic field;
- 3) a key moment of impulse antennas operation is given transformation of signal's waveform due to inherent physics of transient antennas;
- 4) transmitting and receiving antennas demonstrate different features and a reciprocity principle, used widely for sinusoidal antennas, is not applied in this case at all and both antennas demand special cares to explore them [11];
- 5) waveforms of antenna radiating and receiving signals are strictly dependent on spatial position of observation point;
- 6) pattern of impulse antennas in the far-range can be described by energy pattern [10] characterized by wide beam-width or large foot-print of antenna;
- 7) such antennas can implemented in practice by their integration with front-end electronics of transmitter and receiver like so-called active antennas.

3.2. Antenna functioning near a border of two dielectric half-spaces

Theoretical studies and numerical simulations are dominant now in literature about UWB antennas operating in TD near a border between the two dielectric half-spaces and only in a few papers experimental approaches are under investigations. One of the research methodology applied to investigate such antennas in TD is one that based on application of special testing arrangement like "sand-box" [4]. But from the authors' point of view this method is not effective in principle because:

- 1) real operation condition is more complex than any artificial one in sand-box due to inherent internal homogeneity, rough surface and near surface clutters;
- 2) registration of signal waveform inside sounding media by probe spaced in it, employed in sand-box studies, is time-consuming and impossible for wide range of distances and observation angles;
- 3) any transient probe applied in such measurement assembly is characterized by its own unavoidable waveform transformations as well, especially under perturbation of surrounding medium where such probe should be implemented.

Moreover, application of subsurface radars in practice has very specific features that can not be involved properly in the sand-box arrangement. These important features include the three kinds of wave events registered in bistatic antenna set-up (Fig. 1) like shown schematically in Fig. 4: 1) scattering wave events produced by subsurface targets and scatterers, 2) direct coupling waves between transmitting and receiving antennas, 3) lateral waves that are very common event for real radar operation [13]. As seen in Fig. 4, useful wave component born by lengthy target is superposition of signal's replicas due to partial scattering by pieces of a buried target thanks inherent large diameter of impulse antenna footprint mentioned above. Separation of those replicas to restore real geometry of target, as well as to take into consideration others indicated events, are not possible for single point measurement. This enables by post-processing of radar data obtained for some set of measurement points, which implement in fact by the synthetic-aperture technique in 2-D or 3-D mode. So it is necessary to estimate influence of antennas on radar performances including post-processing aspects.

To do this the antennas discussed should be studied in operation conditions similar to real one by the proposed research approaches:

- 1) developed theoretical models must be used to predict basic physical regularities of impulse antennas behavior by their computer simulation;
- 2) results of simulations should be supplemented or corrected with consideration of experimental or measured real data;
- 3) the measurement should be implemented initially in air-filled operation environment for simplicity reason being applied to radio wireless link formed by two impulse antennas;
- 4) influence of real operation condition due to sounding medium can be estimated by special experimental approaches, which in fact are based on subsurface radar arrangements where possibility to set various operation modes of antennas should exist without direct measurement in operation medium,.

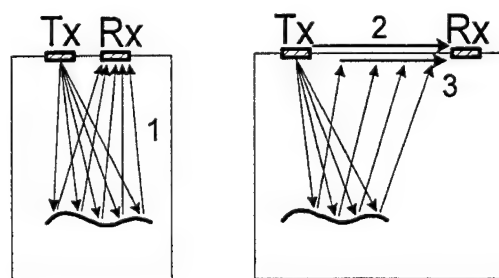


Fig 4. Classification of wave events in bistatic antenna arrangement over sounding medium where 1- scattered waves, 2 - direct coupling waves, 3-lateral waves.

4. Theoretical Concepts of UWB Impulse Antennas

4.1. Monopole as basic antenna structure

Monopole antenna in Fig. 5a, as a thin linear perfectly conducting wire, can be treated as a simplest basic element to build and study other antennas with more complex shapes like ones in Fig. 5c. For example, an asymmetric dipole antenna can be considered as combination of two opposite excited collinear monopoles as seen in Fig. 5b. Other practically important center-fed antennas in Fig. 5c with complicated shapes include symmetrical dipole, V-shaped dipole, bow-tie antenna, and TEM horn-like antenna. It is evidently that those antennas are originated directly from monopole one by its corresponding step-by-step complications. The last approach enables to investigate real geometry of UWB antennas in Fig. 3 without sufficient time spending based on monopole analysis.

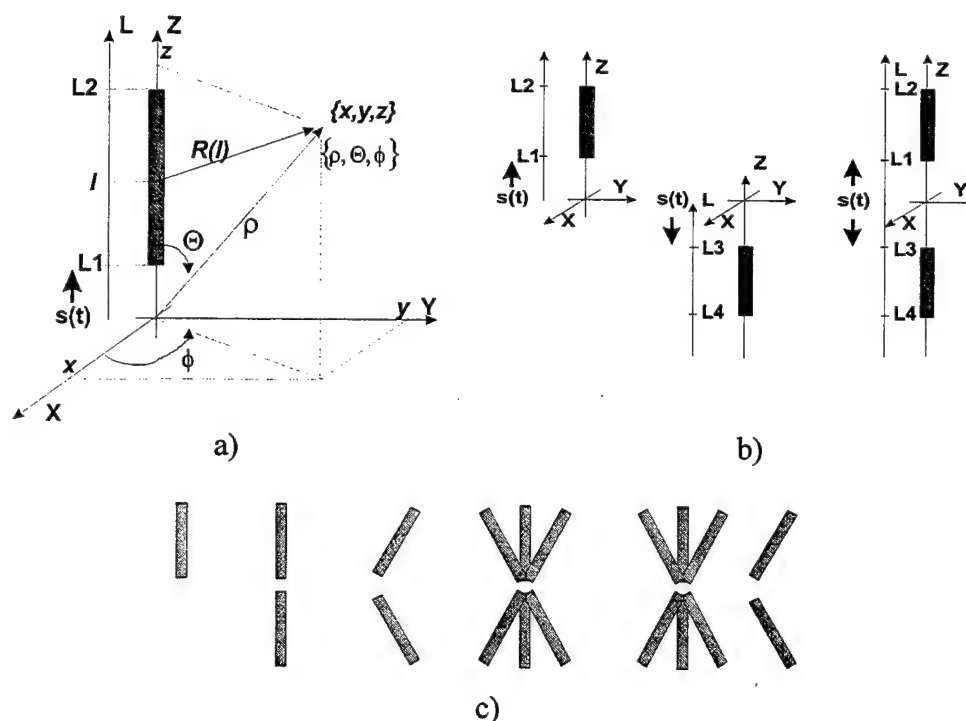


Fig. 5. (a) General geometry of radiation problem under consideration for monopole of length $L_a = L_2 - L_1$ excited by transient signal $s(t)$ at feeding point $l = L_1$. (b) Representation of asymmetric dipole antenna as combination of two opposite excited collinear monopole antennas. (c) The series of antenna wire-like structures originated from monopole antenna by its step-by-step complications (dipole, V-shape, bow-tie, TEM horn).

Formally, monopole antenna in Fig. 5a thanks to simplicity of its geometry can be studied analytically to obtain all necessary expressions for antenna performances in the near- and far-field regions. Features of complex-shaped antennas can be expressed as vector/scalar sums of corresponding features of elementary monopole's antennas, which form complex-shaped one. Let note, that proposed approach is similar to one applied before to sinusoidal-wave antennas in FD [8].

The monopole antenna in Fig. 5a is excited in the its feed point $z = Z1$ by a current of definite waveform $s(t)$ with transient nature. Antenna's excitation is considered as a traveling-wave current pulse by the expression $s(t-l/c)$ as temporal and spatial function, where c is the free-space light velocity. An edge effect, when current pulse reaches the second opened end of antenna at $z = Z2$, can be involved in similar manner as some repeated excitations of antenna with opposite directed wave, as well as all subsequent excitation due to opened-end reflections. As result of such excitation, a current pulse is propagated along antenna produced a electromagnetic field in external space. It is necessary to determine this radiated field and its dependence versus problem's parameters, like antenna geometry $La = L2 - L1$, kind of excitation waveform $s(t)$, arbitrary spatial coordinate of field observation point assigned by the Cartesian coordinates $\{x, y, z\}$ or the spherical ones $\{\rho, \Theta, \phi\}$, and arbitrary moment of time t given. In accordance to the basic principles of electromagnetics [14], to study a radiated electromagnetic field of monopole, one can use the vector of magnetic potential for linear finite-size straight segment, i.e. monopole. In the force of task's axial symmetry only the A_z component of the problem's magnetic potential vector exists:

$$A_z = \int_{L1}^{L2} \frac{s(t - (R + l)/c)}{R} dl, \quad (1)$$

where R is distance from the original of the coordinate system to spatial observation point where electromagnetic radiation is observed:

$$R \equiv R(\rho, \Theta, l) = \sqrt{(\rho \sin \Theta)^2 + (\rho \cos \Theta - l)^2} \quad (2)$$

The radiated vector electromagnetic field is determined by the system of the Maxwell equations that can be solved versus the magnetic vector potential (1). So, a magnetic vector component of the radiated field is expressed as [14]:

$$\vec{H} = \frac{1}{4\pi} \text{rot}[0, 0, A_z] = \frac{1}{4\pi} \begin{bmatrix} \vec{1}_x & \vec{1}_y & \vec{1}_z \\ d/dx & d/dy & d/dz \\ 0 & 0 & A_z \end{bmatrix}, \quad (3)$$

where $\vec{1}_x, \vec{1}_y, \vec{1}_z$ denote the unit vectors of the corresponding axes of the Cartesian coordinates. An electrical radiated field component is determined like:

$$\vec{E} = \frac{1}{4\pi} \int \text{rot}(\vec{H}) dt. \quad (4)$$

For instance, after some not complicated analytical transformation the principal elevation electric E_Θ component of TD radiated field can be expressed:

$$E_\Theta = -\frac{\sin \Theta}{4\pi} \left\{ \int_{L_1}^{L_2} \frac{s'(t - (R+l)/c)}{R} dl + \int_{L_1}^{L_2} \frac{s(t - (R+l)/c)}{R^2} dl \right\} \quad (5)$$

The expression (5) and similar ones for all electromagnetic field components can be employed easy for TD antenna studies by application of universal mathematical software like Mathcad, Maple, Matlab, Mathematica etc. One can obtain important valuable data in this manner that will be not evident from numerical techniques like finite difference time domain (FDTD) without tremendous programming and computing efforts. Using opportunities of modern computer algebra system offers analytical investigation of the 3-D TD vector electromagnetics problems to understand general physics of problems. It is possible due to capabilities of mentioned above computer mathematics to solve within a uniform framework of used software the three important for research: symbolic manipulations, numerical computations and visualization of results.

4.2. Some simulating results for transmitting monopole

Starting from (5) by employment of Mathcad or other math software it is possible to explore fundamental features of TD electromagnetics concerning spatial-temporal wavelet transformation in impulse antennas. Some of those features listed shortly in subsection 3.1 are shown and discussed below. Note that proposed approach is more easy in implementation than other known ones [5-7] with complex formal techniques and time-spending programming and computing.

The two additive components in (5) can be easy interpreted as far- and near-field components. Fig. 6 shows the "near-to-far-field transformation" effects in impulse monopole antenna with single-passing excitation by the 1-nanosecond Gauss pulse. The presented data allow estimating a some "empirical" criterion of the far-field range that corresponds to the distance between antenna and observation point, which is equal or more than ten times of antenna linear dimension. Qualitative sign of the far-field range is symmetrical radiated wavelet as seen in Fig. 6. A set of antenna energy patterns for various antenna lengths is presented in Fig. 7 that are physically evident like for any traveling-wave antenna. The energy

patterns for dipole antennas, for instance, are demonstrated in Fig. 8 where form of antenna pattern change from single- to double-lobe shape while antenna length is growth. In order to give direction of maximum radiation of such antenna at elevation angle $\Theta=90^\circ$ we must transform it in V-shape or horn antenna with apex angle $180^\circ - \Theta_0$, where Θ_0 is angle between split lobes of pattern in Fig. 8.

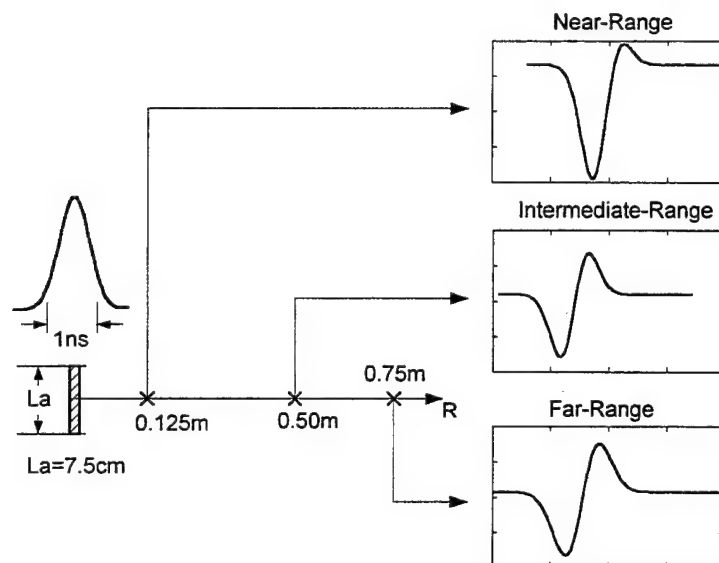


Fig. 6. Near-to-far-field range transformation in impulse monopole antenna with single-passing excitation by the 1-nanosecond Gauss pulse.

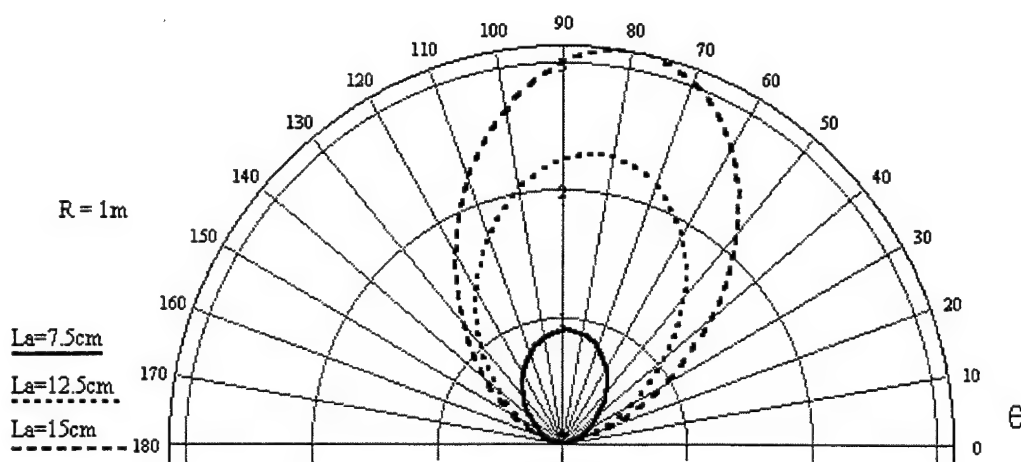


Fig. 7. E-plane energy patterns of impulse monopole antenna of various length with single-passing excitation by the 1-nanosecond Gauss pulse.

Generally speaking the principal features of impulse antennas include: 1) signal waveform versus spatial coordinates of observation point, 2) energy pattern, 3) gain, 4) efficiency. Some of those features, requiring special detailed separated considerations, have been studied successfully on the base of developed approaches and depend strongly on such antenna initial properties like:

1. General geometry: monopole, dipole, V-shape, bow-tie, horn-antenna.
2. Additional construction elements: reflector, shielding, etc.
3. Excitation mode: ideal and non-ideal single- and double-passing.
4. Antenna functioning: radiation, reception, wireless link with the antennas.
5. Waveform of exciting signal: short or long, symmetrical or asymmetrical etc.

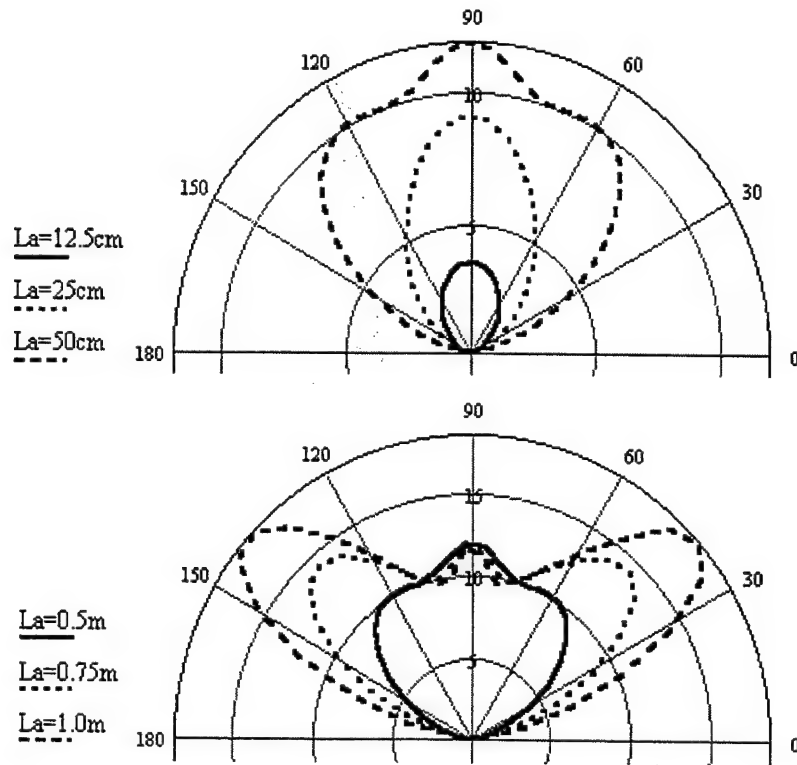


Fig. 8. E-plane energy pattern of impulse dipole antenna of various length with its single-passing excitation by the 1-nanosecond Gauss pulse.

4.3. Far-field region approximations

It is possible to obtain the far-field region approximation for radiated impulse field of monopole antenna [11]. For example, an elevation electric component of the electromagnetic field, produced by a monopole antenna in the far-field region of free space (Fig. 5a) under travelling-wave excitation (Fig. 2a) by an impulse signal with waveform $s(t)$, can be expressed:

$$E_{\Theta}(\rho, \Theta, t, La) \cong \frac{\sin \Theta}{1 - \cos \Theta} \cdot \left\{ s\left(t - \frac{\rho}{c}\right) - s\left(t - \frac{\rho}{c} - \frac{La}{c}(1 - \cos \Theta)\right) \right\} \quad (6)$$

Similarly, a load current (voltage) of monopole receiving antenna with traveling-wave excitation mode, excited by external incident plane electromagnetic wave with impulse waveform $E(t)$, is determined like [11]:

$$I_n(t, \Theta, La) \cong \frac{\sin \Theta}{1 - \cos \Theta} \cdot \left\{ e\left(t - La/c\right) - e\left(t - La/c \cdot \cos \Theta\right) \right\} \quad (7)$$

where

$$e(t) = \int E(t) dt. \quad (8)$$

Note, that the presented expressions (6) and (7) demonstrate similar general form but quite principal difference concerning regularities of transformation of primary waveforms of exciting signals due to integration (8) in (7). So the classical principal of reciprocity used widely for sinusoidal antennas is not applicable in this case at all. Some differences between transmitting and receiving antennas are summarized in Table 1 where the following auxiliary expressions are used:

$$T(\Theta) = \sin \Theta / (1 - \cos \Theta) \quad (9)$$

is the pattern function common for both trasmitting and receiving antennas,

$$F(j\omega, \Theta) = T(\Theta)[1 - \exp\{-j\omega La/c \cdot (1 - \cos \Theta)\}] \quad (10)$$

is the ordinary complex pattern function for traveling-wave linear antenna with sinusoidal excitation. $\dot{S}(j\omega)$, $\dot{S}_E(j\omega)$ are complex spectra resulted from the Fourier transform of the exciting signal $s(t)$ and $E(t)$ for corresponding antennas. Table 1 illustrates also connection of antenna representation in TD and FD, as well as behavior of electrically short antennas used as field probes.

Table 1.

	Transmitting Monopole Far-region Waveform	Receiving Monopole Antenna Load Voltage
Time Domain	$\sim T(\Theta) \cdot \left\{ s(t) - s\left(t - \frac{La}{c}(1 - \cos \Theta)\right) \right\}$	$\sim T(\Theta) \cdot \left\{ e(t) - e\left(t - \frac{La}{c}(1 - \cos \Theta)\right) \right\}$
Frequency Domain	$\sim \dot{F}(j\omega, \Theta) \cdot \dot{S}(j\omega)$	$\sim \frac{\dot{F}(j\omega, \Theta) \cdot \dot{S}_E(j\omega)}{j\omega}$
Short Probe	$\sim \sin(\Theta) \cdot \dot{s}(t)$	$\sim \sin(\Theta) \cdot E(t)$

4.4. Influence of operation media

Environmental effects on antenna's features, caused by a sounding medium with its quite different electrical properties in contrast to the air-filled upper half-space, are significant aspect to study them. In general, this problem is complex electromagnetics one, but there are some opportunities to solve it approximately based on an approach under simplified assumption about uniform, isotropic, non-disperse nature of subsurface medium. Estimating of the modified antenna features can be implemented with consideration of: 1) slow-wave factor, 2) input impedance and 3) pattern, which can be involved in studies by model of equivalent transmission line in Fig. 9. A slow-wave modifies a velocity of excitation signal in antenna and offers possibility to evaluate focussing effects, produced by a redistribution of electromagnetic field energy in a cross-section of equivalent transmission line. The last changes antenna pattern doing it inward to a sounding medium in most degree. Variations of antenna input impedance under its loading by dielectric half-space should be studied to estimate resulting impedance mismatch between antenna and electronics circuits that is important subject for antenna adaptation considered later in this paper.

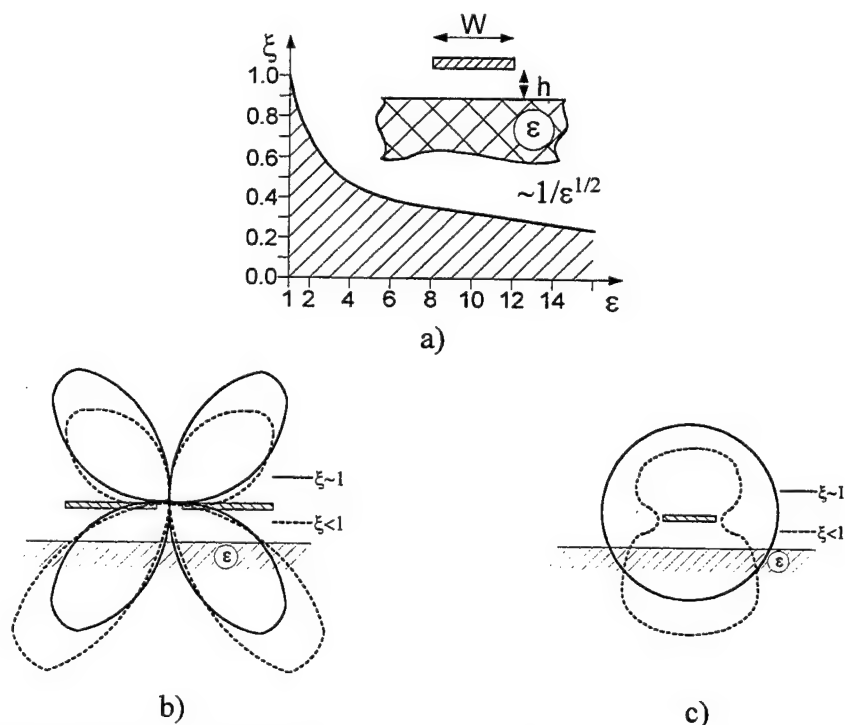


Fig. 9. Equivalent transmission line model to estimate of modification of antenna features due to presence of the lower dielectric half-space: (a) slow-wave factor, (b) E-plane energy pattern, (c) H-plane energy pattern.

5. Experimental TD Techniques for Examination of Impulse Antennas

5.1. Concept of active antennas

Concept of active impulse antennas, when antenna is directly terminated to transmitter/receiver front-end circuit, has been chosen as productive one due to possibility to reach high-level of antenna performances with excluding unwanted waveform distortions caused by cable interconnections common for most experimental studies [4]. The positive feature of such approach involves also absence of traditional balun passive circuit and employment of active electronics circuit for symmetrization of antenna feeding. Additional opportunities for adaptation is also accessible in this case. The concept used is depicted by convection in Fig. 10 for wireless link formed by two antennas where characteristic waveforms with double-passing excitation are shown too.

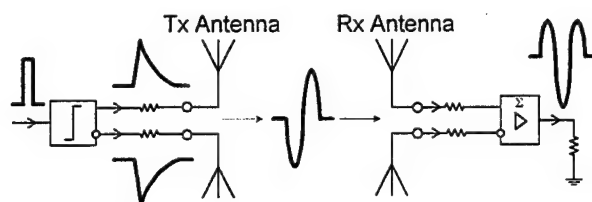


Fig. 10. Active antennas in impulse wireless radio link with far-field setting.

5.2. TD antenna measurement set-up on the base of impulse radar

Components of modified subsurface radar in Fig. 11 have been used to implement active transmitting and receiving antennas as well as total TD testing assembly.

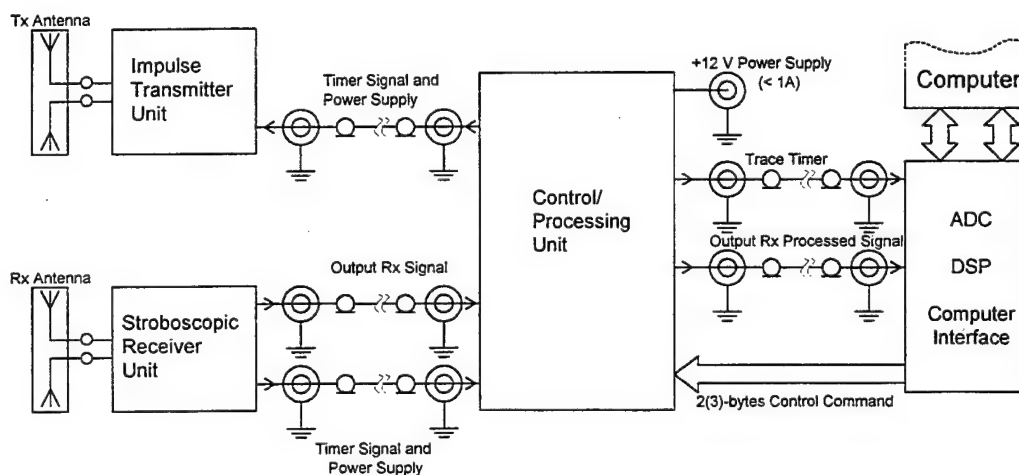


Fig. 11. General schema of impulse radar system used for TD antenna testing.

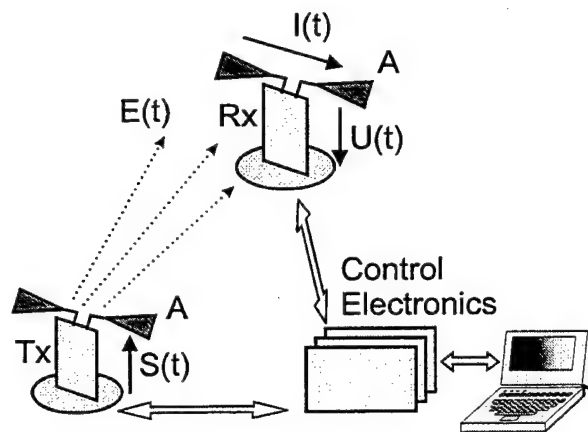
In general, a TD experimental technique has sufficient benefits in comparison with FD experimental investigations due to the fact that the TD examinations can be accomplished in ordinary laboratory rooms without necessity to use special very expensive anechoic chambers. In this case, interference scattering electromagnetic events caused by various external objects inside laboratory can be eliminated by a simple temporal range gating applied to a signal received [9]. The considered testing procedures have been conducted by using components of own-designed UWB impulse radar (Fig. 11) with a nanosecond and subnanosecond impulse generators, i.e. transmitter, and a stroboscopic receiver unit with digital data registration by computer ADC/DSP card and the following computer data storing and processing [12].

5.3. Testing active antennas

Implementation of the radar schema in Fig. 11 for antenna TD measurement assembly is shown schematically in Fig. 12 where simulated waveforms for the two exciting signals are presented on the definite stages of waveform transformation in testing wireless link. These waveforms correspond to the double-passing excitation of dipole antenna and have been computed on the base of the discussed above theoretical models. Practical realization of the presented antenna TD measurement assembly is shown in Fig. 13 and in Fig. 14 where dipole antennas are under examination in the free space [12].

Photos in Fig. 15 demonstrates the bow-tie antenna with the 1GHz middle frequency or about equivalent 1 nanosecond pulse duration. And short-dipole antennas is in Fig 16. Both antennas are connected directly to input symmetrical circuit of receiver with anti-ringing input resistors. Concept of active bow-tie impulse antenna with reflector is shown schematically in Fig. 17 and by its implementation in Fig. 18. An electronics plates of receiver and transmitter are installed on the back side of reflector making antenna compact and preferable for free-space operation, as well as be applicable for functioning near a border between air and lower dielectric half-spaces. Those antennas have been used for estimation of some antenna adaptation opportunities discussed later in section 6.

The next advanced version of impulse antennas for subsurface sounding is presented in Fig. 19 where packaged electronics modules of transmitter and receiver (Fig. 20) are used. The receiver of this version does not contain input compensation resistors like previous one but includes special input circuit resulted in 5 dB noise figure in contrast to 10dB noise figure of receiver in Fig. 15-16 with input resistors included. Printed circuit antenna is employed in Fig. 19 and all construction is covered by special case to implement cavity-backed antenna.



Signal waveform	Gauss pulse excitation	Error function excitation
Tx Antenna Exciting Current $S(t) \sim$		
Far-Zone Radiated Field $\Theta=90^\circ$ $E(t) \sim$		
Rx Antenna Induced Current $\Theta=90^\circ$ $I(t) \sim$		
Rx Antenna Output Voltage $U(t) \sim$		

Fig. 12. Schema of experimental set-up of impulse antenna testing with simulated waveform: A – testing antennas, Tx – transmitter with exciting signal $S(t)$, Rx – receiver, $E(t)$ – E-far-field component of radiated field, $I(t)$ – waveform of Rx antenna current induced, $U(t)$ – voltage waveform dropped on Rx antenna load.

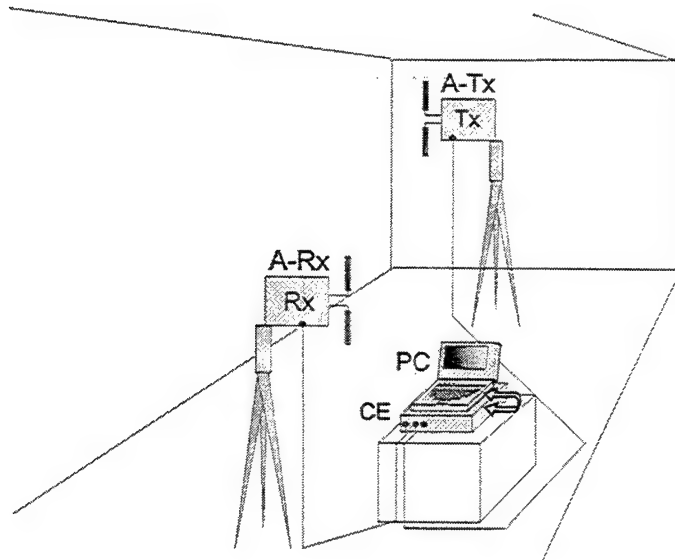


Fig. 13. Schematic presentation of TD antenna measurement setup in free-space.

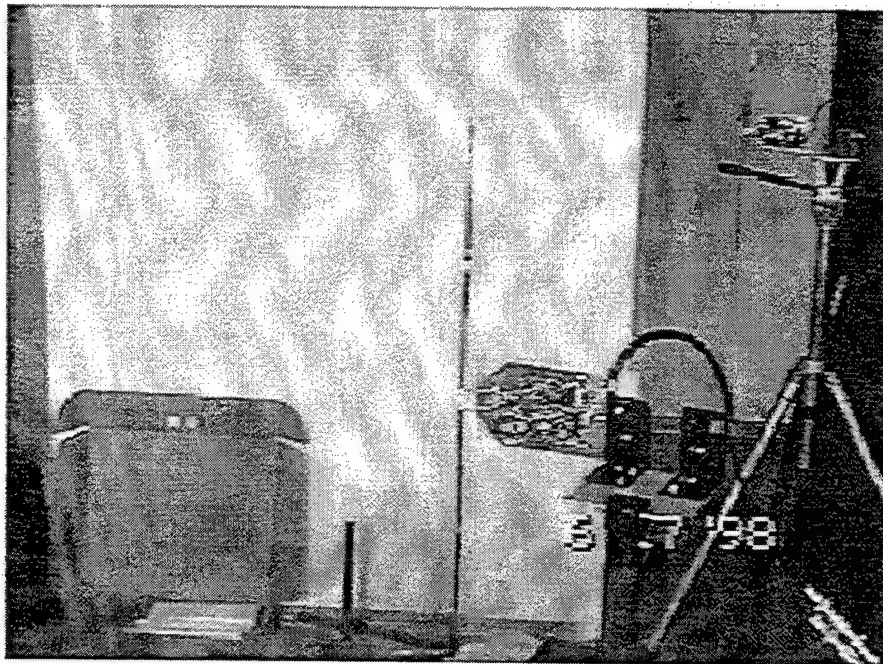


Fig. 14. Photo of TD antenna measurement assembly in a laboratory room.

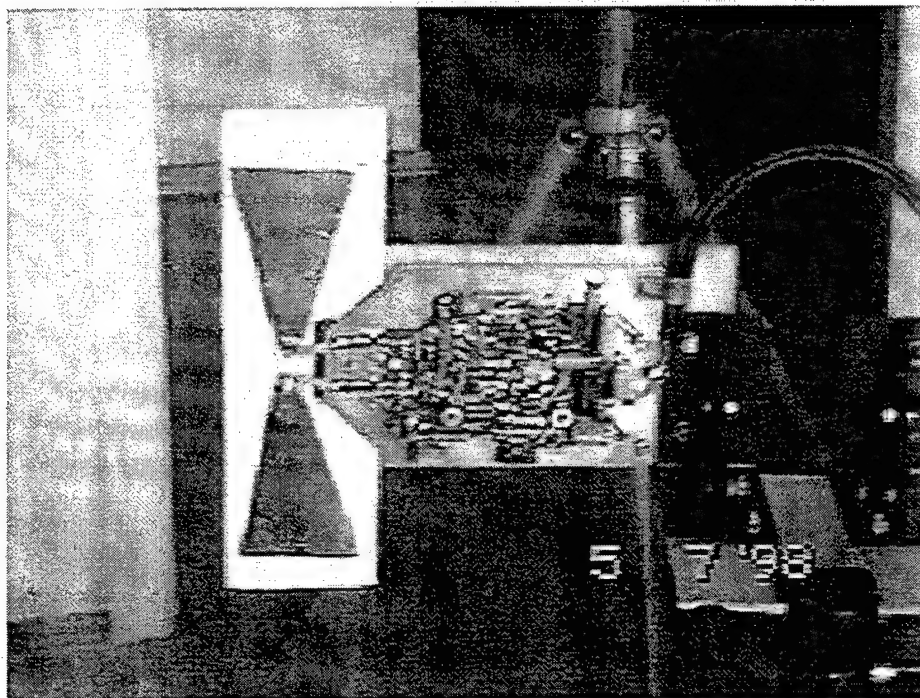


Fig. 15. Bow-tie impulse active antenna terminated directly to receiver unit.

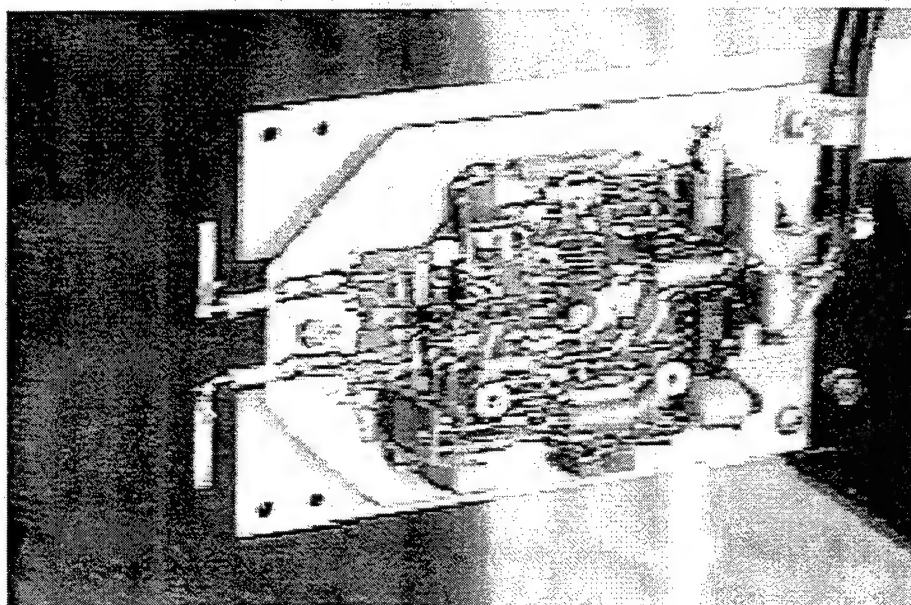


Fig. 16. Short-dipole impulse active antenna with receiver in measurement setup.

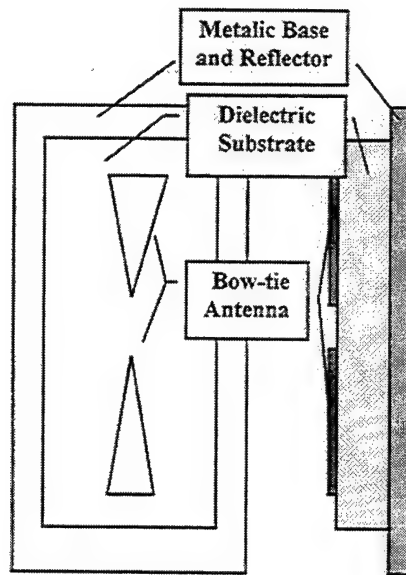


Fig. 17. Schematic presentation of bow-tie reflector-backed antenna.

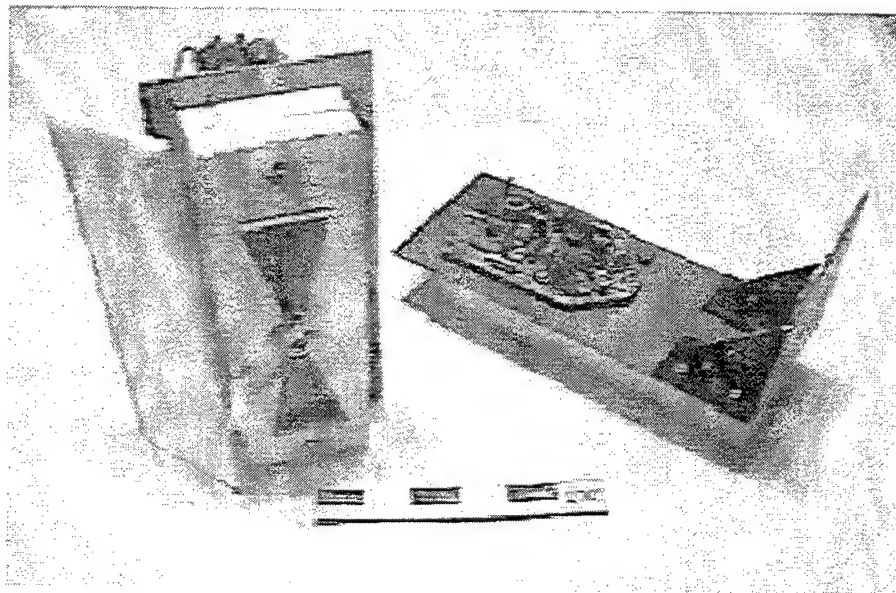


Fig. 18. Photo of experimental bow-tie reflector-backed antennas with transmitter and receiver electronics on rear side of reflector plate.

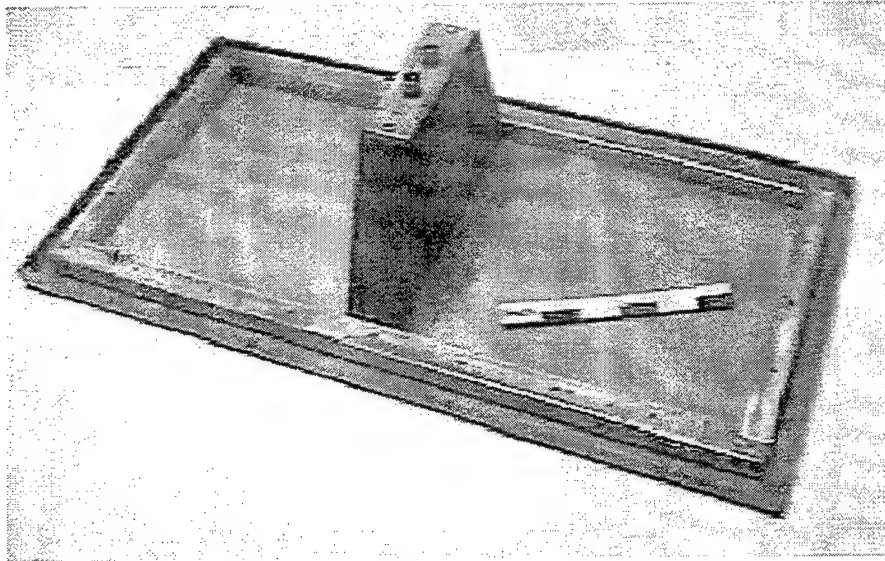


Fig. 19. Impulse printed-circuit antenna for subsurface radar with installed receiver or transmitter electronics packaged module. Antenna is accomplished by etching below the plate where electronics module is mounted.

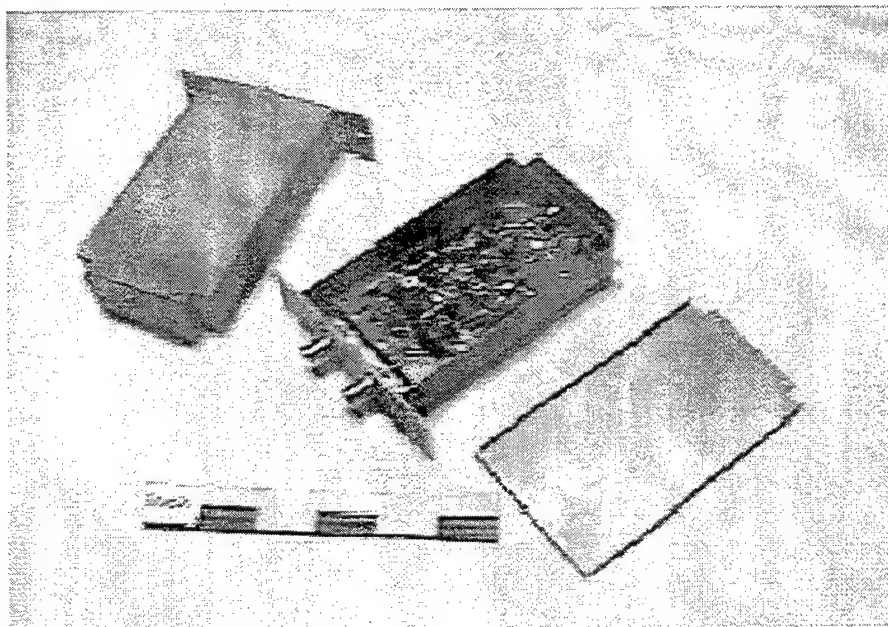
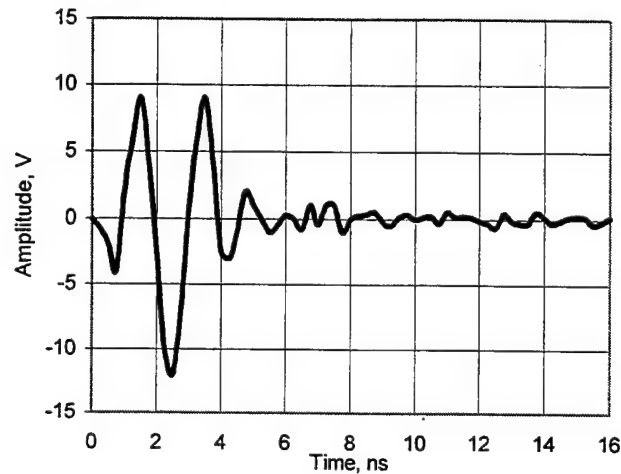


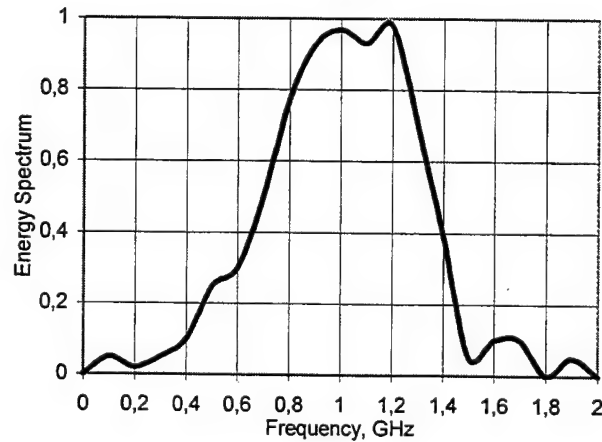
Fig. 20. Impulse transmitter/receiver electronics modules in the special package.

6. Experimental Studies

The presented above equipment offers wide opportunities to study experimentally in TD all aspect of impulse antennas functioning including possibility of examination of discussed above theoretical considerations. For instance, in Fig. 21a a typical signal waveform measured for the free-space operation condition in the far-filed range of the wireless radio link with same bow-tie antennas (Fig. 15) with the Gauss pulse double-passing excitation is shown. The corresponding energy spectrum computed with evident UWB features is depicted in Fig. 21b.



a)



b)

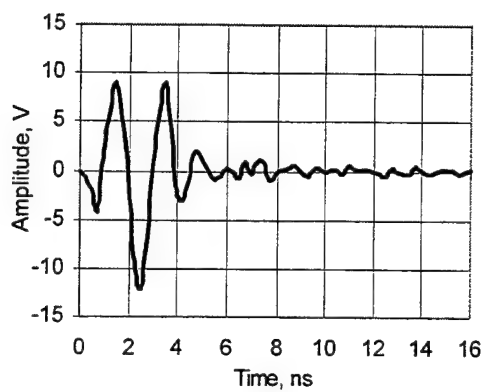
Fig. 21. Typical signal waveform measured (a) and corresponding energy spectrum computed (b) in the wireless radio link with same bow-tie antennas in far-field region with the Gauss pulse double-passing excitation.

The presented waveform in Fig. 21a is similar in outward appearance to simulated one in Fig. 12 for the Gauss pulse excitation. Some inescapable differences between simulated and measured waveforms exist, of course, due to asymmetrical shape of experimental wavelet and presence of its additional ringing signal component in Fig. 21a. Such differences are very common when simulated and measured data are under comparison and forced by the following reasons: 1) some antenna pure symmetry takes place, 2) terminal matching is not perfect in practice, 3) setting of antennas in the TD measurement assembly is not ideal with some misalignment of antenna beams; 4) unavoidable electromagnetic scattering produced by neighbor elements of testing equipment in Fig. 14 is presence. Other important issues of impulse antenna operation in TD listed above in subsection 4.2 can be involves in experimental investigations in the similar ways due to capabilities of developed measurement equipment for antenna examination in the free space and near a border between two dielectric half-spaces.

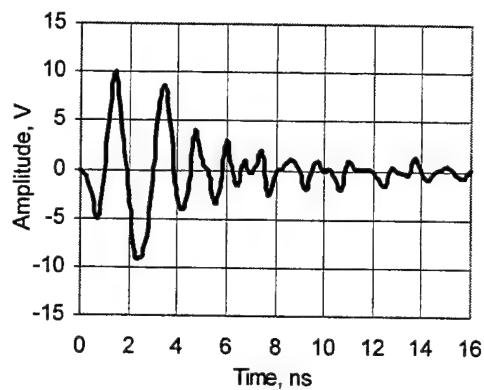
At the same time there are some principal difficulties of experimental studies of impulse antennas operating near a border between two electrically different media when antenna is disturbed by the sounding medium. As stated before direct TD measurement of antenna electromagnetic fields in operation media is very complex expansive method with time spending and limited results obtained. Let present the authors' experimental approach that allows receiving practically important data concerning antenna interaction with medium under radar sounding. This approach gives valuable opportunities to study and develop the corresponding antennas and electronics components by using TD measurement assembly in the free space described above. It will be shown further that this gives additional opportunities for development of active impulse antennas with adaptation capabilities.

The idea of experiments with using of reflector-backed bow-tie antennas (Fig. 17 and Fig. 18) in the free-space antenna measurement assembly (Fig. 13) is the following. Due to discussed in subsection 4.4 effects of operation environment on antenna we can study this phenomena separately in easy way with the free-space arrangement to estimate total degradation of radar properties especially radar performances factor or total system energy potential [1].

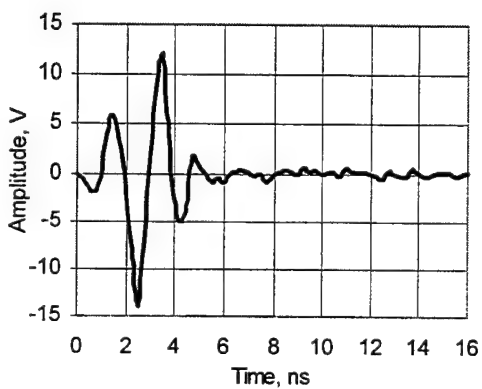
The previous waveform in Fig. 21a is depicted repeatedly in Fig. 22a. The next picture in Fig. 22b contains the waveform registered in the measurement assembly (Fig. 13) with the two same bow-tie antennas (Fig. 17), which are covered only by with foam plastic plate, seen in Fig. 18 on the right, with heterogeneous stochastic dielectric impurities with dielectric constant $\epsilon \approx 4-6$. As results of such experiment we can observe qualitatively some degradation of registered waveform that illustrate effects of antenna random perturbation.



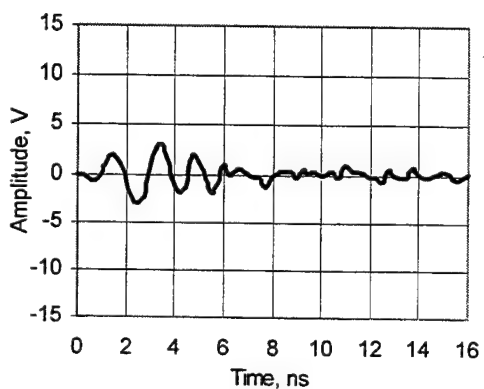
a)



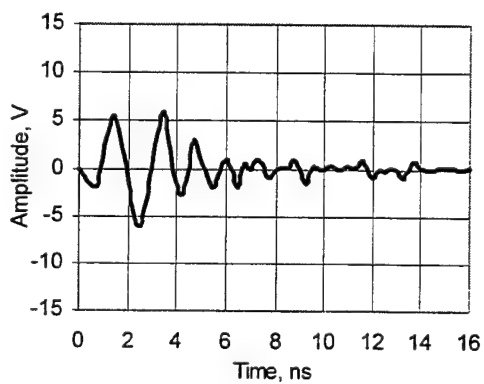
b)



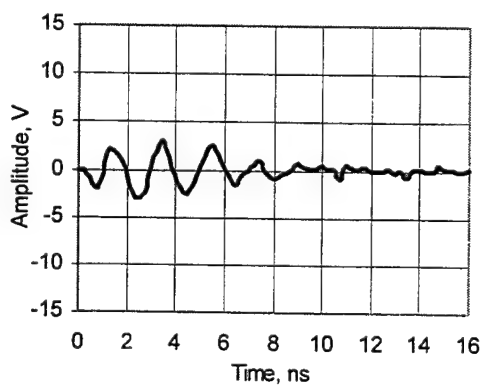
c)



d)



e)



f)

Fig. 22. Experimental investigation of the impulse antenna to estimate influence of operation medium and adaptation opportunities.

Next, the horizontal pair of waveforms in Fig. 22c-d reflects the situation when reflector is setting at optimal distance (Fig. 22c) and when distance between antennas and reflector is twice small than optimal one (Fig. 22d). The last situation is very common for subsurface radar antennas like cavity- or reflector-backed bow-tie ones (Fig. 17) with some distance between reflector and antenna. This distance can be optimal for definite operation condition like air-field medium and is not optimal when antenna is placed on a border between two half-spaces with dielectric contrast $\Delta\epsilon \geq 6-9$ that is common value in subsurface radar practice. Amplitude decreasing in three times takes place in this case that corresponds to about $L1 \approx -9\text{dB}$ of radar performances degradation.

Effects of impedance mismatch between antenna and front-end circuits of transmitter and receiver is illustrated in Fig. 22e-f relatively to fig. Fig. 22c with optimal antenna setting. As analyzed before, antenna spacing near dielectric half-space has effect on its characteristic impedance. In place of antenna impedance variation due medium loading, we change impedance of both electronic front-end circuits of transmitter and receiver where antennas are terminated. Increasing by two times (Fig. 22e) and decreasing by three times (Fig. 22f) of such impedance difference provoke decreasing of resulting signal amplitude registered in TD measurement assembly in Fig. 13. This allows estimating system performances factor degradation that amounts for this case about $L2 \approx -6...-9\text{dB}$.

Obtained figure of total radar system degradation due to antenna $L=L1+L2 \approx -15...-18\text{ dB}$ agrees with estimation in [3] that is sufficient figure for subsurface radar with total performance factor of 120-140dB with the exception of other unfavorable aforementioned factors. Note that presented above experimental figures have been obtained for subsurface antenna measurement too by in more complex way accomplished by antennas in Fig. 18 and Fig. 19.

At the same time, presented experimental studies give some opportunities to solve adaptation problem in subsurface radar by minimization of negative influence of variable operation environment on antenna features. First of all, the effects of impedance mismatch is overcome by electronic tuning of impedance of both front-end circuits of transmitter and receiver that can be implemented for devices in Fig. 20. Correction of changing of antenna electrical length disturbed by sounding medium can be implemented by electronically tuning of antenna accomplished as some non-linear active transmission line. This solution is best one among others like mechanical tuning of distance refelector-antenna or using some hypothetical material with variable dielectric constant filled space inside cavity-backed antenna et cetera. All these issues of antenna adaptation are now in progress and demands additional sufficient research efforts.

Conclusions

This paper dealt with the task of impulse antenna studies in time-domain, especially antennas for subsurface videopulse radar with transient functioning to obtain short-pulse high-resolution performances. One of vital problems of subsurface radar arises from "antenna-sounding medium" interaction makes worse antenna features and ultimately total radar system performances. The research strategy to explore such antennas, developed in this paper and based on discussed above principals, is reasonable and effective to reach practically valuable results. Final goal of investigation conducted here is to seek optimal set of technical measures when subsurface radar's antennas can maintain their main operation function in radar under influence of unfavorable working conditions, i.e. to radiate and to receive electromagnetic signals with given spatial-temporal features.

Starting point of studies of such antennas is systematization of their internal and external operation modes in accordance to the realized electromagnetic excitation and interaction with operation media. The next important step in this exploration involves theoretical models, which are attractive from the authors' point of view due to their analytical simplicity and numerical efficiency that allows employing the universal mathematical software for their treating. The last offers a problem solution within single software with key opportunities of symbolic manipulations, numerical computations and visualization of results.

Let note that a prejudice exists that the TD electromagnetics is more complex to explore than FD one. At the same time, the authors share opinion [15] stated fifty years ago, that direct investigation of TD electromagnetics events by special analytical and numerical methods allows obtaining results distinguished by amazing simplicity of perception and productive physical meaning to understand problem. The presented theoretical part of this paper illustrates this thesis implementation by obtaining valuable results with clear physical pictures of the TD electromagnetics phenomena that are important for academic and engineering goals in general meaning.

As mentioned above, impulse antennas are characterized by the signal waveform transformation to ensure short-time signal with inevitably low pattern features reached simultaneously. From philosophical point of view, one can state that some conservation law of "signal spatial-temporal volume" takes place. Namely, short-time signal can be obtained by finite-size electrodynamics structure at the sacrifice of deterioration signal localization in space, i.e. worsening of spatial distribution of radiated energy. In part, an improving of spatial distribution of signal energy, i.e. antenna pattern, can be reached at the sacrifice of signal stretching in time.

Presented experimental equipment is based entirely on the components of own-designed UWB impulse radar that involves set of active antennas, and electronics units of transmitter, receiver, digital data registration and processing, computer interface and signal processing software. The developed module architecture of radar allows carrying out all necessary antenna TD studies in free-space and for subsurface sounding. Some experimental series have been performed to confirm the validity of the proposed theoretical concepts and to study experimentally some complex aspects of problems, including antenna disturbance by medium under radar survey. Numerical estimation of radar performances deterioration due to antenna improper operation has been obtained in original way without complex time-spending experiments that reaches about -15...18 dB for radar performance factor. Applied way of such estimation gives simultaneously technical solution to minimize this effect by adaptation where alignment of impedance mismatch between disturbed antenna and transmitter/receiver front-end circuits is employed.

Some aspects of presented above studies are now in progress including non-linear antennas with some signal processing and adaptation opportunities, effects of non-uniform and stochastic nature of sounding media, influence of random rough surface on border between two media, improvement of signal processing of radar data based on antenna behavior and so on.

Acknowledgements

The author wish to thank to Mr. and Mrs. Schakirows, to Mr. and Mrs. Boryssenkos for all kinds of support of presented studies.

References

- [1] M.I. Finkelstein, V.L. Mendelson, V.A. Kuteev. *Radar for Sensing of Layered Subsurface Regions*, Sov. Radio, Moscow, 1977.
- [2] H.F. Harmut. *Nonsinusoidal Waves for Radar and Radio Communication*, Academic Press, New York, 1981.
- [3] J.D. Young, L. Peters Jr. "A Brief History of GPR Fundamentals and Applications", *Proceedings of the 6th International Conference on Ground Penetrating Radar*, Tohoku, Japan, 1996, pp. 5-14.
- [4] R.V. de Jongh, L.P. Ligthart, I.V. Kaploun, A.D. Schukin. "Design and Analysis of New GPR Antenna Concepts", *Proceedings of the 7th International Conference on Ground Penetrating Radar*, Lawrence, USA, 1998.

- [5] G. Franceschetti, C.P. Papas. "Pulsed Antennas", *IEEE Trans. on Antenna and Propagation*, Vol. AP-22, No. 5, 1974, pp. 651-661.
- [6] N. Zaiping. "Radiation Characteristics of Traveling-Wave Antennas Excited by Nonsinusoidal Currents", *IEEE Trans. on Electromagnetic Compatibility*, Vol. EMC-25, No. 1, 1983, pp. 24-661.
- [7] A. Shlivinski, E. Heyman. "Time-Domain Near-Field Analysis of Short-Pulse Antennas", *IEEE Trans. on Antenna and Propagation*, Vol. AP-47, No. 2, 1999, pp. 271-286.
- [8] S.A. Schelkunoff. "Theory of Antennas of Arbitrary Size and Shape", *Proceedings of the IEEE*, Vol. 72, No. 9, 1984, pp. 1165-1190.
- [9] J.D. Young, D.E. Svovoda, D.W. Burnside. "A Comparison of Time- and Frequency Measurement Techniques in Antenna Theory", *IEEE Trans. on Antenna and Propagation*, Vol. AP-21, No. 7, 1973, pp. 581-583.
- [10] A.O. Boryssenko. "Analytical Time-Domain Model of Impulse Antenna", *Proc.s of Int. Symp. on Electromagnetic Theory*, Thessaloniki, Greece, May 1998, Vol. 2, pp. 545-547.
- [11] A.O. Boryssenko. "Time-Domain Studies of Ultra-Wide Band Antennas", *Proc. of the 1999 IEEE Canadian Conf. on Electrical and Computer Engineering*, Edmonton, Canada, 1999.
- [12] A.O. Boryssenko. "Time-Domain Experimental Studies of Ultra-Wide Band Antennas", *Proc. of 22nd ESTEC Antenna Workshop on Antenna Measurements*, ESTEC, Noordwijk, Netherlands, 1999, pp. 101-106.
- [13] A.O. Boryssenko. "The Lateral Wave Phenomenon of Ground Penetrating Radar Survey", *Proc. of IEEE 1999 Int. Geoscience and Remote Sensing Symp.*, Hamburg, Germany, 1999.
- [14] S. Ramo, J. Winnery, J. Van Duzer. *Fields and Waves in Communications Electronics*, J. Wiley and Sons, New York, 1984.
- [15] A.A. Charkevitch. *Unsteady Wave Phenomena*, Moscow, 1950.

INTEGRATED OMNI-DIRECTIONAL MICROSTRIP ANTENNA SYSTEM ON A BALLISTIC HELMET

Dr. Probir K. Bondyopadhyay
GSA SYSTEMS INC.
14418 Oak Chase Drive
Houston, Texas 77058
E Mail : p.bondy@worldnet.att.net

ABSTRACT

Invention of a novel integrated conformal microstrip antenna system on a soldier's helmet is described. Using part of the Kevlar material as the substrate material, microstrip antennas have been fabricated in the ballistic Kevlar helmet and tested for performance in an omni-directional communication system applications for battlefield communications.

1. THE INTEGRATED CONFORMAL ANTENNA DESIGN

The schematic of the integrated conformal, circular polarized, microstrip antenna system on a ballistic Kevlar helmet is shown in Figure 1.

United States Patent (19)		(11) Patent Number:	5,886,667
Bondyopadhyay		(45) Date of Patent:	Mar. 23, 1999
(54) INTEGRATED MICROSTRIP HELMET ANTENNA SYSTEM		5,231,408 7/1993 Sennarasa	343700 MS
(76) Inventor: Probir K. Bondyopadhyay, 14418 Oak Chase Dr., Houston, Tex. 77058		5,176,842 12/1994 Shiga	343700 MS
(21) Appl. No.: 926,836		5,438,702 8/1995 Jackson	43589
(22) Filed: Sep. 10, 1997		5,354,985 9/1994 Joo	343700 MS
Related U.S. Application Data		Primary Examiner—Don Wong	
(50) Provisional application No. 60/027,177, Oct. 1, 1996.		Assistant Examiner—Tan Ho	
(51) Int. Cl. ⁶ H01Q 1/38; H01Q 1/12		Attorney, Agent, or Firm—Marvin J. Maruck	
(52) U.S. Cl. 343/700 MS; 343/718		(57) ABSTRACT	
(53) Field of Search 343/700 MS; 343/718		An integrated helmet and omnidirectional microstrip antenna system comprising a ballistic helmet constructed of rigid non-metallic material with a sheet of dielectric material as the top layer thereof and an omnidirectional microstrip antenna system having one or more antenna radiator elements affixed to the top surface of the dielectric sheet. The antenna radiator elements are circularly polarized by a microstrip feed network designed to provide circular polarization of a desired sense. A conductive layer of metallic material bonded to the underside of said dielectric sheet and integrated in the helmet structure serves as the electrical ground for the antenna.	
(56) References Cited		21 Claims, 9 Drawing Sheets	
U.S. PATENT DOCUMENTS			
3,542,951 6/1971 Almyre		343718	
3,977,000 8/1976 Kasher		343718	

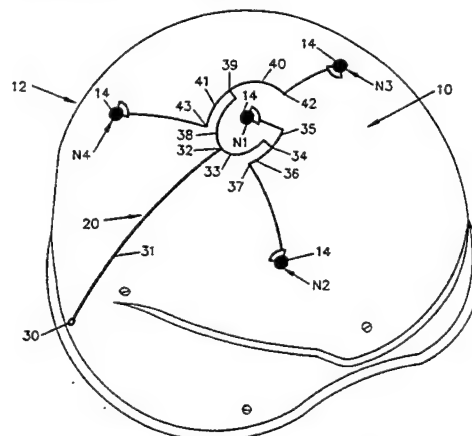


Figure 1. An outline of the integrated conformal microstrip antenna on a ballistic helmet.

For robust and durable communications, dismounted war fighters need efficient antennas that remain reasonably matched to the communication system in a mobile environment over the required frequency band. The top surface of the ballistic Kevlar helmet provide the prime real estate for integrating a conformal antenna operating in frequency bands in the 1 GHz - 30 GHz range. For terrestrial communication, like a localized communication environment in the battle field operating in the 1GHz - 3 GHz frequency range, microstrip antennas can be integrally fabricated using part of the Kevlar material as the substrate. Whereas for satellite communications, in the higher end of the frequency spectrum(10 GHz and

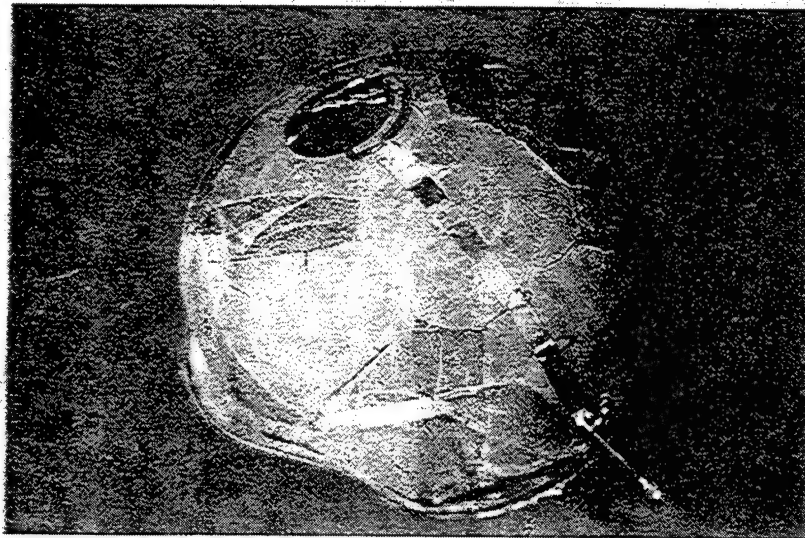




Figure 2. A circular polarized circular microstrip patch integrated into an actual ballistic helmet is shown here.

above) thin substrates are needed and the substrate material like thermount polyimide substrates, or better thin substrates, could be molded into the helmet during the helmet manufacturing process without causing appreciable weight increase.

For operation around 1.8GHz, several helmets with integrated microstrip antennas have been fabricated. During the helmet manufacturing process, in the preforming stage, a thin conducting screen mesh was placed in the middle layer and molded into the helmet. The conducting screen provides the antenna ground surface.



BALLISTIC DATA SHEET
 ARMY RESEARCH LABORATORIES
 PERSONNEL VULNERABILITY TEAM
 PEEP SIGHT RANGE 20



CUSTOMER: MAHANAD COMMUN

SAMPLE ID & DESCRIP: PASGT HELMET W/ALUM. SCREEN INSIDE & COPPER ON OUTSIDE

OBLIQUITY: 0 DEG **OTHER:** V-50

DATE: 12-18-97 **0.5** **DIST (m):** **0.25** **PROJECTILE:** 17GR FSP/STEEL

LOAD (g)	TYPE	ROUND NO.	STRIKE TIME (μSEC)	VEL-(-) (m/s)	RESIDUAL TIME (μSEC)	VEL-(-) (m/s)	RESULTS
0.375	BE		1003	499			vel
0.500	BE	1	820	610			PP
0.550	BE	2	777	644			CP
0.530	BE	3	799	626			PP-IMPACT ON EAR FLAP
0.540	BE	4	782	639			PP-DELAMINATED INTERIOR OF HELMET
0.550	BE	5	777	644			CP
0.540	BE	6	800	625			CP-IMPACT ON COPPER LAYER
0.540	BE	7	784	638			PP-IMPACT ON COPPER LAYER
0.540	BE	8	783	639			CP-IMPACT ON COPPER LAYER
0.540	BE	9	796	626			CP-IMPACT ON COPPER LAYER
0.530	BE	10	797	627			PP-IMPACT ON COPPER LAYER

These V₅₀'s compare favorably with others generated on the PASGT helmet.

12/18/97 [Signature]

V50, WHOLE HELMET = 631.8 M/S, 2073 F/S
 V50, KEVLAR ONLY = 638.3 M/S, 2095 F/S
 V50, KEV + COPPER = 629 M/S, 2064 F/S

THIS IS NOT AN OFFICIAL ENDORSEMENT OF THIS PRODUCT

TYPE CODE: BE= BULLEYE
CC= 2400

SCREEN (2) TO TARGET: 0.25
TARGET TO SCREEN (3): NOT USED

DD= 4895
EE= OTHER: _____

DATA COLLECTOR: RKANE

Figure 3. The results of the successful ballistic test on the PASGT Kevlar Helmet.

It also will act as the electromagnetic or microwave shield for the head of the soldier. The screen adds very little to the weight and allows bonding resins to pass through without degrading the integrity of the helmet structure. Thin copper sheet was molded onto the top surface during the one step helmet manufacturing process.

Ballistic tests were performed at U.S Army Aberdeen Proving Ground to confirm that this modified structure meets the performance standards.

2. EXPERIMENTAL RESULTS

The microstrip patch antenna was etched into the top surface using a special fabrication technique. Open microstrip line as well as shielded thin strip lines were used to feed the patch antenna at the top surface of the helmet. In excess of 80 MHz bandwidth was obtained at 1.8GHz center frequency. The open microstrip line was found to be lossy if the helmet material is used as its substrate and because of the curvature of the surface, excessive radiation losses occurred. Both of these problems were eliminated by using thin shielded stripline feed bonded into the top surface.

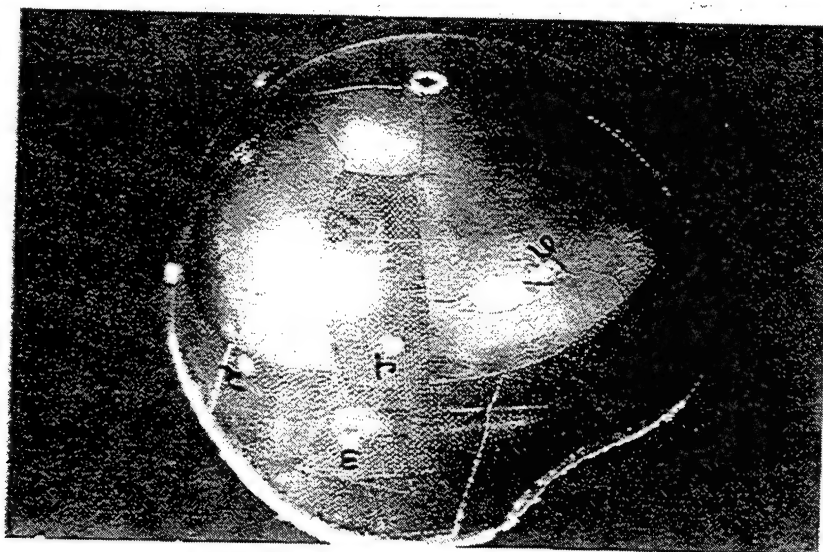


Figure 4. The Kevlar ballistic helmet with the bonded copper sheet on the top surface. It passed the ballistic test. The projectile holes are visible.

It was found that sufficiently thick copper sheets need to be used for bonding onto the top surface of the helmet for microstrip antenna fabrication because the pressure applied during the one step helmet manufacturing process is quite high.

Antenna patterns were measured. It was found that unless the feed lines are shielded, radiation from the feed line significantly distorts the antenna pattern.

One advantage of this antenna is that it is hidden with the helmet external surface coating and could be used in search and rescue operations for missing soldiers.

3. REFERENCES

- [1] P. K. Bondyopadhyay, "Integrated Microstrip Helmet Antenna System", U.S. Patent No. 5,886,667, March 23, 1999.

CIRCULAR POLARIZED MICROSTRIP LENS ARRAY ANTENNA SYSTEM FOR SATELLITE SIGNAL RECEPTION

Part 1. Preliminary Design Considerations

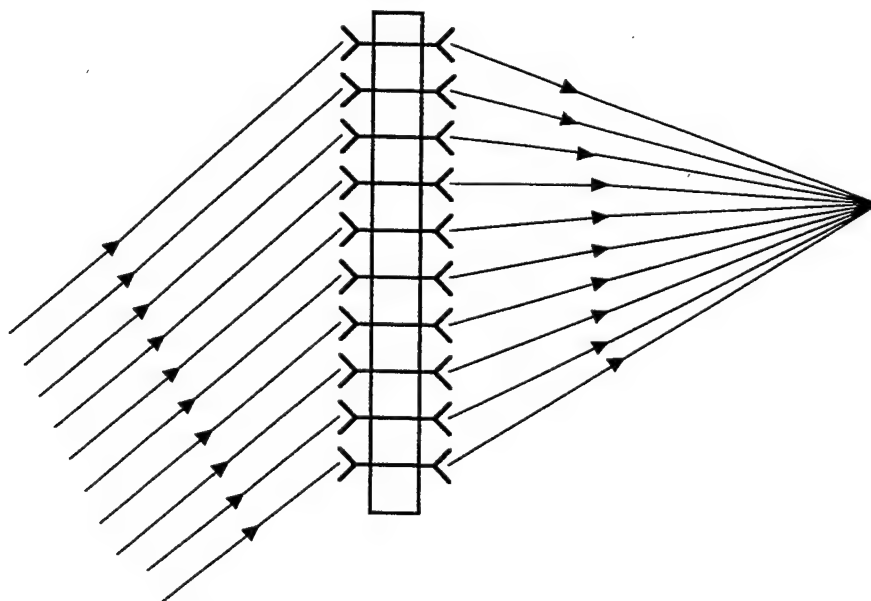
Dr. Probir K. Bondyopadhyay
GSA SYSTEMS INC.
14418 Oak Chase Drive
Houston, Texas 77058
E Mail : p.bondy@worldnet.att.net

ABSTRACT

Invention of a novel planar microstrip lens array[1] that receives circular polarized microwave signal from any given direction on one side and focuses the signal at any point on the other side *without requiring any phase shifters* is described. This antenna has applications in receiving broadcast signals at home through the roof from geosynchronous satellites.

1. PRINCIPLES OF THE LENS ANTENNA DESIGN

The schematic of the circular polarized planar microstrip lens array is shown in Figure 1. A planar array of circular polarized microstrip element clusters receive satellite signals from any chosen direction and transmits it to the other side to focus



Circular Polarized Microstrip Lens Array

Figure 1. Circular polarized microstrip lens array for satellite signal reception.

at any arbitrarily chosen point as depicted in the diagram. A planar $N \times N$ array of sensors can be designed to receive plane wave signals from a given direction by providing the array elements with a linear phase gradient pertinent to that direction.

In particular, consider a planar array of $N \times N$ elements. The m th element is located at (x_{mn}, y_{mn}) in the Cartesian coordinate frame. The array is at $z = 0$ plane and the origin is at the center of the array.

1.1 The Focusing Action

Let the array elements focus the signal at the point **F** located at (x_F, y_F, z_F) . The distance between the m th element and the focal point is

$$d_{mn} = \sqrt{(x_F - x_{mn})^2 + (y_F - y_{mn})^2 + z_F^2} \quad \dots (1)$$

The m th element is provided with a phase shift of $e^{j\frac{2\pi}{\lambda_0}d_{mn}}$ where λ_0 is the wavelength at the center frequency of operation. The uniformly excited array will then focus at point **F**. The focusing action can be numerically verified by computing and plotting the array factor of the planar array:

$$\text{Array Factor} = \sum_{m=1}^N \sum_{n=1}^N A_{mn} e^{j\frac{2\pi}{\lambda_0}d_{mn}} e^{-j\frac{2\pi}{\lambda_0}\sqrt{(x-x_{mn})^2 + (y-y_{mn})^2 + z^2}} \quad \dots (2)$$

For a 16×16 element square array with element spacings of $d_x = d_y = 0.6\lambda_0$ and uniform excitation, the array factor magnitude has been computed and is shown in Figure 2. The focus is at $(0, 0, 5\lambda_0)$. The focusing action is clearly visible.

1.2 The Phase Shift for the Focusing Action

The relative phase shifts to the circular polarized antenna elements (or cluster elements in the present case) corresponding to the respective focal path lengths in (1) are provided by relative rotation of the elements (or clusters) around its axis with respect to the reference axis of the array. The antenna elements are discussed next.

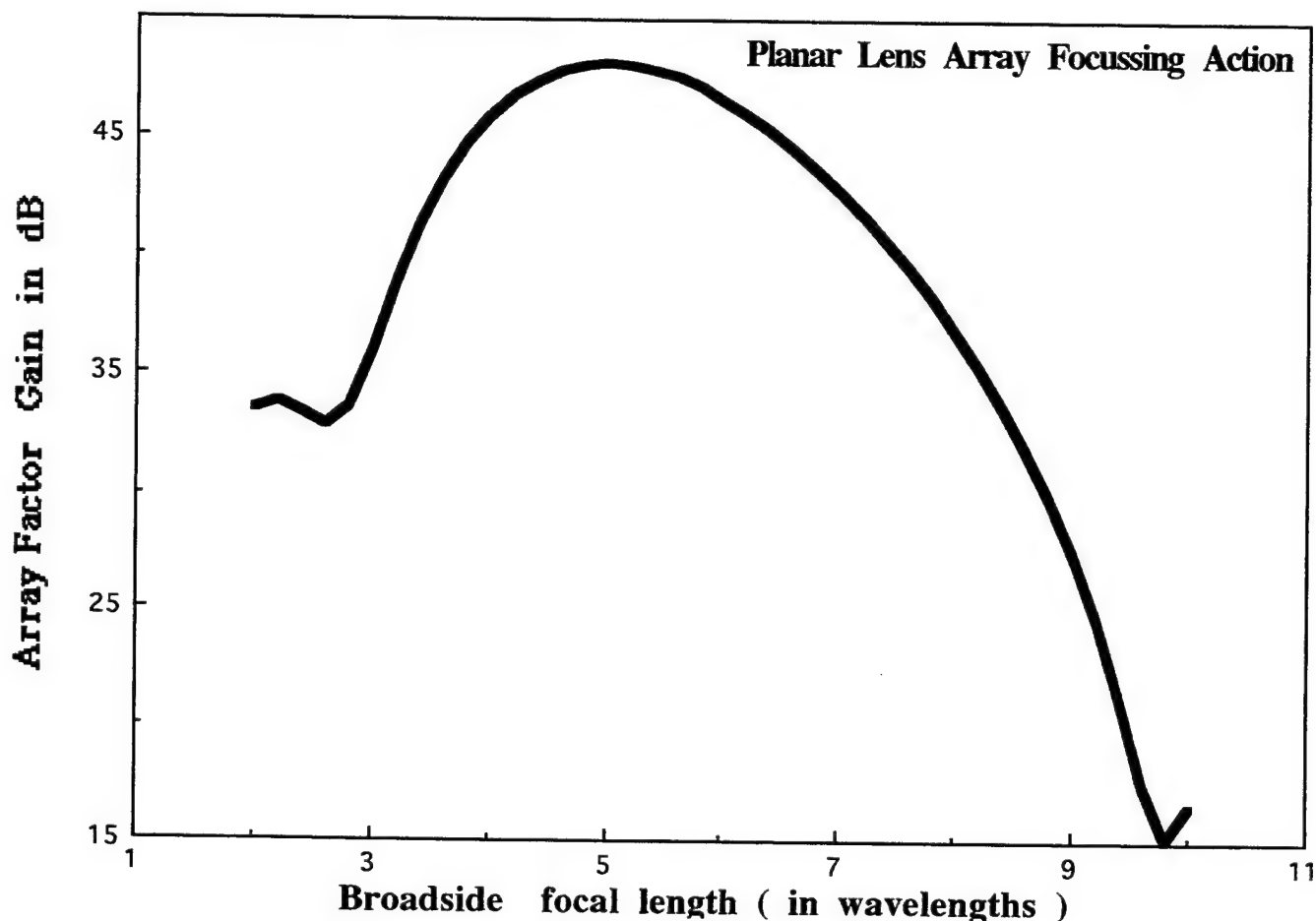


Figure 2. The focusing action exhibited by the array factor of the 16x16 element array.

2. CIRCULAR POLARIZED LENS ARRAY ELEMENT

As shown in Figure 3 and 4, the planar lens array element on both sides is a 2x2 cluster of circular polarized microstrip antennas. The elements could be either circular or square; each element of the cluster is circular polarized with dual microstrip line feed. Sequential rotation and phasing technique has been applied to the 2x2 cluster to increase the axial ratio bandwidth as well as the impedance bandwidth.

The feed structure is matched at the center frequency with a 50 ohm end feed line which is appropriately terminated such that the 2x2 cluster performs as a circular polarized (in this case RHCP) resonant 'tank circuit' or reservoir of the received as well as retransmitting signal. The printed clusters on two sides are

conductively connected with coaxial feed lines. It is possible to introduce fixed attenuators or LNA's along this connecting lines to provide predetermined amplitude tapers to improve the side lobe levels of the focusing planar array.

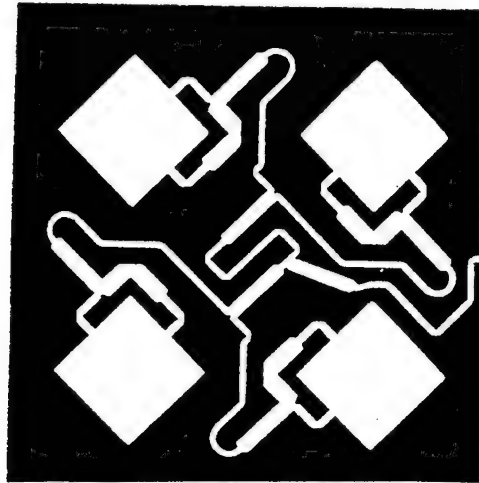


Figure 3. Schematic of the 2x2 circular polarized microstrip antenna element cluster receiving right circular polarization. This is the antenna element building block for this novel planar lens array.

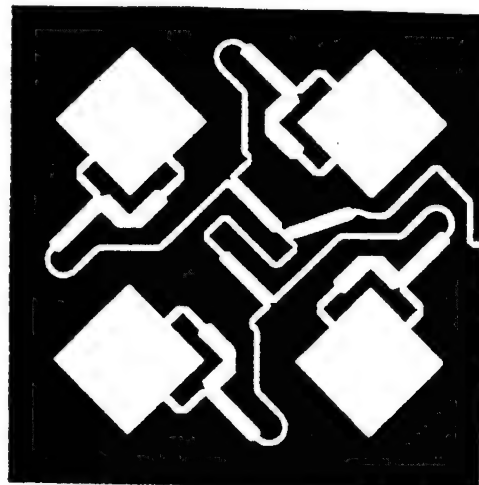


Figure 4. Schematic of the 2x2 circular polarized microstrip antenna element cluster receiving left circular polarization. This is the antenna element building block for this novel planar lens array.

3. PRELIMINARY EXPERIMENTAL RESULTS

The antenna cluster elements shown in Figure 3 and 4 have been designed built and tested[2] in the Ku band as well as in Ka band. A sixteen element subarray built on a 10 mil(0.254 mm) thick low loss substrate is found to have well over 1 GHz bandwidth (axial ratio as well as impedance bandwidths) at 29.5GHz center frequency.

The design is to be optimized by experimental iterations and tuning stubs are to be generally avoided. A superstrate layer of similar radiating elements are placed on top of this array layer with electromagnetic coupling to avoid exposing the cluster element feed lines.

There are several ways dual circular polarization operations could be realized. One of them being having the two dimensional array with alternate positioning of RCP and LCP elements. In stead of the four element cluster, sixteen element clusters are also the possibility.

Efforts are underway to extend this subarray based phase shifter less lens array to the non planar case in the form of a parabolic toroid to explore the possibility of LEO satellite signal reception[1].

4. PRACTICAL APPLICATIONS

The novel planar lens array described above has direct practical applications in the reception of satellite or terrestrial signals in the microwave and millimeter wave frequency bands at home, office buildings and other structures. This planar lens array will merge with the planar roofs or walls and the signals are received inside at a convenient fixed location thus eliminating the need for a nonconformal dish. This lens can be designed for either sense of circular polarizations or for dual circular polarizations.

5. REFERENCES

- [1] Probir K. Bondyopadhyay, "Circular Polarized Microstrip Lens Array for Satellite Signal Reception, U.S. Patent Application, United States Patent and Trademark Office, Washington, D.C. November 1998.
- [2] P. K. Bondyopadhyay, "High Performance Circularly polarized microstrip array antenna ", NASA Johnson Space Center, Houston, U.S. Patent No. 5,661,494, 26th August 1997.

Antenna Applications Symposium
University of Illinois
September 15-17, 1999

Performance Testing of a Wideband Phased Array for Shipboard Application

By

Peter Beyak, Dan Bobowicz and Don Collier
Northrop Grumman Corp.
Baltimore, MD

1. Abstract:

In a joint venture with the Naval Research Laboratory (NRL), engineers from Northrop Grumman have designed and fabricated a wideband phased array transmitting antenna to meet the Navy's ECM (Electronic Countermeasures) needs into the 21st Century. This Advanced Technology Demonstration (ATD) antenna underwent extensive range tests in 1998 and the spring of 1999. At sea testing was completed in July of this year.

Unique features of this 2-D scanned array include time delay beam steering using a photonics feed manifold that limits frequency dispersion losses and undesirable time delay grating lobes. The utilization of a photonic feed also permits the location of the beam steering computer and RF transmitter well inboard of the array, as much as two hundred feet removed from the antenna. This represents an important cost savings, because the operating environment below decks is much less severe for this equipment. By limiting the frequency dispersion, a wide instantaneous bandwidth can be achieved.

The rectangular transmit array consists of 480 radiating elements, 240 horizontally oriented, 240 vertically oriented. Each element is a patented stepped notch radiator design, which features a stable beamwidth with good impedance match over a frequency bandwidth in excess of 1.5 octaves.

Photographs, block diagrams and a partial array of the radiating elements will be included in the presentation, as well as far field patterns of the antenna under test.

2. Background

This paper complements a technical paper delivered at the 1997 Antenna Applications Symposium. The first paper was essentially a progress report on the design, development and testing of the Northrop Grumman/ NRL wideband ECM transmit array. The following presentation reports on the outdoor range and at-sea test phases of this on-going project.

The Advanced Technology Demonstration (ATD) transmit antenna described in this paper is an active ECM array capable of scanning in azimuth and elevation, and was designed to provide fleet protection over a wide frequency bandwidth.

2.1 ECM Transmitter Block Diagram

As illustrated in Figure 1, the ECM Transmitter is partitioned into outboard and inboard subsystems, to allow operation of the signal formation and control section in a moderate environment within the ship, while the antenna portion is mounted at an optimum site on the ship structure for proper angular coverage.

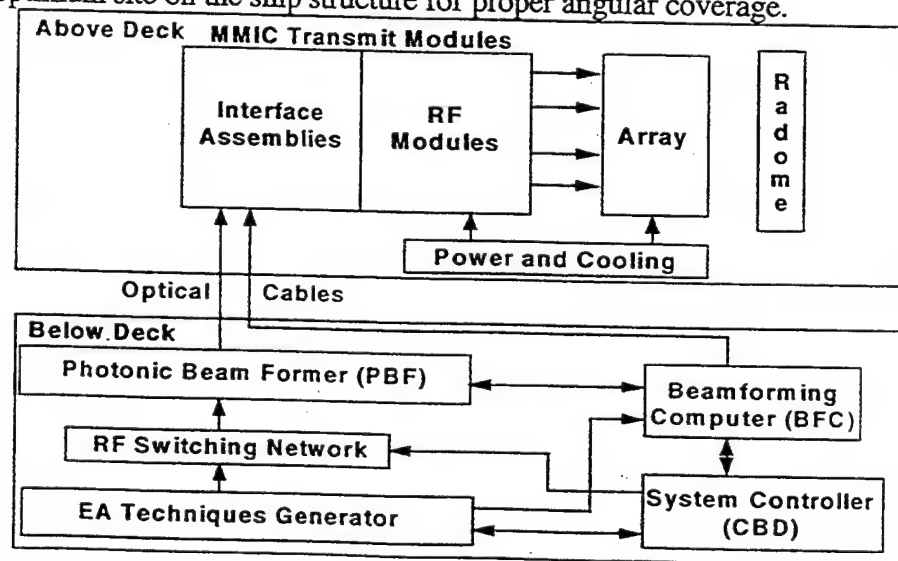


Figure 1 - ECM Transmitter Functional Block Diagram

With the exception of the Beamforming Computer (BFC), NRL engineers designed and built all the below decks equipment, and Northrop Grumman engineers designed and built all the above decks equipment.

The planar array in the outboard section of the ECM Transmitter is an active aperture design (a power amplifier and phase shifter accompany each radiating element) which permits a modular, platform-adaptable approach. Sections of the array face can be allocated to counter separate, specific in-coming threats. The array consists of radio frequency (RF) photo-detectors, power amplification and phase shift modules, a planar aperture of radiating elements and a wideband radome. The inboard section is made up of a fiber-optic beamforming, switching and distribution network, along with a waveform/techniques generator for RF signal generation. The complete ECM Transmitter System forms and radiates the required number of beams at selected power levels, time intervals, frequencies, and pointing angles in either simultaneous or time shared modes.

2.2 The Transmit Array

The ECM System Transmit array is illustrated in the functional schematic of Figure 2.

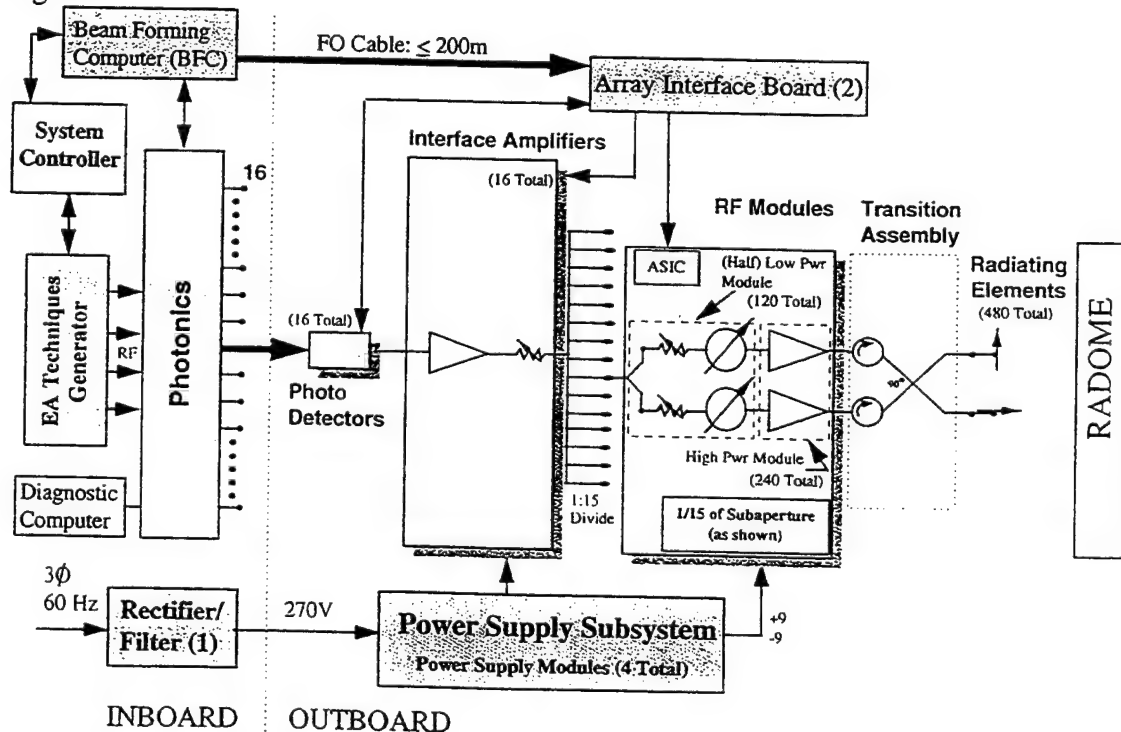


Figure 2. ECM System Functional Schematic

The transmit array consists of four subarrays, each independently controlled to form and point/steer a beam. RF-modulated photonics energy is transmitted from below decks via 16 fiber-optic cables to Photo Detectors located in the 16 transmit array subapertures. See Figure 3 for array nomenclature.

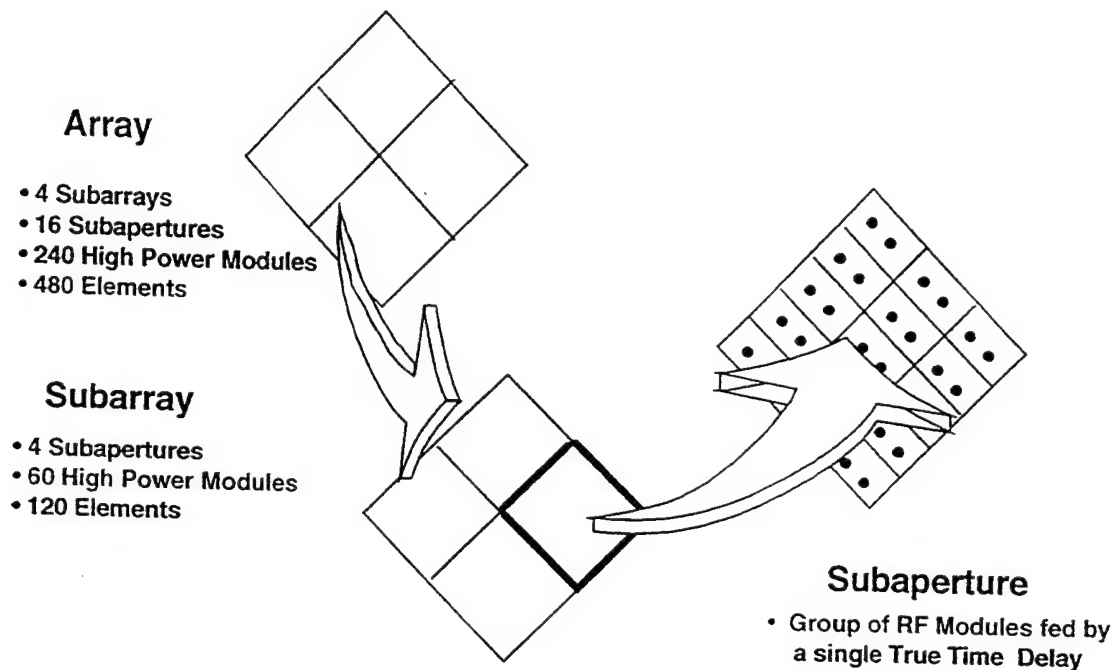
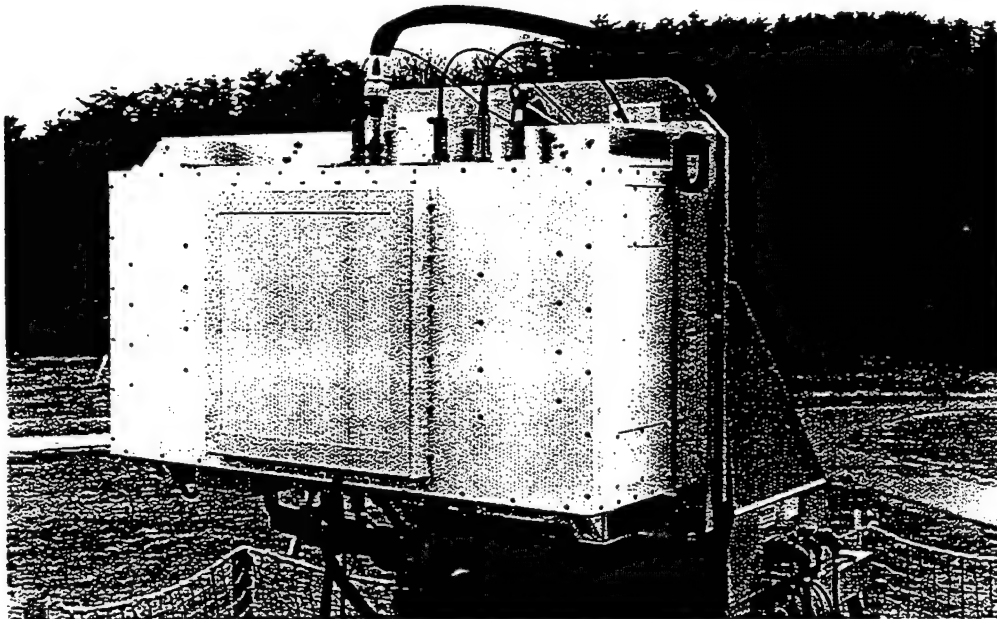


Figure 3. Array Nomenclature

The Photo Detectors recover the RF and convey it to one of 16 Interface Amplifiers, where array gain control is performed in cases where non-uniform power distribution is required. The RF then passes through a 1-to-15 stripline power divider to low- and high-power modules, where the digital phase shifters and final stage amplifiers are located. The active aperture planar array has sufficient radiating elements and associated Microwave Monolithic Integrated Circuit (MMIC) power amplifiers to achieve the effective radiated power (ERP) needed to protect the ship from incoming missile or aircraft attack radars. A wideband radome provides antenna protection from the environment with minimal impact on antenna performance.

3. Range Testing

After assembly and extensive bench testing in a Northrop Grumman engineering laboratory, the transmit array was conveyed to the far field range at Linthicum, Maryland, where it was linked to the NRL photonics unit for software de-bugging and array calibration. Figures 4 and 5 show the assembled antenna mounted for testing on the far field range. The antenna is rotated on its pedestal 45 degrees to measure an intercardinal axis.



4. . Array Mounted for Testing at Outdoor Antenna Range with Radome in Place

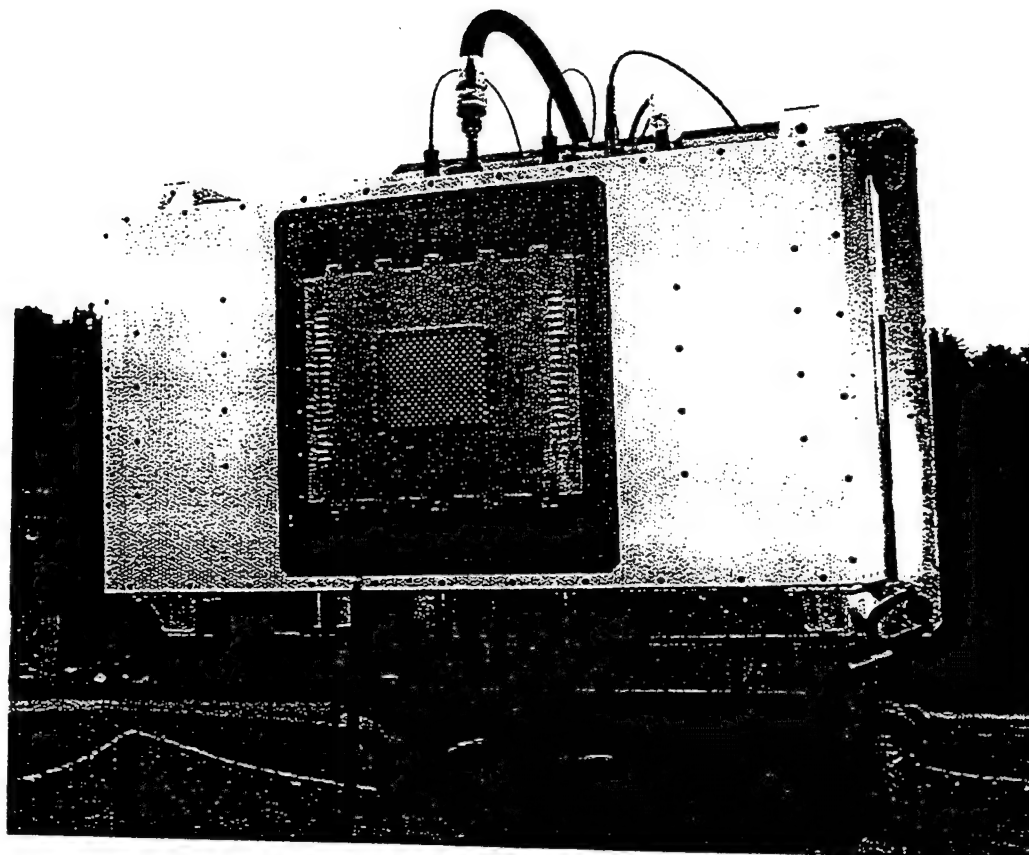


Figure 5. Array Mounted for Testing with Radome Removed

When installed on board ship, the array antenna is oriented in a diamond configuration to minimize sidelobes on the principal azimuth and elevation axes. The array consists of 240 pairs of wideband, stepped notch radiating elements aligned vertically and horizontally. Several radiator designs were considered, including the stripline exponential notch, but investigation by computer simulation showed that over the required frequency bandwidth, the stepped notch performed best. The limited interelement spacing imposed by the need to minimize grating lobes at extreme scan angles was an important factor. A closeup of the array face with the radome removed is shown in Figure 6.

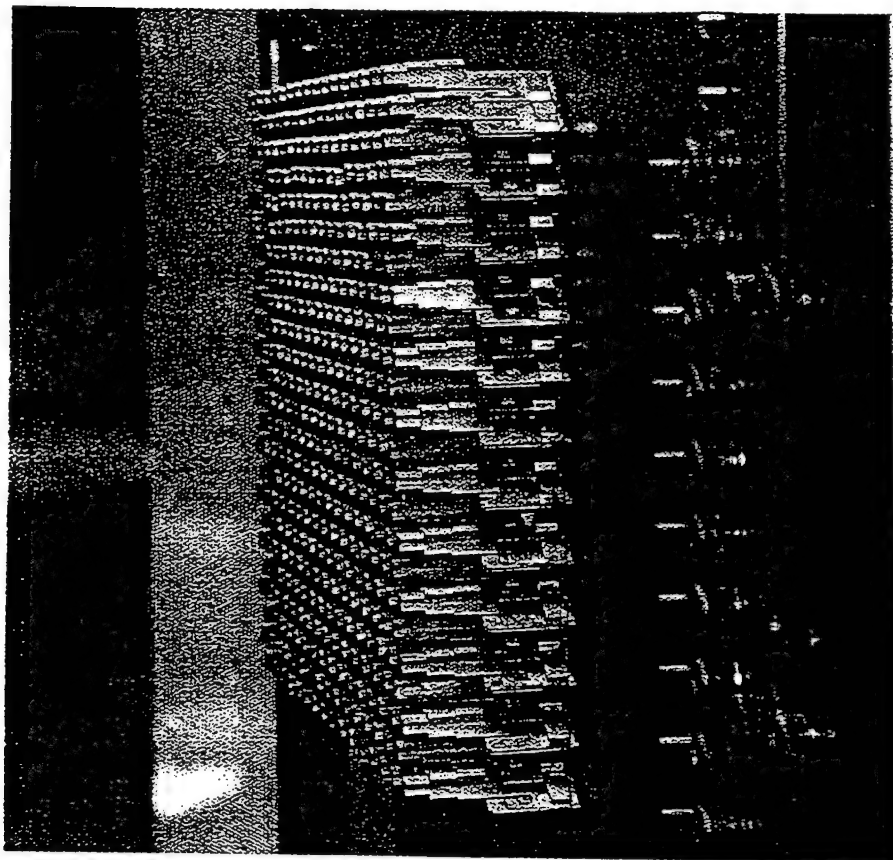


Figure 6. Array Showing Detail of Individual Radiating Elements

The notch radiators transition from coaxial push-on connectors to stripline to slot-line to free space. Impedance matching at each stage is achieved using Northrop Grumman-developed optimization routines. The stepped notch design itself is described in two Northrop Grumman patents (See References 1. And 2.). Details of the individual stepped notch element design can be seen in the photo of Figure 7.

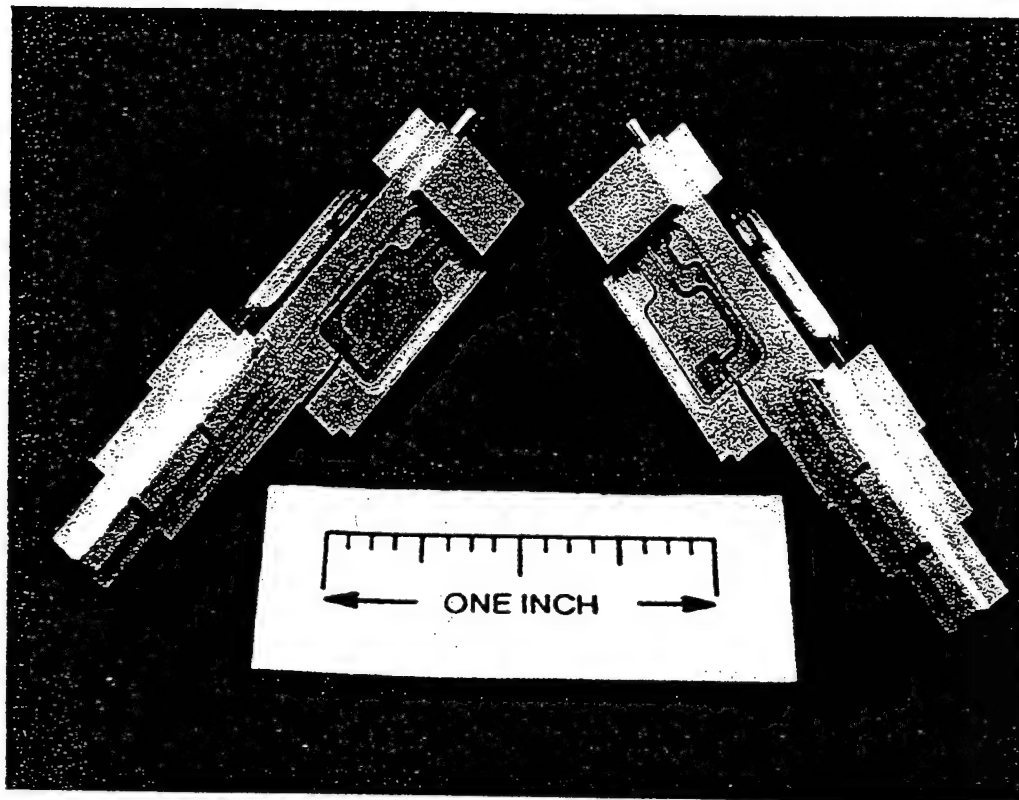


Figure 7. Radiating Elements With Ground Plane Cover Removed, Showing Stripline Feeds

3.1 Antenna Element Patterns

Prior to transporting the assembled antenna to the far field range, the array was mounted in an indoor anechoic chamber and patterns were measured on individual radiating elements over a 1.5 octave frequency band.

Figure 8 shows four patterns of an individual radiating element taken in the E- and H- planes, at the high and low frequency extremes. The pattern shapes remain similar, permitting the array antenna to scan over wide angles, regardless of the operating frequency. Cross-pol radiation was also recorded.

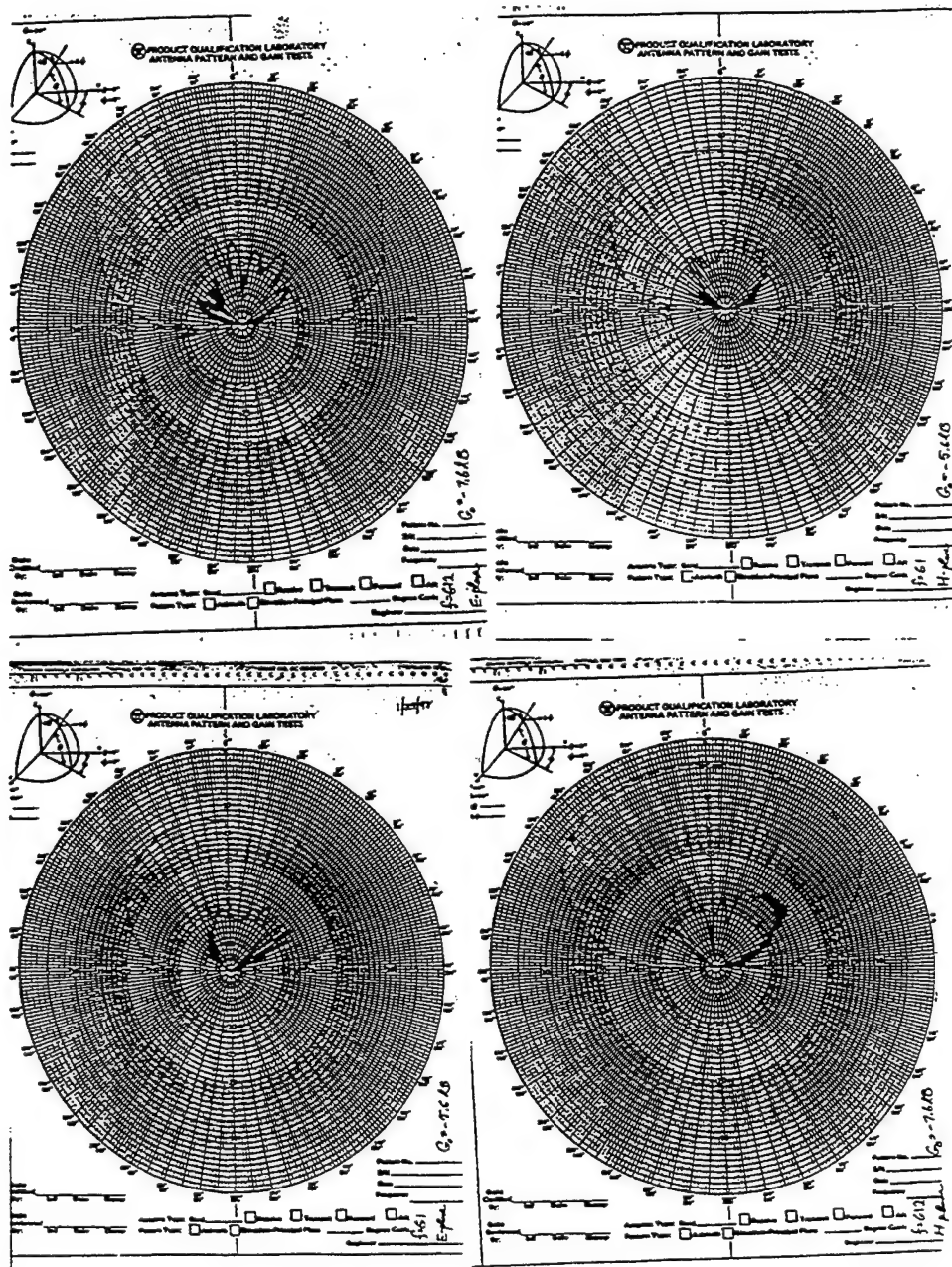


Figure 8. E- Field and H- Field Element Patterns Taken at Two Frequencies
1.5 Octaves Apart

3.2 Phase Shifter Linearization

The Northrop Grumman phase shifters employed in this array were located in the Low Power Modules to minimize RF power handling requirements. They consisted of gallium arsenide MMIC devices with FET switching, and were digitally controlled from the beamforming computer below decks.

Slight variations in individual phase shifter performance, caused by built-in manufacturing tolerances, were expected. As each phase shifter was cycled from 0 to 354 degrees, deviations in the slope from one shifter to the next were noted. It was therefore necessary to linearize each of the 480 phase shifters in the array. This was accomplished digitally with aid of the beamforming computer, and results were stored in RAM files in the computer.

3.3 Array Calibration

When phase shifter linearization was completed, the transmit modules were next calibrated. This step is required to assure a uniform phase front when RF is radiated by the individual transmit elements. Small variations in path length from the photonics detectors through the amplification stages and phase shifters to the array radiating elements must be compensated for by calibration of each RF channel. This is accomplished by causing each channel to radiate individually on the far field range, detecting the energy received, and correcting the phase with the aid of the beamforming computer. Once these preliminary steps were completed, pattern testing could begin.

3.4 Pattern Testing

After completion of the transmit array linearization and calibration procedures, the photonics unit was transported to the Northrop Grumman outdoor range from the Naval Research Laboratory near Washington. The photonics unit included eight wavelength-tuneable lasers, two for each antenna subarray. Several weeks were required to set up and integrate the two systems, after which pattern testing commenced.

As a result, the quality of the array patterns improved considerably. Figure 9 is a typical pattern taken at a frequency near the low end of the array pass band.

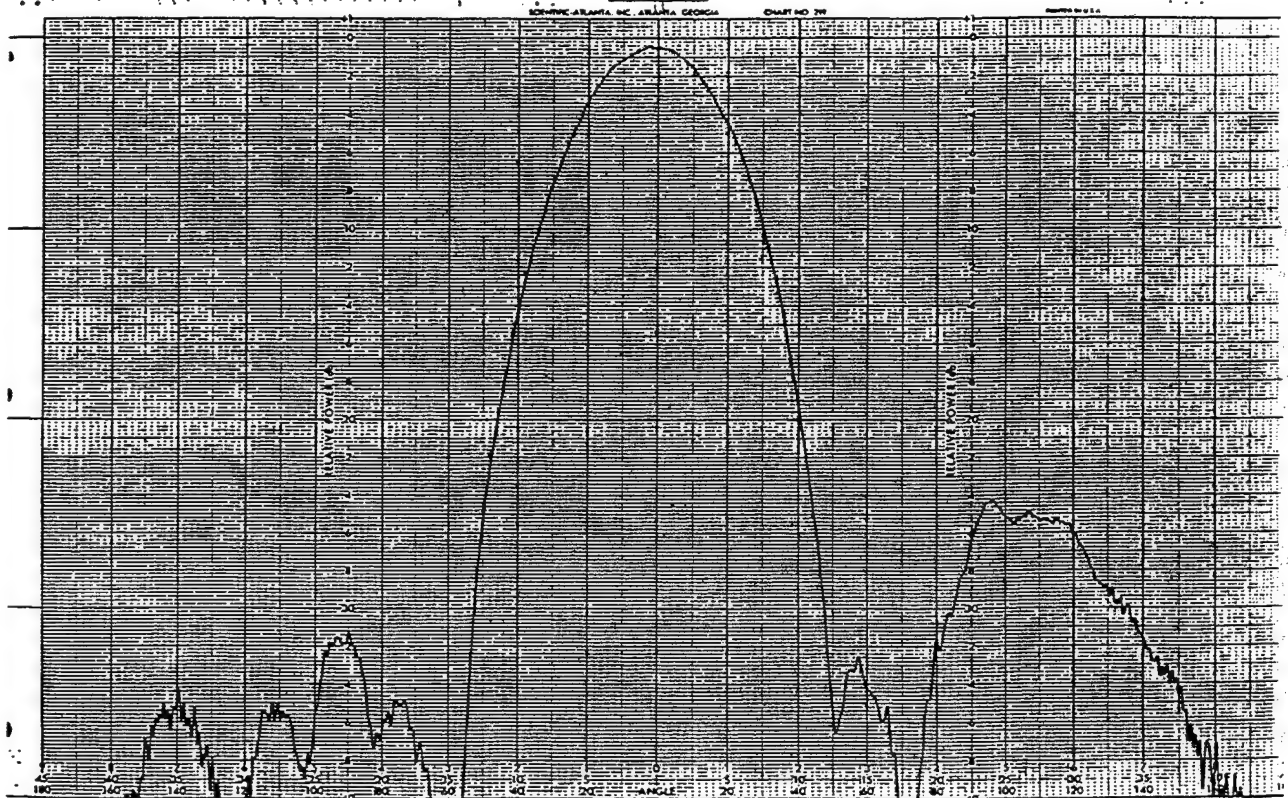


**Figure 9. A Typical Array Pattern at Low Frequency
Phase Errors Nulled Out**

The antenna modules transmitted equal power, producing a uniform amplitude distribution across the array face. However, since the antenna was mounted in the

diamond configuration, computer simulations predicted sidelobes in the -20 to -24 dB range along the principal axes, which proved accurate in most cases. Individual transmit modules performed better at some frequencies than at others, consequently there was variation noted, depending on desired frequency and polarization.

3.4.1 Cross-Polarization Component

The amount of RF energy wasted in cross-polarization was of interest to the Navy project managers. Depending on the tactical requirements, RF was transmitted through a 90 degree hybrid coupler to either of two radiating elements. Since the couplers are not perfect, some energy radiates in the unwanted polarization orientation. Figures 10a and 10b illustrate cross-polarization levels for beams in the unscanned and scanned positions.

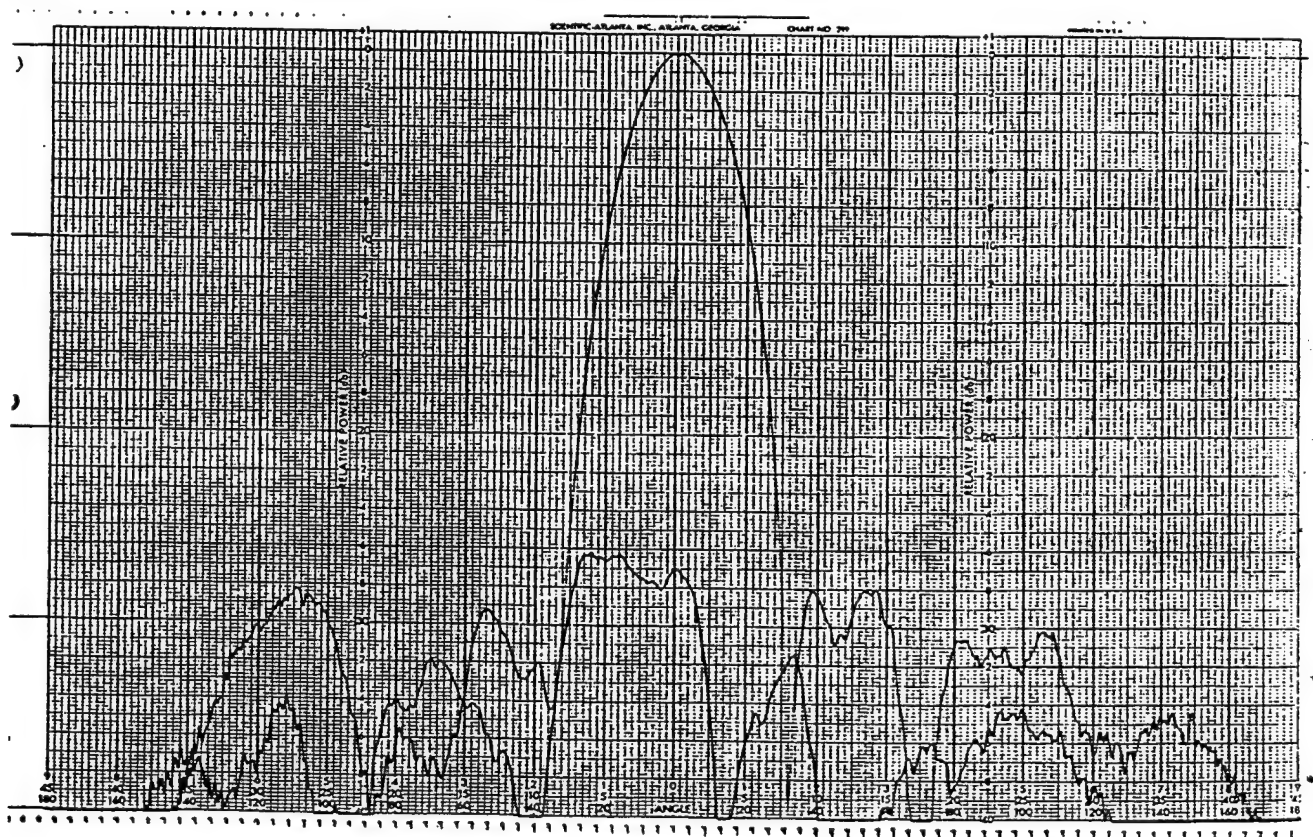


Figure 10a. Azimuth Pattern Near Center Frequency Showing Cross-Polarized Component

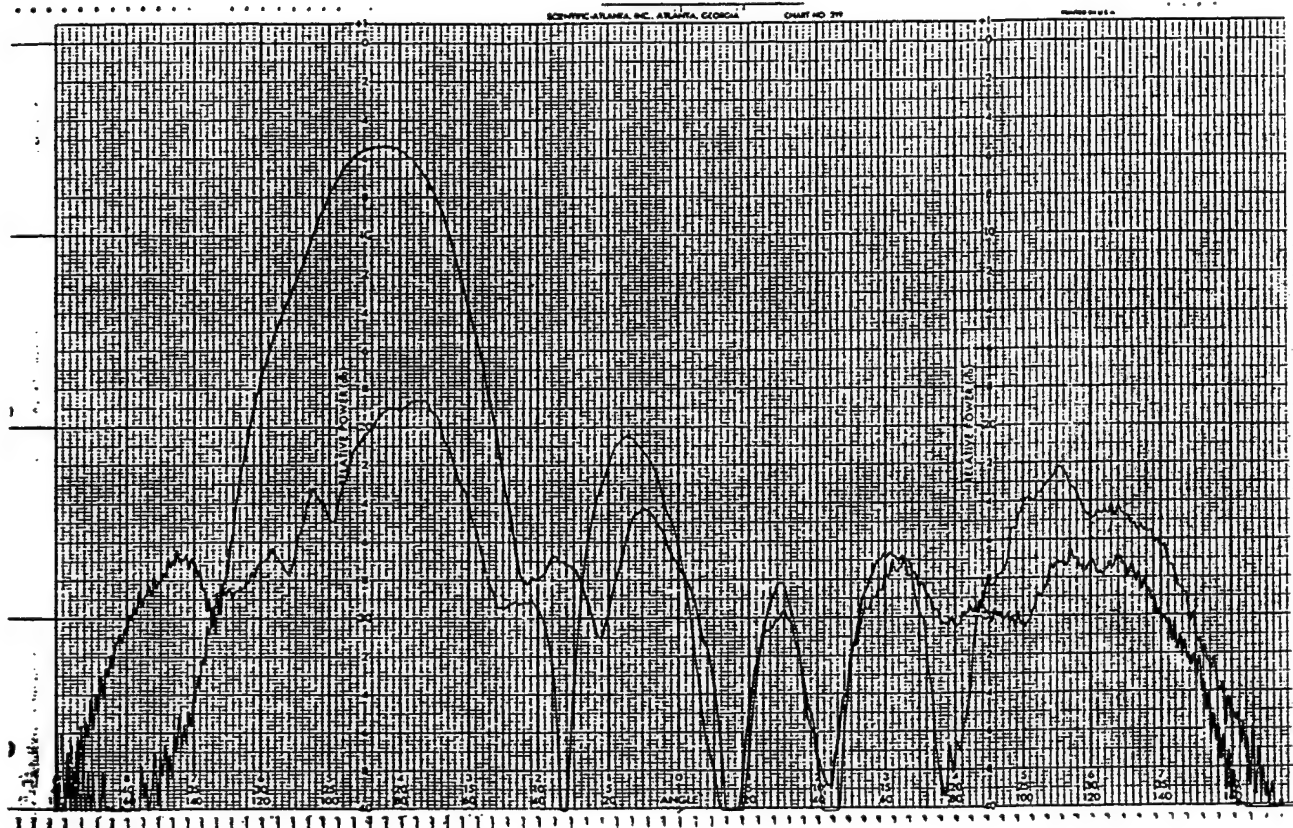


Figure 10b. Scanned Azimuth Pattern Near Center Frequency Showing Cross- Polarized Component

An interesting feature of the cross-pol pattern is the skewed nature of the power distribution. Instead of having a maximum in the same direction as the principal pattern, the cross-pol beam points off to one side by several degrees. This is evident in both the array and the individual element patterns. Dr. Dan Schaubert and others at the University of Massachusetts have studied this phenomenon and attribute it to the asymmetric construction of the radiating element, as noted in Figure 11. The element load is off to one side in this stripline design. Subsequent computer simulations showed that when this load was relocated along slot center line, the cross-pol pattern aligned with the main beam.

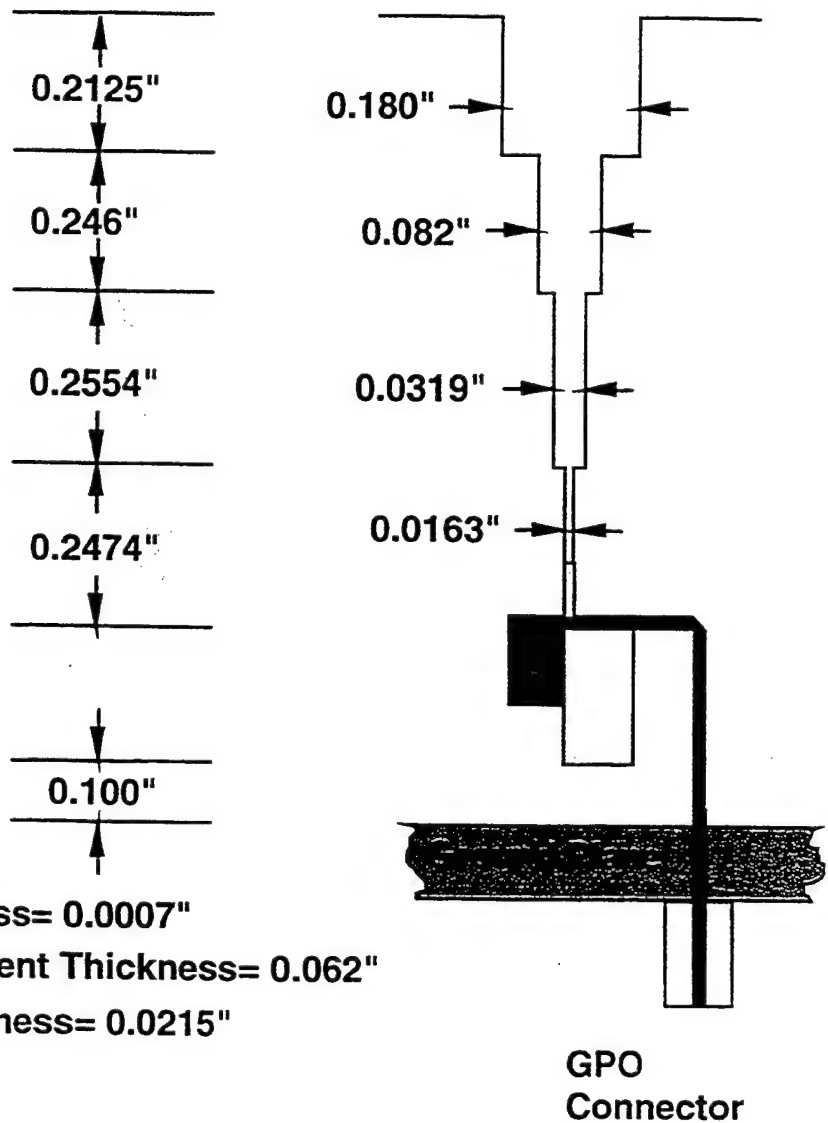


Figure 11. Detail of the Radiating Element Design Showing Asymmetric Load Location

3.4.2 Scanned Beams

Modern ECM transmitters must provide wide angular coverage to assure protection of the ship from attack at all approach angles. The capability to scan to 60 degrees or more was therefore built into the Northrop Grumman/NRL ECM system. Figures 12a and 12b show the antenna beam scanned to plus and minus 45

degrees, and Figure 13a and 13b illustrate a main beam scanned to +30 and -60 degrees, respectively. The transmit frequency was near the low end of the band in Figure 12, and around center frequency for Figure 13.

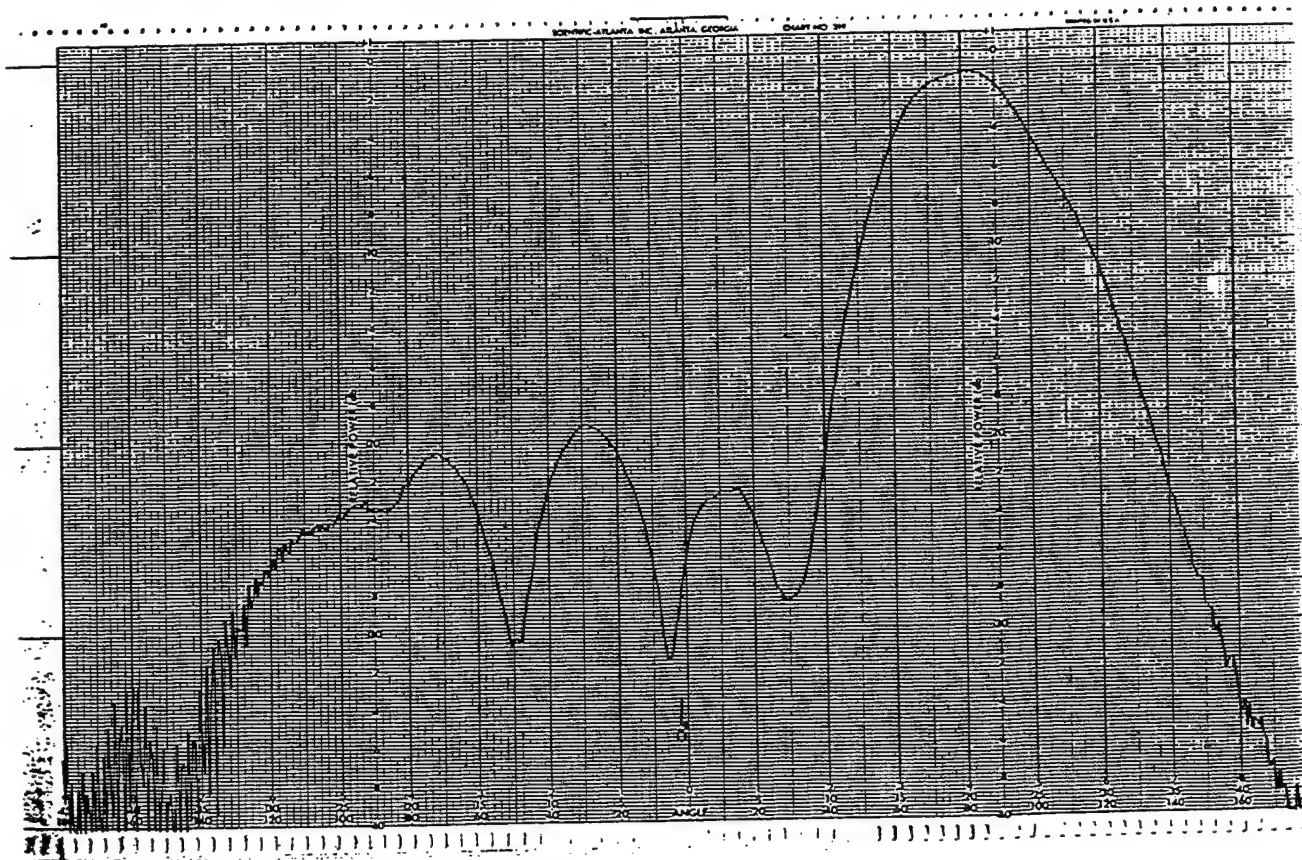


Figure 12a. Azimuth Pattern of Beam Scanned to + 45 Degrees at Low Frequency

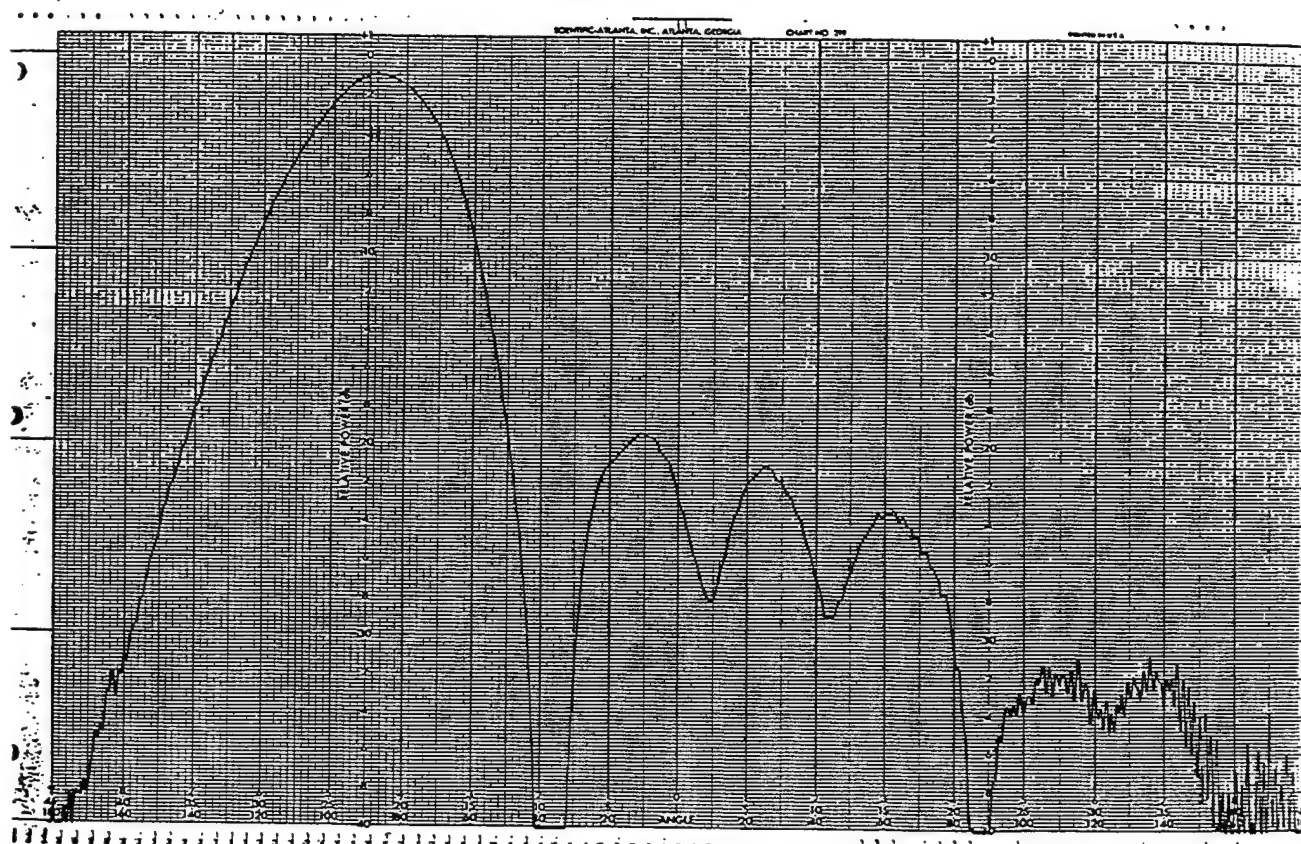


Figure 12b. Azimuth Pattern of Beam Scanned to - 45 Degrees at Low Frequency

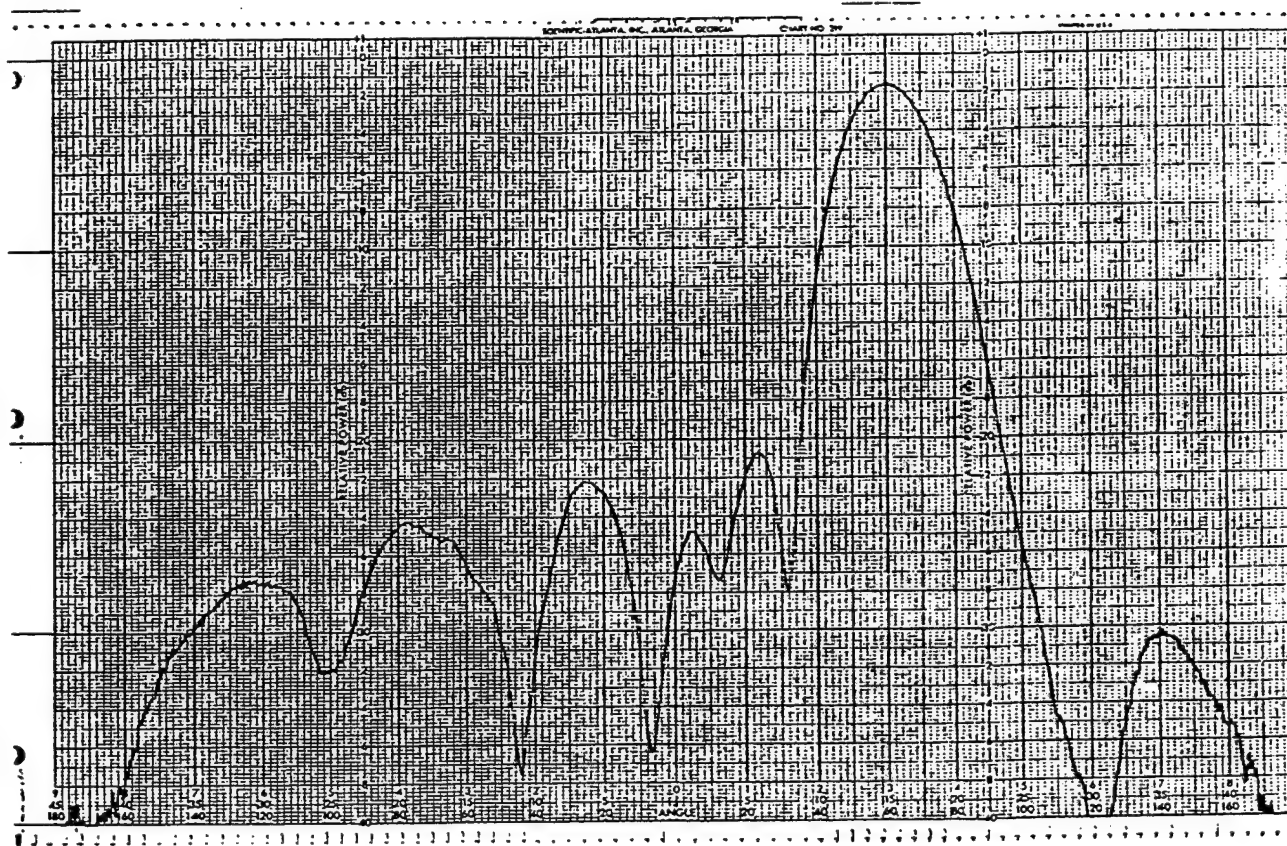


Figure 13a. Azimuth Pattern of Beam Scanned to +30 Degrees Near Center Frequency

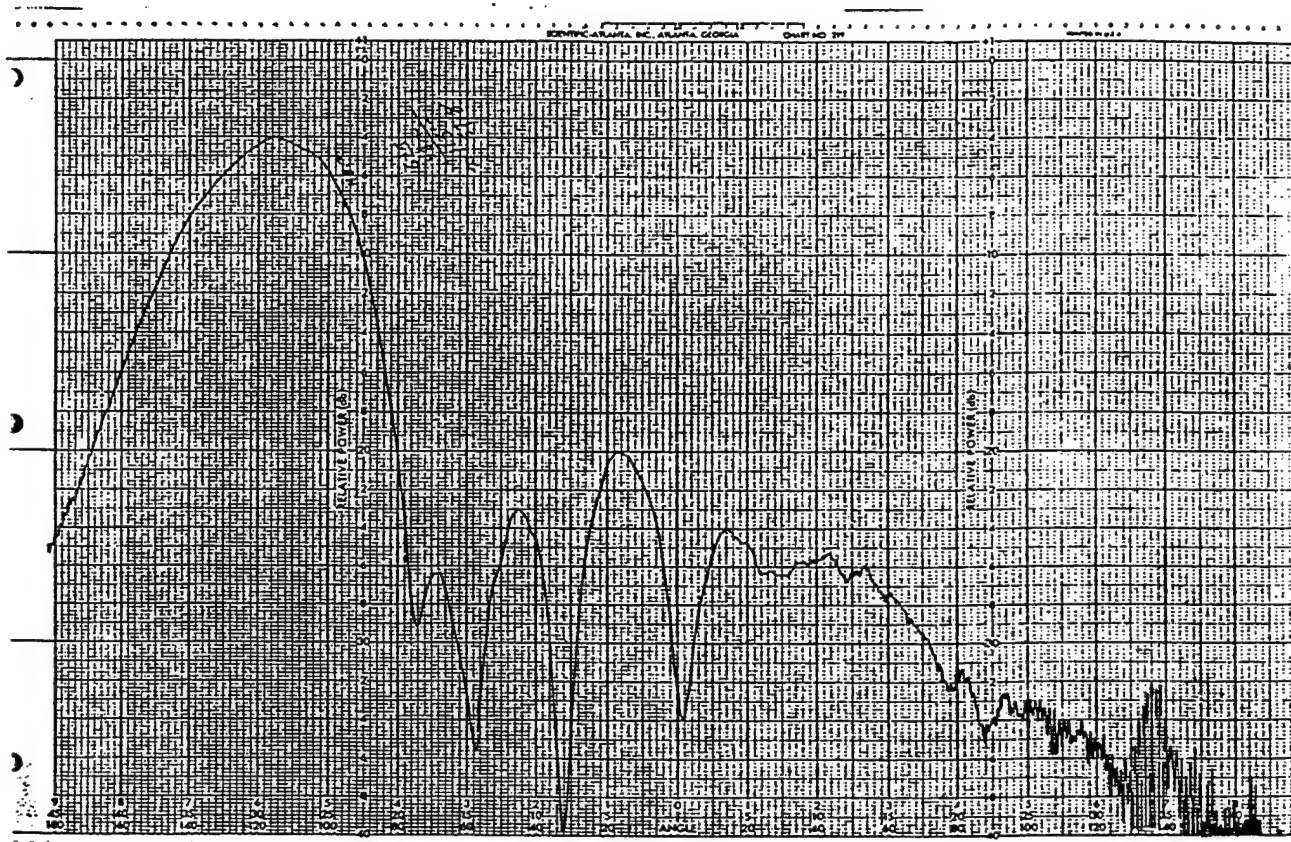


Figure 13b. Azimuth Pattern of Beam Scanned to -60 Degrees Near Center Frequency

3.5 Instantaneous Bandwidth

A wide instantaneous bandwidth is important in ECM transmitters, not only to emit wideband jamming noise, but also to transmit precisely shaped signals used in deception and communication.

Testing of the transmitter instantaneous bandwidth consisted of three steps:

- 1) Tuning the modules and phase shifters to optimize at a nominal frequency such as 9.5 GHz. The stored calibration tables are utilized for this purpose.

- 2) Causing the transmitter to accept and transmit RF from the Techniques Generator at a different frequency, such as 9.0 GHz.
- 3) Observe the pattern degeneration and determine what is acceptable.

Figures 14 and 15 illustrate the test results. Figure 14a is three superimposed patterns of the unscanned transmit antenna tuned to 8.5, 9.0 and 9.5 GHz with the Techniques Generator operating at 9 GHz. Though there is some pattern deterioration, good quality RF can still be reproduced at a receiving site normal to the transmit array.

Figure 14b illustrates three superimposed patterns of the unscanned transmit antenna tuned to 8.0, 9.0 and 10.0 GHz with the Techniques Generator operated at 9 GHz. Though pattern deterioration and some scanning off axis are evident, the directed beam is still useable.

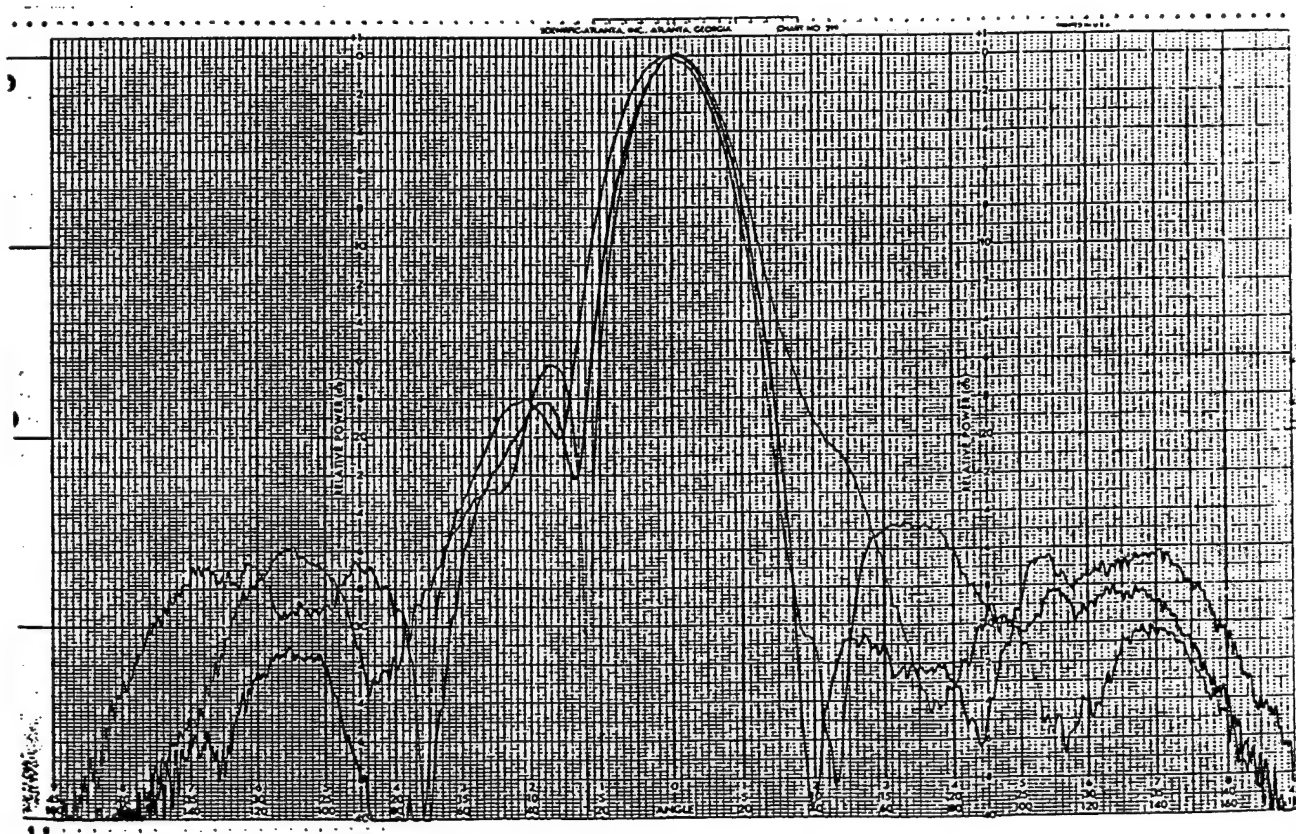


Figure 14a. Three Superimposed Unscanned Patterns Testing Instantaneous Bandwidth of 1 GHz.

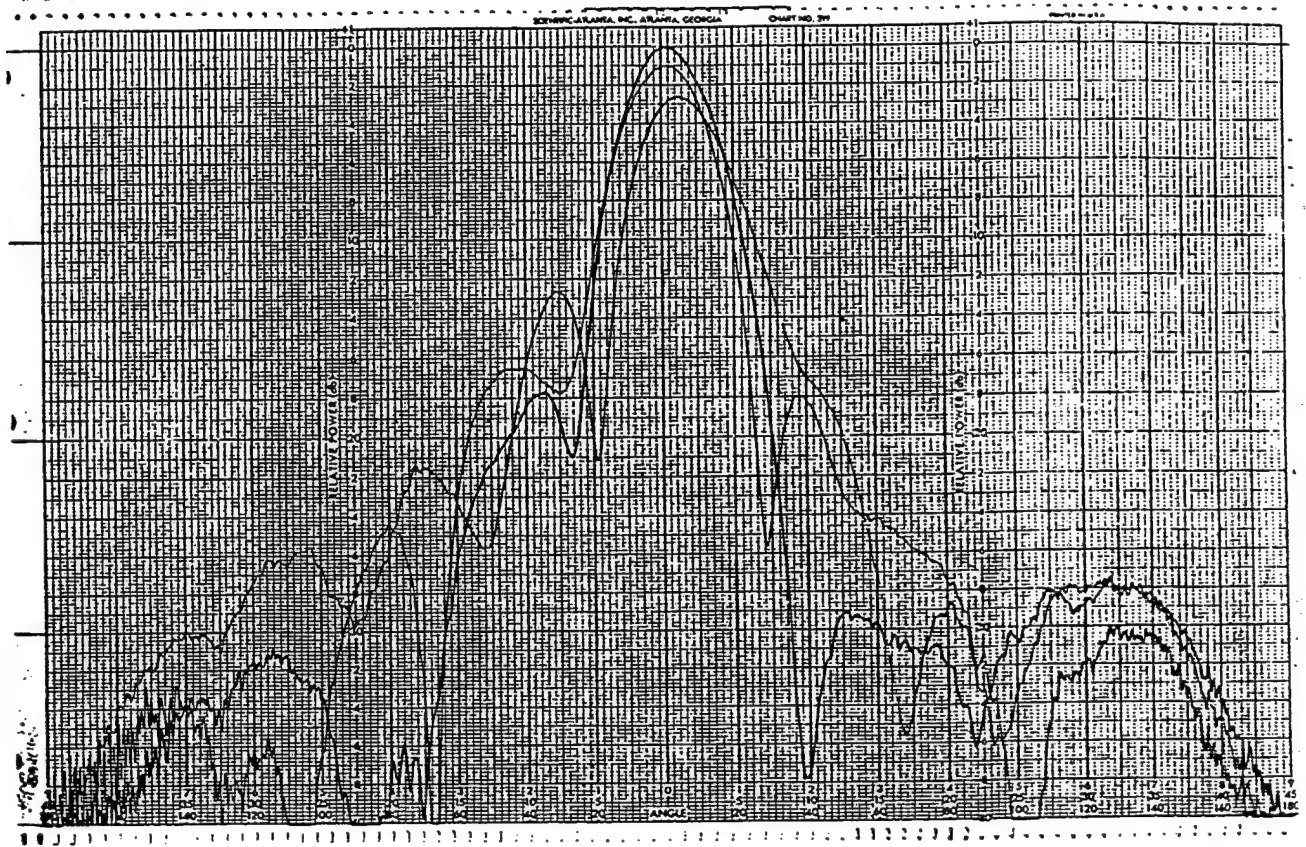


Figure 14b. Three Superimposed Unscanned Patterns Testing Instantaneous Bandwidth of 2 GHz.

Behavior of the array when scanned is seen in Figure 15. Once again, the array modules were tuned to their calibrated values at 8, 9 and 10 GHz, the Techniques Generator operated at 9 GHz, and patterns were recorded. Beam scan deviation is more marked, but since resulting gain loss is less than 1 dB, the error was deemed acceptable.

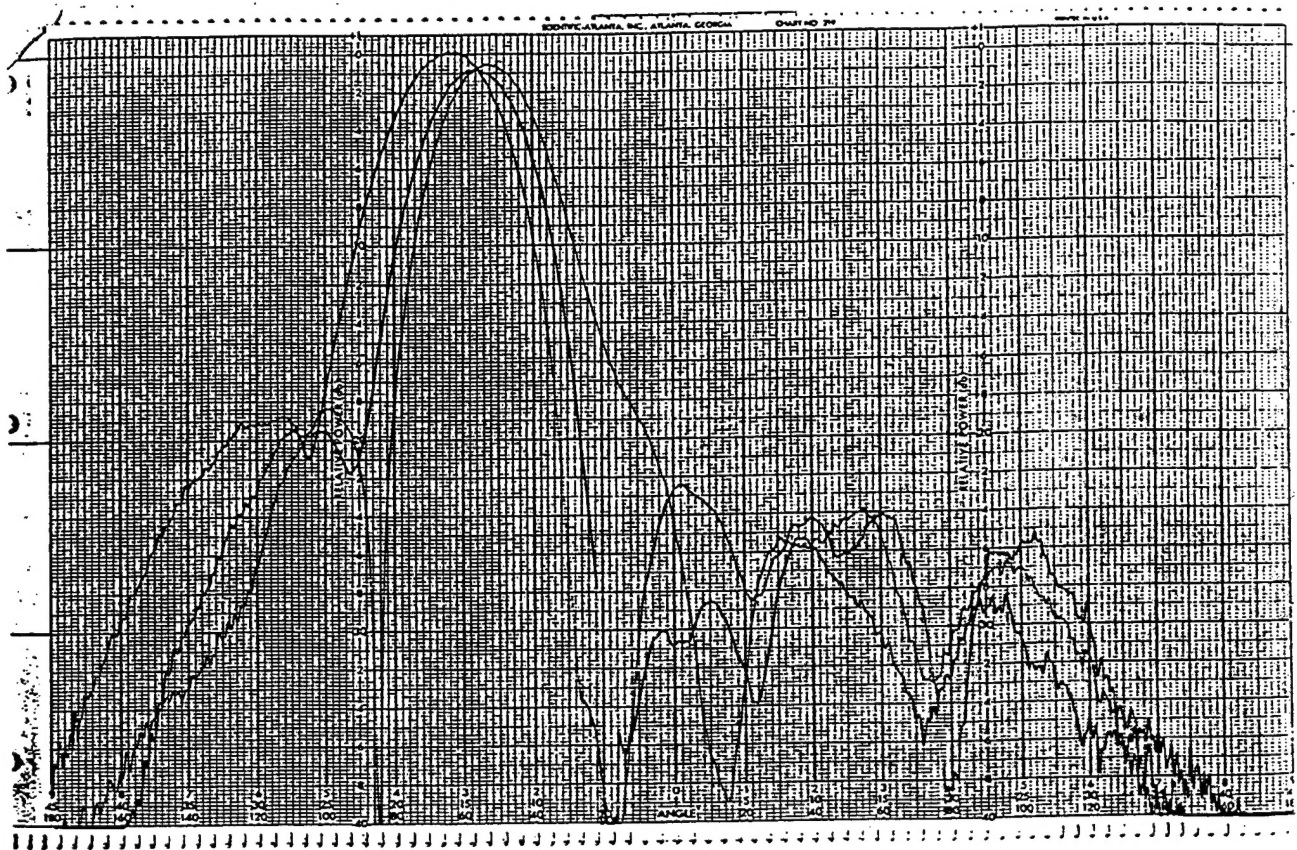


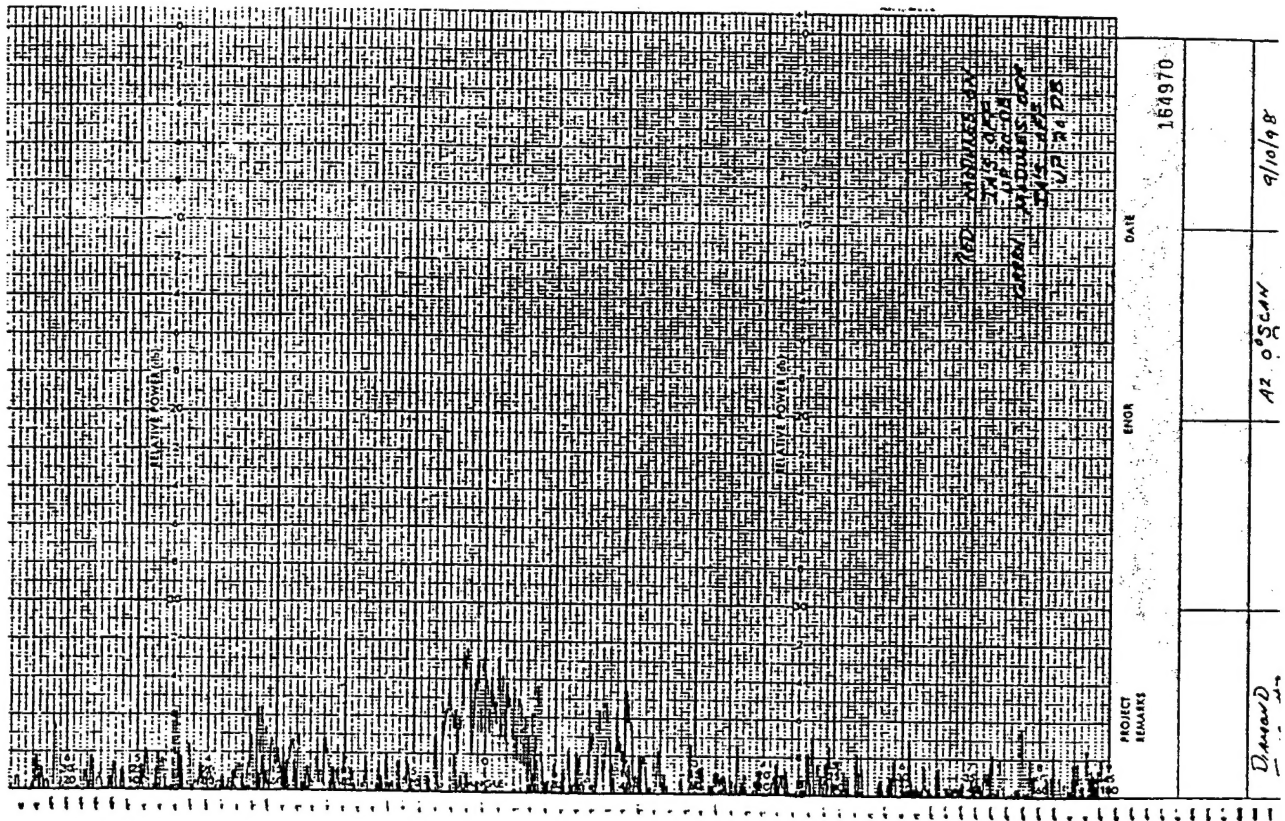
Figure 15. Three Superimposed Scanned Patterns Testing Instantaneous Bandwidth of 2 GHz.

Thus, the ECM transmit array illustrated an instantaneous bandwidth on the order of 2 GHz, ample for transmission of wideband noise as well as deception and communications signals.

4. Unfocussed Noise

It is important to minimize RF radiation from transmitters in the quiescent state. Ships at sea in certain tactical situations do not wish to advertise their presence by turning on their radar or ECM systems. Keeping radiation to a minimum when the transmitters are turned off is therefore critical. Such radiation is called

During the range test, the interface amplifiers were turned off to assure no input from the RF power source. Figure 16 illustrates the results. With the output amplifiers turned off, the outdoor range noise level was on the order of -60 dB below main beam peak. Superimposed over this noise is the trace of array unfocussed noise with the output amplifiers turned on, which showed a maximum value about -50 dB below main beam peak.



536

5. At Sea Testing

The ECM transmit array was operated and evaluated at sea on a research vessel in the Gulf of Mexico. This demonstrated the usefulness of the system and its suitability to the real life situations and environment needed to be an effective EW asset for the Navy.

The array was flush mounted on a convenient broadside surface of the ship. The DC power supply was secured safely below decks. The beam-forming computer was located in the operations room along with the photonics source and the RF Techniques Generator. Coolant and dry nitrogen were fed to the array from below.

The ECM transmit array is fitted with one mutual coupling receive radiator for each quadrant of the aperture. These radiators were remotely monitored as single RF modules were turned on one at a time. The magnitudes of these readings were compared to the same readings taken at the antenna range at Northrop Grumman during the calibration process. This provided a baseline to verify healthy operation of the RF network as well as proper array timing and control. As a final end-to-end check of performance, CW was radiated from the array to a test horn and power meter on the pier. The ERP measured was compared to readings taken previously at the far field range. After making adjustments for the difference in array-to-horn distance, the power readings were as expected.

The underway testing went smoothly. The cooperative engagement with an aircraft lasted for a few hours a day for most of a week. Wide and narrow band techniques were demonstrated by the ECM transmit array, which was being controlled by a PC set up as system controller via an Ethernet. Many different frequencies and modes were successfully demonstrated.

The conclusions drawn from the at-sea exercise are that the ECM transmit array was well suited, both electrically and mechanically, for shipboard applications. The design parameters of the array and associated electronics proved capable of withstanding the rigors of real life conditions, ambient temperature as well as vibration, of operation on board naval ships.

6. References

- 1.) U.S. Patent No. 5,175,560; December, 1992; "Notch Radiator Elements"; E.W. Lucas, M.A. Mongilio, K.M. Leader, C.P. Stieneke, J.W. Cassen; Northrop Grumman Corp.
- 2.) U.S. Patent No. 5,194,875; March, 1993 ; "Notch Radiator Elements"; E.W. Lucas; Northrop Grumman Corp.
- 3.) "A Photonics-Steered, Wideband Phased Array for Shipboard Application"; Dan Bobowicz, Don Collier and John Wojtowicz, Antenna Applications Symposium Digest, September 1997.
- 4.) "Development of a Fiber_Optic Beamformer Network for True Time_Delay Control of an Array Transmitter"; Michael Frankel et al, Antenna Applications Symposium Digest, September 1997.
- 5.) "Wideband Transmit Modules Designed for Production"; Ty L. Barkdoll et al, 1998 IEEE MTT International Symposium, pp.1707-1710, June, 1998.